ROCK PHYSICS OF LOW-POROSITY SANDSTONES FOR SEISMIC RESERVOIR CHARACTERIZATION

A DISSERTATION
SUBMITTED TO THE DEPARTMENT OF GEOPHYSICS
AND THE COMMITTEE ON GRADUATE STUDIES
OF STANFORD UNIVERSITY
IN PARTIAL FULFILLMENT OF THE REQUIREMENTS
FOR THE DEGREE OF
DOCTOR OF PHILOSOPHY

Roseline Emma Rasolovoahangy

August 2002

I certify that I have read this dissertation and that, in my opinion, it is fully adequate in scope and quality as a dissertation for the degree of Doctor of Philosophy.

_____
Amos Nur (Principal Adviser)

I certify that I have read this dissertation and that, in my opinion, it is fully adequate in scope and quality as a dissertation for the degree of Doctor of Philosophy.

_____
Jack Dvorkin (Geophysics)

I certify that I have read this dissertation and that, in my opinion, it is fully adequate in scope and quality as a dissertation for the degree of Doctor of Philosophy.

_____
Gary Mavko (Geophysics)

I certify that I have read this dissertation and that, in my opinion, it is fully adequate in scope and quality as a dissertation for the degree of Doctor of Philosophy.

_____
Jerry Harris (Geophysics)

Approved for the University Committee on Graduate Studies

_____

ABSTRACT

We consider low-porosity sandstones those with porosity below 15%. Gas production from such formations in the U.S. and Canada has played an important role in the past and is likely to be crucial for the future domestic gas supply. According to the Gas Research Institute, the United States currently imports approximately 3 billion barrels of crude oil a year, which is equal, on a Btu basis, to 17 TCF of gas. According to the U.S. Geological Survey, low-porosity gas sands contain more that one-third of the 1,295 TCF technically-recoverable U.S. gas reserves. For this reason, it is very important to improve seismic reservoir characterization in low-porosity gas sands.

The task of this thesis is to develop rock physics techniques for low-porosity sandstone reservoir characterization and then apply these techniques to seismic data. The data come from an Alberta gas field operated by PanCanadian.

The proposed work is subdivided into seven work tasks:

Task 1. Geology background
Task 2. Data organization and quality control
Task 3. Analysis of rock physics trends from log and core data
Task 4. Laboratory measurements and analysis
Task 5. Effective medium model development
Task 6. Upscaling of rock physics transforms
Task 7. Application of rock physics to real seismic

For the last decade the rock physics of low porosity sandstones has been relatively neglected. The practical importance of the proposed work is determined by the importance of improving domestic gas supply. The basic-science contribution and novelty of this study is that for the first time we linked rock physics theory to field well log and seismic data from low-porosity sandstones. Our work went beyond conventional reservoir characterization that is limited to mapping geological structures. We used rock physics relations to map lithology, porosity, and permeability from seismic.

ACKNOWLEDGMENTS

I would like to take this opportunity to offer my deeply felt thanks to everyone who helped, taught, encouraged, and otherwise supported me throughout my graduate study at Stanford.

My foremost thanks go to my advisors Amos Nur and Jack Dvorkin for their continuous support. I am particularly grateful for Dr. Nur's encouragement at critical points in my academic development, and for the countless hours that Dr. Dvorkin devoted to thrashing out challenging questions in rock physics. This dissertation would have been impossible without them.

I feel privileged to have interacted with all my dissertation committee members. I am grateful to Gary Mavko for his illuminating questions and suggestions, and to Jerry Harris for his support and inspiring advice. I thank James Sweeney for chairing my dissertation committee with such grace and humor.

I would also like to offer special thanks to Manika Prasad for her tireless efforts in helping me, especially during the laboratory experiments; to PanCanadian for providing the data and Holger Mandler for his support; to Margaret Muir and Agnes Kehoe for keeping me administratively safe; to Tapan Mukerji for many valuable discussions; to Keehm Youngseuk for his computing wizardry; to my officemate Juan Florez, who was always willing to share a geologists's point of view; and to all the many others at the Stanford Rock Physics Laboratory and the Stanford Geophysics Department who made my years at Stanford so rewarding.

Finally, I would like to thank my family and Peter Hallinan for their great help and caring.

CONTENTS

Chapter 7

UPSCALING

Chapter 8

APPLICATION OF ROCK PHYSICS TO REAL SEISMIC

Chapter 9

CONCLUSION

APPENDIX

LIST OF TABLES

LIST OF FIGURES

CHAPTER 1

INTRODUCTION

1.1 MOTIVATION AND RESEARCH OBJECTIVES

In the U.S. and Canada, gas production from low-porosity sandstones, generally defined as sandstone formation of porosity below 15%, has played an important role in the past and is likely to be crucial for the future domestic gas supply. According to the U.S. Geological Survey, the United States currently consume approximately 94.27 BTU of energy a year, which is equal, on a BTU basis, to 92.12 TCF of gas a year. Low-porosity gas sands contain more that one-third of the 135.1 TCF estimated U.S. gas reserves. For these reasons, it is very important to improve seismic reservoir characterization in low-porosity gas sands.

In the past decade, rock physics has been mainly focused on high-porosity clastic reservoirs. The rock physics of low porosity sandstones has been relatively neglected, yet various technical problems related to low porosity sands remain unsolved. There is a number of geologically dependent interpretation problems related to the complex depositional, diagenetic and structural histories of low porosity, low permeability sandstones. In low porosity sandstones, many grain-contact rock physics models are not valid. Fluid effects are not apparent, so fluid monitoring from seismic is very difficult. Conventional log interpretation techniques sometimes do not accurately define porosity or water saturation in low porosity sands. Problems exist with determination of rock matrix density, clay volume and type, true porosity, and permeability. Another important issue is estimating reservoir quality from logs and seismic.

In particular, in BQ field, the source of the data, the rigorous rock physics models created for high-porosity clastic sediments are not applicable. Permeability in BQ may vary up to 3 orders of magnitude in the same porosity range. The question is how this variation is related to lithology and grain size and how these properties can be inferred from in-situ measurements.

The objective of this thesis is to develop a consistent rock physics methodology for

seismic reservoir characterization in low-porosity sandstone reservoirs. We develop rock physics models from core and log data and then apply these rock physics relations to map porosity, lithology, and permeability from seismic data. The research is data-driven (BQ field in Alberta) and based on rational rock physics. Data at different scales, from laboratory measurements to seismic images are integrated into a unified methodology.

The practical importance of the study is determined by the importance of improving domestic gas supply. The basic-science contribution and novelty is that for the first time we will link rock physics theory to field well log and seismic data from low-porosity sandstones.

1.2 CHAPTER DESCRIPTIONS

The strategy for this thesis is to develop rational rock physics transforms between rock elastic properties, petrophysical properties, and reservoir conditions from core and log data, and then applied these transforms to P- and S- impedance inverted seismic data to enable mapping porosity, lithology, and permeability for low porosity sandstones. This thesis is organized as follows:

Chapter 2 reviews the geological background of the field study. In this chapter, we display the map and the location of the data sources. We review the structural configuration, cross section, the depositional environment, and lithostratigraphy. We summarize the different diagenetic processes such as compaction, cementation, uplift, and dissolution that occurred in this field and their impacts on the rock properties throughout the Paragenetic sequence.

Chapter 3 covers the analysis of the data. In this chapter, we describe all the data available. We display the original well log profiles. We carry out the data organization and quality control. We investigate the effects of drilling mud filtrate invasion on wire line logging tools such as density tool and sonic and dipole tools. We verify the consistency of the well log data with the core data.

Chapter 4 explores the relations between porosity, permeability, and elastic properties in BQ. We cross-plot the petrophysical and elastic properties of the reservoir rocks against each other to reveal the interdependence among them. Then, we identify the main controlling property for sand delineation and characterization. We classify the entire

logged depth into different units based on the characteristics of this main controlling property.

Chapter 5 describes the laboratory experiments setups and the results. We perform laboratory measurements of velocity, porosity, density, and mineralogy on 17 core plugs. These core plugs were selected based on the results from Chapters 2, 3 and 4 to answer questions and resolve problems that will possibly arise from log rock physics analysis. We use the laboratory measurement results to determine the pressure dependence of rock's elastic properties, to quality control log data, to determine the effect of scaling, and to attempt to predict permeability from P-wave velocity.

Chapter 6 is focused on the rock physics diagnostic and theoretical models development. We develop rational rock physics transforms between rock elastic properties, petrophysical properties, and reservoir conditions from core and log data. First, we generate the models to link rock's elastic properties to porosity, lithology, fluid, and pressure. Then second, we establish a link from porosity and lithology to permeability. The final results are transforms, which will be used in Chapter 8, to construct porosity, lithology, and permeability sections from P- and S- impedance inverted seismic data.

Chapter 7 covers the upscaling of rock physics transforms. In this chapter, we determine whether the rock physics models that we developed from core and log data prevail at seismic scale. Our upscaling approach is the moving Backus averaging for the elastic moduli and running mean averaging for porosity and density.

Chapter 8 is the application of rock physics transforms, developed in Chapter 6, to P- and S-impedance inverted seismic data to map porosity, and permeability. In other words, we apply the newly developed rock physics models from Chapter 6 to transform the Ip and Is inverted seismic data to maps of porosity, and permeability. PanCanadian provided real seismic data, processed and inverted for P- and S- impedances.

1.3 REFERENCES

Mavko, G.; Mukerji, T.; Dvorkin, J., 1998, Rock Physics Handbooks, Cambridge University Press.

Spence, B. R., 1997, Sedimentology and Diagenesis of the Basal Quartz Formation, Calgary, Alberta, Master Thesis, University of Calgary, Alberta.

U.S. Geological Survey National Oil and Gas Resource Assessment Team, 1995, 1995 National Assessment of United States oil and gas resources: U.S. Geological Survey Circular 1118, 20 p.

CHAPTER 2

GEOLOGY BACKGROUND

2.1 INTRODUCTION

Understanding the depositional environment, structure configuration, and diagenetic history of the Basal Quartz field is important in developing rock physics models for the advanced characterization of Basal Quartz reservoirs.The term Basal Quartz (BQ) is an informal industry term for the dominantly quartoze sandstone deposited in the basal Mannville Group (Late Jurassic to Early Cretaceous) below the Ostracod Zone in the Western Canada Sedimentary Basin.

The Crossfield/Delacour BQ field has been producing gas since 1966 from the BQ reservoirs. Daily production as of September 3, 2000 is approximately 48 MMcf/d from 39 producing wells. The field has produced approximately 139.5 Bcf with 450 Bcf OGIP (original gas in place) as an initial estimate of reserves.

2.2 LOCATION OF THE DATA SOURCES

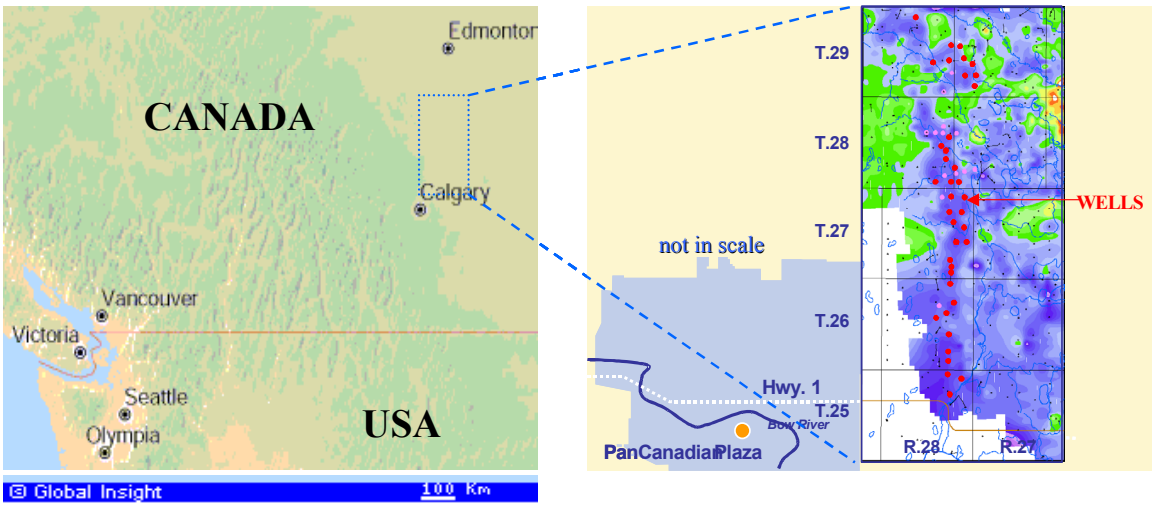

Figure 2.1: Well locations in Crossfield/Delacour BQ field, North East of the city of Calgary; 26 miles long and 1-4 miles wide; 2100 m depth; OGIP estimate of 450 BCF.

The data used in this research come from the Crossfield/Delacour BQ field, which is located adjacent to the city of Calgary (T24 R26W4 to T29 R29W4), Fig. 2.1. It extends from north of Lake Chestemere to north of Airdrie towards Red Deer.

2.3 REGIONAL SETTING

2.3.1 Tectonics and Structure Geology

The BQ formation is within the Lower Cretaceous strata, Fig. 2.2. Jurassic deposits contain detrital K-feldspar and are generally devoid of carbonaceous debris, whereas Cretaceous deposits lack detrital K-feldspar and have significant detrital chert components,. BQ sediments lack K-feldspar and contain abundant chert. Deville is Jurassic age, and consists of clasts and blocks of carbonate and silicified carbonate with a varied matrix of mud and sand.

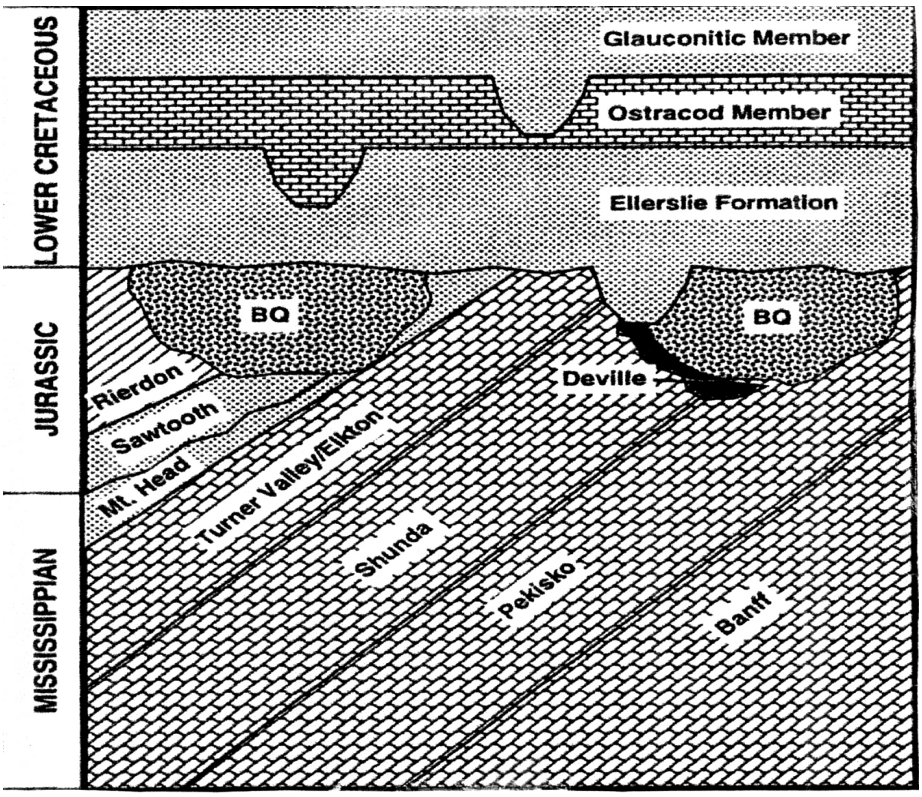

Figure 2.2: Schematic of the stratigraphic relationship from south (left) to north (right) across BQ.

Gamma ray, sonic, and neutron/density well log profiles were used to define the geological formations within the study area, Fig. 2.3 (Spence, 1997). The BQ overlies the Pre-Cretaceous unconformity and is characterized by a gamma curve that implies the sediments decrease in sand content upwards. BQ is subdivided into two sequences, BQA and BQB (Robertson and Edwards, 1994).

The top of the Ellerslie formation occurs 40 – 60 m above the BQ, at the first significant leftward shift of the sonic log curve, which may be a shale associated with a flooding surface. Most of the previous studies interpret the Ellerslie formation as continental sediment. However some studies interpret Ellerslie sediment as deposits of lagoon, estuary, or interdistributary bay environment, suggesting a sea level rise from the north. The top of the Ostracod formation was picked at the last significant leftward shift of the sonic log curve, which may be shale associated with a flooding surface, 10 – 30 m above the Ellerslie formation.

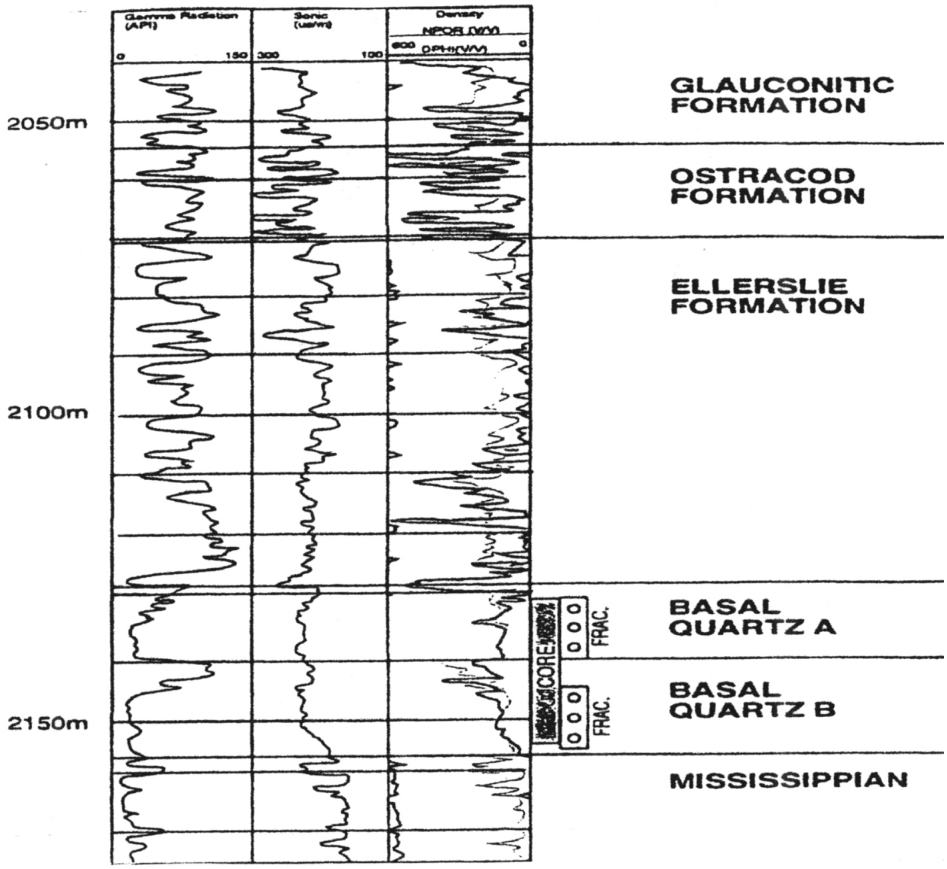

Figure 2.3: Gamma ray, sonic, density log profiles for the illustration of the geological formations.

2.3.2 Facies

Facies are defined as rocks with unique lithologic, sedimentologic, and organic aspect (Middleton, 1978). BQ is classified into six different facies, Fig. 2.4 (Spence, 1997): Facies I consists of chert pebble conglomerate that is mostly deposited at the base of the BQA or BQB. Facies II consists of massive-appearing carbonaceous pebbly sandstones. It is usually less than 50 cm thick and commonly overlays Mississippian strata, but can be less than 20 cm thick, interbedded with Facies III or IIIA. One 25 cm thick zone consists almost entirely of dolomite pebbles. Facies III consists of large-scale bedded sandstones. It is usually confined to the lower 3 - 10 m of each BQ succession, and has an overall fining upward of grain sizes, or gradational upward from Facies I. Facies IIIA consists of apparently massive sandstone with beds commonly 0.5 to 2 m thick, possibly containing mud clasts. Facies IV consists of fine-grained, well-sorted quartzose sandstones. Facies V consists of carbonaceous shale/coal, and U-shaped burrowed sandstone. It is characterized by black massive carbonaceous shale with rare pebbles and sand grains. A 2 to 10 cm thick coal bed occurs predominantly near the top of each succession, but is also interbedded with either facies II or IV, and increases in frequency to the north. Facies I and Facies III compose Facies Association 1, FA1 (Spence, 1997). FA1 is characterized by chert-pebble conglomerates and chert-rich sandstones deposited, fining upwards in 10 - 50 cm thick bed-sets, each eroding into the underlying bed-set, resulting in an overall fining-upwards grain-size trend. FA1 is the principal reservoir unit and can be recognized by a generally blocky gamma radiation log signature. FA1 is interpreted as basal lags, bars, dunes, scour fills and channel-margin deposits in a braided fluvial environment. Facies IV and Facies V compose Facies Association 2, FA2 (Spence, 1997). FA2 is characterized by fine-grained, quartz-rich sandstones with variable mud content and sedimentary structures indicating dominantly uni-directional flow with minor bi-directional flow structures. This indicates that FA2 was deposited in a meandering estuarine tidal channel environment. Facies IIIA probably represents a bedded deposit (facies III) that was deposited rapidly, followed by liquefaction that destroyed all primary-bedding features. Facies II is not characteristic of typical BQ. The most likely source of Facies II sediment is Mississippian strata, which the BQ overlies and erodes. Facies II therefore represents channel margin deposits.

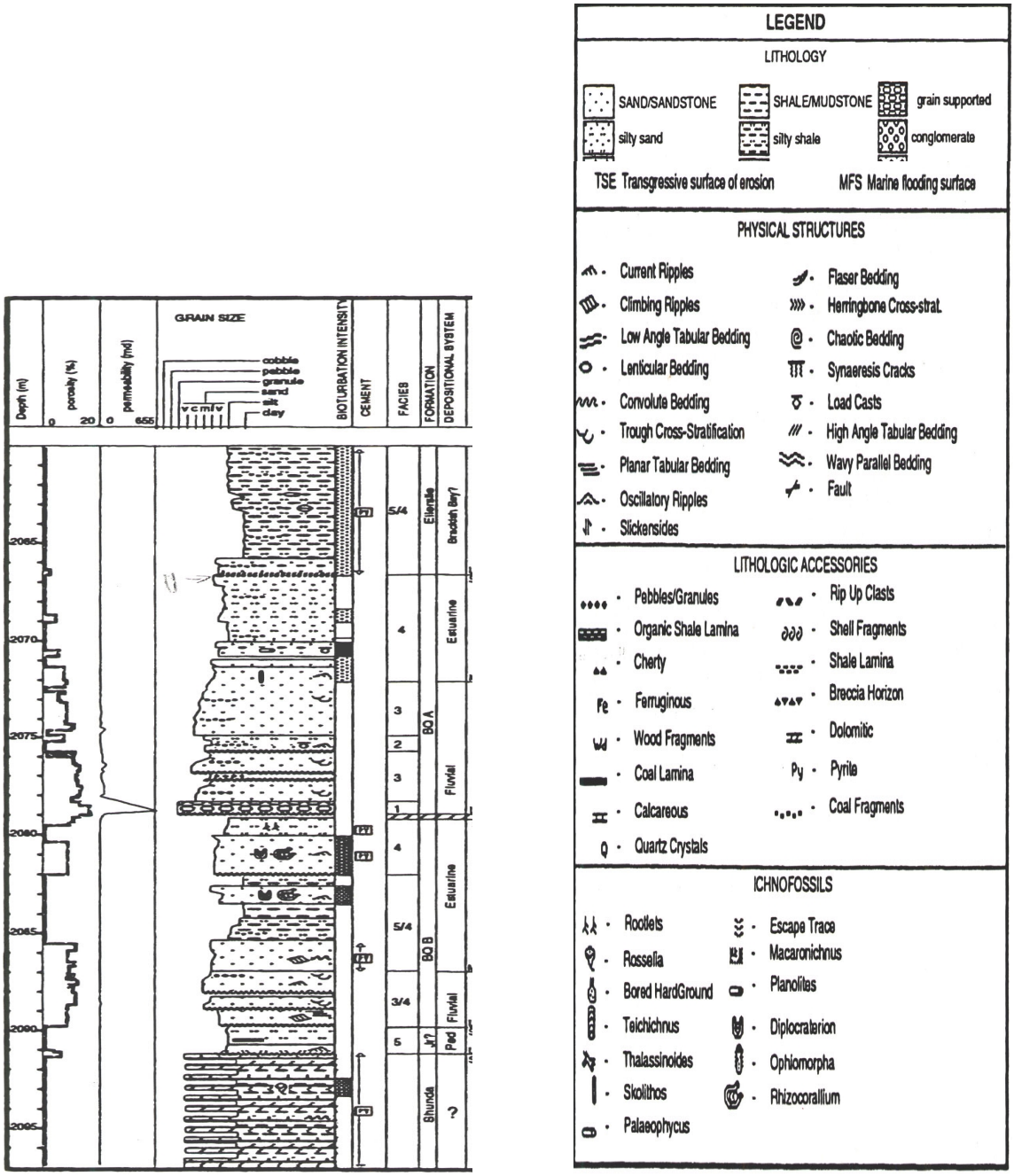

Figure 2.4: Graphic representations of core description, Facies, depositional environment, porosity and permeability from core analysis. Note: the sharp base of BQA at 2079m, and the BQB at 2090m; the existence of two Facies Successions (BQA 2066.5 - 2079 m and BQB 2079 - 2090 m); the overall fining upwards of the grain size trend in both successions.

FA1 and FA2 together form a facies succession. There are two facies successions, the younger BQA and the older BQB. BQA and BQB were deposited during a rising sea

level, and a subsequent fall in sea level and sub-aerial exposure. The facies successions therefore record two transgression-regression cycles (Spence, 1997).

The Crossfield BQ sandstones were deposited in a fluvial environment filling a laterally constructed valley. The BQ valley system at Crossfield is part of a large drainage system that flows northward and empties into the Northern Boreal Sea (Leroux, 2001).

2.4 DIAGENESIS

Diagenesis can be defined as the changes that occur in the character and composition of sediments, beginning from the moment of deposition until the rocks are moved into the realm of metamorphism (Larsen and Chilingar, 1979). Diagenesis includes processes such as compaction, cementation, solution-mediated mineral recrystallization and replacement, dissolution of minerals, coalification and the degradation of organic material and generation of hydrocarbons.

2.4.1 Diagenetic Mineralogy

The dominant diagenetic phases in the BQ are quartz overgrowth, pore-filling kaolinite, pore-rimming and pore bridging illite, pyrite cement and framboids, and rare pore-filling barite cement.

Initial mineralogy controls diagenetic alteration. Additionally, the rate of cementation appears to be a function of the surface area of the grains. Clean quartz seems to be more affected by quartz overgrowth. Fine-grained quartz-rich BQ sands are generally tightly cemented by quartz and not considered potential reservoir rock. However, coarse, chert-rich BQ sands are more affected by compaction, have widely variable porosity, and are the best reservoir quality (Spence, 1997).

The formation water from Mississippian strata tends to be Na-Ca-Cl dominated, while formation water from Mesozoic strata is Na-Cl-HCO3 dominated. Water from Mississippian strata might have mixed with the water in the BQ adjacent to the Jurassic subcrop edge, causing calcite to precipitate. Adjacent to the Jurassic subcrop edge, from T18-23, the BQ formation is highly calcite-cemented.

Quartz-rich estuarine facies are quartz cemented, whereas chert-rich braided fluvial facies contain calcite in places. The exploration efforts for hydrocarbons in BQ have been focused on the braided fluvial facies (north of T23), which have higher reservoir potential than the estuarine facies. South of T18, the strata are heavily compacted and quartz-cemented. Further north of T29, there is a risk of losing the braided fluvial facies (Spence, 1997).

2.4.2 Other Diagenetic Effects

Compaction and dissolution of framework grains and cement have significant effects on the reservoir quality in the BQ field.

2.4.2.1 Compactions

Chemical and mechanical compactions are both reductions in the bulk volume generally induced by lithostatic stresses. Chemical compaction is caused by dissolution of framework grains at points of contact. The volume reduction is characterized by intergranular pressure solution, which produces features such as sutured grain contact and stylolites. Mechanical compaction results from processes other than framework grain dissolution. The volume reduction is characterized by reorientation and repacking of component grains by small scale fractures or cleavage of brittle grains and by plastic deformation of ductile grains. Mechanical compaction dominates the early compaction process in the upper 1000 – 1500 m of burial, reducing the porosity from 40% to 25-30%. Further porosity reduction occurs through chemical compaction, which dominates during later burial stages. Compaction played the largest role in porosity reduction in BQ sediment (Spence, 1997).

Quartz overgrowth may preserve the porosity during burial by propping pores to open. Similarly, the mineral coating may inhibit quartz cementation and preserve primary porosity during burial.

2.4.2.2 Dissolution

Framework grain and cement dissolution can restore some of the porosity lost to compaction and develop secondary porosity. Secondary porosity development may have occurred in the BQ sediments, partially by chert grain dissolution and dissolution of

calcite cement during uplift. To have this secondary porosity preserved, the sediment could not have been subjected to further burial after dissolution.

2.4.3 Paragenetic sequences

"Paragenetic sequence" refers to the order in which diagenetic events have occurred. Fig. 2.5 shows the proposed paragenetic sequence along with the burial history curve for the Lower Cretaceous in the study area.

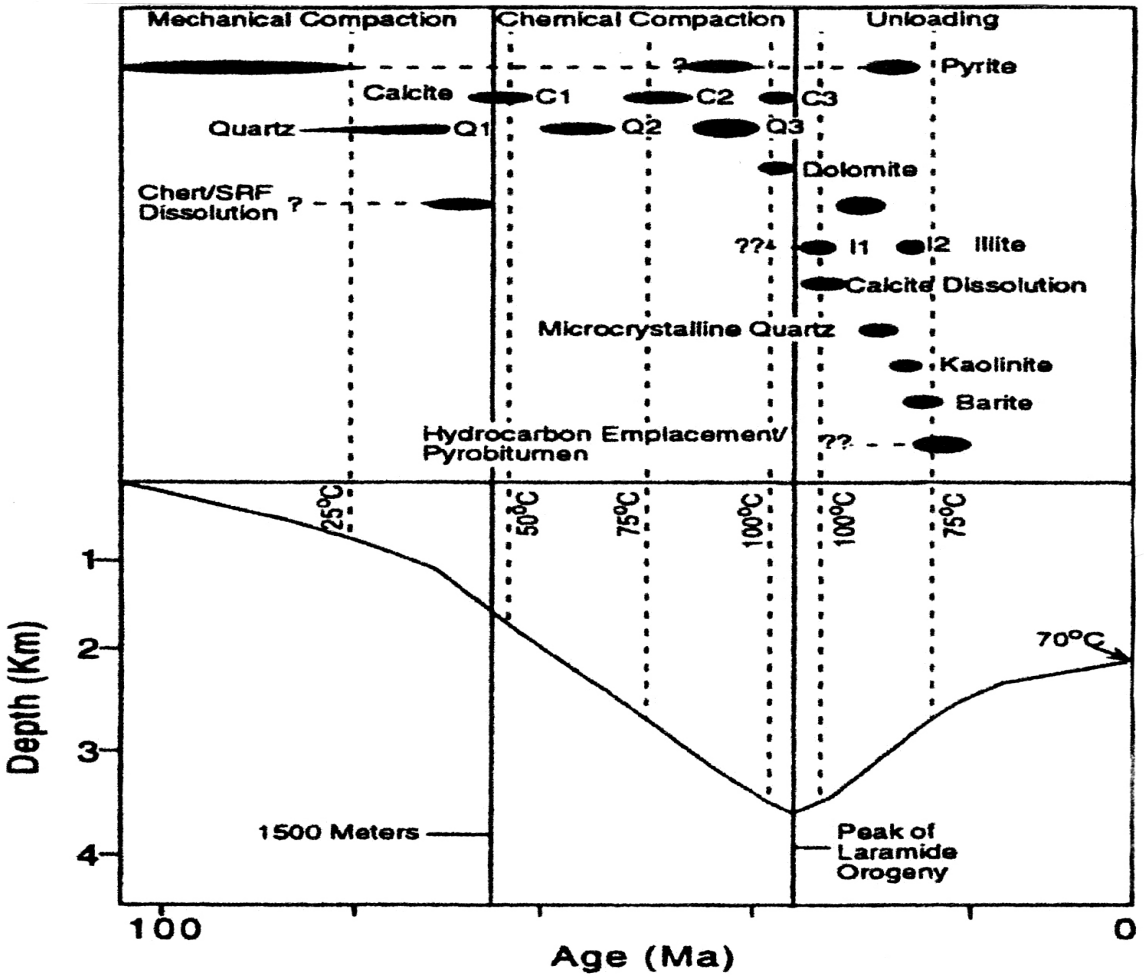

Figure 2.5: Paragenetic sequence of the BQ formation. The width of the symbols represents the magnitude of the diagenetic alteration. Dashed lines for pyrite, hydrocarbon emplacement, and chert dissolution indicate uncertainty of timing and magnitude of diagenetic alteration. Formation temperatures were calculated using a geothermal gradient of 25°C/km and 5°C surface temperature; the present reservoir temperature is 70°C. The burial history curve is modified after Creaney and Allan (1990). 1500 meters is approximately where mechanical compaction reduces porosity to –26%; chemical compaction is responsible for any further porosity loss (Spence, 1997).

During early burial in the upper 1000–1500 m, the initial porosity of BQ sands was decreased mainly due to rearrangement and repacking of grains. More porosity reduction was due to first calcite cementation at depths to about 1500m. Further porosity reduction occurs through chemical compaction processes during later burial stages. Most porosity in the fine-grained quartz sandstone has been filled by the quartz overgrowth, resulting in non-hydrocarbon potential rocks. Grain coating by clay and organic matter may inhibit quartz cementation and thus may preserve primary porosity during burial. Peripheral dissolutions of calcite cement may result in elongated pore geometry and thus may enhance permeability by improving the interconnection between pores.

2.5 CONCLUSIONS

- BQ is classified into six different facies, which are regrouped into two Facies Associations, FA1 and FA2. FA1 is characterized by chert-pebble conglomerates and chert-rich sandstones, and is the principal reservoir unit. FA2 is characterized by fine grain quartz-rich sandstones with variable mud content and sedimentary structures. FA1 and FA2 form two Facies Successions, the younger BQA and the older BQB. Both Facies Successions exhibit a general fining-upward grain size trend.
- The Crossfield BQ sandstones were deposited strictly in a fluvial environment filling a laterally constructed valley. The valley fills are comprised of several facies, including chert-clast breccias, pebbly sandstones and silt-to-mudstones (Leroux, 2001).
- The dominant diagenetic phases in the BQ are quartz overgrowth, pore-filling kaolinite, pore-rimming and pore bridging illite, pyrite cement and framboids, rare pore-filling barite cement, compaction, and dissolution. Compaction played the largest role in porosity reduction in BQ sediment.
- Fine-grained, quartz-rich BQ sands (FA2) are generally tightly cemented by quartz and are generally not considered potential reservoir rock. However, coarse, chert-rich BQ sands (FA1) are more affected by compaction, have widely variable porosity, and are the best reservoir quality.
- The BQ is suspected to have experienced secondary porosity generation due to calcite and chert grain dissolution during uplift.

2.6 REFERENCES

Creaney, S. and Allan, J., 1990, Hydrocarbon generation and migration in the western Canada sedimentary basin, in Brooks, J. (ed.), Classic Petroleum Provinces, Geological Society Special Publication #50, p.189-202.

Larsen, G., and Chilingar, G. V., 1979, Introduction – diagenesis of sediments and rocks, Chapter 1, in Larsen, G. and Chilingar, G. V. (eds.), Diagenesis in Sediments and Sedimentary Rocks. Developments in Sedimentology 25A, Elsevier Scientific Publishing Company, New York, p. 1-29.

Leroux, S., 2001, Geology of Basal Quartz in Crossfield, International Conference on Fluvial Sedimentology in Nebraska.

Middleton, G. V., 1978, Fairbridge, R. W., and Bourgeois, J., (eds) Encyclopedia of seimentology: Stroudsburg, Pennsylvania, Dowden, Hutchinson and Ross, p. 323-325.

Robertson, B., Edwards, D., 1994, Crossfield/Delacour: anatomy of Lower Manville channel play; Canadian Society of Exploration Geophysicist and Canadian Society of Petroleum Geologists Joint National Convention, program, Expanded Abstracts and Biographies, Calgary, Alberta, p.169.

Spence, B. R., 1997, Sedimentology and Diagenesis of the Basal Quartz Formation, Calgary, Alberta, Master Thesis, University of Calgary, Alberta.

CHAPTER 3

DATA DISPLAY AND QUALITY CONTROL

3.1 INTRODUCTION

The data used in this study came from the BQ Crossfield, a large low-porosity gas field located in Alberta east of Calgary. The well log data include P- and S-wave velocity, gamma ray (GR), spontaneous potential (SP), bulk density (ρ_B), neutron density (ϕ_N), deep and shallow resistivity (Rt, Rxo), and caliper (Cali). The core data include porosity, permeability, gamma ray, grain density, and water saturation. Additional information including lithology description and thin sections are also available from few wells. Selected core plugs are available to conduct our own measurements of velocity, porosity, and permeability at the Stanford Rock Physics Laboratory. Furthermore, 3D seismic data, including inversion for P- and S-wave impedance and $\lambda\rho$ and $\mu\rho$ are provided.

The objective of this chapter is to display, analyze, and determine the reliability of the core and well log data.

3.2 DISPLAY OF THE DATA

In Figures 3.1 to 3.11, we display the original well log profiles of the BQ sands from 11 wells located in the BQ Crossfield. The curves displayed are gamma ray (GR), P-wave velocity (Vp), S-wave velocity (Vs), bulk density (RHOB), density porosity (PHID) with the core porosity superimposed on top, and the deep resistivity. Figure 3.1 to 3.11 show that the gamma ray values in BQ sands range between 15 GAPI and 120 GAPI, the P-wave velocity values range between 3.5 km/s and 5.5 km/s, the S-wave velocity values range between 2.25 km/s and 3.25 km/s, the porosity values range between 0% and 15%, and the deep resistivity values range between 5 ohm-m and 75 ohm-m. The gamma ray profiles exhibit two thick clean sand layers (channels): the upper channel (6 - 11m thick) and the lower channel (4 – 8 m thick). The upper channel and lower channel depicted

here correspond to the BQA and BQB by Robertson and Edwards (1994), and the Facies Successions 1 and 2 by Spence (1997).

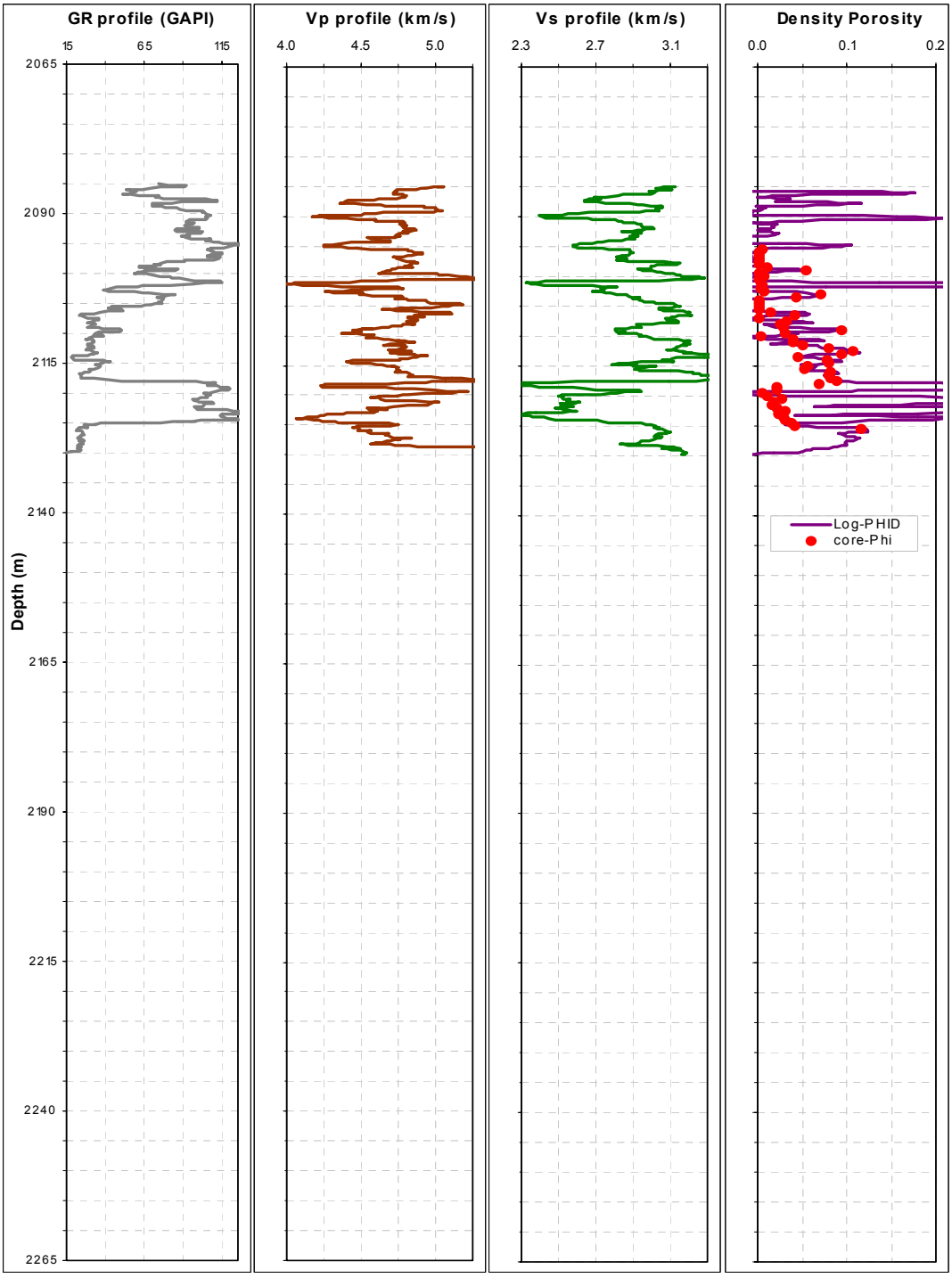

Figure 3.1: Well log profiles: gamma ray, P-wave velocity, S-wave velocity, and density porosity with the core porosity superimposed on top; original data from the upper and lower channels of well WA in BQ field.

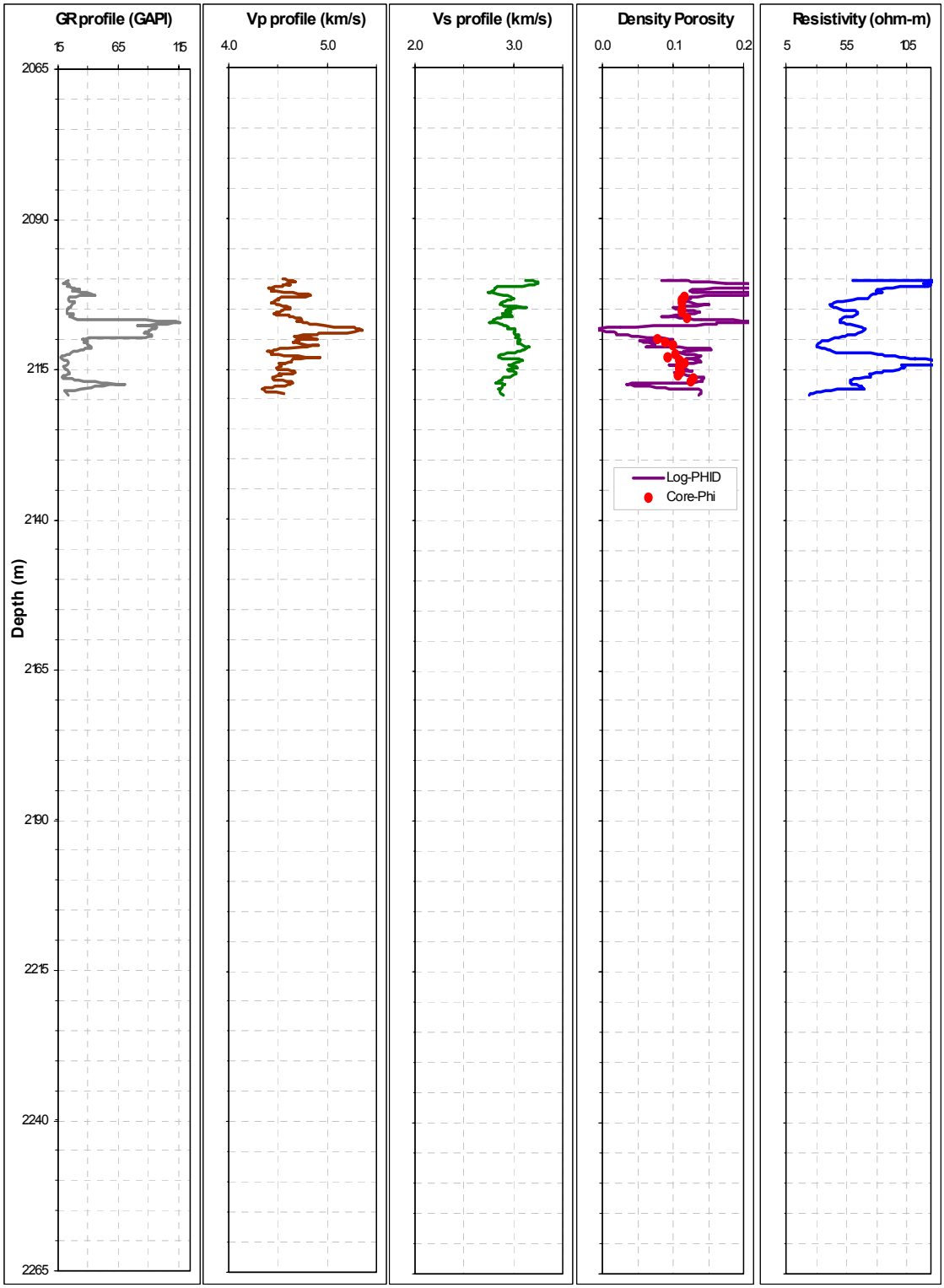

Figure 3.2: Well log profiles: gamma ray, P-wave velocity, S-wave velocity, density porosity with the core porosity superimposed on top, and deep resistivity; original data from the upper and lower channels of well WB in BQ field.

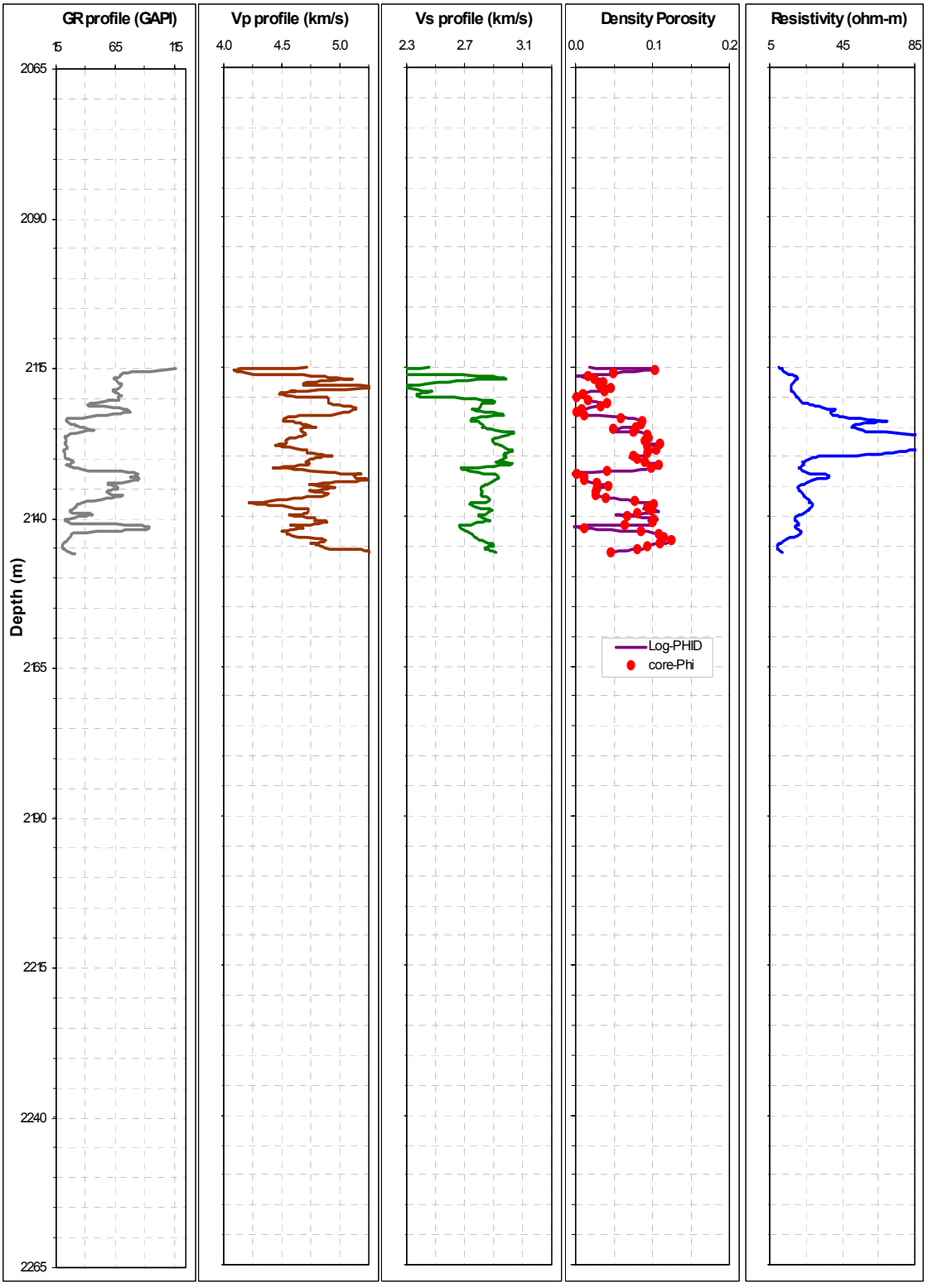

Figure 3.3: Well log profiles: gamma ray, P-wave velocity, S-wave velocity, density porosity with the core porosity superimposed on top, and deep resistivity; original data from the upper and lower channels of well WC in BQ field.

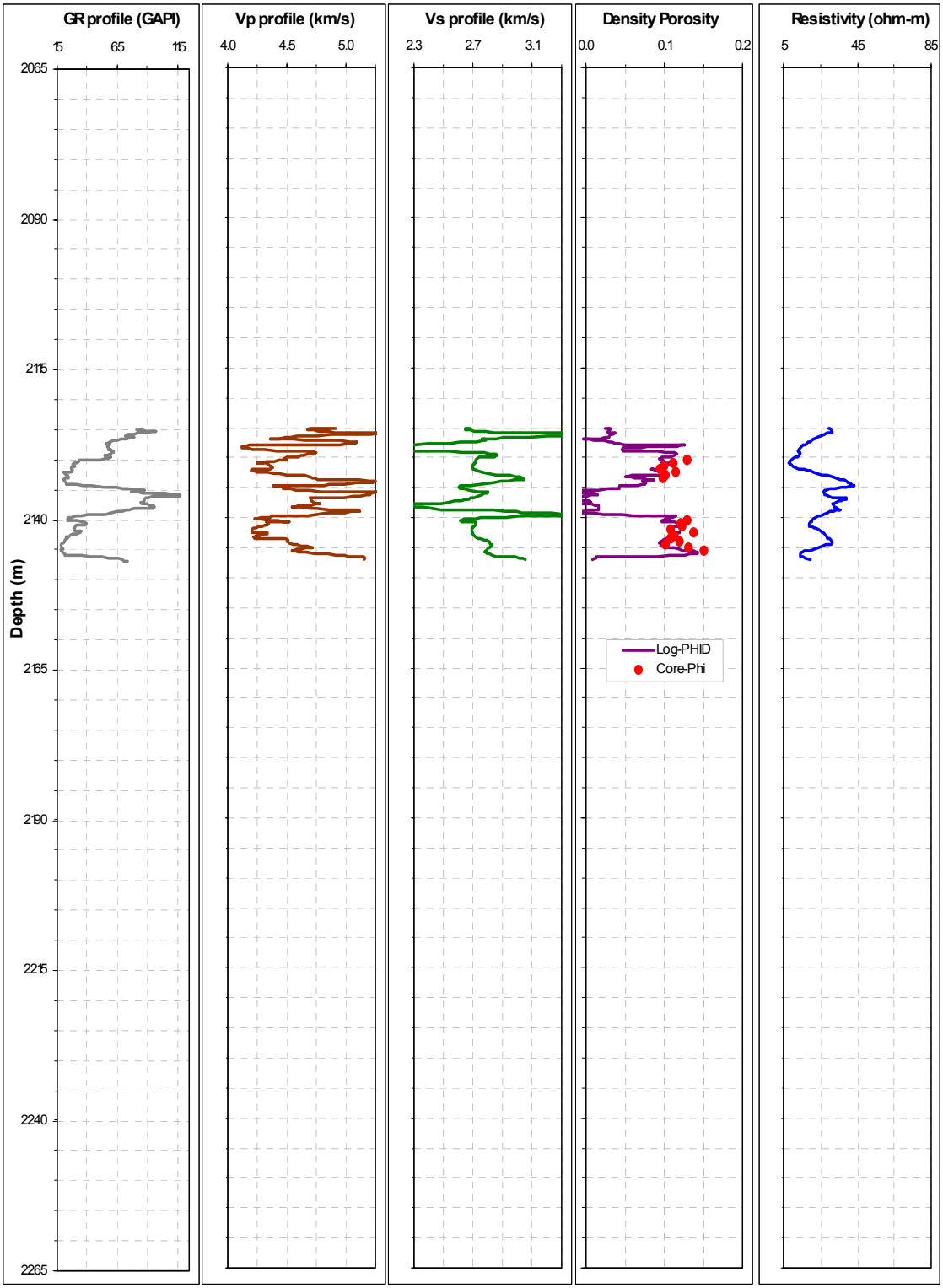

Figure 3.4: Well log profiles: gamma ray, P-wave velocity, S-wave velocity, density porosity with the core porosity superimposed on top, and deep resistivity; original data from the upper and lower channels of well WE in BQ field.

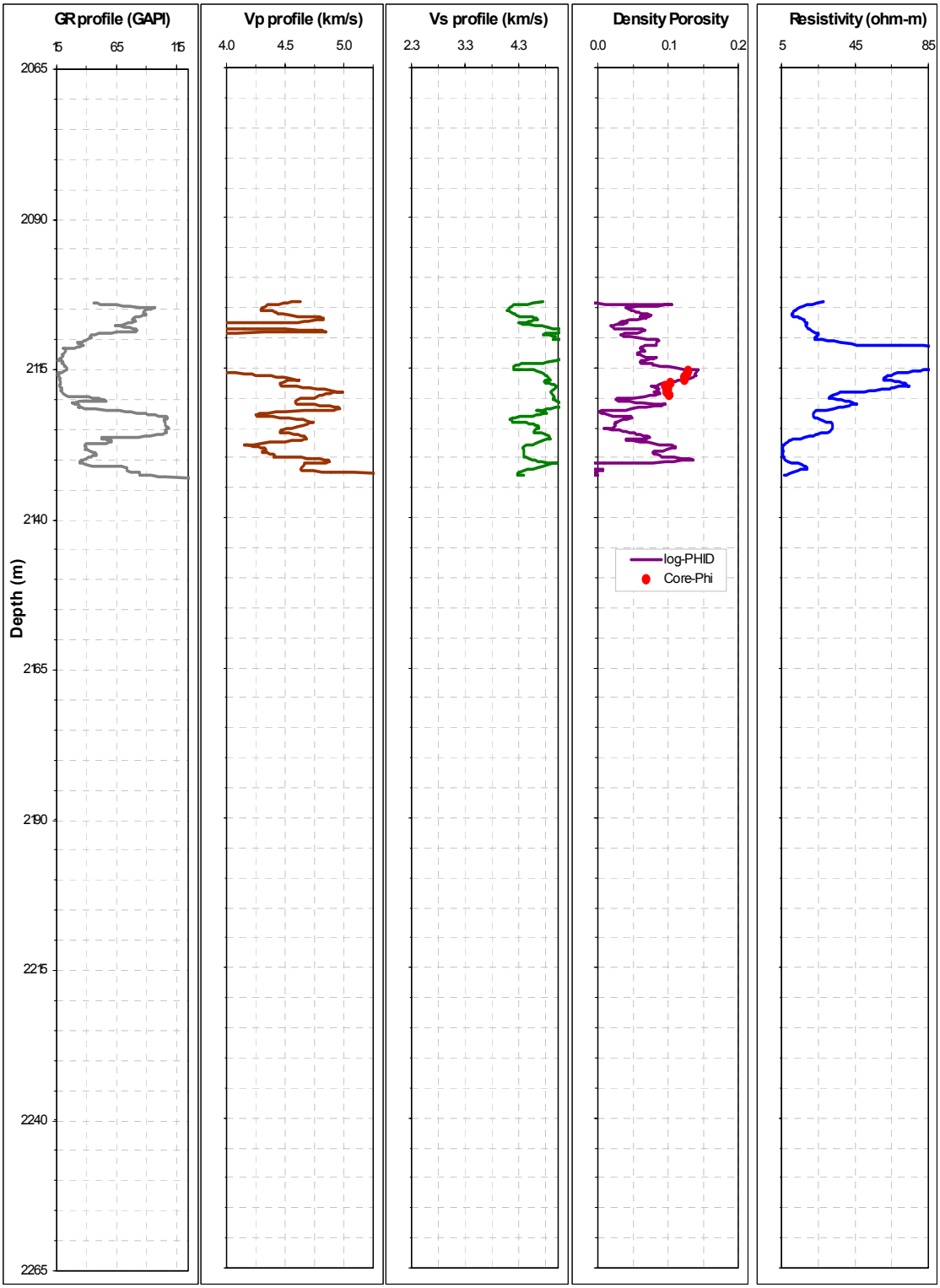

Figure 3.5: Well log profiles: gamma ray, P-wave velocity, S-wave velocity, density porosity with the core porosity superimposed on top, and deep resistivity; original data from the upper and lower channels of well WH in BQ field.

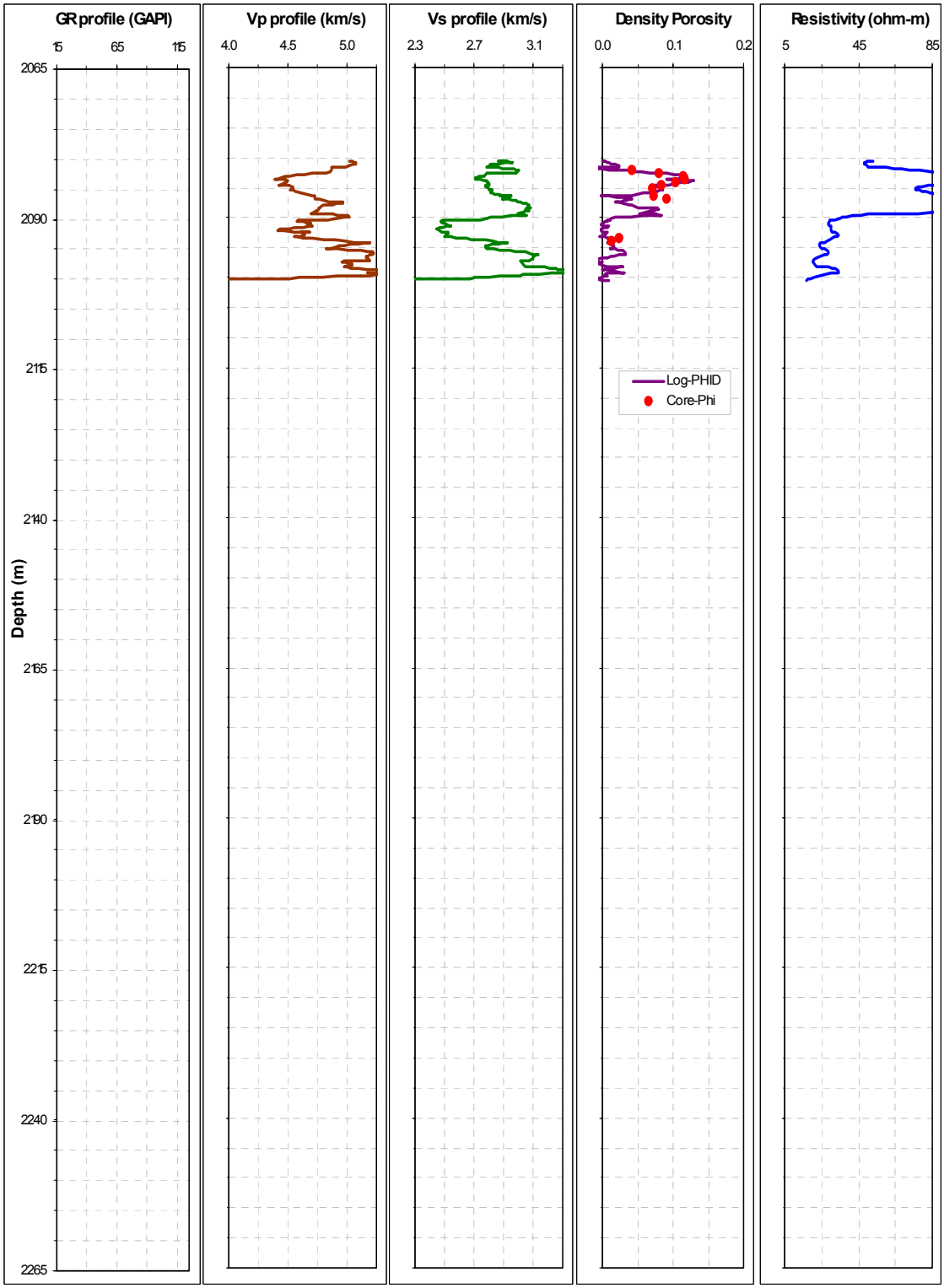

Figure 3.6: Well log profiles: gamma ray, P-wave velocity, S-wave velocity, density porosity with the core porosity superimposed on top, and deep resistivity; original data from the upper and lower channels of well WK in BQ field.

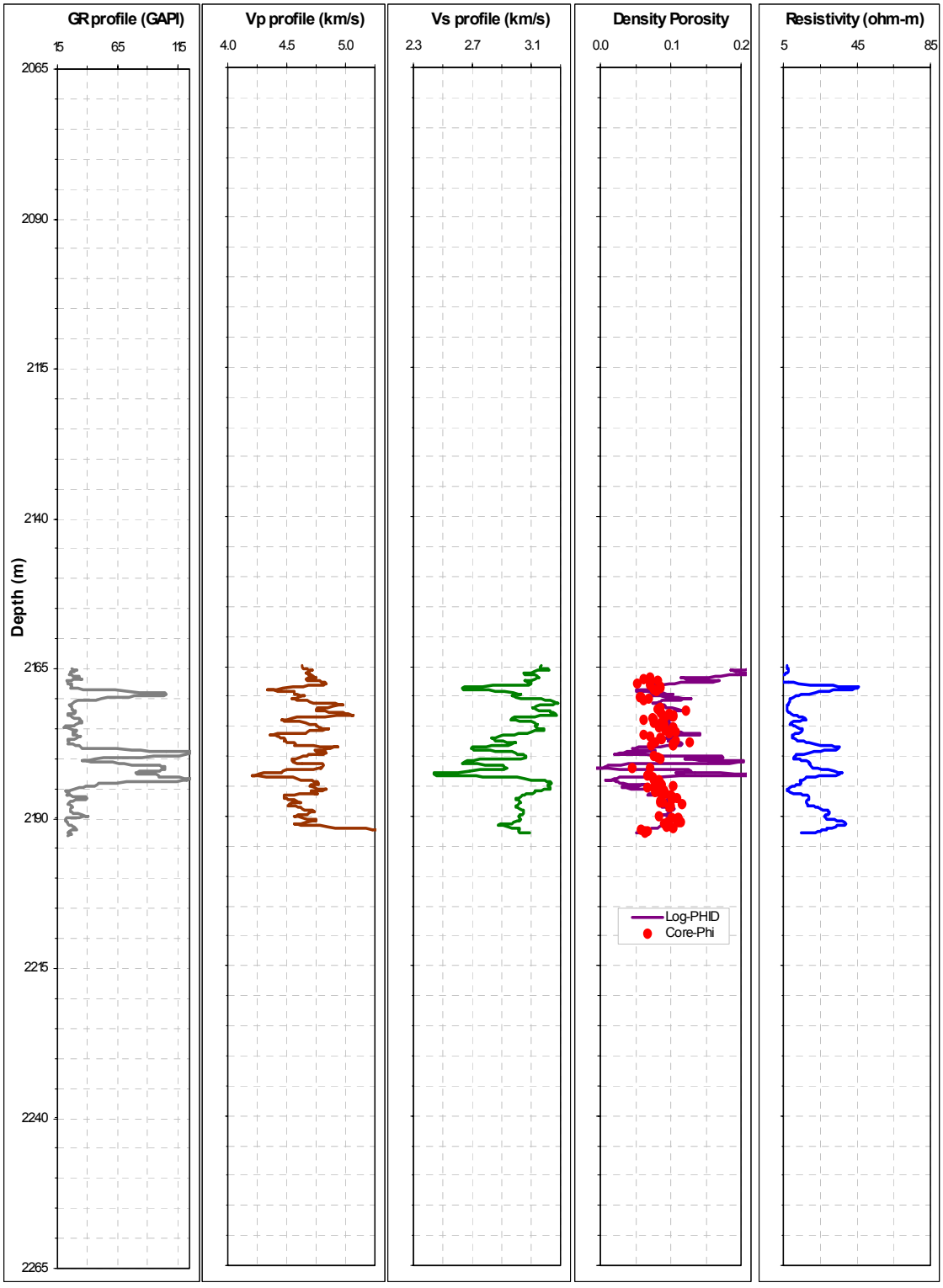

Figure 3.7: Well log profiles: gamma ray, P-wave velocity, S-wave velocity, density porosity with the core porosity superimposed on top, and deep resistivity; original data from the upper and lower channels of well W1 in BQ field.

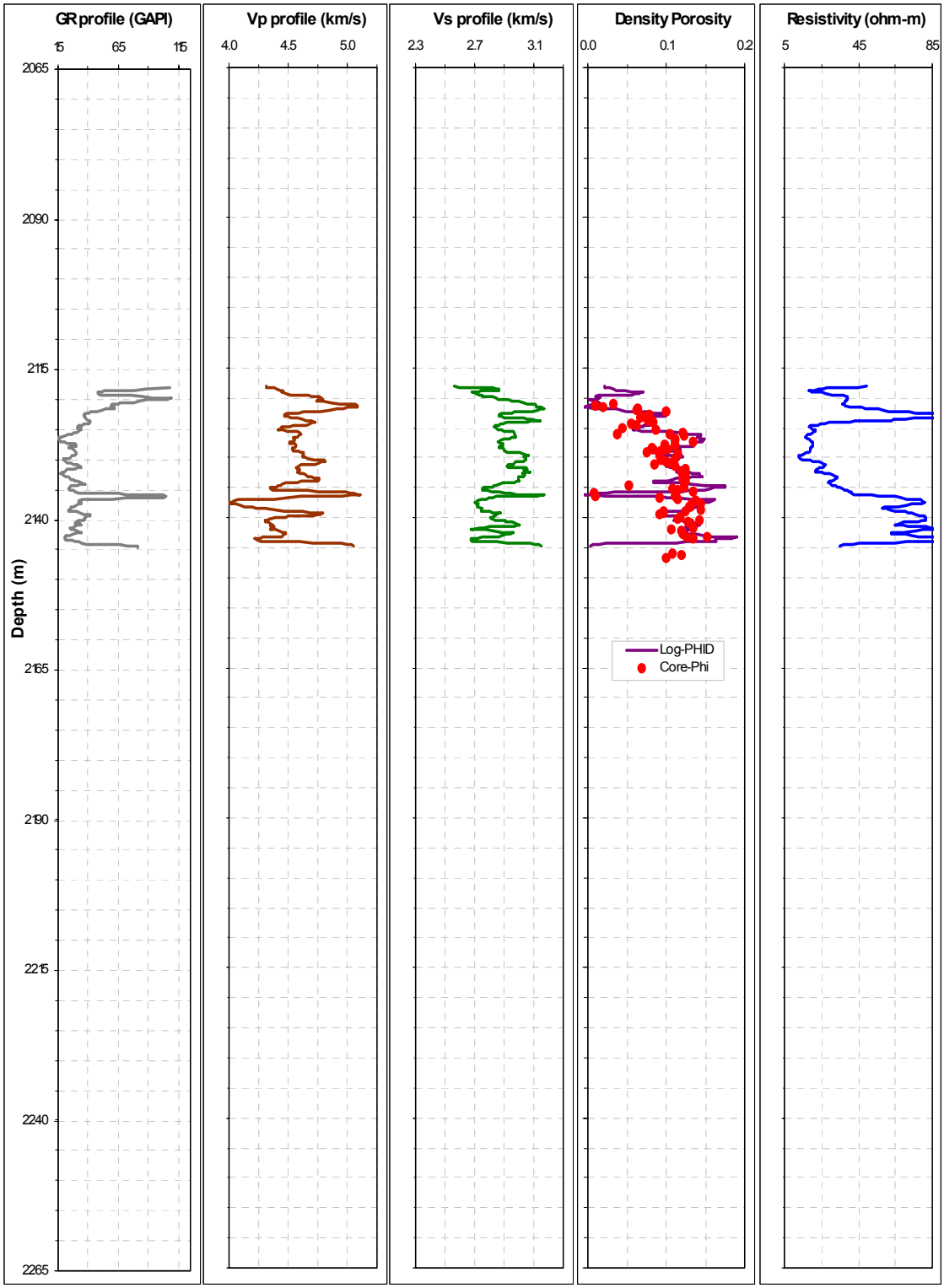

Figure 3.8: Well log profiles: gamma ray, P-wave velocity, S-wave velocity, density porosity with the core porosity superimposed on top, and deep resistivity; original data from the upper and lower channels of well W2 in BQ field.

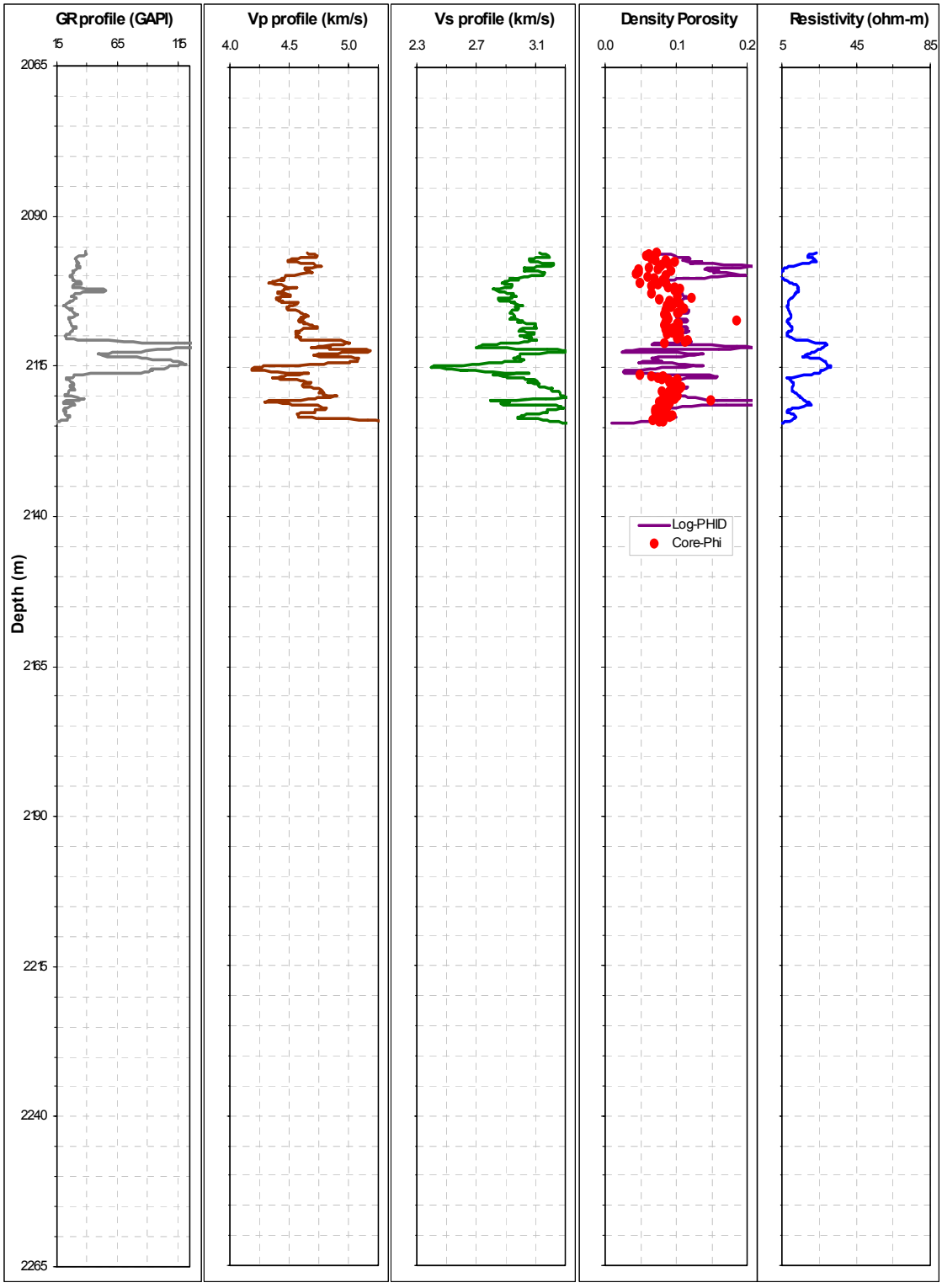

Figure 3.9: Well log profiles: gamma ray, P-wave velocity, S-wave velocity, density porosity with the core porosity superimposed on top, and deep resistivity; original data from the upper and lower channels of well W3 in BQ field.

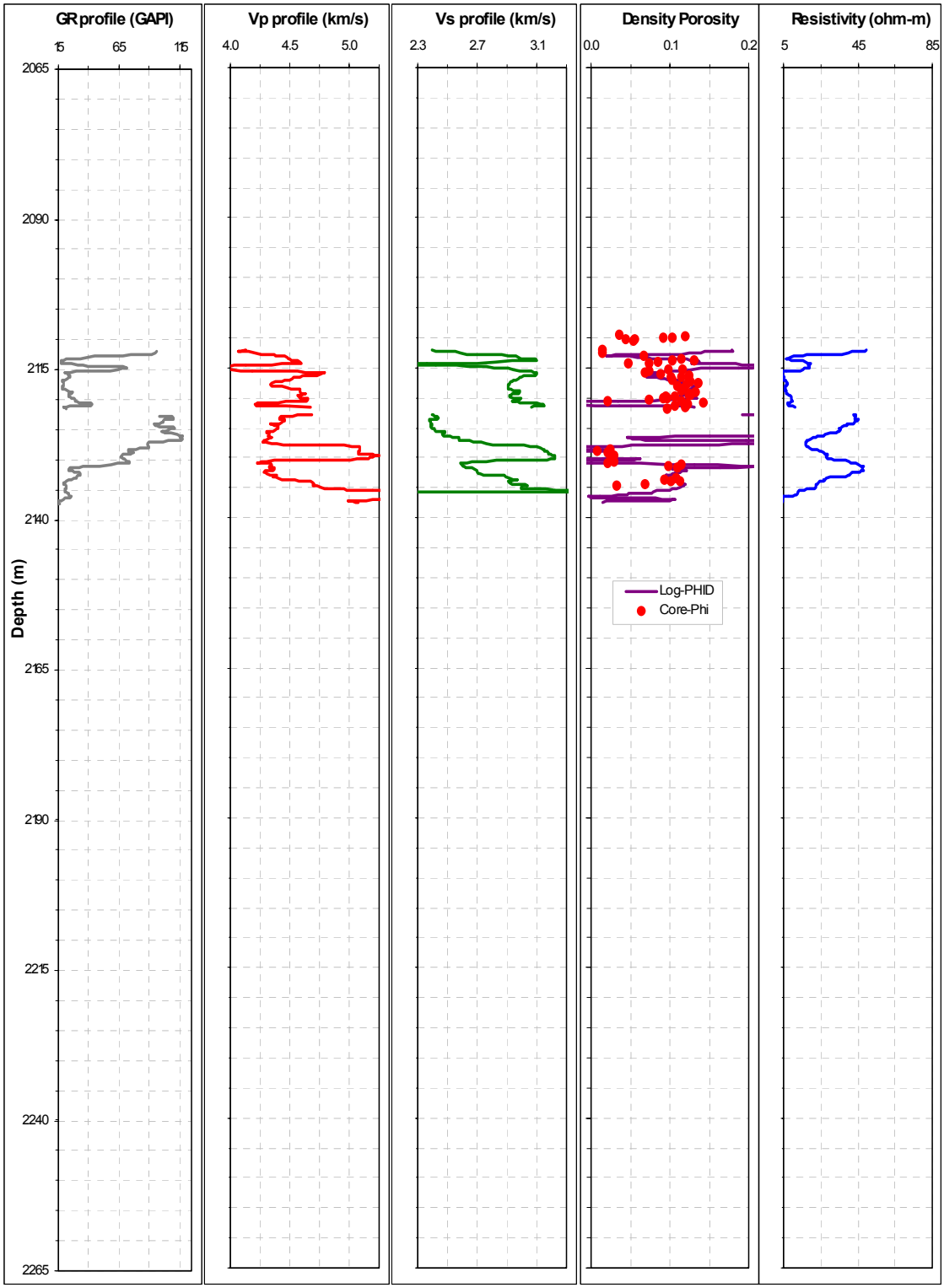

Figure 3.10: Well log profiles: gamma ray, P-wave velocity, S-wave velocity, density porosity with the core porosity superimposed on top, and deep resistivity; original data from the upper and lower channels of well W4 in BQ field.

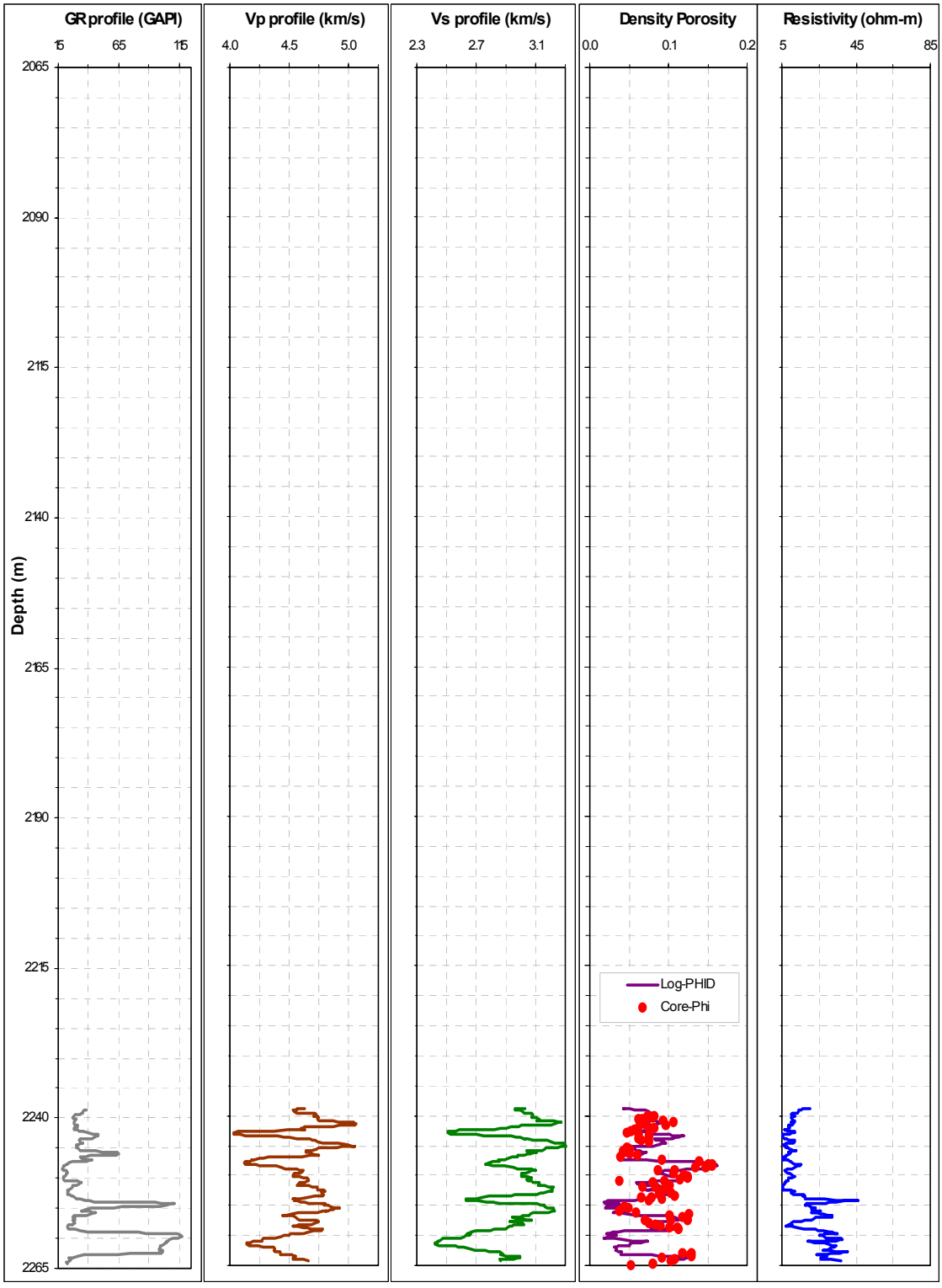

Figure 3.11: Well log profiles: gamma ray, P-wave velocity, S-wave velocity, density porosity with the core porosity superimposed on top, and deep resistivity; original data from the upper and lower channels of well W7 in BQ field.

3.3 QUALITY CONTROL OF THE DATA

During drilling, the mud filtrate may penetrate the formation and partially or entirely replace the original fluid around the well bore. In addition, during the mud circulation, part of the matrix around the well bore may be washed out. Meanwhile, the well log tools, such as the density tool, resistivity tool, and sonic and dipole tools measure the rock volume that extends to a certain distance into the formation from the well bore. So the measurements from these well log tools may be affected by the mud filtrate invasion and/or the washout. These events may affect at least two types of rock properties that we are interested in: the bulk density and the bulk modulus. As a result, both P- and S-wave velocities may be affected. Therefore, before we proceed with our analysis, we need to know whether the density, Vp and Vs are from the virgin formation or from the invaded formation.

3.3.1 Investigation of Bulk Density (ρ_b) for Mud Filtrate Invasion

During drilling, the permeable intervals around the well bore may be invaded by mud filtrate. So, if the density tool measures the vicinity of the well bore, then it measures the mud filtrate density as pore fluid density. However, if the density tool measures past the invaded zone and deep into the formation then it measures the virgin formation density.

Density porosity is computed from bulk density, pore fluid density and grain density. Hence, in the calculation of density porosity, we need to know which pore fluid density to use. Since we are not sure if the density tool measures the invaded zone or the virgin formation, we carry out all calculations considering two cases: upper and lower bounds for porosity. For Case 1, the upper porosity bound, we assume that the density tool measures the invaded zone density. For Case 2, the lower porosity bound, we assume that the density tool measures the virgin formation density.

3.3.1.1 Case 1: Porosity Upper Bound

We assume that the density tool measures the invaded zone. Therefore, the density of the fluid is equal to the brine density, assuming that the mud filtrate's density is the same as that of the formation water. It is the upper bound for the porosity.

Calculation of Porosity, ϕ_{Upper}

$$\phi_{Upper} = \frac{\rho_s - \rho_b}{\rho_s - 1} \tag{3.1}$$

where ϕ_{upper} is the upper bound for the porosity values,

ρ_s is the solid density, and

ρ_b is the log bulk density.

3.3.1.2 Case 2: Porosity Lower Bound

We assume that the density tool measures the true formation. Therefore, the fluid density is the density of the mixture of gas and brine. It is the lower bound for the porosity.

Calculation of the True Fluid-Phase Density, ρ_{ft}

$$\rho_{ft} = S_{wt}\rho_w + (1 - S_{wt})\rho_{gas} \tag{3.2}$$

where S_{Wt} is the true water saturation in the virgin formation,

ρ_w is the brine density, and

ρ_{gas} is the gas density.

Calculation of Porosity, ϕ_{Lower}

$$\phi_{Lower} = \frac{\rho_s - \rho_b}{\rho_s - \rho_{ft}} \tag{3.3}$$

where ρ_{ft} is true fluid-phase density,

ρ_s is solid density, and

ρ_b is the log bulk density.

Figure 3.12 shows the profiles of $\phi_{Upper,}$ $\phi_{Lower,}$ and the core porosity from 5 cored wells. These porosity profiles illustrate that the core porosity falls twice as often on ϕ_{Upper} as on ϕ_{Lower}. The density porosity computed in case-1, ϕ_{Upper}, using the fluid density of 1

g/cc and the mineral (solid) density of 2.65 g/cc, matches the core porosity within 90% in the BQ sands. Case 1 is the simpler of the two cases. Moreover, Figure 3.12 reveals that the maximum difference between ϕ_{Upper} and ϕ_{Lower} is 3%. As a result, we chose to use ϕ_{Upper} throughout the study.

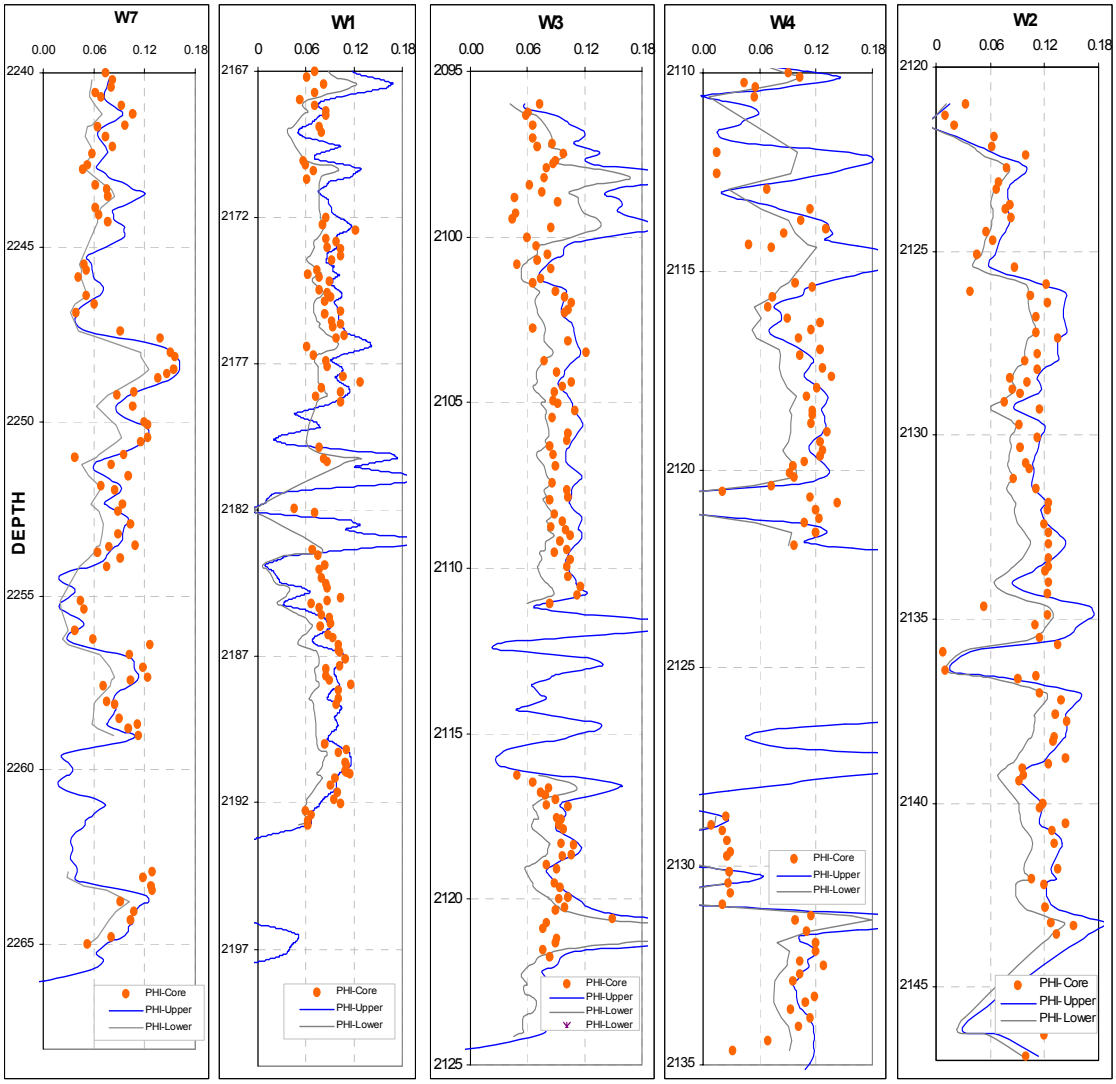

Figure 3.12: Profiles of ϕ_{Upper} (blue), ϕ_{Lower} (gray), and core porosity (orange symbols) from 5 cored wells in BQ field.

3.3.2 Analysis of P-wave (Vp) and S-wave Velocity (Vs) for Mud Filtrate Invasion

Castagna et al. (1993), Castagna (1985), and Han (1986) introduced empirical relations between Vp and Vs in 100% water-saturated sands and shales. We compare the

original well log Vp and Vs data to these relations. On cross-plots of Vp vs. Vs from original log data, we expect that the data points from the gas-bearing intervals will lie below the empirical curves, because hydrocarbon in the pore space acts to reduce the P-wave velocity and slightly increase the S-wave velocity. On the other hand, the data from the 100% water saturated zone should lie on the empirical curves.

In Figure 3.13, we superimpose the Vp-Vs relations for Castagna et al. 1993 (in red), Mudrock (in deep blue), and Han (in green) on top of the original Vp versus Vs data from the same 5 core wells. All of the three models are for water saturated sandstones.

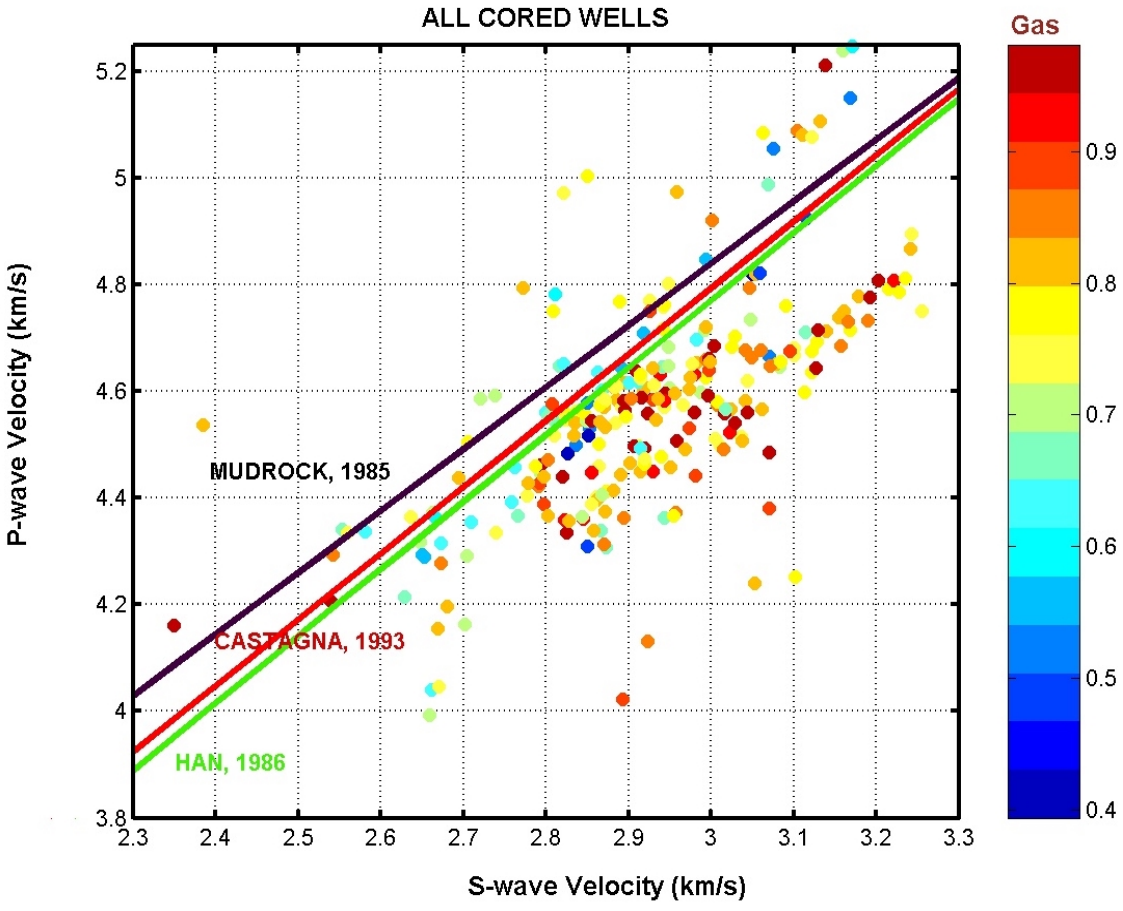

Figure 3.13: Vp-Vs relations for Castagna et al. 1993 (in red), Mudrock (in deep blue), and Han (in green) super-imposed on top of the original Vp versus Vs data from the same 5 cored wells in the BQ field.

Figure 3.13 shows that most of the gas saturated rocks lie below the empirical curves. This suggests that the Vp-Vs relation in BQ sands is in accordance with the Mudrock, Castagna et al. 1993, and Han's Vp-Vs relations. Figure 3.13 also shows that some of the gas saturated rocks fall on or above these empirical curves. We will investigate these issues in chapter 6.

Nore that the P-wave and S-wave velocities were measured from dipole tools of frequency around 5 kHz, so Vp and Vs might come from the virgin formation.

As a result, we can assume that both Vp and Vs come from the virgin formation.

3.4 DETERMINATION OF THE LOG AND CORE DATA CONSISTENCY

Figures 3.14 to 3.18 show the profiles of core and log data, after the depth shifts, within the cored interval from the same 5 cored wells in the BQ Crossfield. These figures demonstrate that there is a good integration between core and log data of the same variables. Moreover, they reveal that the upper and lower channels appear to have the same range of porosity values; however, the upper channels seem to have higher permeability and P-wave velocity values than the lower channels.

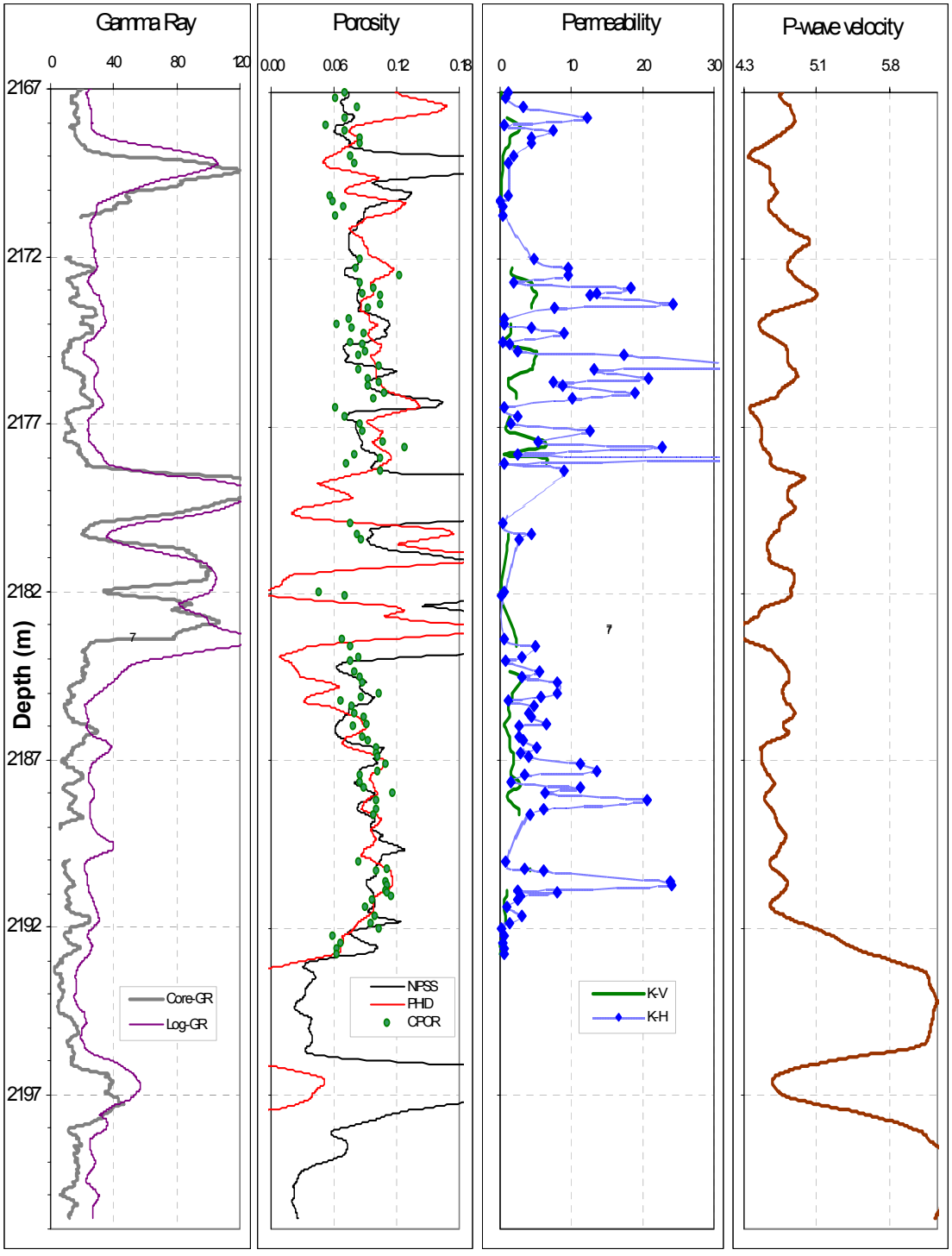

Figure 3.14: Core and log data integration from well W1 cored interval. From left to right: core and log gamma ray profiles; core and log (neutron and density) porosity profiles; core permeability profile; log P-wave velocity profile.

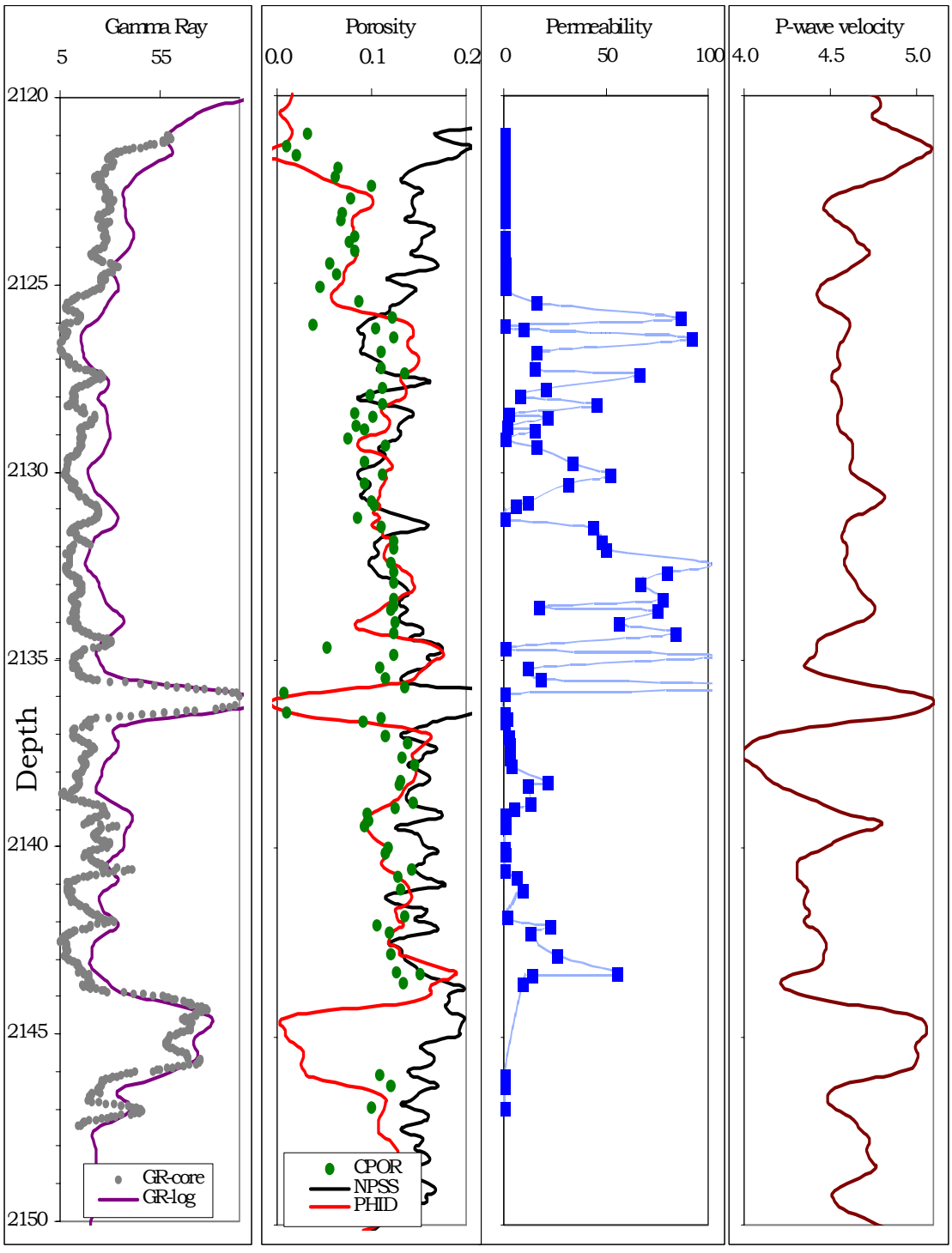

Figure 3.15: Core and log data integration from well W2 cored interval. From left to right: core and log gamma ray profiles; core and log (neutron and density) porosity profiles; core permeability profile; log P-wave velocity profile.

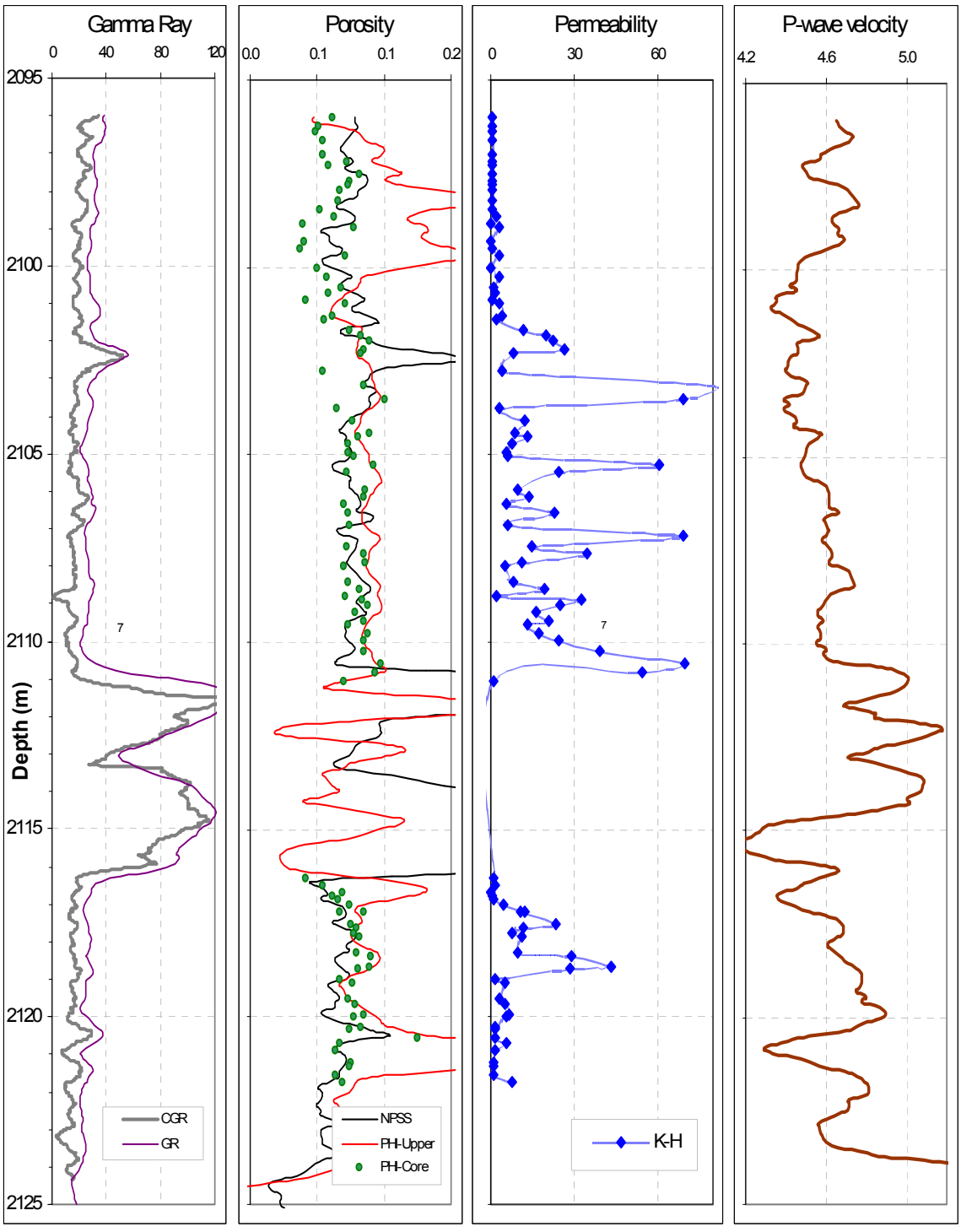

Figure 3.16: Core and log data integration from well W3 cored interval. From left to right: core and log gamma ray profiles; core and log (neutron and density) porosity profiles; core permeability profile; log P-wave velocity profile.

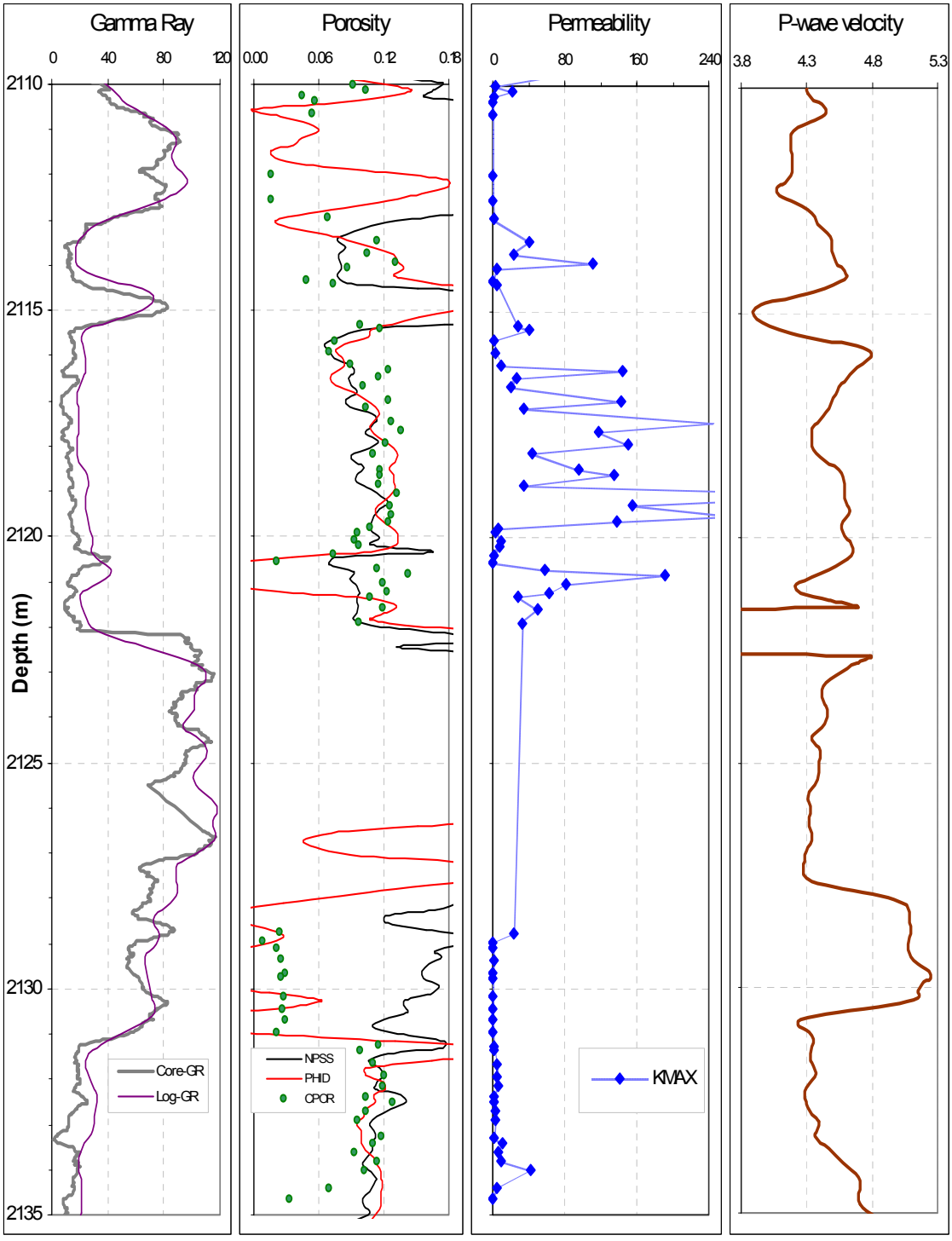

Figure 3.17: Core and log data integration from well W4 cored interval. From left to right: core and log gamma ray profiles; core and log (neutron and density) porosity profiles; core permeability profile; log P-wave velocity profile.

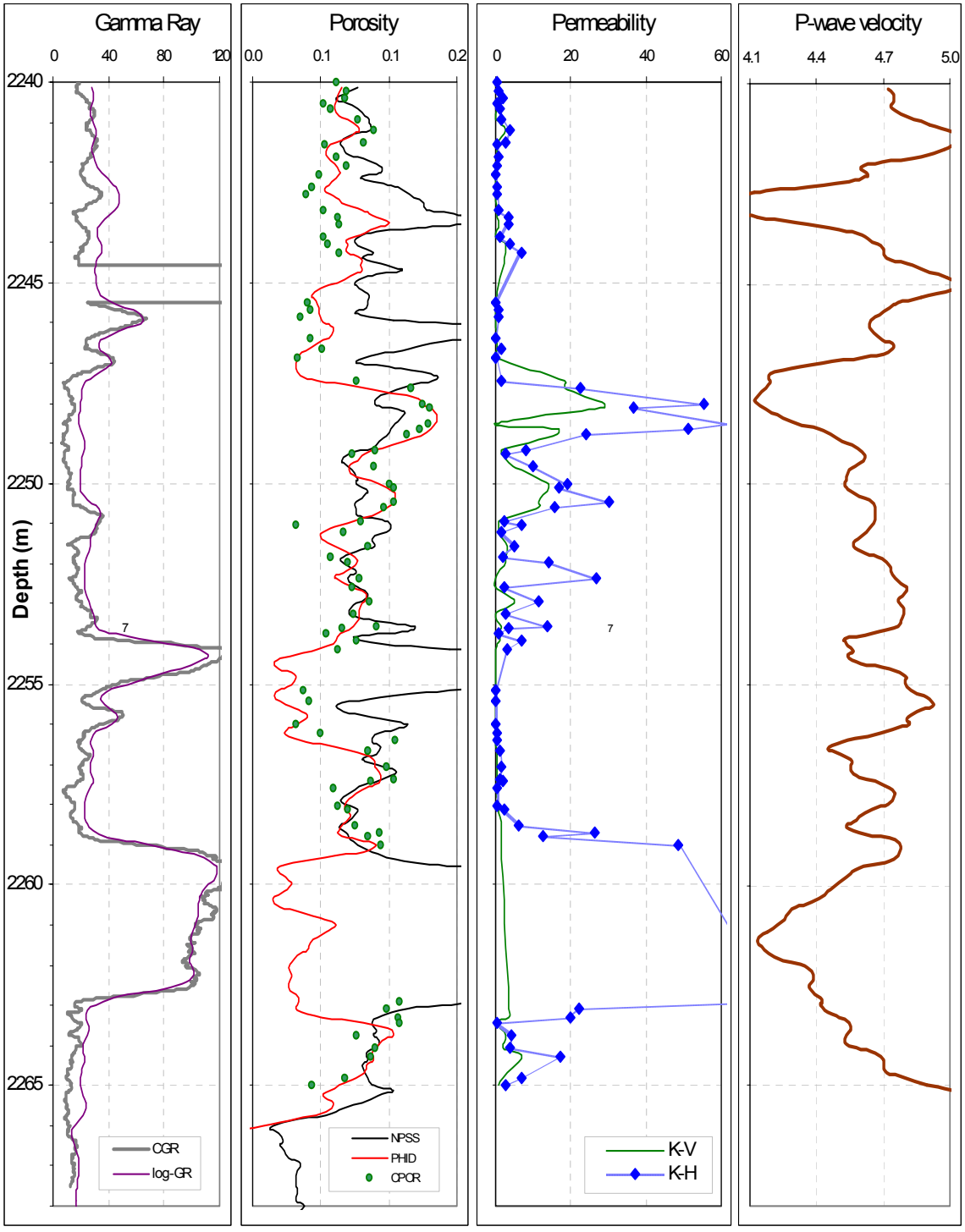

Figure 3.18: Core and log data integration from well W7 cored interval. From left to right: core and log gamma ray profiles; core and log (neutron and density) porosity profiles; core permeability profile; log P-wave velocity profile.

3.5 CONCLUSIONS

- The density porosity computed using the fluid density of 1 g/cc and the mineral (solid) density of 2.65 g/cc matches the core porosity within 90% in BQ sands. The relative difference between Case 1 and Case 2 is about 3 %. We chose to proceed with Case 1.
- We can say that the Vp-Vs relation in BQ sands do not violate the Mudrock (1985), Castagna et al. (1993), and Han's (1986) Vp-Vs relations. We concluded that both P-wave and S-wave velocities come from the virgin formation.
- There is a fairly good correlation between the core and log parameters. Additionally, the upper and lower channels appear to have the same range of porosity values; however, the upper channels seem to have higher permeability and P-wave velocity values than the lower channels.

3.6 REFERENCES

Castagna, J. P., Batzle, M. L., and Eastwood, R. L., 1985, Relationships Between Compressional-wave and Shear-wave Velocities in Clastic Silicate Rocks, Geophysics, 50, 571-581.

Castagna, J. P., Batzle, M. L., and Kan, T. K., 1993, Rock physics, The Link Between Rock Properties and AVO Response, in Offset-Dependent Reflectivity – Theory and Practice of AVO Analysis, J. P. Castange and M. Backus, eds. Investigations in Geophysics, No. 8, Society of Exploration Geophysicists, Tulsa, Oklahoma, 135-171.

Han, D. H., 1986, Effects of Porosity and Clay Content on Acoustic Properties of Sandstones and Unconsolidated Sediments, Ph.D. dissertation, Stanford University.

Spence, B. R., 1997, Sedimentology and Diagenesis of the Basal Quartz Formation, Calgary, Alberta, Master Thesis, University of Calgary, Alberta.

Robertson, B., Edwards, D., 1994, Crossfield/Delacour: anatomy of Lower Manville channel play; Canadian Society of Exploration Geophysicist and Canadian Society of Petroleum Geologists Joint National Convention, program, Expanded Abstracts and Biographies, Calgary, Alberta, p.169.

CHAPTER 4

RELATIONS BETWEEN POROSITY, PERMEABILITY, AND ELASTIC PROPERTIES IN BQ

4.1 INTRODUCTION

The depositional environment determines the initial mineralogy, the grain size and shape, and the sorting of rocks. These properties in turn control the type of diagenetic alterations that the rocks may go through. Rock properties are strongly dependent on these diagenetic alterations and the order in which the diagenetic events occur. In the specific case of the BQ field, sands are deposited in a fluvial environment and are comprised of several facies including chert-clast breccias, pebbly sandstones, sandstones, and silt to mudstones. The fine-grained, clean quartz sandstones are mostly affected by abundant quartz overgrowth, whereas coarse, chert-rich sandstones are more affected by compaction and calcite cementation (Spence, 1997). The relative order of occurrence of diagenetic events in BQ is as follows: (1) during burial: mechanical compaction, precipitation of quartz overgrowths, calcite cementation, (2) during uplift: illite precipitation, calcite cement dissolution, precipitation of microcrystalline quartz, kaolinite, and fibrous illite.

Due to the complex diagenetic history of BQ rocks, establishing the relationship between porosity, permeability, and elastic properties is challenging. Hence, the goal of Chapter 4 is to understand the relationship between the porosity, permeability, lithology, and the elastic properties of BQ rocks for a subsequent link to seismic.

4.2 RELATIONS BETWEEN PETROPHYSICAL AND ELASTIC PROPERTIES IN BQ RESERVOIR ROCKS

We cross-plot the petrophysical and elastic properties of the BQ reservoir rocks to reveal the interdependence among them. We plan to use these cross-plots to infer the rock textures, quantify clay content, identify the lithological units, identify the pore fluid, and

develop a relationship between the porosity and the elastic properties of the rocks from log and seismic attributes.

4.2.1 Permeability – Porosity – Impedance Relationships

Figure 4.1 shows the cross-plots of rock properties of the upper channel (2126 - 2133.6 m) in blue, and the lower channel (2137 - 2142.8 m) in red, within the cored interval of well W2. It reveals that at the same porosity value, the permeability in the upper channel (blue symbol) is larger than the permeability in the lower channel (red symbol). Coincidentally, the impedance in the upper channel is higher than that of lower channel. Therefore, locally, larger impedance at the same porosity could mean better reservoir quality. This opens an avenue to estimating permeability from elastic properties. Moreover, the lower channel has higher gamma ray range than the upper channel. So, clay acts simultaneously to decrease permeability and impedance.

Figure 4.2 displays the lithology description within the cored interval in W2. It shows the fining upwards of grain size and the upward increase in mud content in each channel. Within each channel, the grain size varies from chert-clast breccias and pebbly sandstones on the bottom, to medium grain size sandstones in the middle, to fine and muddy quartz grains on the top. Moreover, Figure 4.2 implies that there could be two depositional cycles in the lower channel.

To investigate the effects of the grain size on the permeability-porosity trends, we plot permeability versus porosity classified by grain size in Fig. 4.3. Figure 4.3 shows that within the same channel, as grain size increases both permeability and porosity increase. For the same grain size, porosity may vary by up to 5% whereas permeability remains relatively constant. Furthermore, Figure 4.3 displays that, for the same grain size, the permeability in the lower channel is lower than in the upper channel. This tells us that the effects of grain size have been altered by some other processes such as diagenesis, maturing (the younger upper channel and the older lower channel), or temperature and pressure that control the degree of diagenesis.

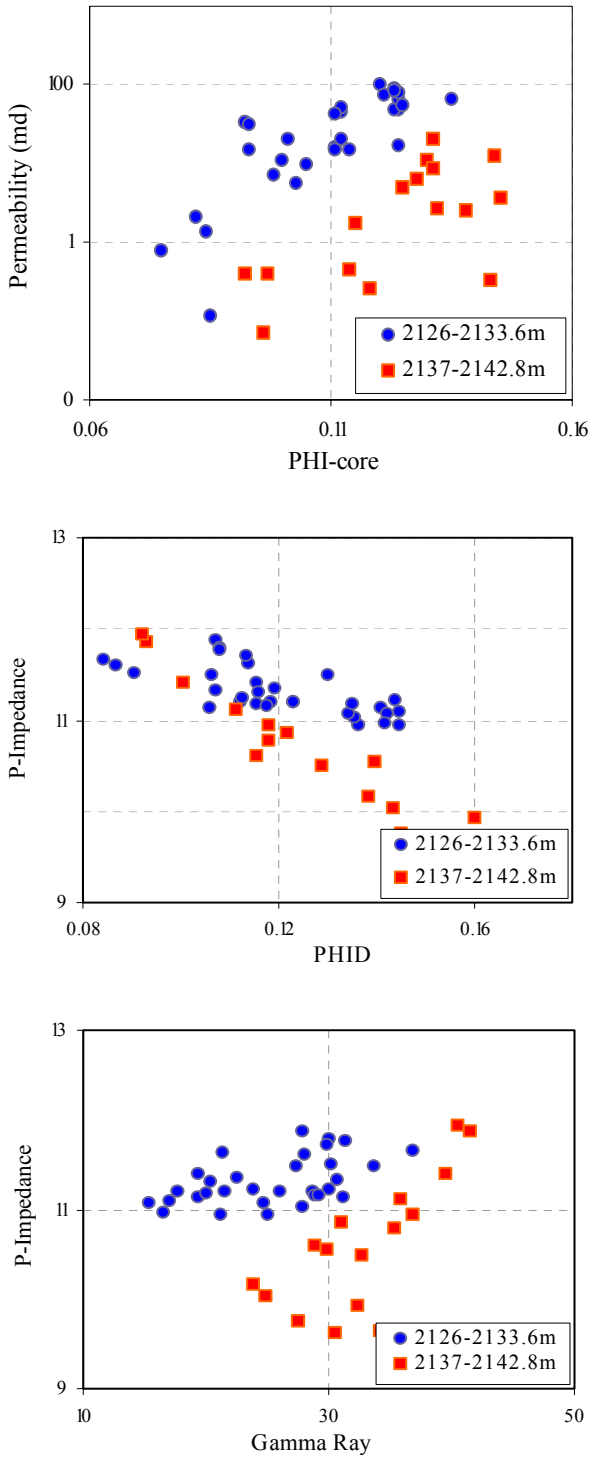

Figure 4.1: From top to bottom: cross-plots of core permeability versus core porosity, log P-wave impedance versus log density porosity, and log P-wave impedance versus log gamma ray of the upper channel (2126 - 2133.6 m) in blue, and the lower channel (2137 - 2142.8 m) in red in well W2.

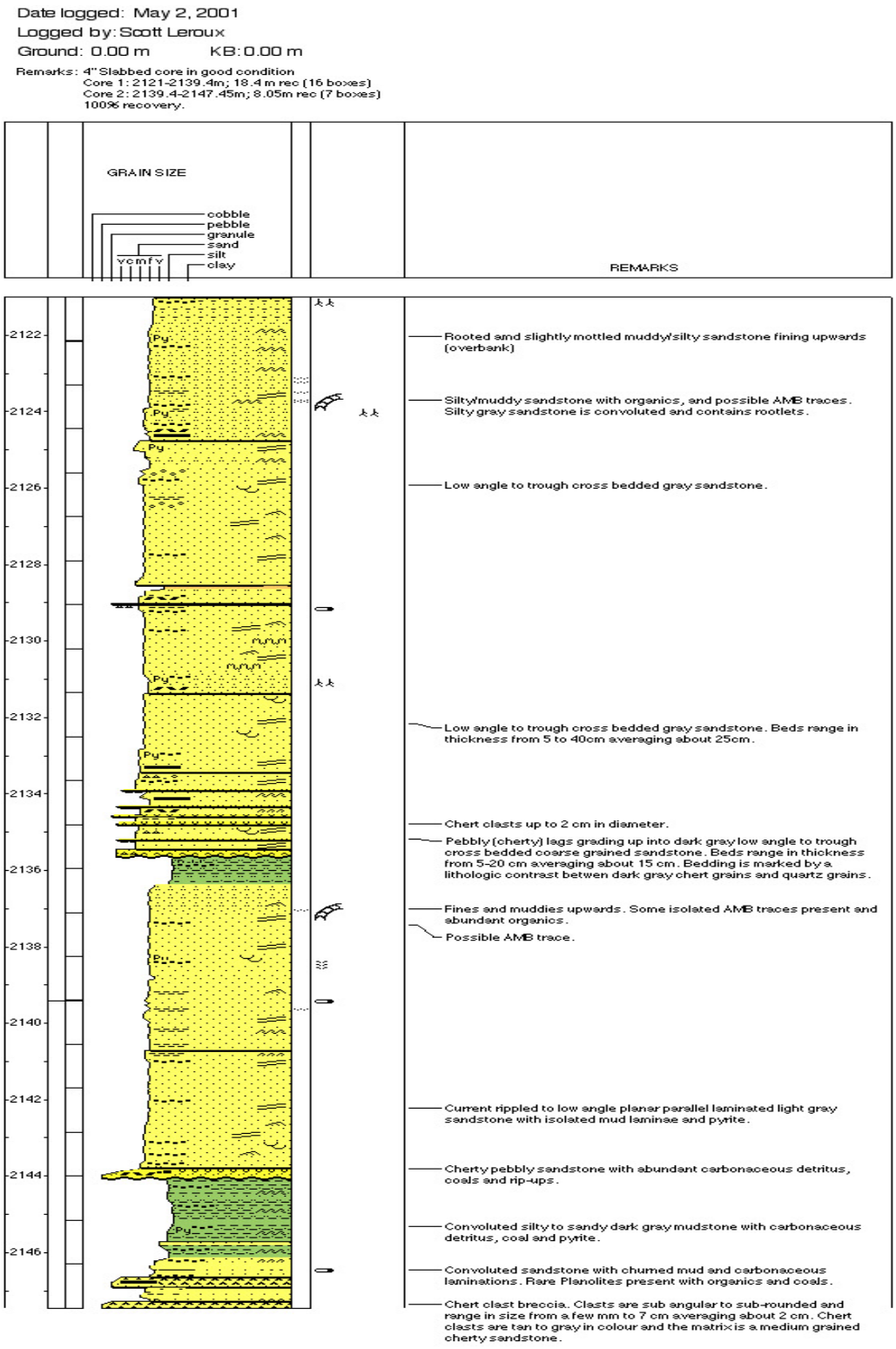

Figure 4.2: Graphic representation of core description on the left side and the written description on the right side; note the existence of two channels (upper 2121 – 2133.6 m and lower 2137 – 2146.5 m); the overall fining upwards of the grain size trend is apparent in both channels.

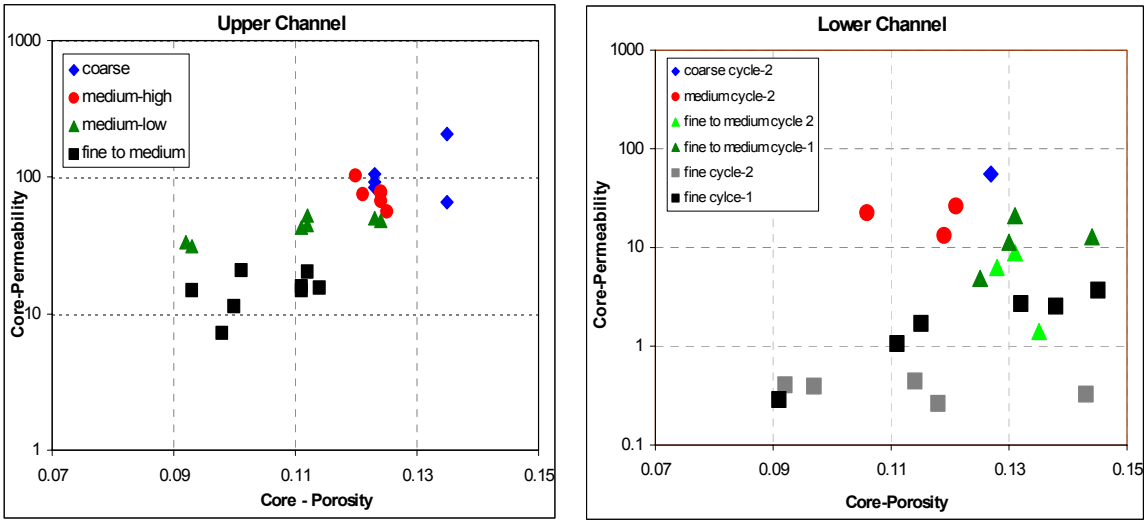

Figure 4.3: Permeability versus porosity for different grain sizes, for the upper channel and the lower channel within the cored interval in well W2.

4.2.2 Bimodal Grain Mixture

Figure 4.4 shows the plot of P-wave impedance versus porosity, color-coded by gamma ray. It shows the effect of mineralogy and textural sorting on porosity and elastic properties of BQ rocks. It displays two branches: in the right branch, as gamma ray increases the rocks become stiffer; in the left branch, as gamma ray increases the rocks become softer. It depicts the behavior of the bimodal grain mixture (Gutierrez, 2001), with sand being the larger grain and silt and clay being the smaller grains. If the volume of the silt and clay are lower than the sand's pore space volume, then as silt and clay contents increase, the rocks become stiffer (right branch). However, if the volume of clay exceeds the sands' pore volume, then as clay increases the rocks become softer (left branch). This may indicate that the sand is suspended in a pore-filling clay matrix.

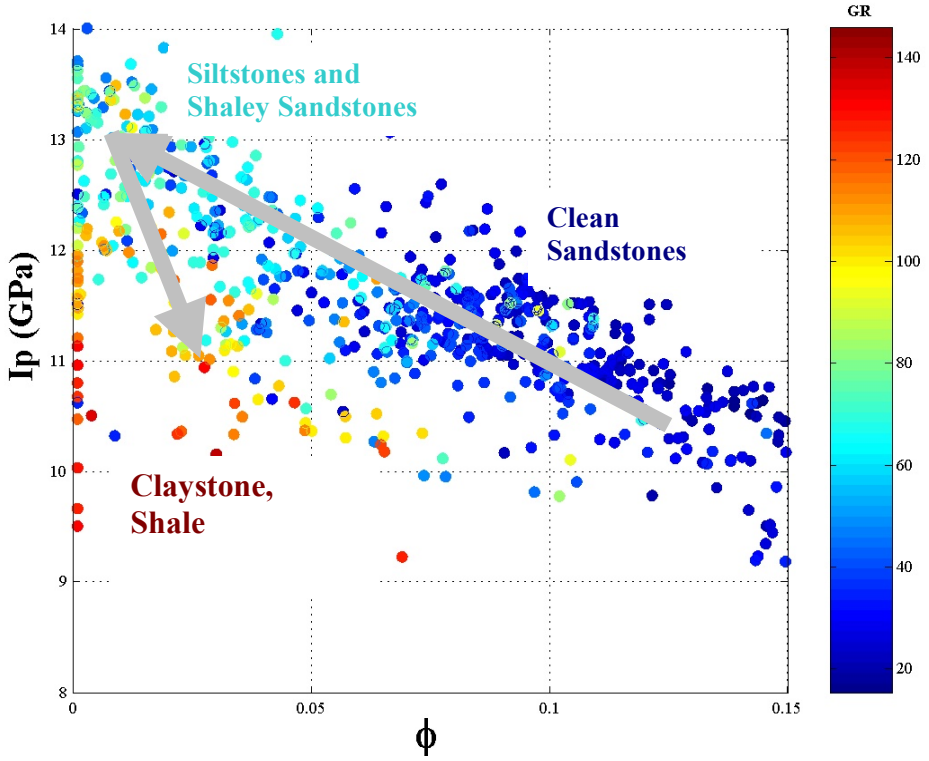

Figure 4.4: P-wave impedance versus porosity color coded by gamma ray. The data are from the 5 cored well in BQ reservoir.

4.2.3 Rock Quality Detection

Figure 4.5 shows, on the left, the profiles versus depth of gamma ray, Poisson's ratio, and P-wave impedance. On the right, it shows the crossplots of the Poisson's ratio versus P-wave impedance color coded by gamma ray for the interval above BQ (1930.3 m to 2115.08 m), BQ sands interval (2121.26 m to 2153.26 m), and the interval below BQ (2153.6 m to 2171.82 m). Figure 4.5 illustrates that the good quality rocks have low gamma ray values (60 < GAPI), low Poisson's ratio values (< 0.2), and P-wave impedance values between 8 – 11.3 km/s g/cc. It demonstrates that it is possible to detect the quality of the reservoir rocks using the Poisson's ratio versus P-wave impedance crossplot.

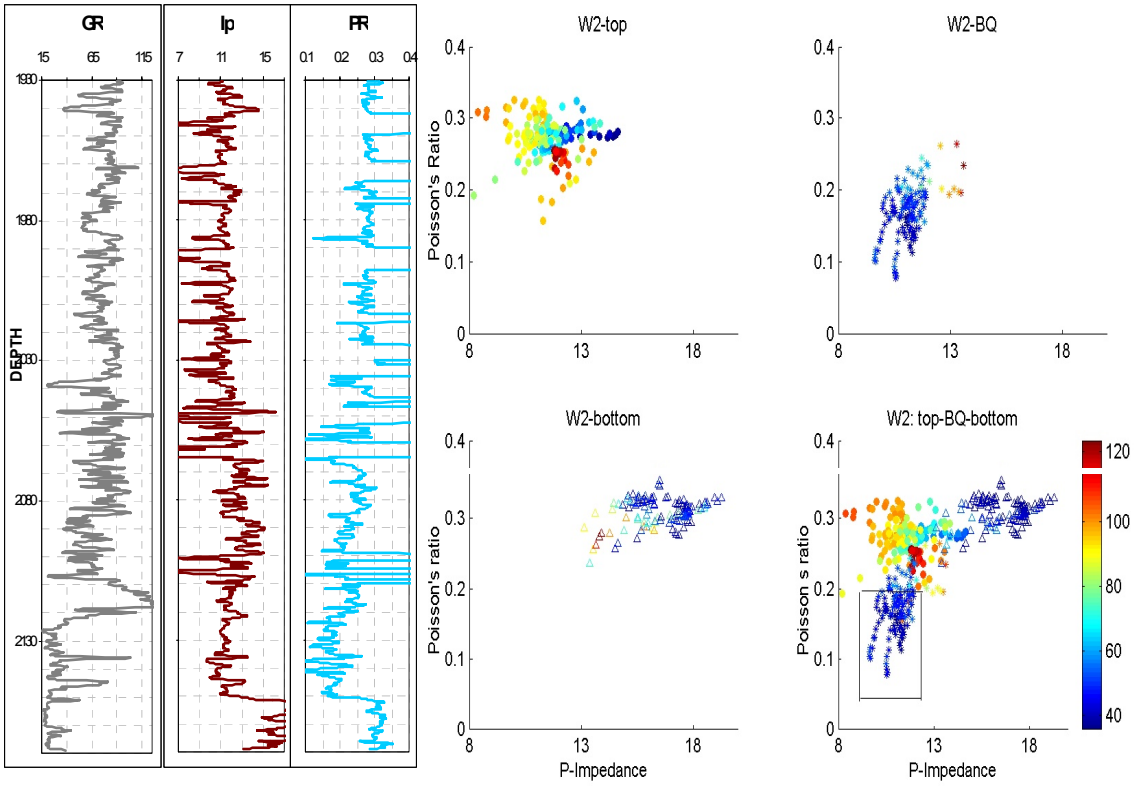

Figure 4-5: On the left, profiles of GR, ν, and Ip. On the right, ν versus Ip color-coded by GR for well W2. top (1930.3 m to 2115.08 m), sand (2121.26 m to 2153.26 m), and bottom (2153.6 m to 2171.82 m). The good quality rocks have low ν, Ip, and GR

4.4 CONCLUSIONS

- Locally, larger impedance at the same porosity could mean better reservoir quality. This opens an avenue to estimating permeability from elastic properties. Moreover, clay acts simultaneously to decrease permeability and impedance.
- For the same grain size, porosity in the BQ reservoir varies by up to 5%, whereas permeability remains relatively constant.
- The plot of P-wave impedance versus porosity depicts the behavior of the bimodal grain mixture.
- The good quality rocks have low Poisson's ratio values, low gamma ray values, and P-wave impedance values between 8 – 11.3 km/s g/cc. There is a strong hope of seismic detectability of the reservoir quality.

4.5 REFERENCES

Gutierrez, M., 2001, Rock Physics and 3-D Seismic Characterization of Reservoir Heterogeneities to Improve Recovery Efficiency, Ph.D. Thesis, Stanford University (SRB).

Mavko, G., Mukerji, T. and Dvorkin, J., 1998, The Rock Physics Handbook, Cambridge University Press.

Spence, B. R., 1997, Sedimentology and Diagenesis of the Basal Quartz Formation, Calgary, Alberta, Master Thesis, University of Calgary, Alberta.

CHAPTER 5

LABORATORY EXPERIMENTS AND ANALYSIS

5.1 INTRODUCTION

A series of laboratory experiments is necessary to assess the influence of subsurface environmental conditions on the physical and elastic properties of rocks. The results from these laboratory experiments are essential for determining the pressure dependence of rock's elastic properties, for detecting interesting seismic response in the rocks, for establishing the effect of scaling, and for attempting to predict permeability from remote geophysics measurements.

In this paper, we will discuss four main measurements: (a) P- and S-wave velocity measurements on dry samples at varying hydrostatic confining pressure up to 50 MPa; (b) porosity measurements at room conditions; (c) Klinkenberg corrected gas permeability measurements at room conditions; and (d) grain size distribution analyses. Altogether 17 samples from well W2 have been investigated.

The main purposes of this experimental program are to: (a) quality-control well log data; (b) understand the pressure dependence of elastic wave velocity; and (c) link porosity, permeability, clay content, and sorting to the elastic rock properties. The latter will allow us to develop a predictive capability based on seismic data.

5.2 SAMPLES STUDIED

Our core samples come from well W2 in the BQ field. These core samples cover a range of grain size (from pebbly sands to silts and mudstones) and different diagenetic patterns (uncemented sand; quartz overgrowth; cemented sands) present in the BQ field. The lithology description of each sample is given in Table 5.1.

Table 5.1: Sample ID, depth, visual description, and lithology for each core sample.

ID	Depth (m)	Visual Description*	Lithology
P2	2121.29 - 21.52	ss, vf, hcc, shy, fri	Shale
P3	2121.52 - 21.64	ss, vf, shy, fri	Shale
P13	2124.28 - 24.46	ss, f - m, lb, vc, om	Fine to medium grained sands
P17	2125.65 - 25.81	ss, m, dg, vp	Medium grained sands
P20	2126.46 - 26.65	ss, m, lg, vp, vb	Medium grained sands
P30	2128.95 - 29.14	ss, m, lg + dg, vp	Medium grained sands
P35	2130.27 - 30.45	ss, m - c, lg + dg, vp	Medium to coarse grained sands
P41	2132.08 - 32.28	ss, m - c, lg + dg, vp	Medium to coarse grained sands
P53	2135.44 - 35.57	ss, c, cgl + cc, str	Coarse grained sands, conglomerate, chert clasts
P54	2135.57 - 35.78	c, cgl + cc, str	Coarse grained sands, conglomerate, chert clasts
P63	2138.12 - 38.25	ss, f - m, lb, vp, h	Fine to medium grained sands
P67	2139.00 - 39.14	ss, vf, lg, fsl, vlm, fri	Very fine grained sands
P71	2140.14 - 40.56	ss, vf, lg, fsl, vlm, fri	Very fine grained sands
P74	2141.10 - 41.79	ss, m, lbg, vp, h	Medium grained sands
P79	2143.27 - 43.35	ss, m, lg + dg, vp, vb	Medium grained sands
P82	2146.02 - 46.29	ss, vf, lg, om, shy, fri	Very fine grained sands
P83	2146.29 - 46.61	ss, vf, lg, om, shy, fri	Very fine grained sands

ss = sandstone, vf = very fine, f = fine, m = medium, c = coarse, shy = shaley, hcc = high clay content, fri = friable, pyr = pyrite, lb = light brown, om = organic materials, lg = light gray; lbg = light brown gray, dg = dark gray, vc = vertical cracks, vp = visible pores, vb = vertical bedding, cgl = conglomerate, fsl = fossil, h = homogenous, str = strong, cc = chert clast, vlm = vertical lamination.

5.3 METHODS

5.3.1 Sample Preparation

The laboratory measurements were made on core plugs. These core plugs were cut to 25.4 mm in diameter and 38.1 mm in length. The sides were parallel within 0.01 mm tolerance. The top and bottom surfaces of these plugs were polished with sandpaper until they were flat and smooth.

5.3.2 Experimental Procedures

We measured porosity, permeability, grain size distribution, and velocity at ambient pressure and temperature. Velocity and porosity were also measured as function of confining pressure.

5.3.2.1 Porosity Measurements

The grain volume of the core plugs in room-dry condition was measured with a helium porosimeter. The porosity and bulk density were computed from the measured grain volume, the sample's dimension and weight using the following formulae:

Porosity:

$$\phi = \frac{VOL_b - VOL_g}{VOL_b} 100 \tag{5.1}$$

where:ϕ is porosity in percent,

VOL_b is bulk volume of the core plug, and

VOL_g is grain volume.

Bulk Density:

$$\rho_b = \frac{W_b}{VOL_b} \tag{5.2}$$

where: ρ_b is bulk density, and

W_b is mass of the core plug.

Grain density

$$\rho_b = \frac{W_b}{VOL_g} \tag{5.3}$$

The relative errors in the helium porosity, estimated within 2%, were mainly due to errors in volume calculations from length and diameter.

5.3.2.2 Permeability Measurements

The permeability of the samples in room-dry condition was measured with a gas permeameter using clean and dry industrial grade Nitrogen gas. Permeability measurements made at different pressures were used to derive Klinkenberg-corrected permeability values.

5.3.2.3 Bench Top Velocity Measurements

The P- and S-wave velocities of the dry samples in room-dry condition were measured using the pulse transmission technique.

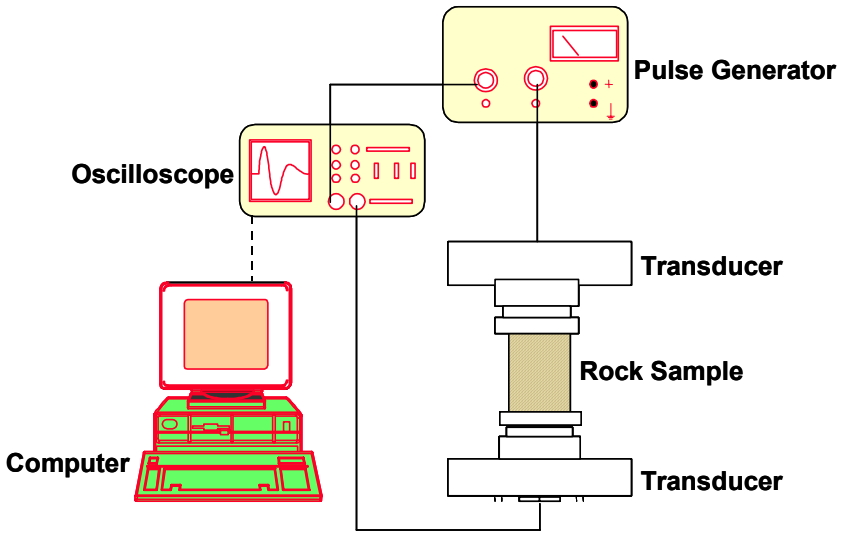

Figure.5.1: Sketch of the bench-top pulse method setup in the Rock Physics Lab at Stanford University

In this technique (Figure 5.1), a pulse from a pulse generator is used to excite mechanical vibrations in a piezoelectric transducer (source). These mechanical vibrations or pulses travel through the rock sample and are received at the other end by an identical transducer (receiver) that transforms the mechanical vibrations back into electrical signals. An oscilloscope used in the experiment receives two signals; a trigger signal from the pulse generator to synchronize the oscilloscope with the initiation of the pulse, and a delayed signal that has traveled through the rock sample to the receiving transducer. The signal received by the oscilloscope is then recorded on a computer.

The time difference between the two signals received by the oscilloscope is the time it takes the signal to travel through the electronics as well as through the sample itself. The electronic delay can be eliminated by measuring the time difference with no sample between the source and receiver, called "head to head" measurements. In our setup, the electronic delay time is 496 ns for the compressional wave and 530 ns for the shear wave. The travel time is measured by detecting the onset of the P- or S- wave. Velocity of the sample is calculated from its length and the travel time of the signal after correcting for the electronic delay time. Thus,

$$V = \frac{L}{t_M - t_T} \tag{5.4}$$

where: V is P-wave (or S-wave) velocity,

L is the length of the sample,

t_M is the travel time of the signal, and

t_T is the electronic delay time from the "head-to-head" measurement.

Velocity Error Calculation

$$\Delta V = \frac{\partial V}{\partial L}\Delta L + \frac{\partial V}{\partial t_M}\Delta t_M + \frac{\partial V}{\partial t_T}\Delta t_T \tag{5.5}$$

$$V_{err} = \Delta L \frac{1}{t_M - t_T} + L\frac{\Delta t_M}{(t_M - t_T)^2} + L\frac{\Delta t_T}{(t_M - t_T)^2} \tag{5.6}$$

where: V_{err} is the relative velocity error,

L is the length of the sample,

ΔL is the error in sample length measurements, $\Delta L \approx \pm 0.05$ mm,

t_M and t_T are the travel times through the sample and the electronic delay respectively, and

Δt_T and Δt_M are the oscilloscope's time resolution.

Since $t_M - t_T$ is usually around 15 μs, the second and the third terms in the Eqn. 5.6 may be neglected. Hence the relative error could be less than 3% in P-velocity estimation and 5%

in S-velocity estimation. Then, the maximum absolute error ΔV for both Vp and Vs is less than 50 m/s. This includes the error in picking.

5.3.2.4 P- and S- Wave Velocity Measurements at Varying Confining Pressure

The P- and S-wave velocities of the dry samples were measured as functions of hydrostatic confining pressure using pulse transmission techniques (Birch, 1960, Prasad et al., 1999).

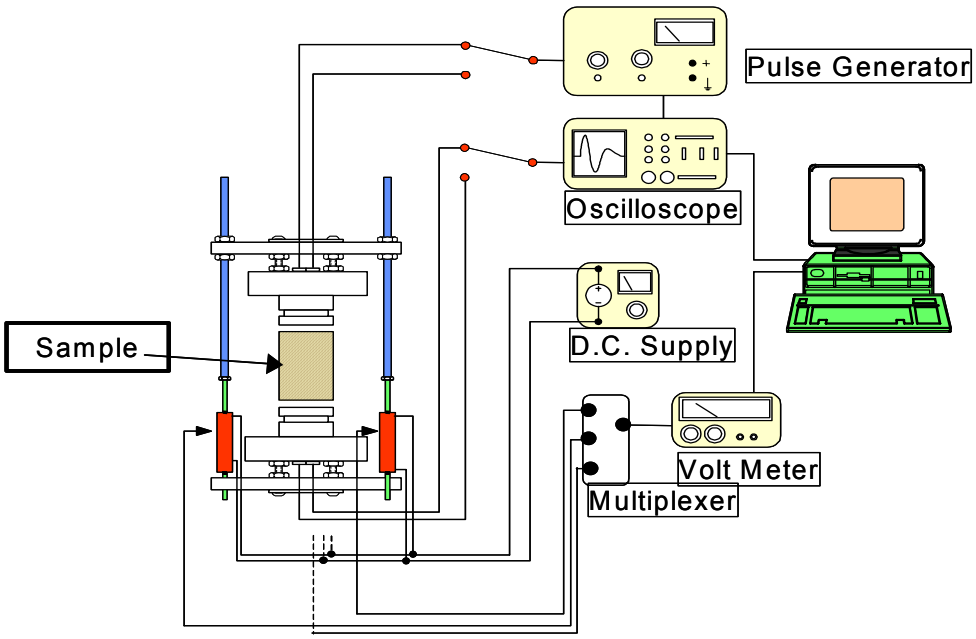

Figure 5.2: Schematic diagram of the pulse transmission techniques (Birch, 1960) at the Rock Physics Lab at Stanford University.

The experiment setup is described in detail by Prasad et al. (1999). Briefly, the samples were jacketed with rubber tubing to isolate them from the confining pressure medium. The principal frequency was about 1 MHz for P-wave and 0.7 MHz for S-wave. In this setup, the electronic delay time are 10.848 μs for the compressional wave and 18.357 μs for the shear wave. Velocities are calculated as before from Eqn. 5.4. P- and S-wave velocities and changes in sample lengths at various confining pressures up to 50 MPa were measured simultaneously. These changes in length were also used to calculate changes in porosity due to pressure

Travel time was measured after digitizing each trace with 1024 points at a time sweep of 5 ms, thus allowing a time resolution of about 5 ns or about 0.2% error in velocity. Actual error due to picking the first arrival is around 1%.

5.3.3 Grain Size Analysis

Table 5.2 shows the grain size distribution of the 12 samples. These 12 samples are representative of the BQ rocks, including chert-clasts breccias, pebbly sandstones and silt to mudstones.

Table 5.2: Specific Grain Size Analysis of the 12 Samples.

SMPL	SAND %						SILT %				CLAY	Vsh	MEAN	
NO	GRVL	VCRS	CRS	MED	FINE	VFIN	CRS	MED	FINE	VFIN	(%)	(%)	(μ)	LITHOLOGY
P2	0	0	0	0.32	8.79	22.62	22.84	14.88	10.61	8.72	11.23	45.43	42.8614	Silt shy
P13	0	0	0.27	25.52	41.78	13.89	5.26	4.81	3.04	2.63	2.80	13.28	176.07	Sd fg cln
P20	0	0	3.19	66.64	30.17	0	0	0	0	0	0	0	298.733	Sd mg cln
P30	0	12.75	39.13	29.38	10.01	3.51	1.29	1.37	1.67	0.83	0.06	3.92	545.151	Sd cg cln
P35	0	0	16.95	66.84	13.25	0.87	1.92	0.17	0	0	0	0.17	369.66	Sd mg cln
P41	0	0	19.54	51.00	21.12	2.67	2.45	1.16	1.26	0.73	0.05	3.21	347.397	Sd mg cln
P54	0	15.70	39.84	30.56	7.74	2.42	1.14	0.92	1.18	0.50	0	2.60	586.06	Sd cg cln
P63	0	0	0	15.49	52.70	23.94	1.24	2.92	1.52	0.88	1.31	6.63	164.666	Sd fg cln
P67	0	0	0	0.39	22.09	42.14	18.09	5.43	5.02	3.31	3.54	17.30	83.9047	Sd vfg vsshy
P74	0	0	0	13.68	51.77	26.77	1.64	2.82	1.45	0.68	1.19	6.14	158.447	Sd fg cln
P79	0	0	13.37	52.44	28.95	2.11	2.38	0.75	0	0	0	0.75	317.296	Sd mg cln
P82	0	0	0	0.84	21.57	42.18	21.35	5.22	3.58	2.52	2.74	14.06	84.7624	Sd vfg cln

SMPL = sample, GRVL = gravel, VCRS = very coarse, CRS = coarse, MED = medium, VFIN = very fine, Vsh =shale volume.

5.4 EXPERIMENTAL RESULTS

5.4.1 Bench Top Measurements Results

Table 5.3 shows the bench-top measurements results for porosity, permeability, P- and S- wave velocity for the 17 samples.

Table 5.3: Lab measurements for porosity, permeability, and P- and S-wave velocity under bench-top conditions.

Samples	Depth (m)	Porosity (fraction)	Permeability (md)	Vp (km/s)	Vs (km/s)
P2	2121.29 - 21.52	0.011	0.01	5.175	3.283
P3	2121.52 - 21.64	0.020	0.02	4.596	2.870
P13	2124.28 - 24.46	0.068	6.75	2.794	1.970
P17	2125.65 - 25.81	0.121	151.82	2.331	1.547
P20	2126.46 - 26.65	0.120	119.52	2.315	1.560
P30	2128.95 - 29.14	0.092	11.75	2.961	2.028
P35	2130.27 - 30.45	0.096	23.95	1.653	1.123
P41	2132.08 - 32.28	0.117	45.73	2.404	1.550
P53	2135.44 - 35.57	0.139	16.68	2.559	1.708
P54	2135.57 - 35.78	0.133	246.25	2.745	1.750
P63	2138.12 - 38.25	0.135	22.13	2.184	1.486
P67	2139.00 - 39.14	0.093	0.12	3.244	2.168
P71	2140.14 - 40.56	0.115	0.50	2.932	2.012
P74	2141.10 - 41.79	0.137	10.60	2.301	1.555
P79	2143.27 - 43.35	0.133	67.84	2.044	1.368
P82	2146.02 - 46.29	0.109	0.16	2.930	2.055
P83	2146.29 - 46.61	0.109	0.26	2.876	2.030

5.4.2 Results of P- and S- wave Velocity Measurements at Varying Confining pressure

Examples of the recorded signals and data for sample P20 as well as the summary plots for all data are shown in this section. All other results are presented in Appendix A.

Figures 5.3 and 5.4 show an example of the P and S signals going through sample P20. Sample P20 was extracted from depth 2126.46 m and has 12 % porosity and 120 mD permeability. Tables 5.4 displays the data recorded for samples P20, tables for each sample are in Appendix A. Figure 5.5: shows the effect of confining pressure on elastic properties of sample P20, plots for each sample are in Appendix A.

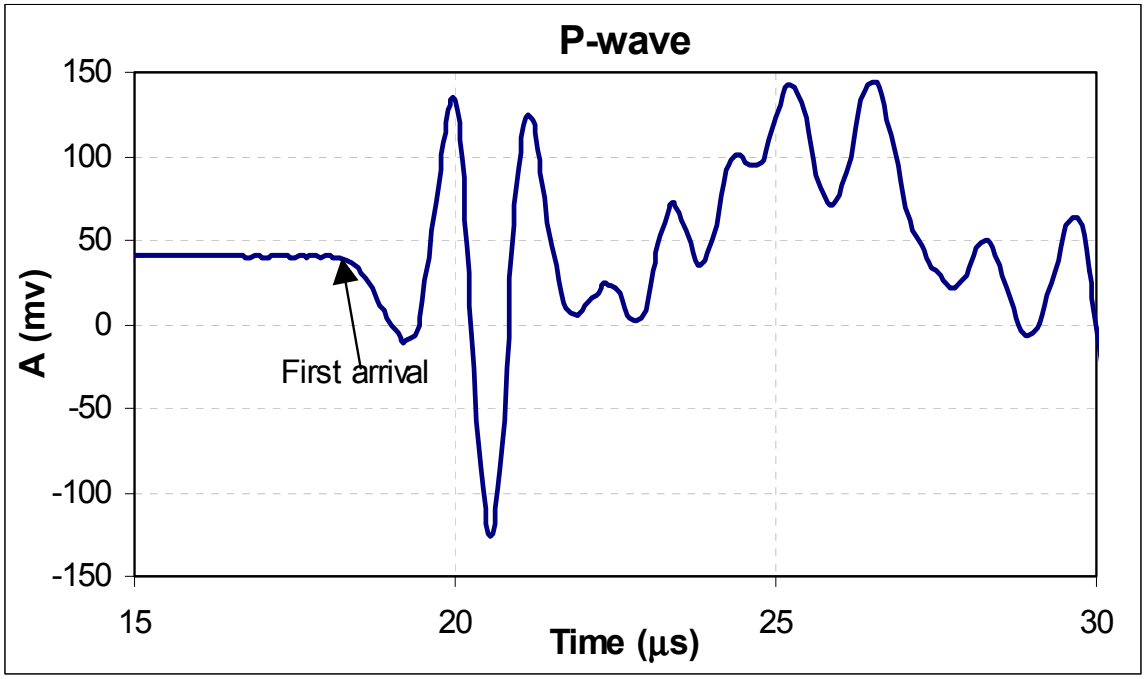

Figure 5.3: Compressional wave through sample P20.

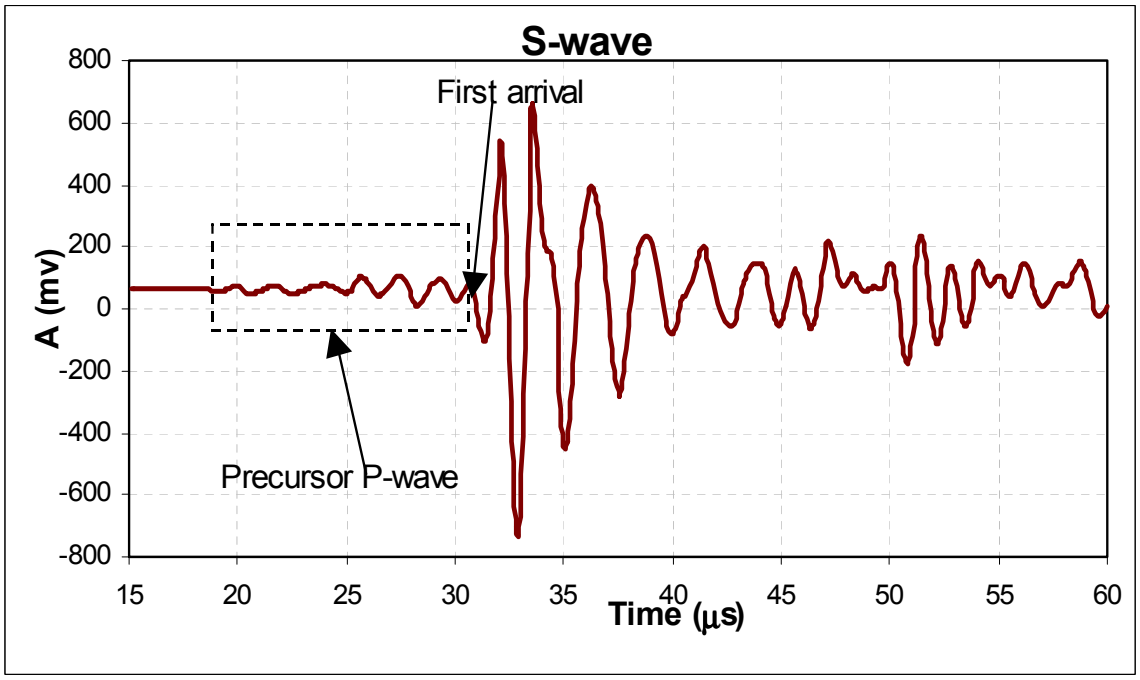

Figure 5.4: Shear wave through sample P20.

Table 5.4: Measured and computed data for P20, an example of the recorded data for each sample.

PanCanadian			Depth (m)	Length (mm)	Diameter (mm)	Mass (g)	Pbi-Pc (%)	Perm (mD)	Rbeg (g/cc)	RboS (g/cc)							
Sample: P20 Dry			2126.46	33.88	24.84	37.43	12	1195	2.64	2.323	We used the plastic rubber instead of the jacket						
File-name P-waves	delta L mm	Pc MPa	L mm	Vp km/s	Vs km/s	File-name S-waves	Vp/Vs	v	Pbi %	dPbi/Pbi %	Rbob (g/cc)	Mu (GPa)	K (GPa)	Ip (km/s g/cc)	Is (km/s g/cc)	μρ (km/s g/cc)^2	λρ (km/s g/cc)^2
UPLOADING									13.64								
P20D1V00	0.00	0.2	33.88	2.147	1.417	P20D2V00	1.52	0.11	13.64	0.00	2.28	4.58	4.41	4.89	3.23	10.44	3.09
P20D1V01	0.03	0.5	33.85	2.168	1.455	P20D2V01	1.49	0.09	13.57	0.53	2.28	4.83	4.28	4.95	3.32	11.02	2.43
P20D1V02	0.09	1.0	33.78	2.198	1.516	P20D2V02	1.45	0.05	13.40	1.77	2.29	5.25	4.04	5.03	3.47	12.01	1.23
P20D1V03	0.22	2.5	33.66	3.051	1.541	P20D2V03	1.98	0.33	13.09	4.04	2.29	5.45	14.09	7.00	3.54	12.50	24.00
P20D1V04	0.70	5.0	33.18	3.364	1.703	P20D2V04	1.98	0.33	11.82	13.36	2.33	6.75	17.34	7.83	3.96	15.72	29.90
P20D1V05	0.84	9.9	33.03	3.774	1.909	P20D2V05	1.98	0.33	11.43	16.19	2.34	8.52	21.94	8.82	4.46	19.92	38.02
P20D1V06	0.91	19.3	32.97	4.303	2.424	P20D2V06	1.78	0.27	11.25	17.51	2.34	13.77	25.03	10.08	5.68	32.25	37.13
P20D1V07	0.94	29.7	32.94	4.396	2.666	P20D2V07	1.65	0.21	11.17	18.09	2.35	16.67	23.09	10.31	6.25	39.09	28.10
P20D1V08	0.96	39.9	32.92	4.580	2.791	P20D2V08	1.64	0.20	11.13	18.41	2.35	18.28	24.85	10.75	6.55	42.88	29.71
P20D1V09	0.97	49.9	32.91	4.687	2.891	P20D2V09	1.62	0.19	11.10	18.61	2.35	19.62	25.40	11.00	6.78	46.04	28.93
P20D1V10	0.98	59.7	32.90	4.706	2.973	P20D2V10	1.58	0.17	11.08	18.76	2.35	20.75	24.32	11.05	6.98	48.71	24.63
DOWNLOADING																	
P20D1V11	0.97	55.0	32.90	4.827	2.954	P20D2V11	1.63	0.20	11.08	18.76	2.35	20.48	27.38	11.33	6.93	48.09	32.22
P20D1V12	0.97	45.5	32.90	4.686	2.887	P20D2V12	1.62	0.19	11.09	18.73	2.35	19.56	25.46	11.00	6.78	45.92	29.14
P20D1V13	0.97	35.8	32.91	4.579	2.790	P20D2V13	1.64	0.20	11.09	18.68	2.35	18.27	24.85	10.75	6.55	42.88	29.74
P20D1V14	0.96	26.0	32.92	4.427	2.659	P20D2V14	1.66	0.22	11.13	18.40	2.35	16.59	23.86	10.39	6.24	38.92	30.04
P20D1V15	0.97	35.8	32.91	4.198	2.409	P20D2V15	1.74	0.25	11.09	18.68	2.35	13.62	23.20	9.85	5.65	31.97	33.15
P20D1V16	0.96	26.0	32.92	3.774	1.888	P20D2V16	2.00	0.33	11.13	18.40	2.35	8.36	22.27	8.85	4.43	19.62	39.16
P20D1V17	0.37	1.0	33.51	2.700	1.414	P20D2V17	1.91	0.31	12.69	6.99	2.31	4.61	10.66	6.22	3.26	10.62	17.49
P20D1V18	0.20	0.5	33.68	2.460	1.362	P20D2V18	1.81	0.28	13.14	3.67	2.29	4.25	8.21	5.64	3.12	9.75	12.31

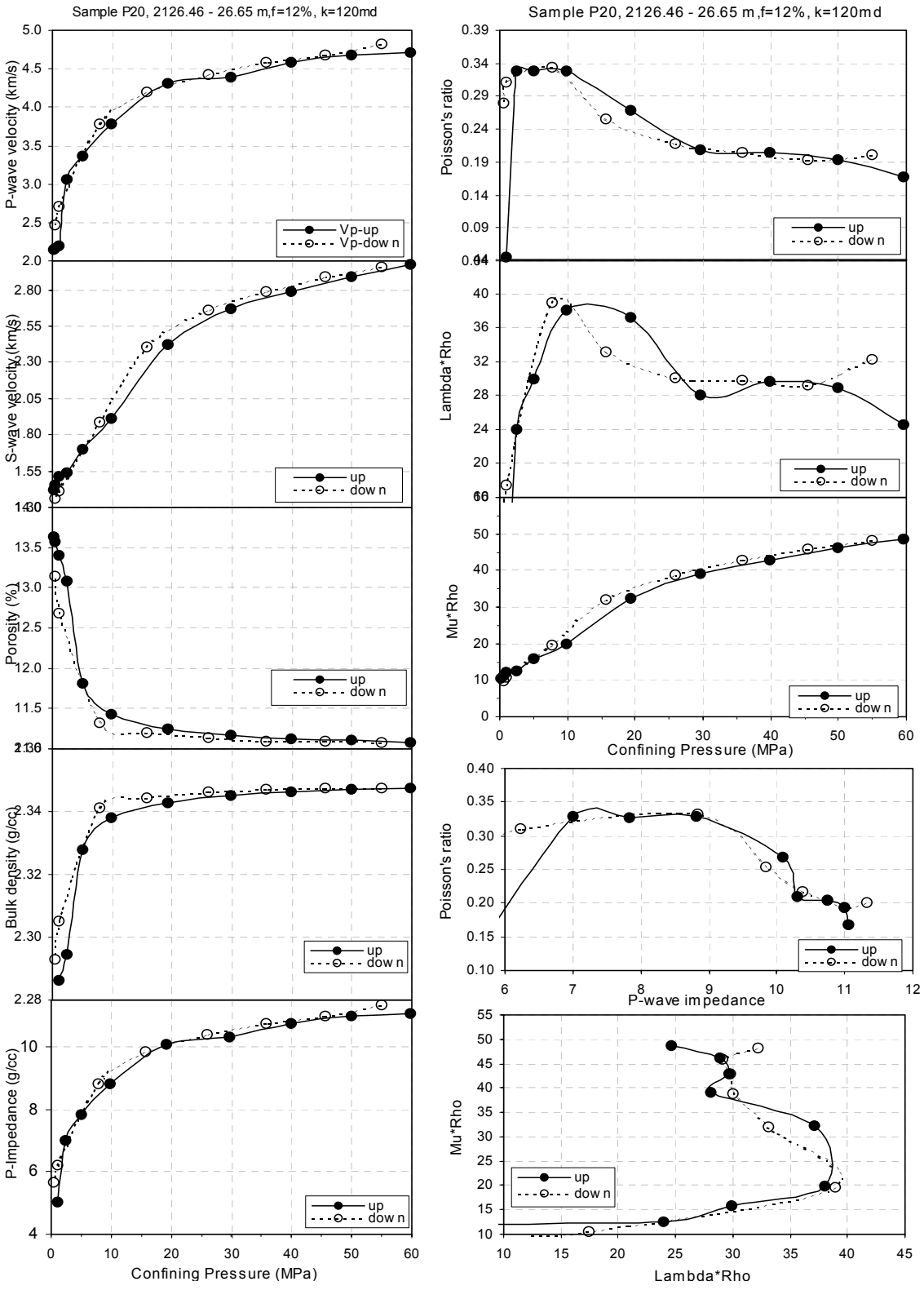

Figure 5.5: Effect of confining pressure on elastic properties of P20 samples, plots for each sample are in Appendix A.

The effects of confining pressure on the elastic properties of dry samples are shown in Fig. 5.6 to 5.7. During the lower confining pressure (0 – 20 MPa), a rapid increase in velocity with increasing confining pressure was observed in all samples, probably because of closing of the fine cracks. There was poor signal quality and high uncertainty in the picks of the first arrivals, and hence larger errors in the velocity calculation. However, little or no increase in velocity was observed with the higher confining pressure (30 MPa). Our speculation is that the majority of the cracks were closed. The signal and the first arrival were clear at high confining pressure, reducing the error in the computation of the velocity. Figure 5.6 and 5.7 show that under pressure all samples behave in the same manner. There is a systematic and predictable behavior of the BQ rocks. Therefore, these graphs can be used for pore pressure monitoring.

The results show clearly that the effects of confining pressure on the rock's elastic properties are high at lower confining pressure values. Therefore, appropriate effective pressures must be applied to the core data before relating them to the log data.

The reservoir, the interval of interest, is located at around 2150 m, corresponding to effective pressure of about 30 MPa. Table 5.5 presents the measured and computed rock properties for all samples at a effective pressure of 30 MPa.

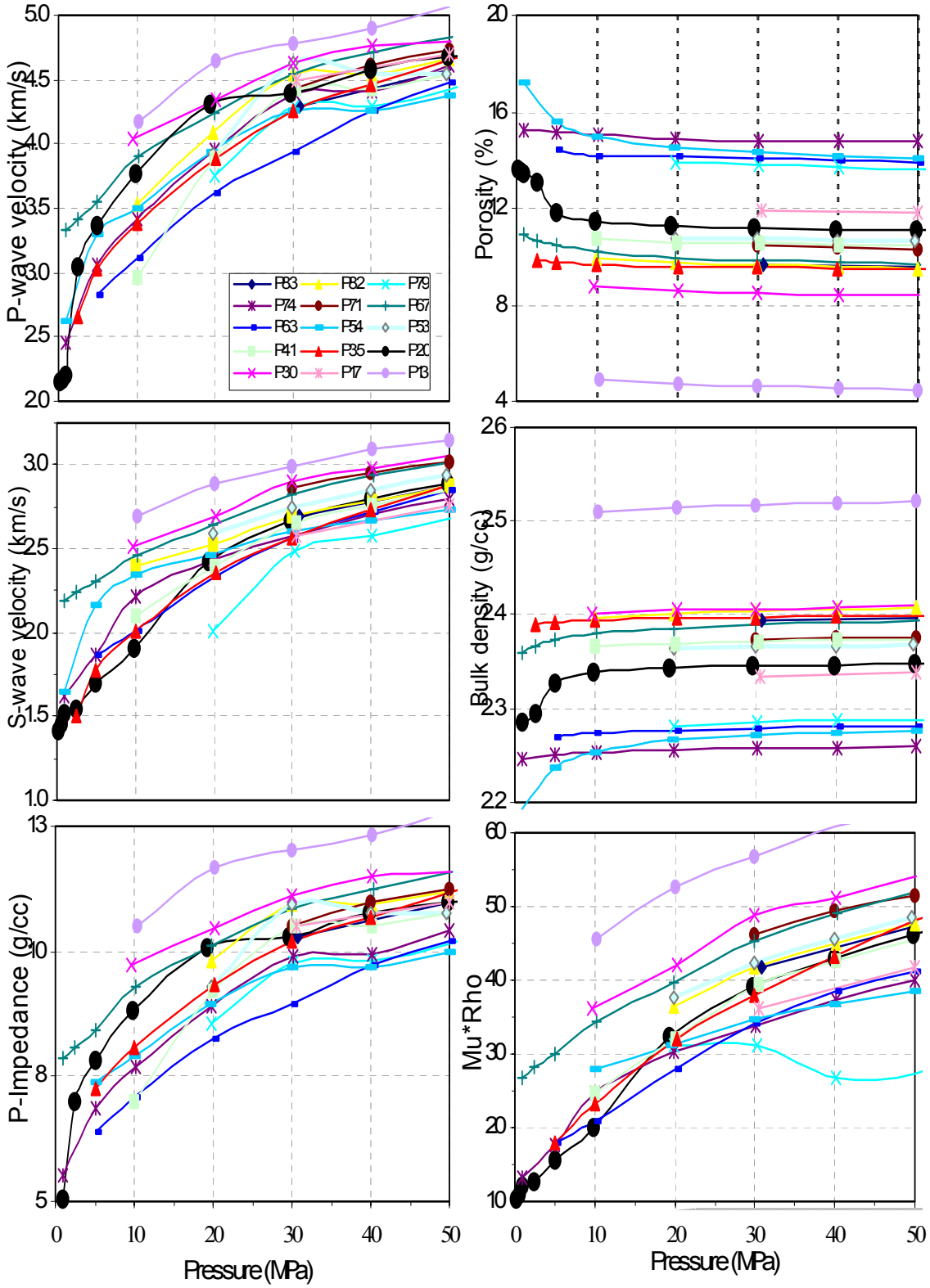

Figure 5.6: Summary plots, effect of pressure on the elastic properties of all samples (P2 and P3 excluded).

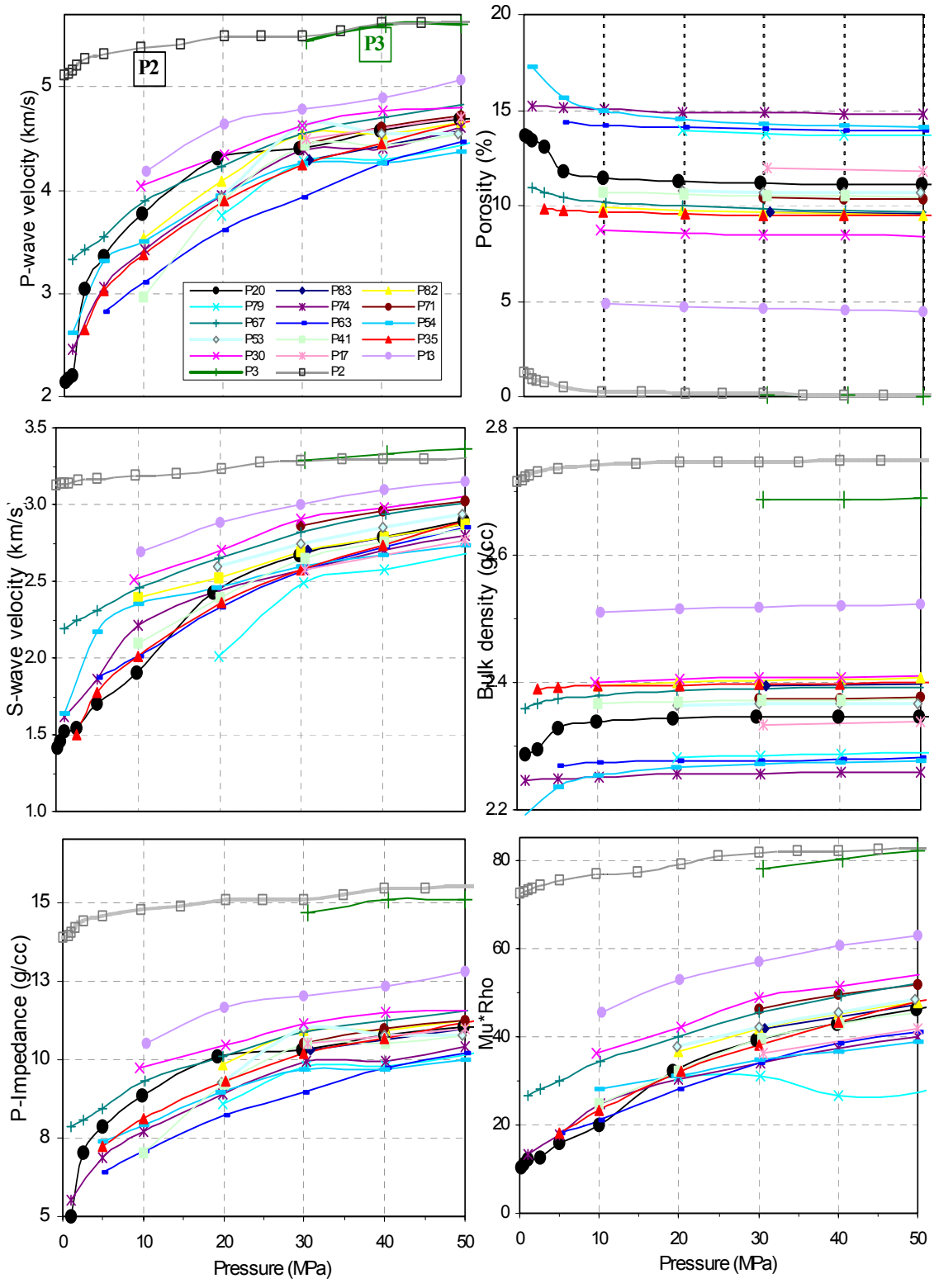

Figure 5.7: Summary plots, effect of pressure on the elastic properties of all samples, including P2 and P3.

Table 5.5: Measured And Computed Properties Of All Samples At 30 MPa Effective Pressure.

Sample	Depth	Rhob air sat.	Rhob water sat.	Phi-core	Vp--core	Vs-core	Ip	Is	K	μ	ν	$\lambda\rho$	$\mu\rho$
ID	(m)	(g/cc)	(g/cc)		(km/s)	(km/s)	(km/s g/cc)	(km/s g/cc)	G Pa	G Pa		$(km/s\ g/cc)^2$	$(km/s\ g/cc)^2$
P2	2121.29	2.69	2.69	0.00	5.49	3.29	14.77	8.85	42.31	29.12	0.17	61.61	78.32
P3	2121.52	2.69	2.69	0.00	5.45	3.28	14.66	8.83	41.18	28.99	0.17	58.79	77.99
P13	2124.28	2.52	2.57	0.05	4.78	3.00	12.04	7.55	27.41	22.60	0.13	31.11	56.96
P17	2125.65	2.33	2.45	0.12	4.50	2.58	10.48	6.01	26.47	15.49	0.21	37.63	36.08
P20	2126.46	2.35	2.46	0.11	4.40	2.68	10.33	6.30	22.89	16.89	0.16	27.33	39.69
P30	2128.95	2.41	2.49	0.08	4.62	2.89	11.14	6.96	24.65	20.13	0.14	27.06	48.51
P35	2130.27	2.40	2.51	0.11	4.25	2.57	10.21	6.17	22.28	15.85	0.16	28.10	38.04
P41	2132.08	2.37	2.48	0.11	4.43	2.67	10.50	6.32	24.07	16.84	0.17	30.44	39.92
P53	2135.44	2.37	2.47	0.10	4.63	2.75	10.97	6.51	26.92	17.88	0.18	35.53	42.39
P54	2135.57	2.27	2.41	0.14	4.27	2.60	9.68	5.90	20.88	15.32	0.16	24.22	34.78
P63	2138.12	2.28	2.42	0.14	3.93	2.56	8.96	5.84	15.29	14.95	0.10	12.14	34.09
P67	2139.00	2.39	2.51	0.12	4.55	2.82	10.86	6.74	24.05	18.99	0.14	27.21	45.39
P71	2140.14	2.37	2.47	0.10	4.43	2.86	10.50	6.78	20.66	19.39	0.11	18.34	45.94
P74	2141.10	2.26	2.41	0.15	4.39	2.58	9.93	5.83	23.61	15.02	0.19	30.72	33.95
P79	2143.27	2.29	2.44	0.15	4.28	2.49	9.81	5.70	23.11	14.18	0.20	31.28	32.48
P82	2146.02	2.40	2.50	0.10	4.55	2.69	10.92	6.46	26.54	17.39	0.18	35.87	41.74
P83	2146.29	2.39	2.49	0.10	4.30	2.70	10.27	6.45	20.94	17.42	0.13	22.29	41.64

5.5 ANALYSIS OF EXPERIMENTAL RESULTS

5.5.1 Quality Control of Log P- and S-Wave Velocity

Figure 5.8 shows the comparison between the laboratory data at 30 MPa effective pressure and the log data at in-situ condition. The red and blue symbols are the laboratory measurements results, and the continuous lines are the log profiles at in-situ conditions. From left to right:

- the density porosities from the laboratory data and those from log are in good agreement,
- the dry sample bulk densities (red) are lower that the log bulk density; whereas, the water-saturated bulk densities (blue) equal those of the log data. Therefore, the logging tools measured a water-saturated formation.
- the P-wave velocities from the lab data match the P-wave velocities from sonic log,
- there is no good consistency between the core and log S-wave velocity. We believe in core measurements, therefore we need to correct the log Vs.

At 30 MPa, the laboratory and the log data are almost the same. Therefore, we can conclude that:

(1) the well log data are of good quality (except the S-wave velocity), (2) the velocity-frequency dispersion can be neglected at 30 MPa effective pressure, which equal the in-situ condition, and (3) log and core data are consistent; therefore, a unified model can be developed for both of them.

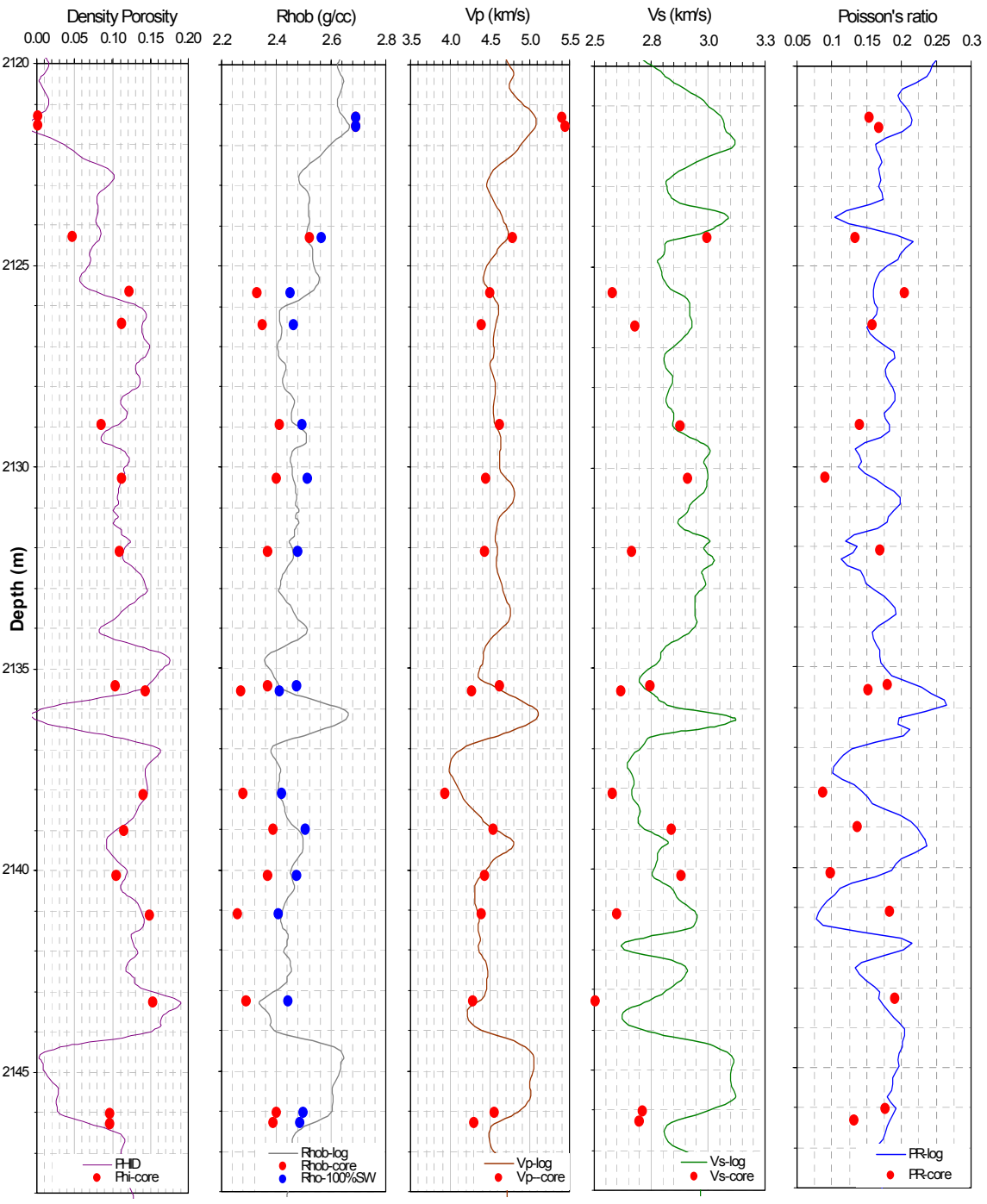

Figure 5.8: Comparison of lab data to log data. From left to right: profiles versus depth of porosity, bulk density, P-wave velocity, S-wave velocity, and Poisson's ratio. The symbols are the measurements from the Stanford Rock Physics lab, and the continuous lines are the log profiles.

5.5.2 Hydraulic Unit Zonation Process

In this section, we will use the bench top porosity and permeability data as well as sample visual description to establish relations between permeability, porosity, and grain properties.

Hydraulic unit zonation involves the application of fundamental theory and statistical analysis to discriminate the data into different subgroups (hydraulic unit) within which the rock and petrophysical properties are homogenous, steady, and predictably different from any other subgroups. Hydraulic unit zonation involves the discrimination of different families of Flow Zone Indicator (FZI). FZI is the parameter that incorporates the geological attributes of texture and mineralogy and allows the discrimination of distinct pore geometrical facies (hydraulic unit). Amaefule et al. (1993) derived, from the Kozeny Carman (Carman, 1961) equation, the formula for calculating FZI as follows:

$$FZI = 0.0314(1-\phi)\sqrt{\frac{k}{\phi^3}} \tag{5.7}$$

where: FZI is the Flow Zone Indicator,

k is the permeability in mD, and

ϕ is the porosity in fraction.

The histogram distribution of FZI, based on data presented in Table 5.3, is shown on Fig.5.9. Four distinct hydraulic units (HU) were identified within the lab data**.** The description of each hydraulic unit is presented in Table 5.6.

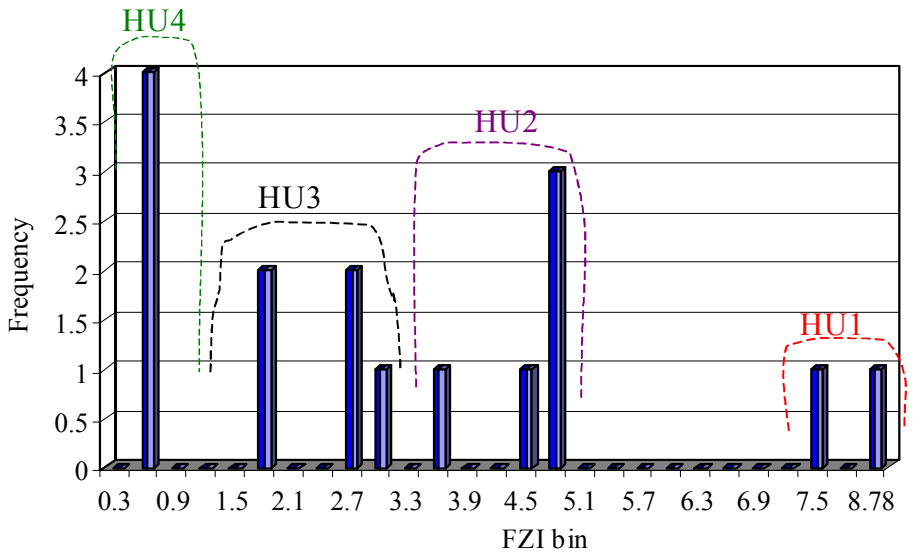

Figure.5.9: Frequency distribution of FZI. Four distinct hydraulic units were identified.

5.5.3 Permeability-Porosity Relationships

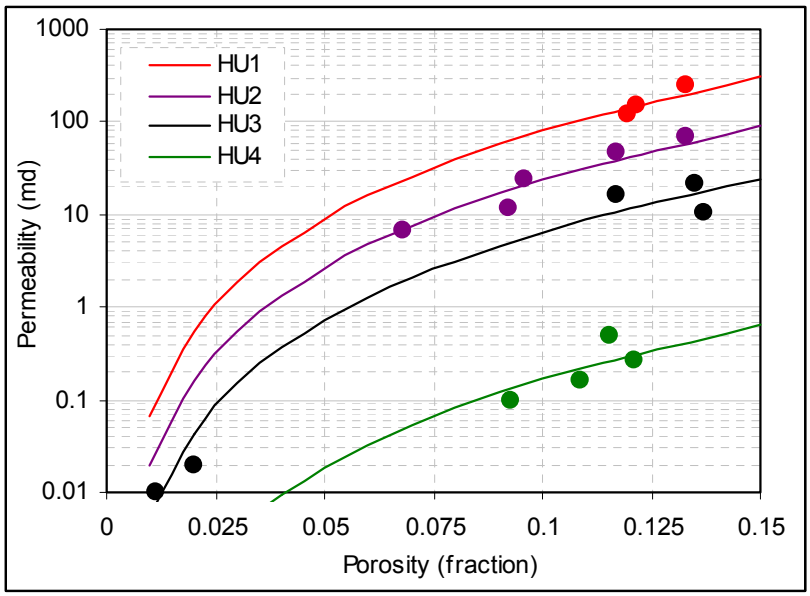

Figure 5.10: Plot of permeability versus porosity, k-ϕ type curves, for each hydraulic unit. The data are color coded by hydraulic unit.

Figure 5.10 shows the k-ϕ type curves for each hydraulic unit. The permeability versus porosity values from the laboratory data are superimposed on these type curves.

Commonly, such k-ϕ type curves are valid for the entire reservoir from which the data were extracted, and also for similar types of reservoirs. The formula for calculating permeability from porosity is the following:

$$k = 1014 FZI^2 \frac{\phi^3}{(1-\phi)^2} \tag{5.8}$$

Table 5.6 shows the parameters for each hydraulic unit.

Generally, FZI can be correlated and predicted from well log variables such as gamma ray, resistivity, bulk density, and/or sonic travel time. Moreover, FZI can be related to pore radius, irreducible water saturation, and initial and/or residual oil saturation, so its value can be estimated from these variables (Amaefule et al., 1989, 1991,1993, 1997). Once FZI is predicted, the equation of permeability as a function of porosity, derived from Eqn. 5.8 and presented in Table 5.6 for each HU, can be used to predict permeability from porosity.

Table 5.6: Description and permeability-porosity models for each hydraulic unit.

Hydraulic Unit	FZI mean	FZI range	$K = f(\phi)$	R^2
1	8.04	7.3 <	$k = 65546.6 \frac{\phi^3}{(1-\phi)^2}$	0.99
2	4.27	3.4 – 4.7	$k = 18488 \frac{\phi^3}{(1-\phi)^2}$	0.96
3	2.27	1.5 – 2.9	$k = 5225 \frac{\phi^3}{(1-\phi)^2}$	0.90
4	0.37	< 0.6	$k = 138.8 \frac{\phi^3}{(1-\phi)^2}$	0.65

Based on the lithology description, sorting, and grain size analyses, these four hydraulic units can be regrouped into three groups, as shown in Table 5.7. Group I contains the best quality reservoir rocks, and Group III comprises the worst quality reservoir rocks. The corresponding permeability versus porosity and permeability versus P-wave velocity plots are shown in Figure 5.11.

Table 5.7: Descriptions of Each Group.

Group	Lithology Descriptions	$K = f(\phi)$	R^2
I	Well sorted, medium or coarse grain size, clean sands	$k = 65546.6\frac{\phi^3}{(1-\phi)^2}$	0.99
II	Poorly sorted, medium or coarse grain size, shaley sands	$k = 11089.4\frac{\phi^3}{(1-\phi)^2}$	0.98
III	Very fine or fine grain size, shale or overbank	$k = 138.8\frac{\phi^3}{(1-\phi)^2}$	0.65

5.5.4 Permeability-Porosity-Velocity Relationships

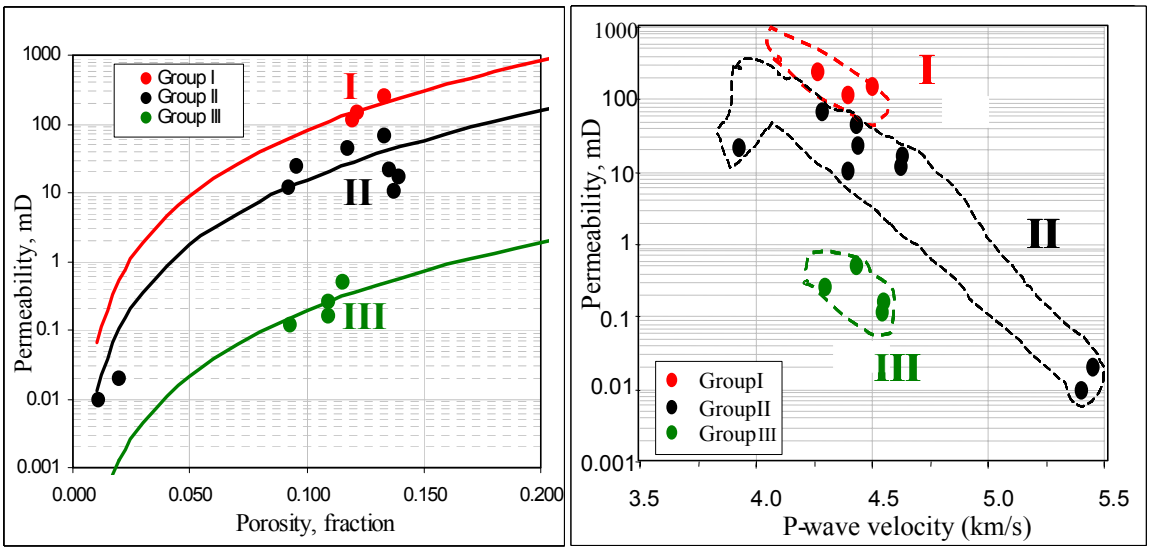

Figure 5.11: Left: Plot of permeability versus porosity color-coded by group number. Right: Plot of Permeability versus bench-top P-wave velocity color-coded by group number.

Figure 5.11 and Table 5.7 illustrate that there are good correlations between permeability and porosity within each group. Moreover, it reveals that there are also good correlation between permeability and velocity within each group. If lithology, sorting, grain size distribution, and/or clay content are known, but FZI is unknown, Table 5.7 can be used to define the group number, and the corresponding models can be used to predict permeability from porosity. The models in Table 5.7 were derived from Eqn. 5.8 for each group.

5.6 CONCLUSION

- Under pressure, there is a systematic and predictable behavior of the BQ rocks, hence possibility of pore pressure monitoring.
- Based on Flow Zone Indicator (FZI) distribution, the lab permeability and porosity values can be classified into 4 distinct hydraulic units. Once FZI is known, models in Table 5.6 can be used to predict permeability from porosity. Based on the lithology description, sorting, and grain size analyses, these four hydraulic units were regrouped into three groups. Group I contains the highest-quality reservoir rock type, and Group III comprises the lowest-quality rock type. If lithology, sorting, grain size distribution, and/or clay content are known, but FZI is unknown, models in Table 5.7 can be used to predict permeability from porosity.
- At 30 MPa differential pressure, the lab and log data are almost the same. Therefore, we can conclude that: (1) the well log data, except the Vs, are of good quality, (2) the velocity-frequency dispersion can be neglected in well log data, and (3) log and core data are consistent; therefore, a unified model can be developed for core and log data.

5.7 REFERENCES

Amaefule, J.O, Njoku, N.A., Edbogah, E.O., Keelan, D.K., Rasolovoanhangy, R.E., Udegbunam,E.O, 1997, Mature Niger Delta Reservoirs Integration of Core and Log Data for Flow Unit Zonation and Permeability Prediction: SPENC 9702.

Amaefule, J.O., Altunbay, M., Tiab, D., Kersey, D., Keelan, D., 1993, Enhanced Reservoir Description: Using Core and Log Data to Identify Hydraulic (Flow) Units and Predict Permeability in Uncored Intervals/wells: SPE 26436.

Castagna, J. P., Batzle, M. L., and Eastwood, R. L., 1985, Relationships between compressional-wave and shear-wave velocities in clastic silicate rocks, Geophysics, 50, 571-581.

Mavko, G., Mukerji, T., Dvorkin, J., 1998, Rock physics handbooks, Cambridge University Press.

Prasad, M., Palafox, G., Nur, A., 1999, Velocity and Attenuation characteristics of Daging sandstones: Effect of permeability and Attenuation anisotropy: AGU Fall Meeting, E08, V.80.

CHAPTER 6

EFFECTIVE MEDIUM MODELS FOR LOW POROSITY SANDS

6.1 INTRODUCTION

An effective medium theory helps estimate the effective elastic properties of rock from the properties of various constituent minerals, pore fluid, and texture. Texture reflects the geometrical details of how various constituents are arranged. Establishing an effective medium theory from first principles, that describes a given medium is one of fundamental tasks in rock physics.

The goal of this chapter is to use laboratory and well log data to select and calibrate a rational effective medium theory suitable for BQ sands. This rational effective medium model will be used to predict porosity, lithology, pore fluid, and permeability from log and seismic data.

We start with the investigation of the existing empirical models for consolidated sandstones: Wyllie et al (1956, 1958, 1963), Raymer et al. (1980), Tosaya et al (1982), and Han (1986). After that, we develop a new empirical model (a regression) for the laboratory data. Finally, we introduce a rigorous model that is a combination of the Hertz-Mindlin theory and modified Hashin-Strikman upper bound (Mindlin, 1949, Dvorkin 1996, Gal et al. 1997). In addition, we offer an alternative model that is a combination of the two empirical models of Raymer et al. (1980) and Greenberg and Castagna (1985).

6.2 DESCRIPTION OF DATA

The laboratory data include: (a) P- and S-wave velocity data measured on dry samples at varying hydrostatic confining pressure from bench top to 50 MPa; (b) helium porosity measured at room conditions and at confining pressure up to 50 MPa; (c) Klinkenberg corrected gas permeability measured at room conditions; (d) and specific grain size analyses. These measurements were done on 17 samples with porosities ranging from 2 % to 15%, clay content ranging from 2 % to 24 %, permeability ranging from 0.01 mD to

250 mD, P-wave velocity ranging from 2 to 5.5 km/s, and S-wave velocity ranging from 1.3 to 3.4 km/s. These 17 core samples are consolidated sandstones and were extracted from well W2 from depth between 2121.9 and 2146.61 m.

The log data consist of all the conventional log variables, such as gamma ray, bulk density, sonic travel times, resistivity, caliper, and spontaneous potential from 17 wells in BQ field.

6.3 EXISTING EMPIRICAL MODELS

First, we review each empirical model. Second, we superimpose all the empirical models on the laboratory data. Last, we assess the accuracy of the fit of each model to the laboratory data.

Wyllie et al (1956, 1958, 1963) found that travel time through water saturated consolidated rocks could be approximately described as the volume weighted average of the travel time through the minerals plus the transit time through the pore fluid. Hence, it is often called the **time average equation**. This time average equation is described as follows:

$$\frac{1}{V_P} = \frac{\phi}{V_{Pfl}} + \frac{1-\phi}{V_{PO}} \tag{6.1}$$

where V_P is the P-wave velocity of the saturated rocks,

V_{Pfl} is the P-wave velocity of the fluid phase,

V_{Po} is the P-wave velocity of the mineral phase, and

ϕ is the porosity.

Eqn. 6.1 presents a simple and convenient, but misleading form of summarizing experimental data. There is no physical reason for the total travel time of a wave in a two-component composite to be the sum of the travel time in the individual components, unless the two components are arranged in layers normal to the direction of propagation, and the wavelength is small as compared to the thickness of an individual layer. Eqn. 6.1 works best for isotropic, consolidated, and fluid saturated rocks at 30 MPa effective pressure or higher (Dvorkin, 1998). Additionally, Eqn. 6.1 can be used to estimate the

expected seismic velocities of rocks with a given mineralogy and pore fluid, and also to estimate porosity from measurements of seismic velocity and knowledge of the rock type and pore-fluid content (Mavko et al., 1998.).

Raymer et al. (1980) suggested an improvement to Wyllie's empirical velocity formula by introducing different laws for different porosity ranges as follows:

$$V = (1-\phi)^2 V_o + \phi V_{fl}, \phi < 37\% \tag{6.2}$$

$$\frac{1}{\rho V^2} = \frac{\phi}{\rho_{fl} V_{fl}^2} + \frac{1-\phi}{\rho_o V_o^2}, \phi > 47\% \tag{6.3}$$

where V, V_{fl}, and V_o are the P-wave velocities of the saturated rocks, fluid phase, and mineral phase respectively,

ϕ is the porosity, and

ρ_{fl} and ρ_o are the density of the fluid phase and mineral phase respectively.

Raymer et al. (1980) recognized the need for two porosity domains: the consolidated-rock domain of Eqn. 6.2, and the suspension domain of Eqn. 6.3. These equations were claimed to work remarkably well for clay–free sandstones, as well as for "dirty" sandstones with clay; however, they fail to describe unconsolidated sandstone (Nur et al., 1998). Moreover, with reasonably chosen solid-phase velocity, these equations can be reliably used for cemented sandstones in the porosity interval from zero to 0.35 (Dvorkin et al., 1998). Eqn. 6.2 and Eqn. 6.3 can be used to estimate the seismic velocities of rocks with a given mineralogy and pore fluid, and also to estimate the porosity from measurements of seismic velocity and knowledge of rock type and pore fluid content (Mavko et al., 1998.)

Tosaya et al. (1982), based on their measurements, developed an empirical model relating P-and S-wave velocity at 40 MPa to porosity and clay content for saturated rocks.

$$V_p(km/s) = 5.8 - 8.6 * \phi - 2.4 * C \tag{6.4}$$

$$V_s(km/s) = 3.7 - 6.3*\phi - 2.1*C \tag{6.5}$$

where ϕ is porosity and C is clay content.

Eqn. 6.4 and 6.5 are empirical, and strictly speaking they should apply only to the set of rocks studied. The regression coefficients in Eqn. 6.4 and 6.5 should be recalibrated from cores or logs at the site being studied. Eqn. 6.4 and 6.5 can be used to relate velocity, porosity, and clay content empirically in consolidated and shaley sandstones (Mavko et al., 1998.)

Castagna et al. (1985), based on their laboratory measurements, determined empirical regressions relating velocity with porosity and clay content in water-saturation, shaley sands of the Frio formation.

$$V_p(km/s) = 5.81 - 9.42*\phi - 2.21*C \tag{6.6}$$

$$V_s(km/s) = 3.89 - 7.07*\phi - 2.04*C \tag{6.7}$$

where ϕ is porosity and C is clay content.

Eqn. 6.6 and Eqn. 6.7 are empirical. They should only be applied to the set of rock studied. They can be used to relate velocity, porosity, and clay content empirically in consolidated and shaley sandstones (Mavko et al., 1998.)

Han (1986) created empirical relations relating ultrasonic velocity, porosity and clay content from consolidated, water-saturated sandstones having porosity ranging from 3 to 30% and clay volume fraction from 0 to 55%. Han's model for shaley sandstones, water saturated, at 30 MPa effective pressure are the following:

$$V_P = 5.55 - 6.96*\phi - 2.18*C \tag{6.8}$$

$$V_S = 3.47 - 4.84*\phi - 1.87*C \tag{6.9}$$

where ϕ is porosity and C is clay content.

For clean sandstones, velocity can be related to porosity alone with very high accuracy. However, if clay is present, it has to be included in the regression in order to obtain high accuracy. Due to the empirical origin of Eqn. 6.8 and Eqn. 6.9, they should only be applied to the set of data studied. However, the results can be extended, in general, to many consolidated sandstones by recalibrating the regression coefficient for the site being studied. Eqn. 6.8 and Eqn. 6.9 can be used to relate velocity, porosity, and clay content empirically in consolidated and shaley sandstones (Mavko et al., 1998.)

6.4 CROSSPLOTS

Figure 6.1 shows the plot of the existing empirical models superimposed on top of the laboratory measured P-wave velocity versus porosity at 30 MPa effective pressure. Since the samples' clay content ranges between 2 to 24% (no pure clean sandstones), the Han, Tosaya et al., Castagna et al., Wyllie, and Raymer models were plotted for clay content of 12 %.

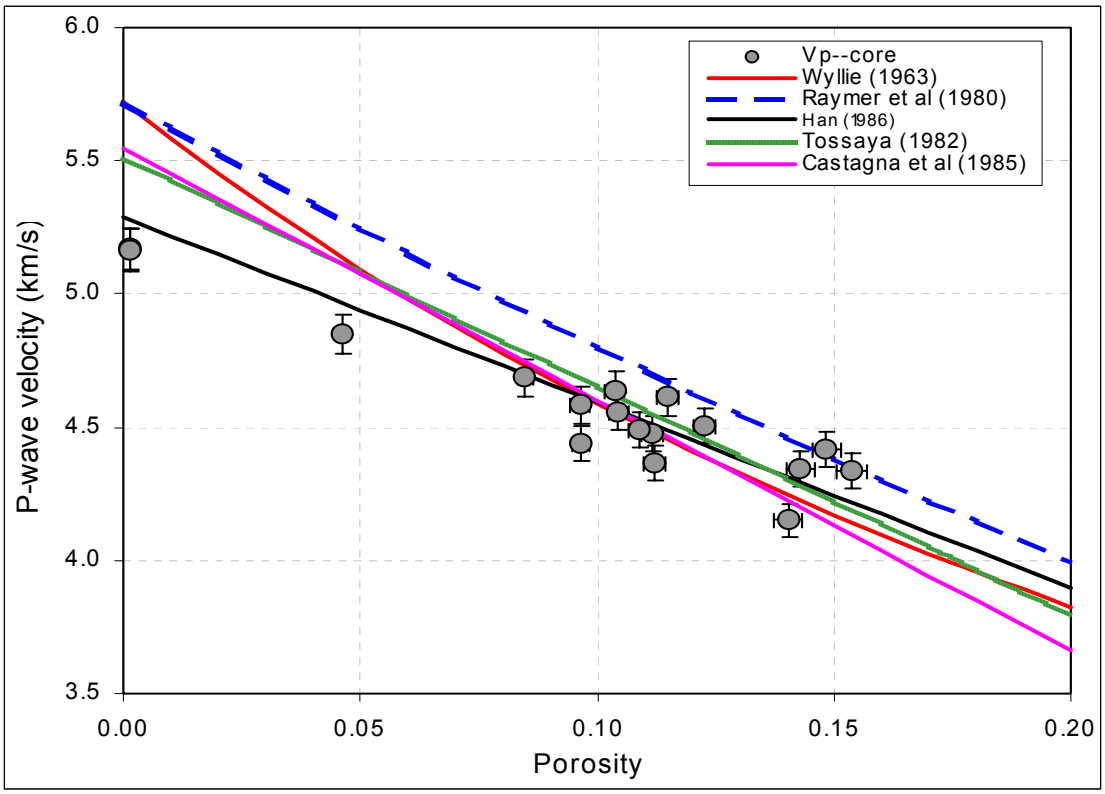

Figure 6.1: Plots of the empirical curves by Wyllie (1963) in red, Raymer et al. (1982) in dashed blue, Han's (1986) in black, Tosaya (1982) in green, Castagna et al. (1985) in pink, superimposed on top of the 100% water-substituted P-wave velocity versus porosity from laboratory data in gray symbols. The laboratory data were measured at room dry at 30 MPa, and then fluid substituted to 100% water using Gassmann's equation.

Among all the empirical models plotted in Fig. 6.1, Han's regression model, which relates P-wave velocity to porosity and clay content at 30 MPa, provides the closest approximation to the trend apparent in the data. Therefore, clay content and pressure are important parameters for quantifying velocity. Still, Figure 6.1 shows that none of the empirical velocity-porosity models characterize the laboratory data with high accuracy. Consequently, a more accurate empirical model needs to be generated from the laboratory data.

Figure 6.2 shows the 3D plot of P-wave velocity versus porosity and clay content for the 100% water-substituted laboratory data at 30 MPa effective pressure. The regression model relating P-wave velocity to porosity and clay content is presented in Eqn. 6.10.

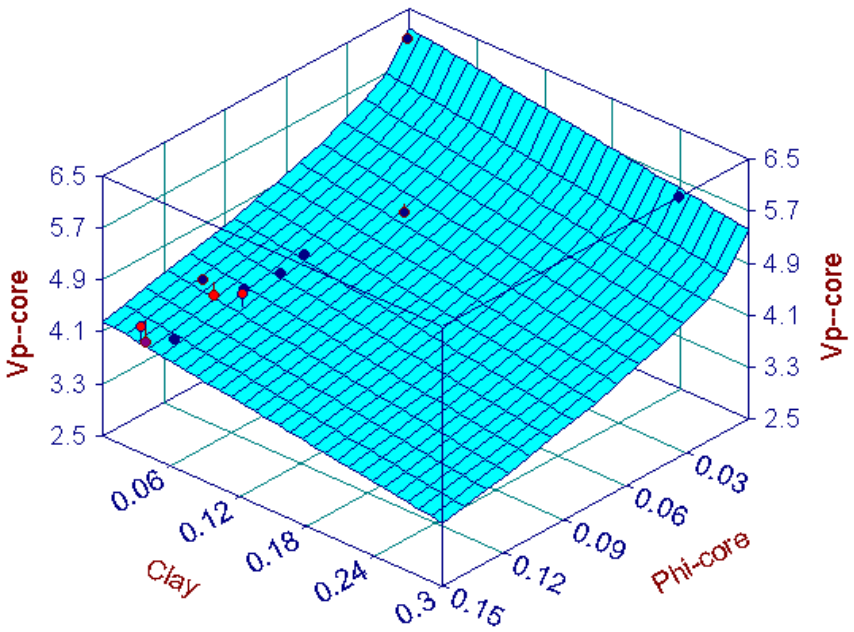

Figure 6.2: Plot of P-wave velocity versus porosity and clay content for 100% water saturated laboratory data at 30 MPa effective pressure.

Figure 6.3 shows the 3D plot of S-wave velocity versus porosity and clay content from laboratory data. The regression model relating S-wave velocity to porosity and clay content is presented in Eqn. 6.11.

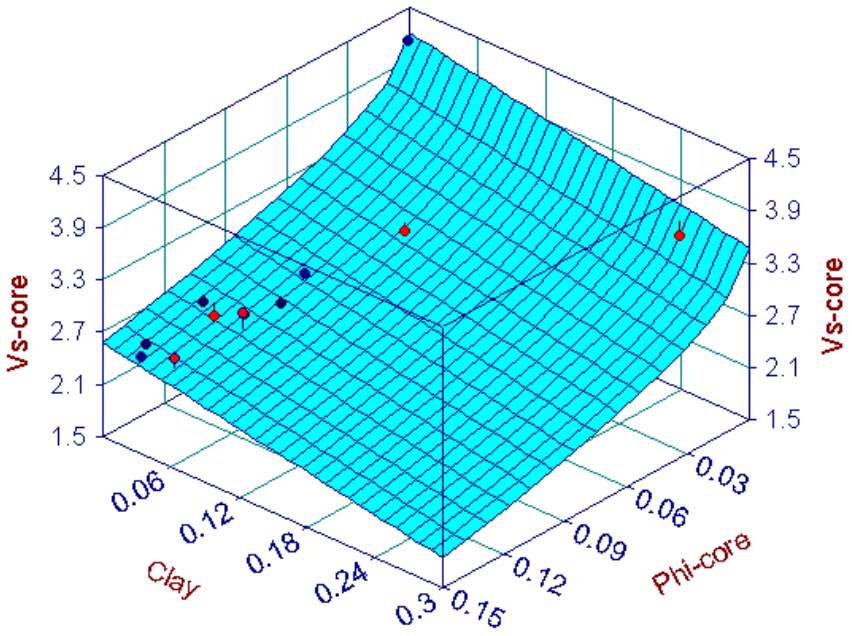

Figure 6.3: Plot of S-wave velocity versus porosity and clay content for the laboratory data at 30 MPa effective pressure.

When deriving the regressions, we supplemented the laboratory data with theoretical zero-porosity points: (a) for pure quartz with Vp = 6.04 km/s and Vs = 4.12 km/s, and (b) for pure clay with Vp = 3.41km/s and Vs = 1.64 km/s.

$$Vp = 6.1743 - 4.6044 * \phi^{0.5} - 2.603 * C \tag{6.10}$$

$$V_S = 4.2047 - 4.134 * \phi^{0.5} - 2.441 * C \tag{6.11}$$

where ϕ is porosity in volume fraction,

C is clay content in volume fraction, and

V_P and V_S are iesthe P- and S- wave velocity respectively.

Eqn. 6.10 and Eqn. 6.11 characterize the laboratory data with high accuracy (with R^2 of 0.991 and 0.989 respectively), however they are empirical multiple regressions based on a laboratory data set; therefore, they may fail to be general. Consequently, there is great need to build a rigorous model based on rational rock physics (first principles) for low porosity sands.

6.5 RATIONAL ROCK PHYSICS MODELS

A rational rock physics model is a model based on first principles. It treats rock as a composite and thus requires specific geometric information about the constituents. If such a model fits the data, it is valid to assume that the rock's internal topology is similar to that used in the model. Examples of rock physics models that are based on first principles are: Hertz-Mindlin (1949) theory with the modified Hashin-Shtrikman upper bound valid for moderate to high porosity rocks, Kurster and Toksoz (1974) for low porosity rocks, Hudson (1990) for cracked rocks, Berryman (1980), for low to medium porosity rocks, and Dvorkin et al. (1994) for high porosity granular rocks.

The Hertz-Mindlin contact theory (Dvorkin, 1996) is expressed in Eqn. 6.12 and Eqn. 6.13 to calculate the effective bulk (K_{cr}) and shear (G_{cr}) moduli of a dry, dense, random pack of identical spherical grains, subject to a hydrostatic pressure P. Eqn. 6.12 and Eqn. 6.13 are used to calculate the effective elastic properties of sand at critical porosity ϕ_{cr}.

$$K_{cr} = \left[\frac{n^2 (1-\phi_{cr})^2 G^2}{18\pi^2 (1-\nu)^2} P \right]^{\frac{1}{3}} \tag{6.12}$$

$$G_{cr} = \frac{5-4\nu}{5(2-\nu)} \left[\frac{3n^2 (1-\phi_{cr})^2 G^2}{2\pi^2 (1-\nu)^2} P \right]^{\frac{1}{3}} \tag{6.13}$$

where ν is the grain Poisson's ratio,

G is the grain shear modulus, and

P is the hydrostatic pressure.

To predict the effective moduli (K_{eff} and G_{eff}) at a different porosity ϕ, we suggest the heuristic Modified Upper Hashin–Shtrikman bound (MUHS).

6.5.1 The theory of Modified Upper Hashin-Shtrikman Bound

The elasticity of dry sandstone was modeled by Gal et al. (1998) by examining an assemblage of different-size quartz spheres filling the whole space (Hashin and Shtrikman, 1962). Each quartz sphere contains a randomly oriented non-spherical pore centered at its origin. All spheres have the same porosity (ϕ_o) and effective bulk modulus (K_o). All pores have the same shape. Hence, the porosity and bulk modulus of the entire assemblage are ϕ_o and K_o respectively. When the assemblage is subject to porosity reduction due to diagenesis, consider a single sphere in the assemblage, like the one presented in Fig 6.4. The porosity of the sphere is reduced from ϕ_o to ϕ by letting the pore inside it shrink uniformly, while the shape of the pore remains the same. The new sphere (with porosity ϕ and bulk modulus K) is simply the downsized version of the original sphere embedded in a spherical quartz shell (added quartz).

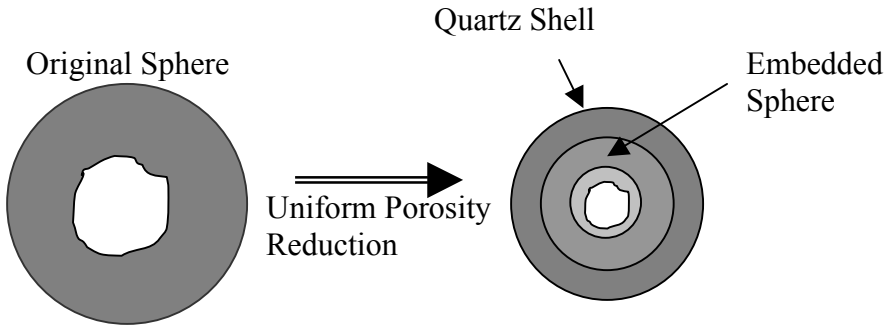

Figure 6.4: Shrinking porosity inside a quartz sphere

The volumetric fraction occupied by the original sphere (the soft end member) is ϕ/ϕ_o, and that occupied by quartz mineral (the stiff end member) is $1-\phi/\phi_o$. The physical realization of the upper Hashin-Shtrikman bound is achieved by repeating the same

process for every sphere in the assemblage. Accordingly, the bulk and shear moduli of each composite sphere are given in the following equations.

$$K = K_q + \frac{\phi/\phi_o}{\frac{1}{K_o - K_q} + \frac{1-\phi/\phi_o}{K_q + \frac{4}{3}\mu_q}}$$

$$G = G_q + \frac{\phi/\phi_o}{\frac{1}{G_o - G_q} + \frac{2(1-\phi/\phi_o)(K_q + 2G_q)}{5G_q(K_q + \frac{4}{3}\mu_q)}}$$

The above equations are the original Hashin-Shtrikman upper-bound formulas scaled from the [0,1] porosity interval to the [0,ϕ_o] interval. The combination of Hertz-Mindlin theory and the theory of Modified Upper Hashin-Shtrikman bound results in Eqn. 6.14 and Eqn. 6.15.

$$K = \left[\frac{\phi/\phi_o}{K_{cr} + \frac{4}{3}G_{cr}} + \frac{1-\phi/\phi_o}{K_o - \frac{4}{3}G_{cr}} \right]^{-1} - \frac{4}{3}G_{cr} \tag{6.14}$$

$$G = \left[\frac{\phi/\phi_o}{G_{cr} + \frac{G_{cr}}{6}\left(\frac{9K_{cr} + 8G_{cr}}{K_{cr}+2G_{cr}}\right)} + \frac{\phi/\phi_o}{G_o + \frac{G_{cr}}{6}\left(\frac{9K_{cr} + 8G_{cr}}{K_{cr}+2G_{cr}}\right)} \right]^{-1} - \frac{G_{cr}}{6}\left(\frac{9K_{cr} + 8G_{cr}}{K_{cr}+2G_{cr}}\right) \tag{6.15}$$

where K_o and G_o are the original rock's bulk and shear moduli respectively,

K_{cr} and G_{cr} are the bulk and shear moduli calculated from Eqn. 6.12 and 6.13,

ϕ_o is the high-porosity end member, and

ϕ is the porosity at which the effective properties are going to be computed.

The theoretical curves predicted by these formulas are plotted on fluid-substituted laboratory data, assuming 100% water-saturation. The theoretical curves are computed and plotted for constant porosity at 5% increments, and for constant clay content at 10%

increments (see Fig. 6.5). The high-porosity end member chosen was the critical porosity for sandstone, $\phi_o=\phi_{cr}$= 40%. The mineral and fluid properties used in the calculation are given in Table 6.1. The plots are shown in Fig. 6.5.

Table 6.1: Elastic properties and density of the pore fluid and minerals.

	K (GPa)	G (GPa)	Density (g/cc)	Vp (km/s)	Vs (km/s)	Poisson's ratio
Quartz	36.6	45	2.65	6.04	4.12	0.064
Clay	21	7	2.6	3.41	1.64	0.35
Air	0.000131	0	0.00119	0.332	0	0.5
Gas	0.04784	0	0.1576	0.551	0	0.5
Water	2.6524	0	1.0134	1.643	0	0.5

6.5.2 Model Fitting of the Lab Data

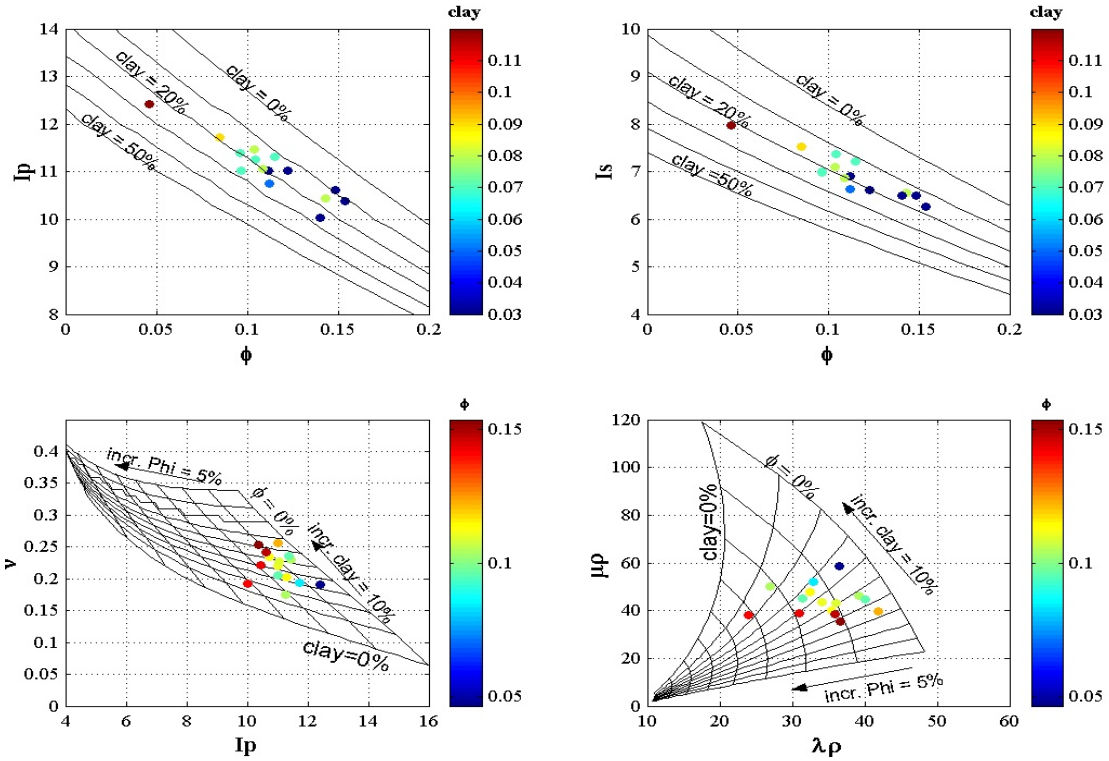

Figure 6.5: From left to right and then top to bottom: plot of I_p versus ϕ; I_s versus ϕ; ν versus I_p, $\mu\rho$ versus $\lambda\rho$ of 100% water saturated laboratory data, color coded by gamma ray or porosity. The lines are the Modified Upper Hashin-Shtrikman bound theoretical curves for 10% clay increments and 5% porosity increments.

6.6 LOG DATA PREPARATION FOR MODEL FITTING

6.6.1 Quality Control of Log Density Porosity

The wells in the BQ field were drilled with fresh water base mud with density of 1g/cc and PH of 11. Figure 6.6 shows that the 100% water saturated bulk density from laboratory measurements match the in situ log bulk density. This tells us that the formation measured by the wireline logging density tool is fully invaded by the mud filtrate. Figure 6.6 also shows that the porosity from laboratory data and the log density porosity computed using Eqn. 6.16 are in good match. Therefore, it is suitable to use the density porosity calculated from Eqn. 6.16 in our calculations and predictions.

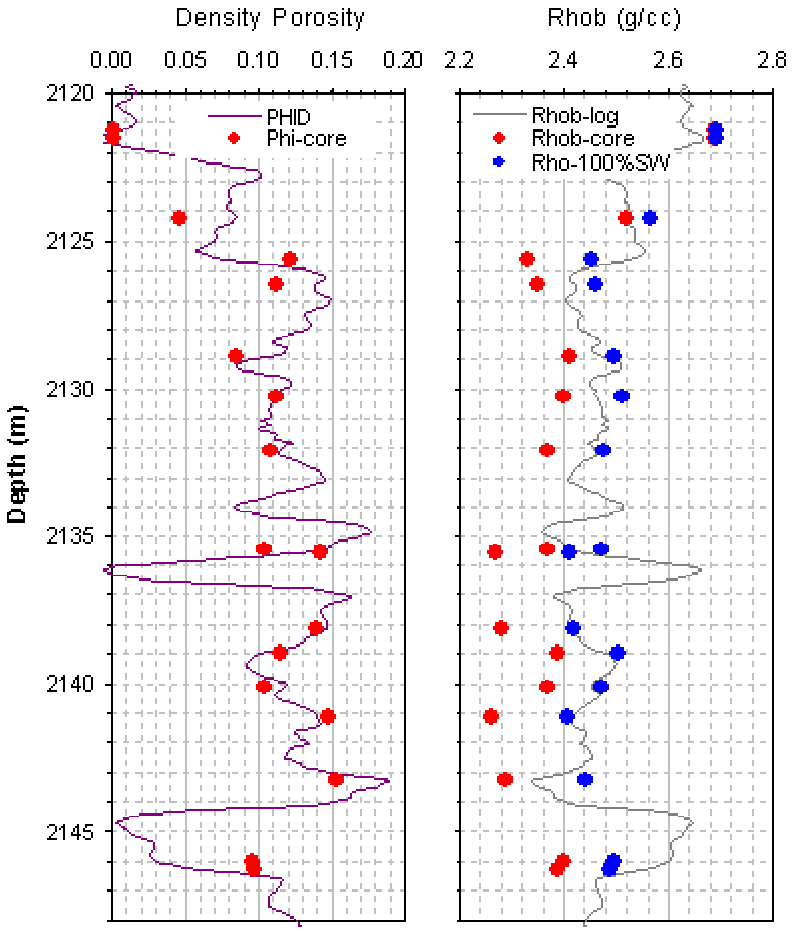

Figure 6.6: On the left, profiles of laboratory-measured porosity at 30 MPa in red symbols superimposed on top of the density porosity from log in purple line. On the right, profiles of laboratory measured bulk density at 30 MPa, with air in red symbols and with 100% water saturation in blue symbols, superimposed on top of the bulk density from the log.

$$\phi_D = \frac{2.65 - \rho_{B-\log}}{1.65} \tag{6.16}$$

Where ϕ_D is the density porosity in fraction, and

$\rho_{B\text{-}log}$ is the bulk density from log, g/cc.

6.6.2 Methods of Fluid Substitution

Velocities depend, not just on saturation, but also on the scales at which the phases are mixed. When the phases are mixed at a fine scale (e.g., imbibition), the pore pressure increments can equilibrate with each other to a single average value, causing a relaxed viscoelastic behavior, thus in good agreement with the Gassmann theory. The effective bulk modulus of the fluid mixture can be described well by the Reuss average. However, if the phases are mixed at a coarse scale (e.g. drainage), it is called patchy saturation. It creates an unrelaxed viscoelastic behavior. Thus, the effective bulk modulus of the mixture of fluids is described well by the Voigt average as follows:

$$K_{fl} = \sum X_i * K_i \tag{6.17}$$

where X_i is the volume fraction of fluid constituents, and

K_i is the bulk modulus of fluid constituents.

It is demonstrated in Fig. 6.6 that the formation measured by the density tool is fully invaded by mud filtrate. Furthermore, Figure 6.7 shows that the saturation calculated from the deep resistivity (S_w) is almost the same as that calculated from shallow resistivity (S_{xo}). This could imply that the mud filtrate invasion may have reached deep into the formation. Because of the effect of fast fluid displacement by mud filtrate, we expect patchy saturation to occur in rock sampled by the Vp tool. Thus, we calculated the effective fluid bulk moduli using the patchy saturation model. The fluid modulus was then used to calculate the elastic moduli of 100% water saturated formation from the available log data.

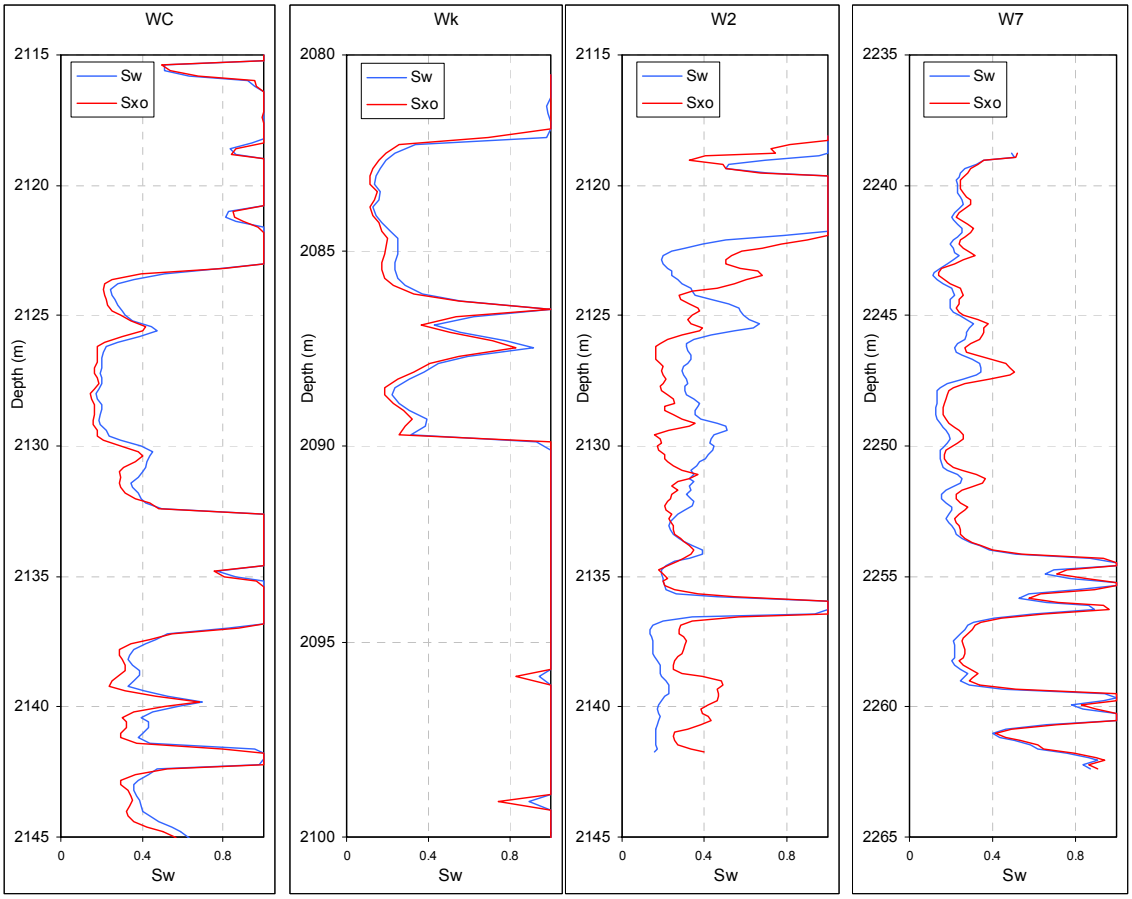

Figure 6.7: From left to right, profiles of water saturation calculated from deep resistivity (S_w) in blue lines and that from shallow resistivity (S_{xo}) in red lines for WC, WK, W2,and W7 wells.

6.6.3 Quality Control of Log S-Wave Velocity

Figure 6.8 shows the plot of P- to S-wave velocity ratio versus P-wave velocity from 100% water saturated laboratory data superimposed on the empirical curves of Williams (1990) water-bearing sands and shales, and the Mudrock line. The figure shows that the laboratory data fall between the sand and the shale lines, so the laboratory data and the empirical curves are in good accordance.

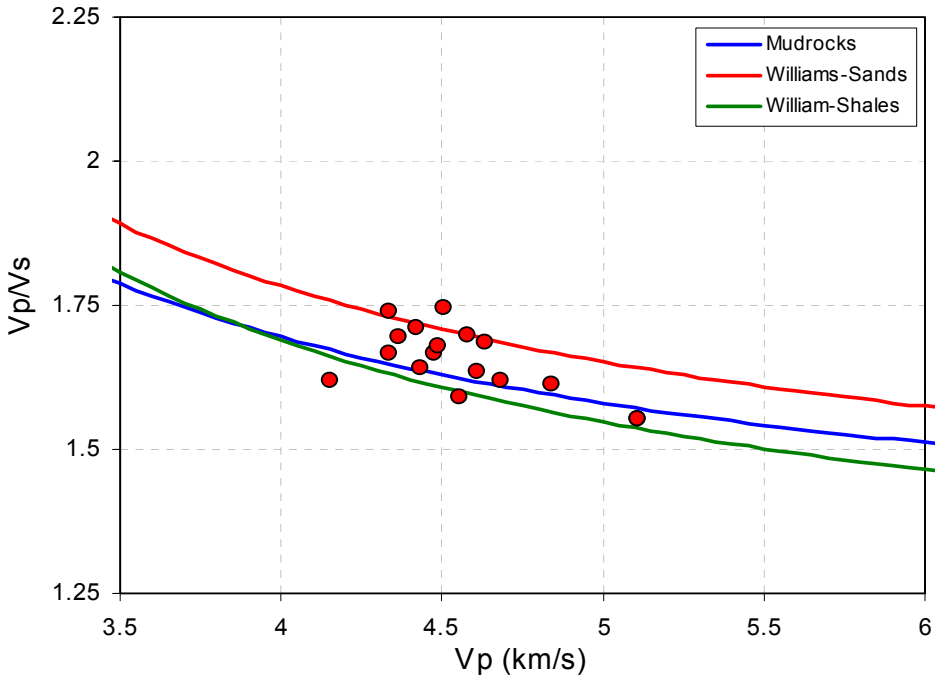

Figure 6.8: Plot of P- to S-wave velocity ratio versus P-wave velocity from laboratory data superimposed on the empirical curves of Williams (1990) for water-bearing sands and shales, and Mudrock.

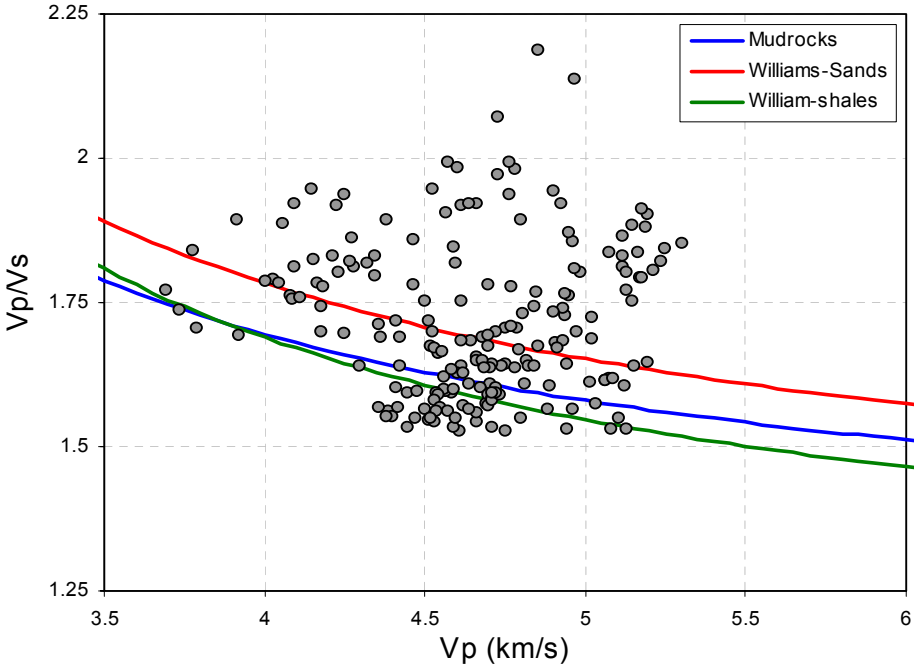

Figure 6.9: Plot of P- to S-wave velocity ratio versus P-wave velocity from log data on top of the empirical curves of William (1990) water bearing sands and shales, and Mudrock.

Figure 6.9 shows the plot of P- to S-wave velocity ratio versus P-wave velocity from log data superimposed on the empirical curves of Williams (1990) for water-bearing sands and shales, and Mudrock. It shows that most of the log data fall above these empirical curves, meaning that at a given P-wave velocity, the log S-wave velocity is lower than predicted by the empirical curves. Figure 5.8 shows that there is discrepancy between core and log S-wave velocity. The laboratory data agree with the well established empirical curves. We believe in laboratory data, therefore the log S-wave velocity data need to be corrected.

Greenberg and Castagna (1992) introduced a relation for estimating S-wave velocity from P-wave velocity in multimineralic, brine-saturated rocks based on empirical, polynomial Vp-Vs relations in pure monomineralic lithologies (Castagna et al 1993).

$$Vs = \frac{1}{2}\left\{\left[\sum_{i=1}^{L} X_i \sum_{j=0}^{N_i} a_{ij} V_P^j\right] + \left[\sum_{i=1}^{L} X_i \left(\sum_{j=0}^{N_i} a_{ij} V_P^j\right)^{-1}\right]^{-1}\right\} \tag{6.18}$$

where L is number of pure monomineralic lithologic constituents,

X_i is volume fraction of the i^{th} lithological constituent,

A_{ij} is an empirical regression coefficient,

N_i is order of polynomial for constituent i, and

V_p, V_s is P- and S- wave velocities (km/s) in composite brine-saturated, multi-mineralic rocks.

Figure 6.10 shows the plot of the predicted S-wave velocity from the 100% water saturated laboratory P-wave velocity using the Greenberg and Castagna (1992) Vp-Vs relations. It shows that the predicted S-wave velocities match the S-wave velocities from laboratory data. Thus, the Greenberg and Castagna Vp-Vs relation can be used to adjust the log S-wave velocity.

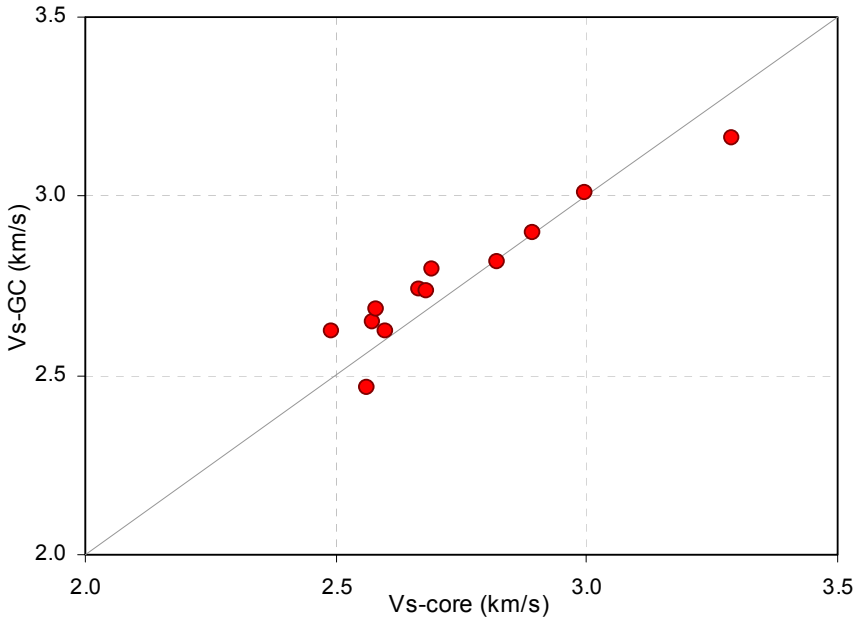

Figure 6.10: Plot of the predicted S-wave velocity using the Greenberg and Castagna (1992) equation versus S-wave velocity measured from laboratory.

6.6.4 Fluid Substitution of Log Data

Since the Greenberg and Castagna equation predicts S-wave velocity from the 100% water saturated P-wave velocity, we need to substitute water into the log. First, we calculated the effective fluid P-wave moduli using patchy theory (Eqn. 6.19), and then performed the approximated P-wave moduli fluid substitution (Mavko et al., 1995) on the log data using Eqn. 6.20.

$$M_{fl} = \sum X_i * M_i \tag{6.19}$$

where X_i is the volume fraction of i^{th} fluid constituents, and

M_i is the P-wave modulus of i^{th} fluid constituents.

$$\frac{M_{sat}}{M_o - M_{sat}} \approx \frac{M_{dry}}{M_o - M_{dry}} + \frac{M_{fl}}{\phi\left(M_o - M_{fl}\right)} \tag{6.20}$$

where M_{sat}, M_{dry}, M_o, and M_{fl} are the P-wave moduli of saturated rock, dry rock, mineral, and pore fluid respectively.

The 100% water saturated bulk density can be calculated from the original density using the following equation:

$$\rho_{100\%Sw} = \rho_S(1-\phi) + \phi\rho_W \tag{6.21}$$

where $\rho_{100\%Sw}$, ρ_s, and ρ_w are the densities of 100% water saturated rock, solid, and water respectively.

The 100% water saturated P-wave velocity can be calculated from 100% water saturated compressional moduli and density computed from Eqn. 6.20 and Eqn. 6.21 using the following equation:

$$Vp_{100\%Sw} = \frac{Msat_{100\%Sw}}{\rho_{100\%Sw}} \tag{6.22}$$

where $Vp_{100\%Sw}$, $Msat_{100\%Sw}$, $\rho_{100\%Sw}$, are the 100% water saturated P-wave velocity, P-wave modulus, and bulk density respectively.

The 100% water saturated P-wave velocity computed from Eqn. 6.22 is then used in Eqn. 6.18 to compute the new 100% water saturated S-wave velocity. We used the constant shear modulus principles to transform the new 100% water saturated S-wave velocity values back to any desired corresponding fluid saturation values. To do this, we calculate the new 100% water saturated shear modulus using Eqn. 6.23, and then divided this new shear modulus by the bulk density of the desired fluid saturation using Eqn. 6.24.

$$G_{100\%Sw} = Vs^2_{100\%Sw} * \rho_{100\%Sw} \tag{6.23}$$

where $G_{100\%Sw}$ is the new shear modulus, and $Vs_{100\%Sw}$ is the new shear velocity computed from Greenberg and Castagna.

$$Vs_{80\%g,20\%Sw} = \frac{G_{100\%Sw}}{\rho_{80\%g,20\%Sw}} \tag{6.24}$$

where $Vs_{80\%g20\%W}$ and $\rho_{80\%g20\%W}$ are the S-wave velocity and bulk density of the 80% gas and 20% water saturated rocks.

6.7 APPLICATION OF THE EFFECTIVE MEDIUM MODEL TO WELL LOG DATA

6.7.1 HMwMUHS

Figures 6.11 to 6.14 show the plots of log data at in situ condition from wells WC, WK, W2, W7, and W16 superimposed on the theoretical curves predicted by the Eqn. 6.14 and 6.15. These theoretical curves are from the HMwMUHS model for 80% gas and 20% water saturation. They are plotted for constant porosity at 5% increments, and for constant clay content at 10% increments. The high-porosity end member used was the critical porosity for sandstone, ϕ_{cr}=40%. The mineral and fluid properties used are from Table 6.1.

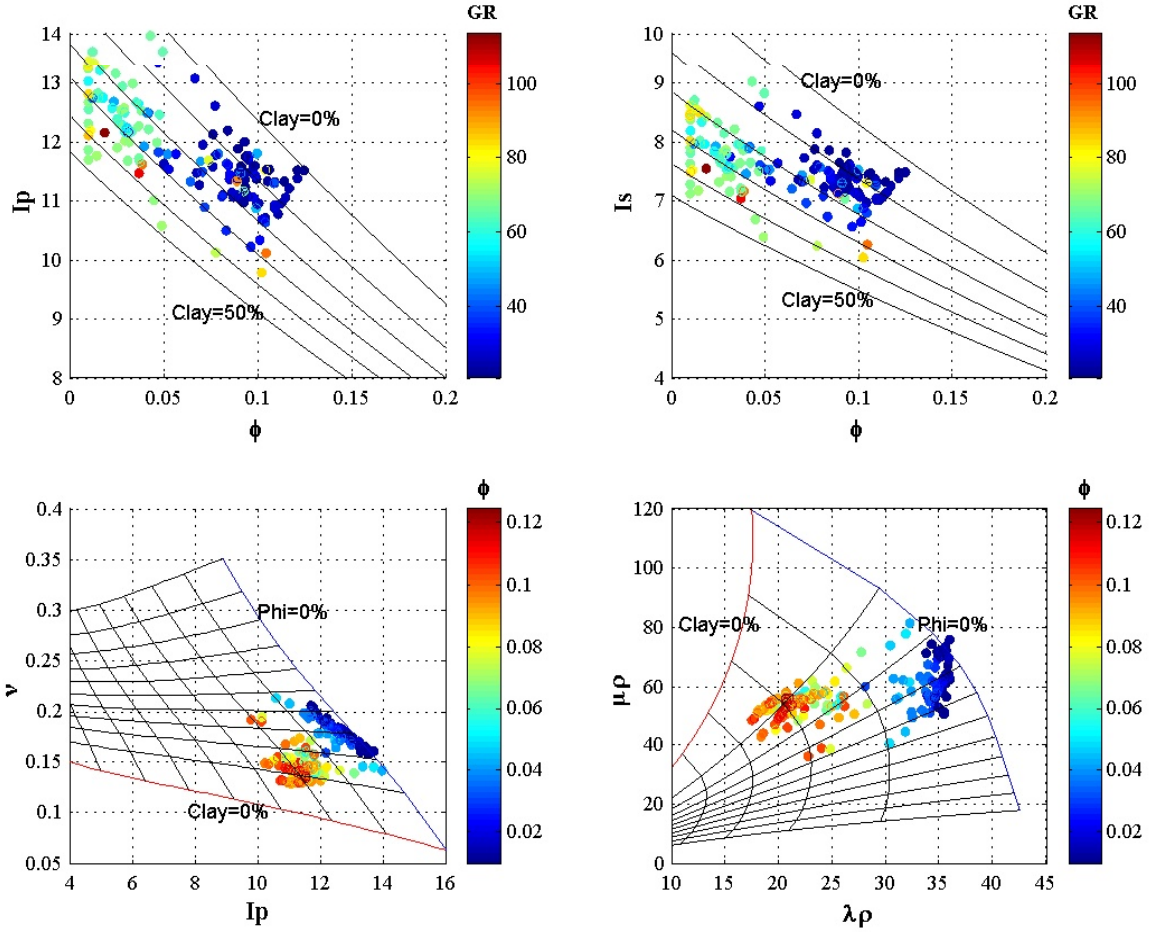

Figure 6.11: From left to right on top and left to right on bottom: plots of I_p versus ϕ; I_s versus ϕ; ν versus I_p, $\mu\rho$ versus $\lambda\rho$ of the log data from WC at in-situ conditions

color coded by gamma ray or porosity. The lines are the HMwMUHS theoretical curves for 10% clay increments and 5% porosity increments.

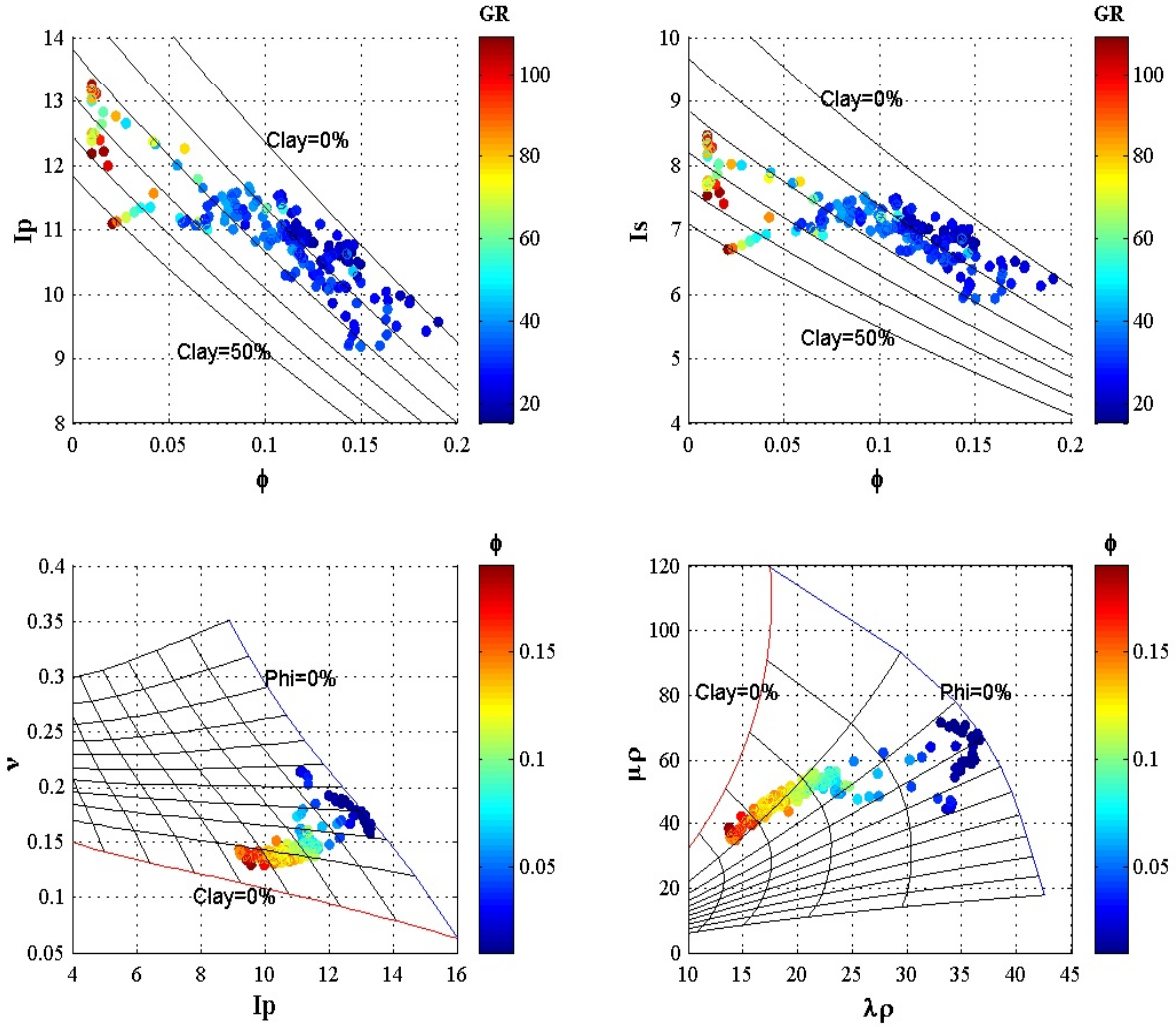

Figure 6.12: From left to right on top and left to right on bottom: plots of I_p versus ϕ; I_s versus ϕ; ν versus I_p, $\mu\rho$ versus $\lambda\rho$ of the log data from W2 at in-situ conditions color coded by gamma ray or porosity. The lines are the HMwMUHS theoretical curves for 10% clay increments and 5% porosity increments.

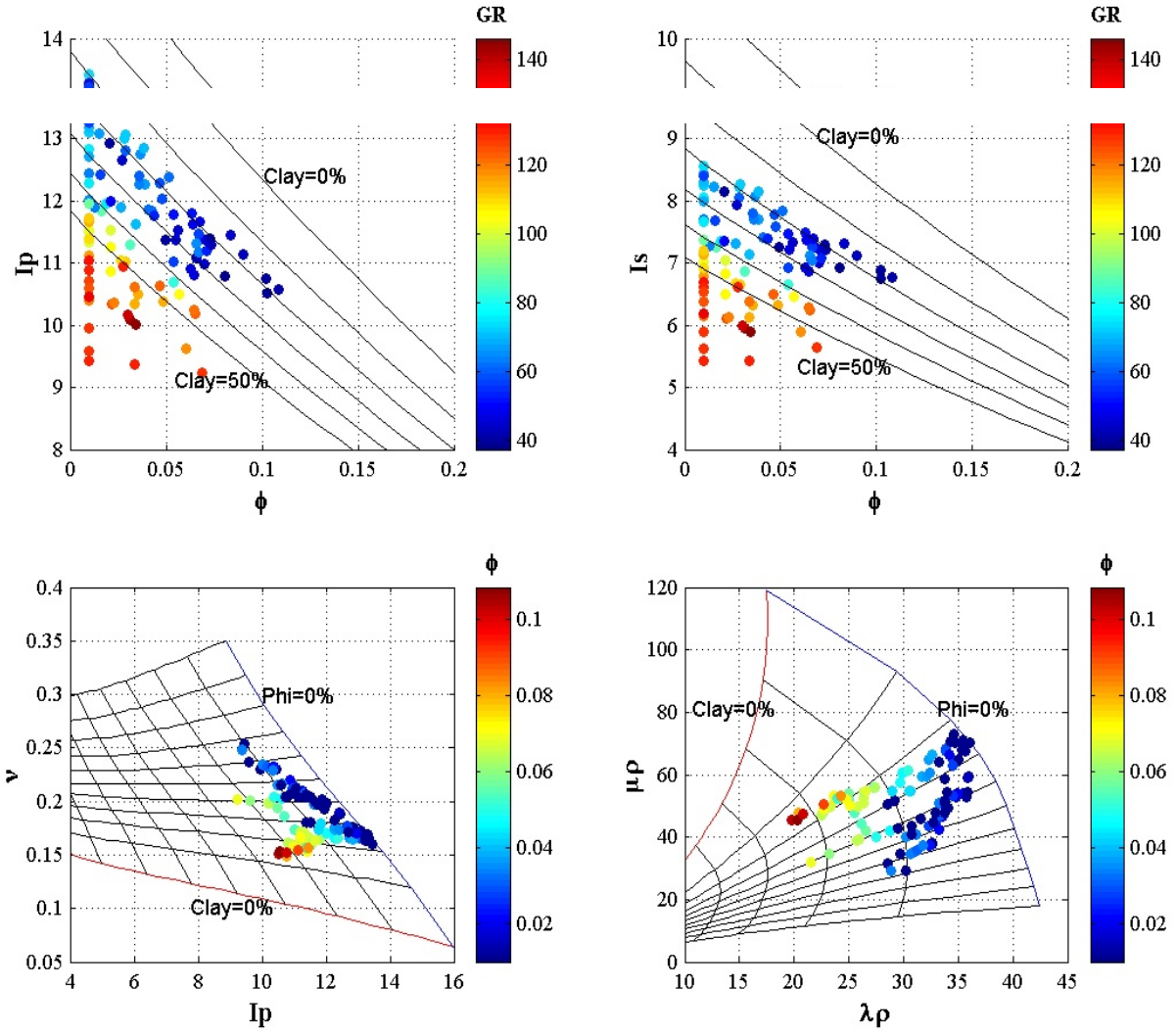

Figure 6.13: From left to right on top and left to right on bottom: plots of Ip versus ϕ; Is versus ϕ; ν versus Ip, μρ versus λρ of the log data from W16 at in-situ conditions color coded by gamma ray or porosity. The lines are the HMwMUHS theoretical curves for 10% clay increments and 5% porosity increments.

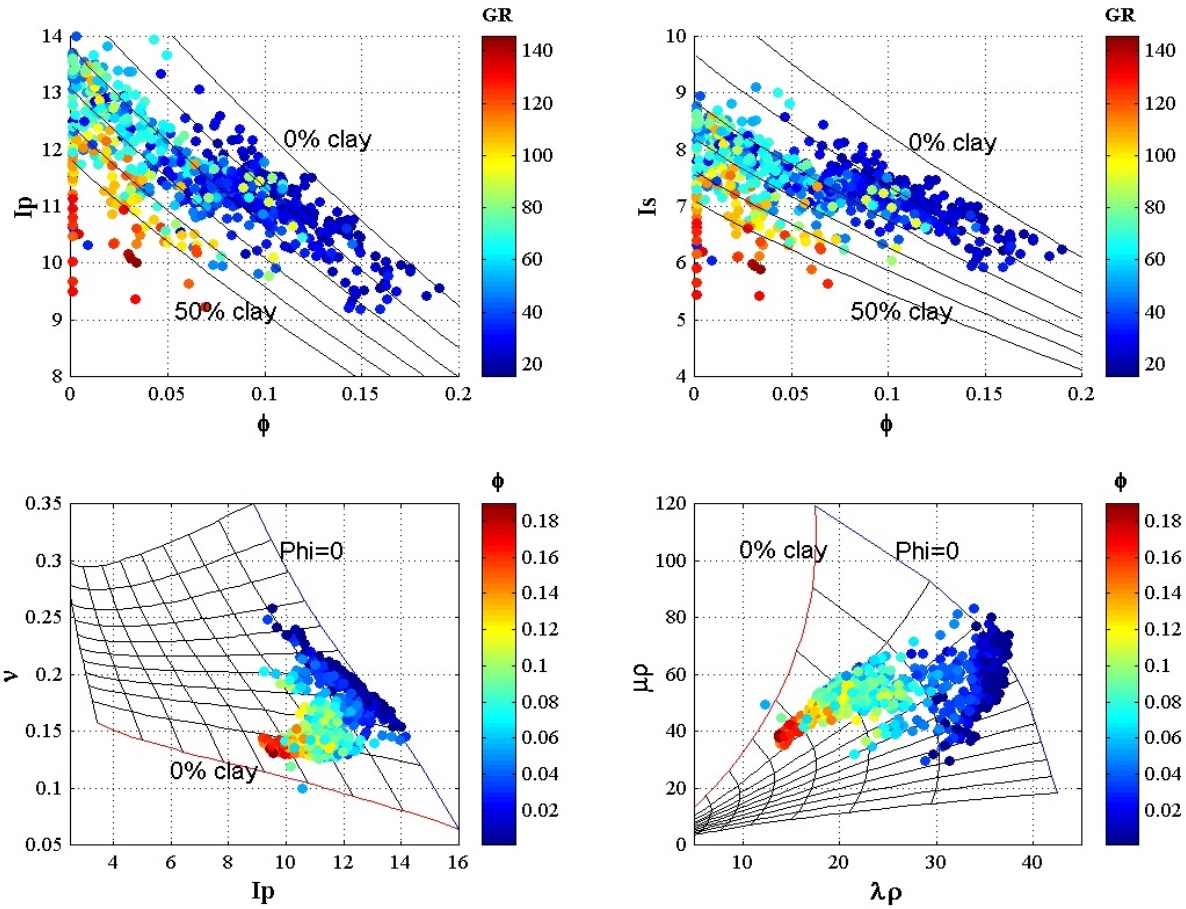

Figure 6.14: From left to right on top and left to right on bottom: plots of I_p versus ϕ; I_s versus ϕ; ν versus I_p, $\mu\rho$ versus $\lambda\rho$ of the log data from WC, WK, W2, W7 and W16 at in-situ conditions color coded by gamma ray or porosity. The lines are the HMwMUHS theoretical curves for 10% clay increments and 5% porosity increments.

Figure 6.11 to 6.14 prove that the Hertz-Mindlin theory with Modified Upper Hashin-Shtrikman bounds scaled to critical porosity can be used to characterize the BQ reservoir.

6.7.2 Combination of Raymer et al (1980) and Greenberg and Castagna (1992), RGC

As an alternative we offer a simpler model that is a combination of Raymer et al (1980) and Greenberg and Castagna (1992) models. These curves are generated by using Raymer et al (1980) to predict P-wave velocity and then using Greenberg and Castagna (1992) to predict S-wave velocity. Because both models (Raymer and G-C) have been originally developed for 100% water saturated rock, we apply RGC to the log data fluid substituted for 100% water saturation. Figure 6.15 shows the plots of 100% water saturated log data from 5 wells (WC, WK, W2, W7 and W16) superimposed on the

theoretical curves generated from RGC. Figure 6.15 shows that the theoretical curves from RGC can be used to describe the elastic properties of the BQ sands.

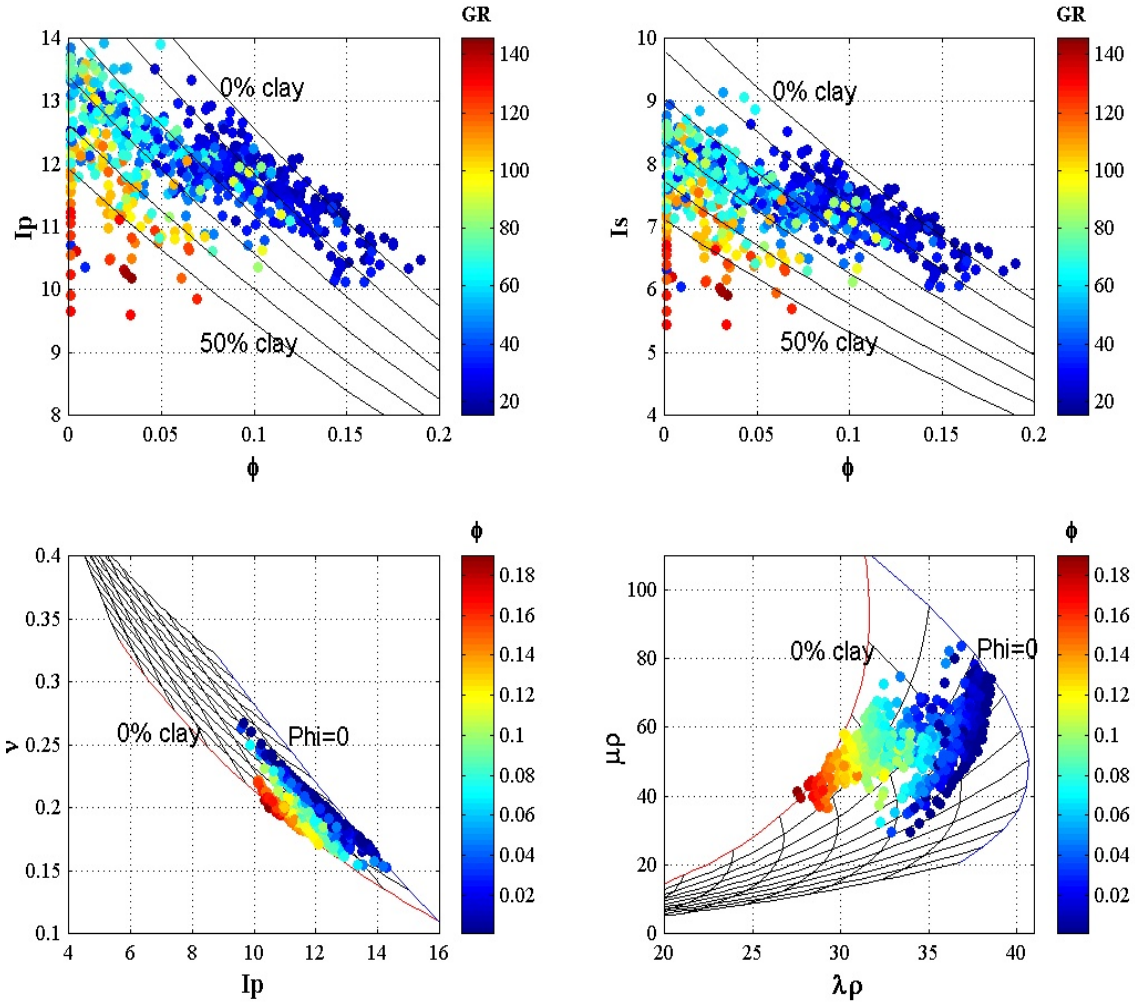

Figure 6.15: From left to right on top and left to right on bottom: plots of I_p versus ϕ; I_s versus ϕ; ν versus I_p, $\mu\rho$ versus $\lambda\rho$ of the log data from WC, WK, W2, W7, AND W16 at 100% water saturation color coded by gamma ray or porosity. The lines are the theoretical curves from Raymer et al (1980) and Greenberg and Castagna (1992).

6.7.3 Comparison of the HMwMUHS Model with RGC Model

Figure 6.16 shows that the HMwMUHS model and RGC model do not predict exactly the same values of porosity and clay content. However, they are qualitatively consistent with each other and the data. Moreover, Figure 6.15 shows that HMwMUHS characterizes the data with better accuracy. This is why, we will use the HMwMUHS for the purpose of the seismic interpretation.

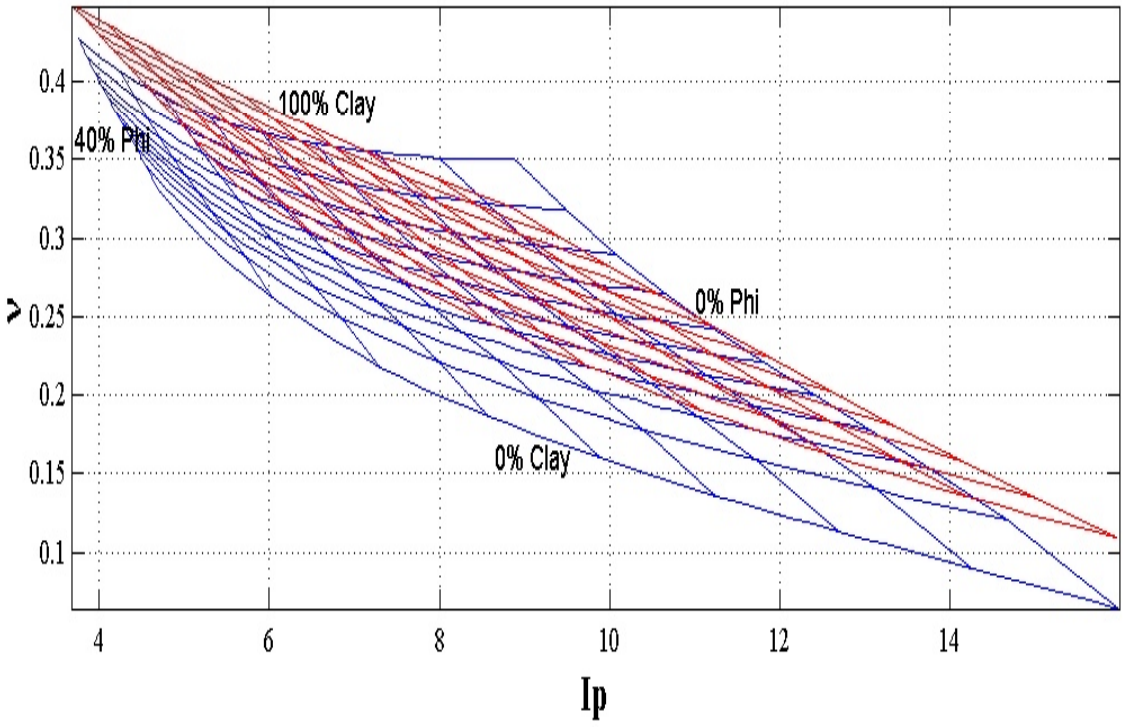

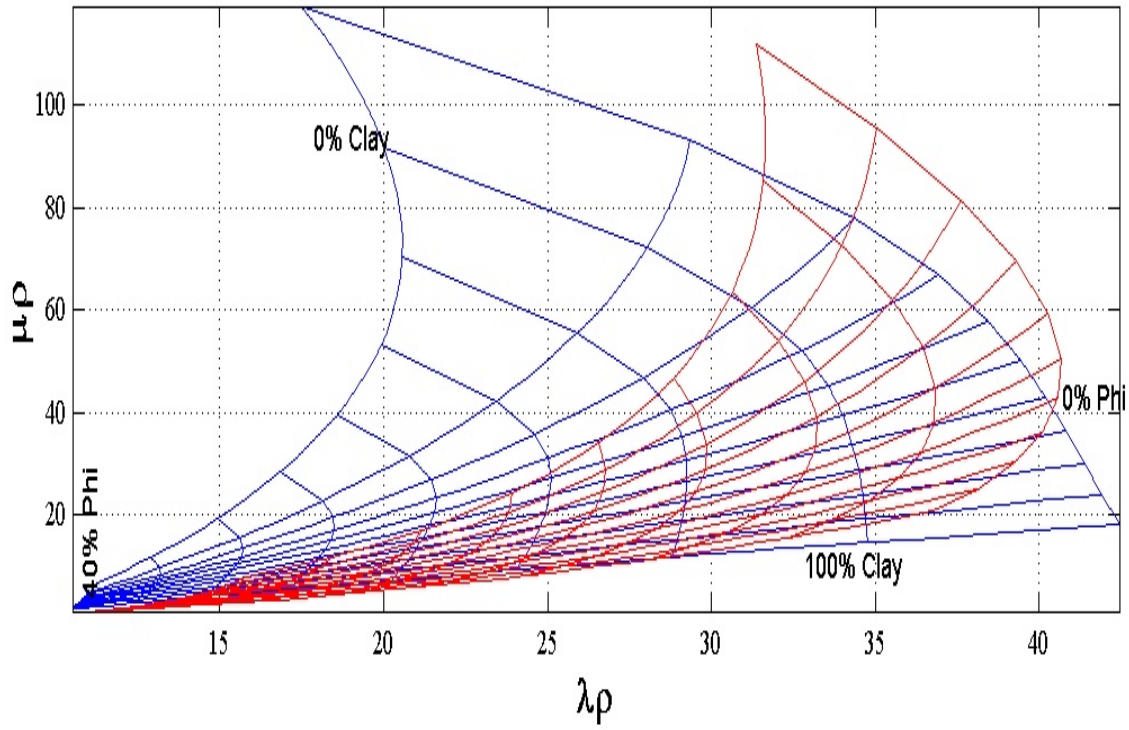

Figure 6.16: Plot of the RGC model in red lines superimposed on top of the HMwMUHS model in blue lines.

6.8 CONCLUSION

- The empirical equations, relating P-wave (S-wave) velocity to porosity and clay content, developed for the laboratory data set characterize the laboratory data with high accuracy (with R^2 of 0.991 and 0.989 respectively).
- BQ reservoir rocks can be characterized with both the Hertz-Mindlin theory with Modified Upper Hashin-Shtrikman bounds model scaled to critical porosity (HMwMUHS) and the combination of Raymer et al (1980) and Greenberg and Castagna (1992) (RGC) models. It is possible to discriminate the ranges of porosity and clay content using these two models, hence possible to delineate the different lithologies.
- The HMwMUHS model and RGC model do not predict exactly the same values of porosity and clay content. However, they are qualitatively consistent with each other and the data.
- HMwMUHS models the data better that RGC. Hence, for the purpose of the seismic interpretation, we will use the effective-medium HMwMUHS.

6.9 REFERENCES

Castagna, J. P., Batzle, M. L., and Eastwood, R. L., 1985, Relationships Between Compressional-wave and Shear-wave Velocities in Clastic Silicate Rocks, Geophysics, 50, 571-581.

Castagna, J. P., Batzle, M. L., and Kan, T. K., 1993, Rock physics, The Link Between Rock Properties and AVO Response, in Offset-Dependent Reflectivity – Theory and Practice of AVO Analysis, J. P. Castange and M. Backus, eds. Investigations in Geophysics, No. 8, Society of Exploration Geophysicists, Tulsa, Oklahoma, 135-171.

Dvorkin J., and Nur A., 1996, Elasticity of High-Porosity Sandstones: Theory for Two North Sea Data Dets: Geophysics, vol. 61, No. 5 (September-October 1996); P. 1363-1370, 10 FIGS.

Dvorkin J., and Nur A., 1998, Time-Average Equation Revisited, Geophysics, Vol. 63, No. 2 (March-April 1998); P. 460-464, 5 FIGS.

Dvorkin J., and Nur A., Chaika C., 1996, Stress Sensitivity of Sandstones, Geophysics, Vol. 61, No. 2 (March-April 1996); P. 444-455, 22 FIGS.

Gal D., Dvorkin J., Nur A., 1998, A Physical Model for Porosity Reduction in Sandstones, Geophysics, Vol. 63, No. 2 (March-April 1998); P. 454-459, 8 FIGS.

Gal D., Dvorkin J., Nur A., 1999, Elastic-Wave Velocities in Sandstones with Non-Load-Bearing Clay, Geophysical Research Letters, Vol. 26, No. 7, April 1999; P. 939-942.

Han, D. H., 1986, Effects of Porosity and Clay Content on Acoustic Properties of Sandstones and Unconsolidated Sediments, Ph.D. dissertation, Stanford University.

Mavko G., Mukerji T., Dvorkin J., 1998, Rock physics Handbooks, Cambridge University Press.

Mindlin, R. D., 1949, Compliance of Elastic Bodies in Contact, J. Appl. Mech., 16, 259-268.

Nur A., Mavko G., Dvorkin J., Galmudi D., 1998, Critical Porosity: a Key to Relating Physical Properties to Porosity in Rocks, the Leading Edge (March 1998.)

Raymer, L. L., Hunt, E. R., and Gardner, J. S., 1980, An Improved Sonic Transit Time-to-Porosity Transform, Trans. Soc. Prof. Well Log Analysts, 21st Annual Logging Symposium, Paper P.

Tosaya, C., and Nur, A., 1982, Effects of Diagenesis and Clays on Compressional Velocities in rocks, Geophysics, Res., Lett., 9, 5-8.

William, D. M. 1990. The Acoustic log hydrocarbon indicator. Soc. Prof. Well Log Analysts, 31st Ann. Logging Symp., Paper W.

Wyllie, M. R. J., Gregory, A. R., and Gardner, L. W., 1956, Elastic Wave Velocities in Heterogeneous and porous media, Geophysics, 21, 41-70.

Wyllie, M. R. J., Gregory, A. R., and Gardner, G. H. F., 1958, An Experimental Investigation of Factors Affecting Elastic Wave Velocities in Porous Media, Geophysics, 23, 459-493.

Wyllie, M. R. J., Gardner, G. H. F, and. Gregory, A. R., 1963, Studies of Elastic Wave Attenuation in Porous Media, Geophysics, 27, 569-589.

CHAPTER 7

UPSCALING OF ROCK PHYSICS TRANSFORMS

7.1 INTRODUCTION

Upscaling is the determination of the seismic signatures of an interval from well log measurements. Upscaling of reservoir properties is critical for interpreting parameters measured in the laboratory or the well at a much larger seismic scale. Upscaling is essential in advanced seismic reservoir characterization, and is often required in forward modeling. When upscaling from log to surface seismic, scale effects can introduce travel time errors (Rio et al., 1996). Fine details in the subsurface may not be always detected by seismic. Upscaling allows us to predict the seismic visibility of such details.

The goal of this chapter is to establish whether the rock physics models that we developed from core and log data will hold at the seismic scale. Our upscaling approach uses moving Backus averaging for the elastic moduli and running mean averaging for porosity and density.

7.2 PREPARATION OF DATA

We demonstrated, in Chapter 6, that the S-wave velocity from log is unreliable. Therefore, prior to upscaling, we need to predict the S-wave velocity using the Greenberg and Castagna (1992) method. To achieve this, we used fluid substitution to calculate the log P-wave velocity for 100% water saturation. Then, we calculated the water saturated S-wave velocity from this water saturated P-wave velocity using the Greenberg and Castagna (1992) formula. Finally, we converted the P- and S-wave velocities back to the in-situ condition.

7.3 UPSCALING

To investigate the effects of upscaling on the rock property estimates and the rock physics models, we applied the Backus averaging method with different sizes of

windows. By doing this, we replaced a heterogeneous elastic medium with a smoother, less heterogeneous medium.

7.3.1 Effective Density and Porosity

We averaged the density and porosity within a given window using the arithmetic averages.

$$\rho_{eff} = \frac{1}{n}\sum_{i=1}^{n}\rho_i \tag{7.1}$$

$$\varphi_{eff} = \frac{1}{n}\sum_{i=1}^{n}\varphi_{eff} \tag{7.2}$$

where ϕ_i , ρ_i are the porosity and density, respectively, at a depth i,

ϕ_{eff} , ρ_{eff} are the effective porosity and bulk density, respectively, within the specified window, and

n is the window size.

7.3.2 Effective Bulk and Shear Moduli

We averaged the bulk and shear moduli within a given window using the geometric Backus average. We achieved this by first taking the inverse of the modulus (Eqn. 7.3 and Eqn. 7.4), then calculating the arithmetic average of these inverses (Eqn. 7.5 and Eqn. 7.6), and finally taking the inverse of the latter to get the effective bulk and shear modulus (Eqn. 7.7 and Eqn. 7.8).

$$\frac{1}{M_i} = \frac{1}{\rho_i V_{Pi}^2} \tag{7.3}$$

$$\frac{1}{G_i} = \frac{1}{\rho_i V_{Si}^2} \tag{7.4}$$

where M_i, G_i are the bulk and shear moduli, respectively, at a depth i, and

V_{Pi} and V_{si} are the P- and S-wave velocity, respectively, at a given depth i.

The inverse moduli calculated from Eqn. 7.3 and Eqn. 7.4 are averaged within a window of length "n" as shown in Eqn. 7.5 and Eqn. 7.6.

$$\left(\frac{1}{M}\right)_{eff} = \frac{1}{n}\sum_{i=1}^{n}\frac{1}{M_i} \tag{7.5}$$

$$\left(\frac{1}{G}\right)_{eff} = \frac{1}{n}\sum_{i=1}^{n}\frac{1}{G_i} \tag{7.6}$$

where M_{eff} and G_{eff} are the inverses of the effective bulk and shear moduli, respectively, within the specified window.

Finally, we computed the inverses of the results from Eqn. 7.5 and Eqn. 7.6 to get the values of effective bulk and shear moduli for a given window as shown in Eqn. 7.7 and Eqn. 7.8.

$$\mathrm{M_{eff}} = \left(\frac{1}{\mathrm{M_{eff}}}\right)^{-1} \tag{7.7}$$

$$\mathrm{G_{eff}} = \left(\frac{1}{\mathrm{G_{eff}}}\right)^{-1} \tag{7.8}$$

7.3.3 Other Upscaled Elastic Rock Properties

Other effective elastic and acoustic properties can be calculated from the upscaled effective density, bulk and shear moduli:

$$I_{Peff} = \sqrt{\rho_{eff} * M_{eff}}$$

$$I_{Seff} = \sqrt{\rho_{eff} * G_{eff}}$$

$$\nu_{eff} = \frac{1}{2}\frac{(M_{eff}/G_{eff} - 2)}{(M_{eff}/G_{eff} - 1)}$$

$$\lambda\rho_{eff} = \rho_{eff}(M_{eff} - 2G_{eff})$$

$$\mu\rho_{eff} = \rho_{eff} * G_{eff}$$

where I_{peff}, I_{seff}, ν_{eff}, $\lambda\rho_{eff}$, $\mu\rho_{eff}$ are the effective P-wave impedance, S-wave impedance, Poisson's ratio, Lambda*Rho, and Mu*Rho, respectively.

7.4 NUMERICAL RESULTS OF UPSCALING

Figures 7.1 to 7.3 show the profiles versus depth of the actual log values (black lines) and the corresponding upscaled values (red lines) from well WC. They illustrate the effects of upscaling on the rock properties. The original log sampling interval in well WC is 0.2 m, fixed throughout the entire depth. We started with n = 6, equivalent to a window of 1.2 m (Fig. 7.1). Figure 7.1 shows that the upscaled values and the actual values are almost the same. The upscaled parameters reflect most of the heterogeneity (fluctuations) and cover the entire range of the actual values. We increased n to 20, equivalent to a 4 m window (Fig. 7.2), and then to n = 50, equivalent to a 10 m window (Fig. 7.3). Both Figures 7.2 and 7.3 show significant reduction of fluctuations. The upscaled parameters trace only the main trend of the actual log parameters, skipping the fine details.

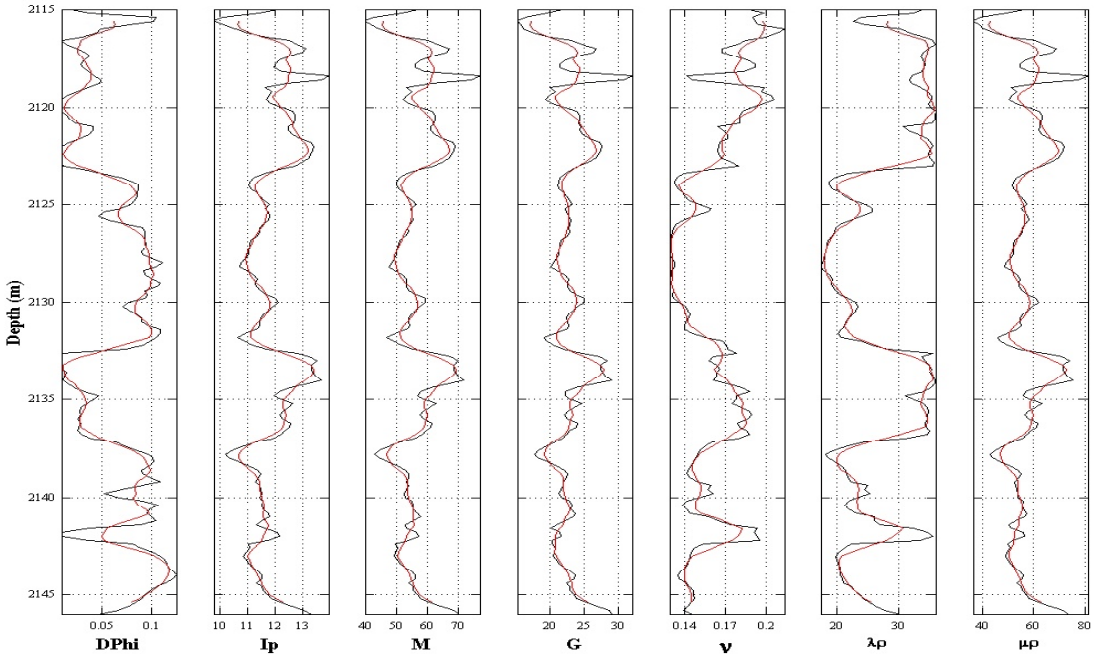

Figure 7-1: Profiles versus depth of the actual log values (black lines) and the corresponding upscaled values (red lines) from well WC. From left to right: density porosity, P-wave impedance, bulk modulus, shear modulus, Poisson's ratio, Lambda times bulk density, and shear modulus times bulk density. n = 6; the window size is 1.2 m.

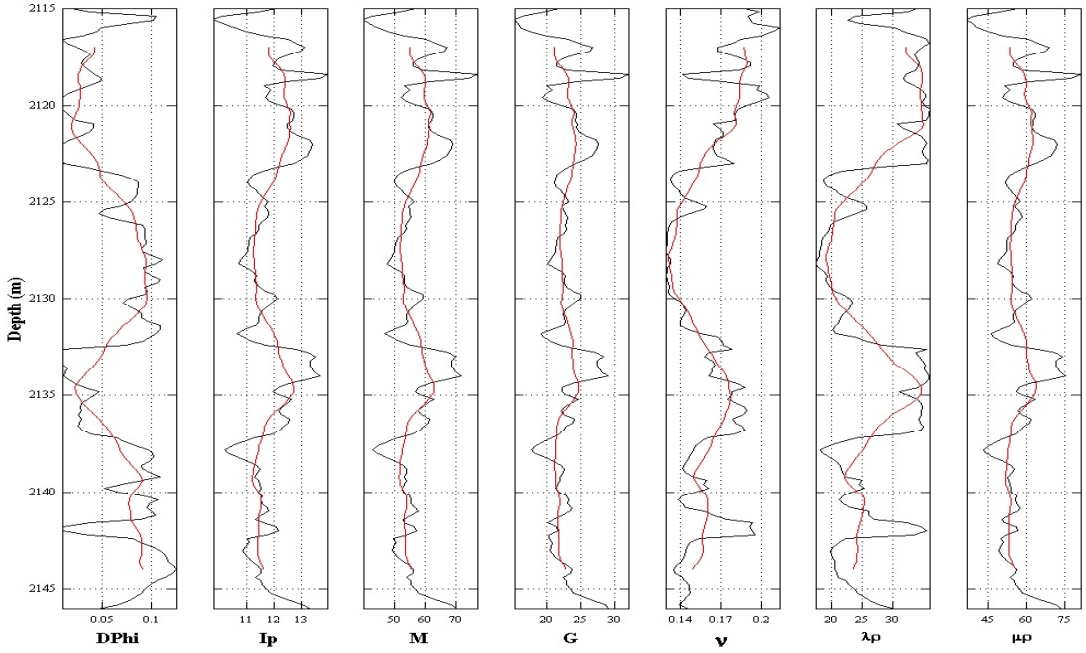

Figure 7.2: Profiles versus depth of the actual log values (black lines) and the corresponding upscaled values (red lines) from well WC. From left to right: density porosity, P-wave impedance, bulk modulus, shear modulus, Poisson's ratio, Lambda times bulk density, and shear modulus times bulk density. n = 20; the window size is 4 m.

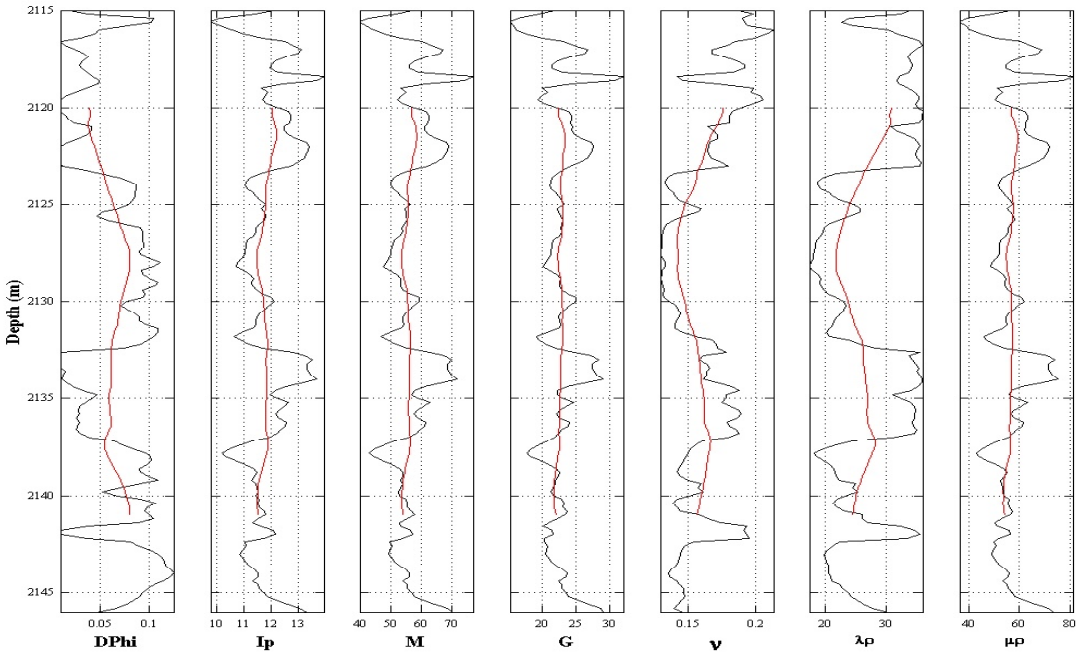

Figure 7.3: Profiles versus depth of the actual log values (black lines) and the corresponding upscaled values (red lines) from well WC. From left to right: density porosity, P-wave impedance, bulk modulus, shear modulus, Poisson's ratio, Lambda times bulk density, and shear modulus times bulk density. n = 50; the window size is 10 m.

7.5 EFFECT OF UPSCALING ON ROCK PHYSICS MODELS

Figures 7.4 to 7.21 show the crossplots of elastic and acoustic properties, from wells WC, WK, W2, W7, and W16 respectively, superimposed on the porosity and clay lines, as given by HMwMUHS. The actual log values are in black symbols, whereas the upscaled values are color coded by gamma ray or porosity. Figures 7.4 to 7.18 illustrate the effects of upscaling on the data and the applicability of rock physics models, using the same window sizes as in figures 7.1 to 7.3. These figures demonstrate that the elastic properties of the upscaled log data could be characterized by HMwMUHS. It is possible to discriminate the ranges of porosity and clay content, in the upscaled data which proves the possibility of delineating the different lithology and porosity from seismic. Therefore, we conclude that HMwMUHS remains valid at the seismic scale.

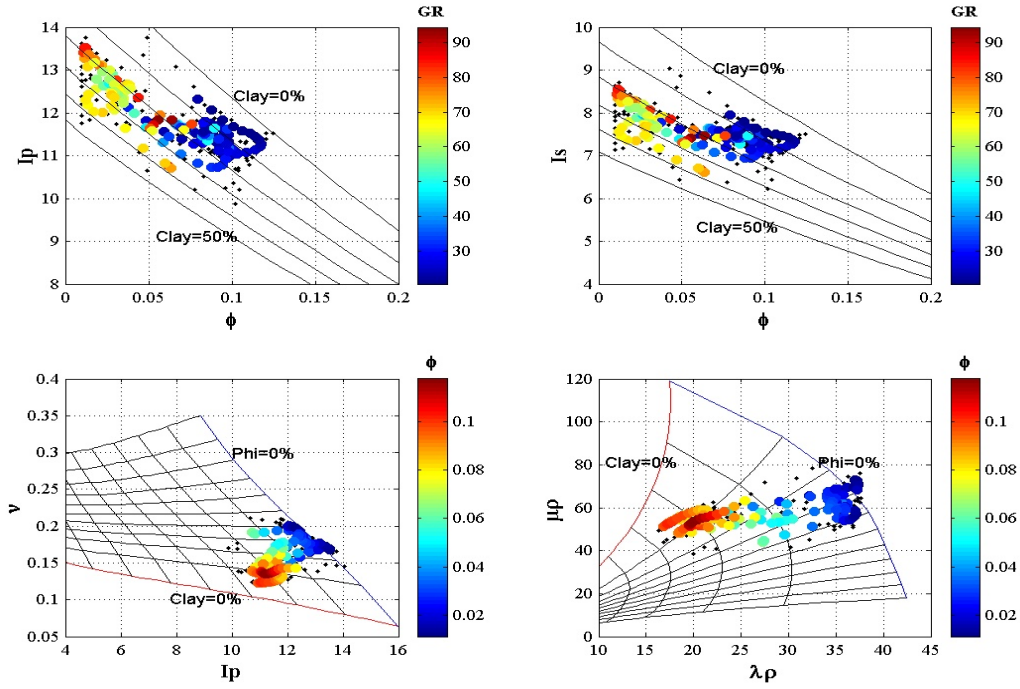

Figure 7.4: Plots of Ip versus ϕ; Is versus ϕ; ν versus Ip, μρ versus λρ from well WC. The lines are the theoretical curves for 10% clay increments and 5% porosity increments. The actual log values at in situ conditions are in black symbols, whereas the upscaled values are color coded by GR or ϕ. n = 6; the window size is 1.2 m.

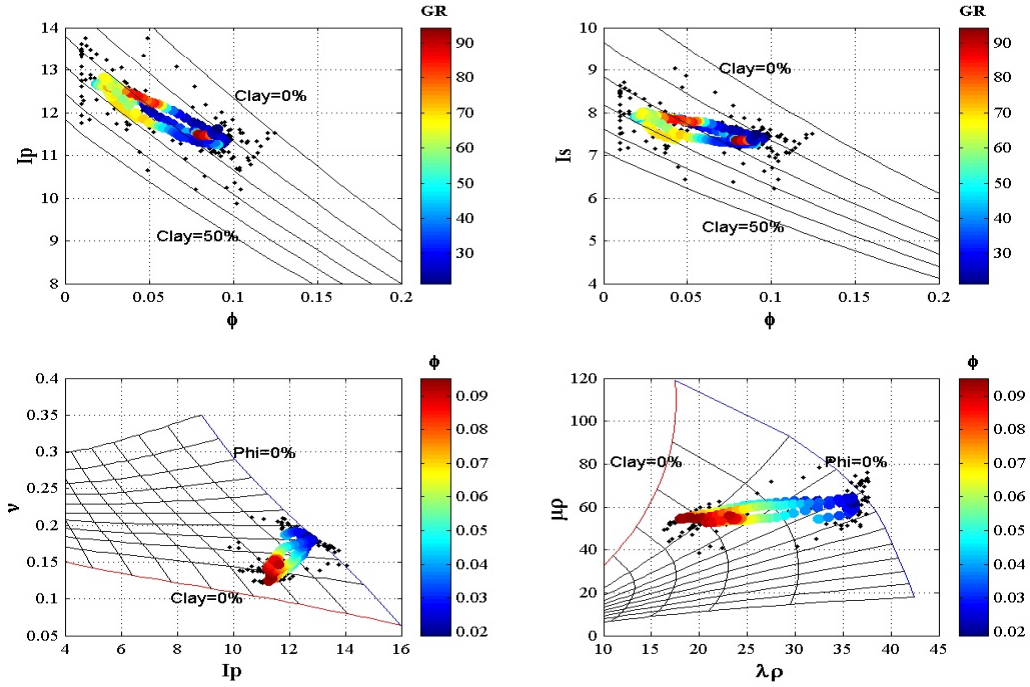

Figure 7.5: Plots of Ip versus ϕ; Is versus ϕ; ν versus Ip, μρ versus λρ from well WC. The lines are the theoretical curves for 10% clay increments and 5% porosity increments. The actual log values at in situ conditions are in black symbols, whereas the upscaled values are color coded by GR or ϕ. n = 20; the window size is 4 m.

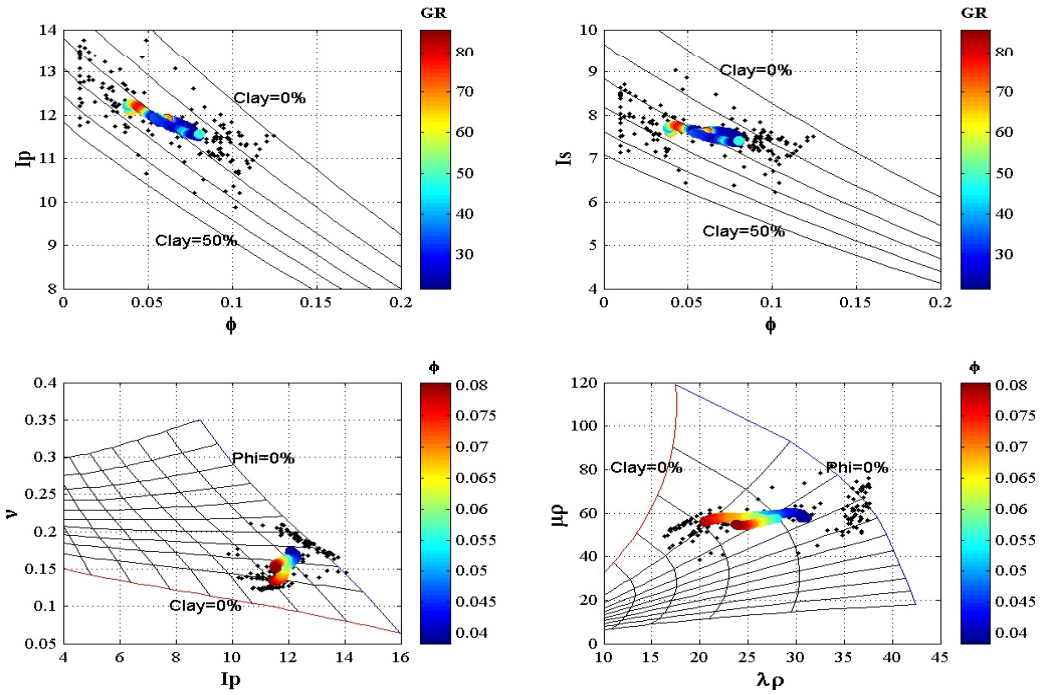

Figure 7.6: Plots of Ip versus ϕ; Is versus ϕ; ν versus Ip, μρ versus λρ from well WC. The lines are the theoretical curves for 10% clay increments and 5% porosity increments. The actual log values at in situ conditions are in black symbols, whereas the upscaled values are color coded by GR or ϕ. n = 50; the window size is 10 m.

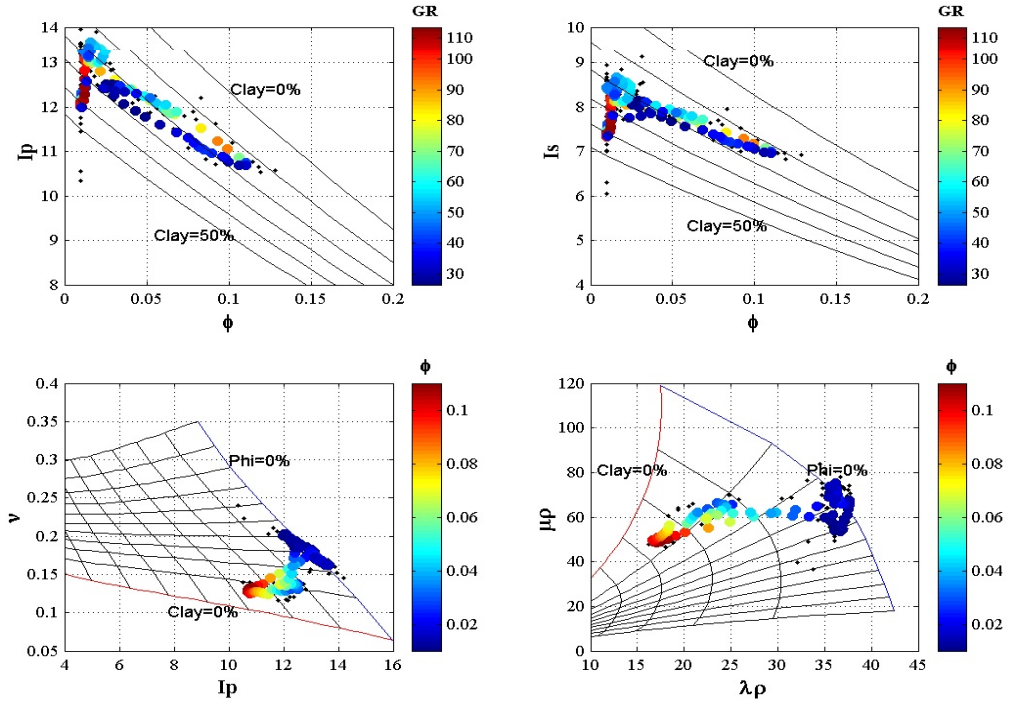

Figure 7.7: Plots of Ip versus ϕ; Is versus ϕ; ν versus Ip, μρ versus λρ from well WK. The lines are the theoretical curves for 10% clay increments and 5% porosity increments. The actual log values at in situ conditions are in black symbols, whereas the upscaled values are color coded by GR or ϕ. n = 6; the window size is 1.2m**.**

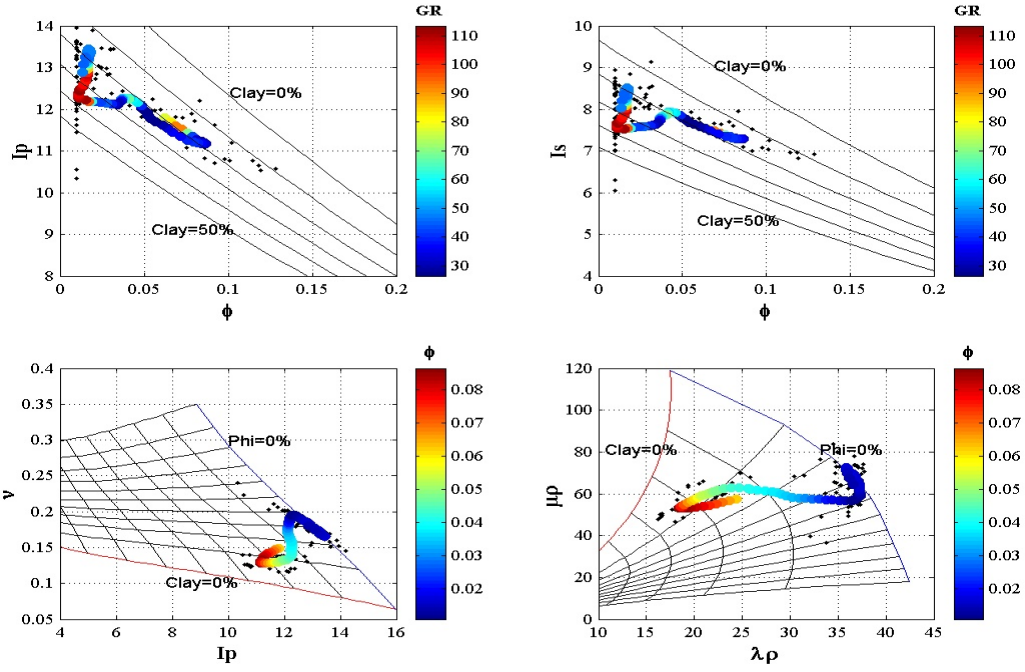

Figure 7.8: Plots of Ip versus ϕ; Is versus ϕ; ν versus Ip, μρ versus λρ from well WK. The lines are the theoretical curves for 10% clay increments and 5% porosity increments. The actual log values at in situ conditions are in black symbols, whereas the upscaled values are color coded by GR or ϕ. n = 20; the window size is 4 m.

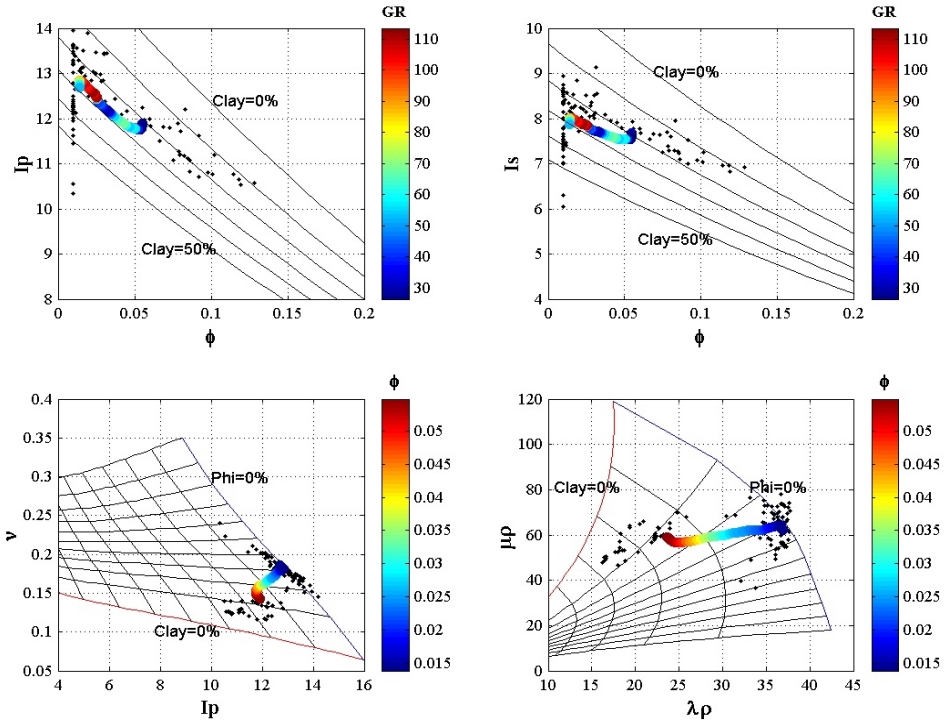

Figure 7.9: Plots of Ip versus ϕ; Is versus ϕ; ν versus Ip, μρ versus λρ from well WK. The lines are the theoretical curves for 10% clay increments and 5% porosity increments. The actual log values at in situ conditions are in black symbols, whereas the upscaled values are color coded by GR or ϕ. n = 50; the window size is 10m.

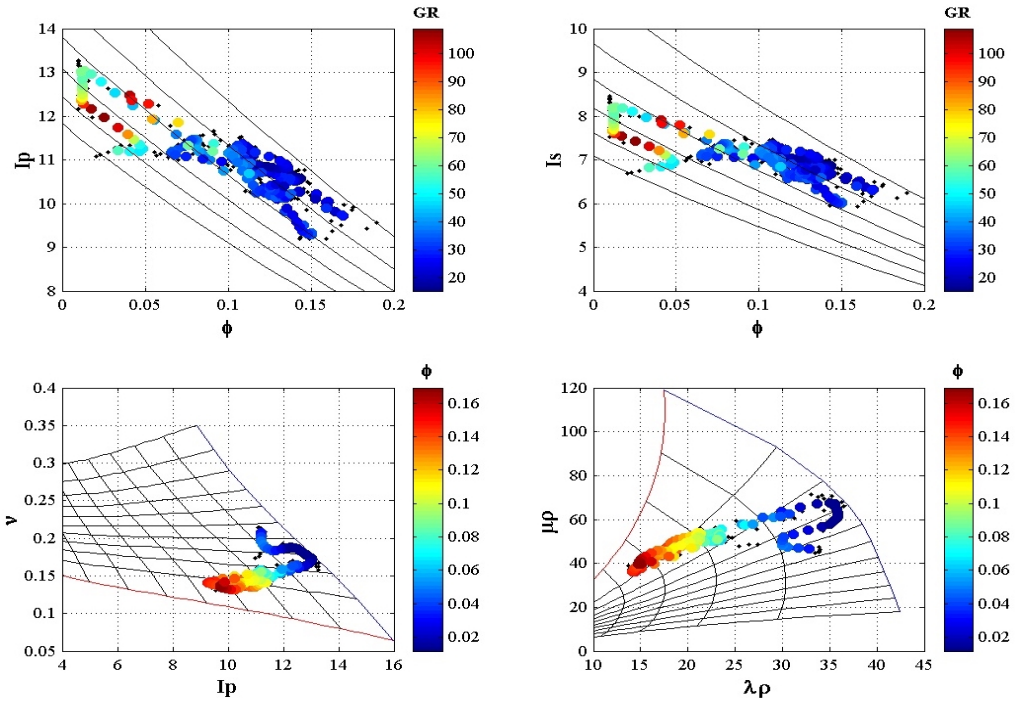

Figure 7.10: Plots of Ip versus ϕ; Is versus ϕ; ν versus Ip, μρ versus λρ from well W2. The lines are the theoretical curves for 10% clay increments and 5% porosity increments. The actual log values at in situ conditions are in black symbols, whereas the upscaled values are color coded by GR or ϕ. n = 6; the window size is 1.2 m.

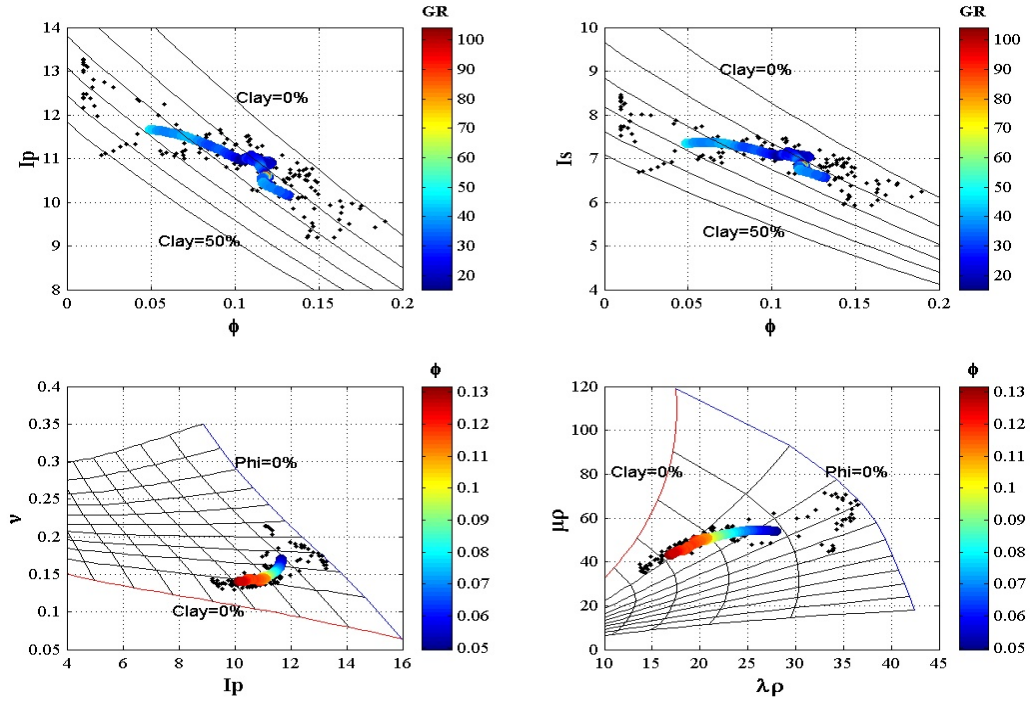

Figure 7.11: Plots of Ip versus ϕ; Is versus ϕ; ν versus Ip, μρ versus λρ from well W2. The lines are the theoretical curves for 10% clay increments and 5% porosity increments. The actual log values at in situ conditions are in black symbols, whereas the upscaled values are color coded by GR or ϕ. n = 20; the window size is 4 m.

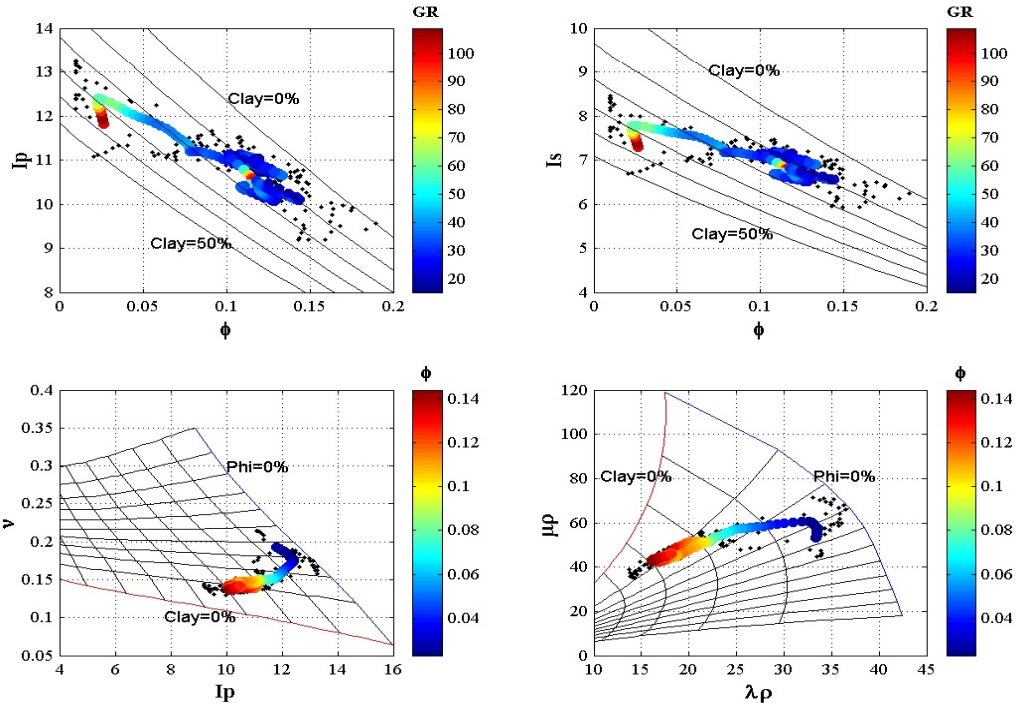

Figure 7.12: PLots of Ip versus ϕ; Is versus ϕ; ν versus Ip, μρ versus λρ from well W2. The lines are the theoretical curves for 10% clay increments and 5% porosity increments. The actual log values at in situ conditions are in black symbols, whereas the upscaled values are color coded by GR or ϕ. n = 50; the window size is 10 m.

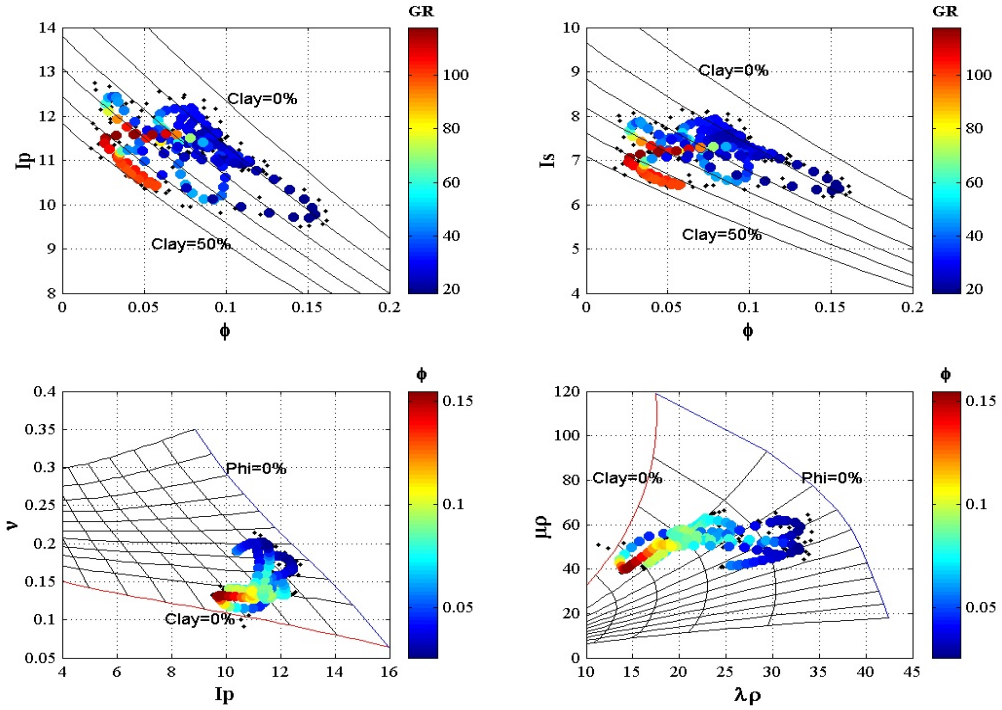

Figure 7.13: Plots of Ip versus ϕ; Is versus ϕ; ν versus Ip, μρ versus λρ from well W7. The lines are the theoretical curves for 10% clay increments and 5% porosity increments. The actual log values at in situ conditions are in black symbols, whereas the upscaled values are color coded by GR or ϕ. n = 6; the window size is 1.2 m.

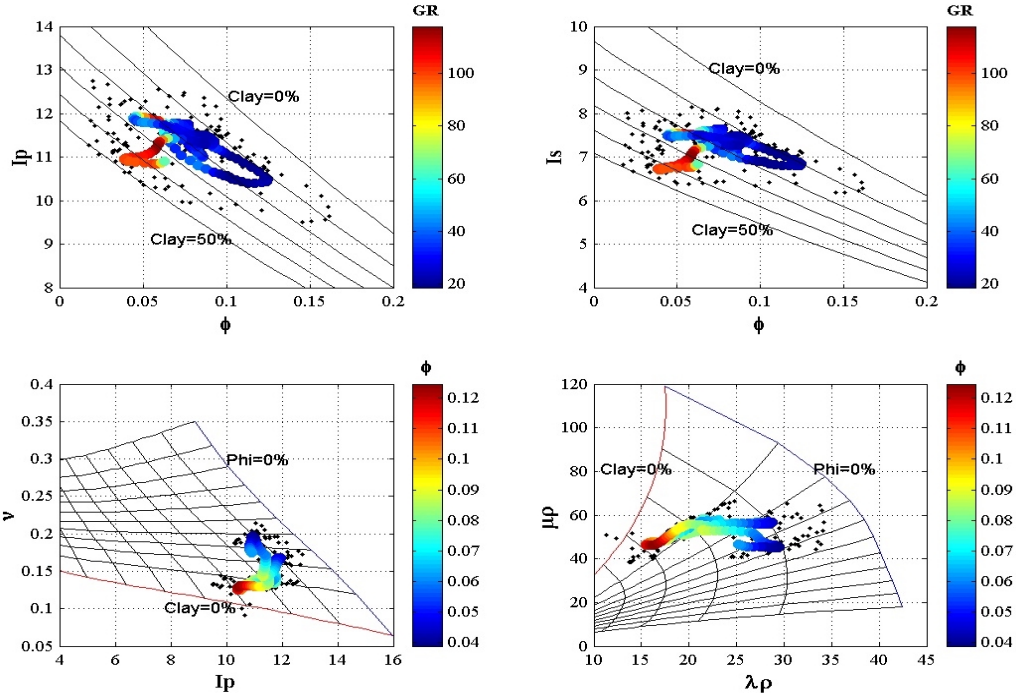

Figure 7.14: Plots of Ip versus ϕ; Is versus ϕ; ν versus Ip, μρ versus λρ from well W7. The lines are the theoretical curves for 10% clay increments and 5% porosity increments. The actual log values at in situ conditions are in black symbols, whereas the upscaled values are color coded by GR or ϕ. n = 20; the window size is 4 m.

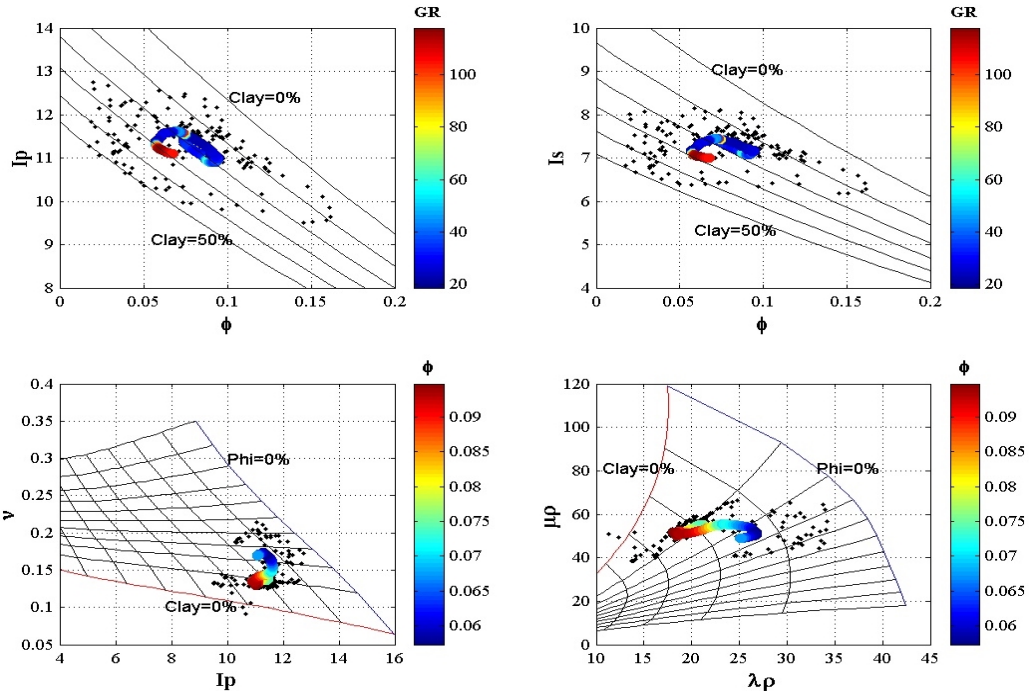

Figure 7.15: Plots of Ip versus ϕ; Is versus ϕ; ν versus Ip, μρ versus λρ from well W7. The lines are the theoretical curves for 10% clay increments and 5% porosity increments. The actual log values at in situ conditions are in black symbols, whereas the upscaled values are color coded by GR or ϕ. n = 50; the window size is 10m.

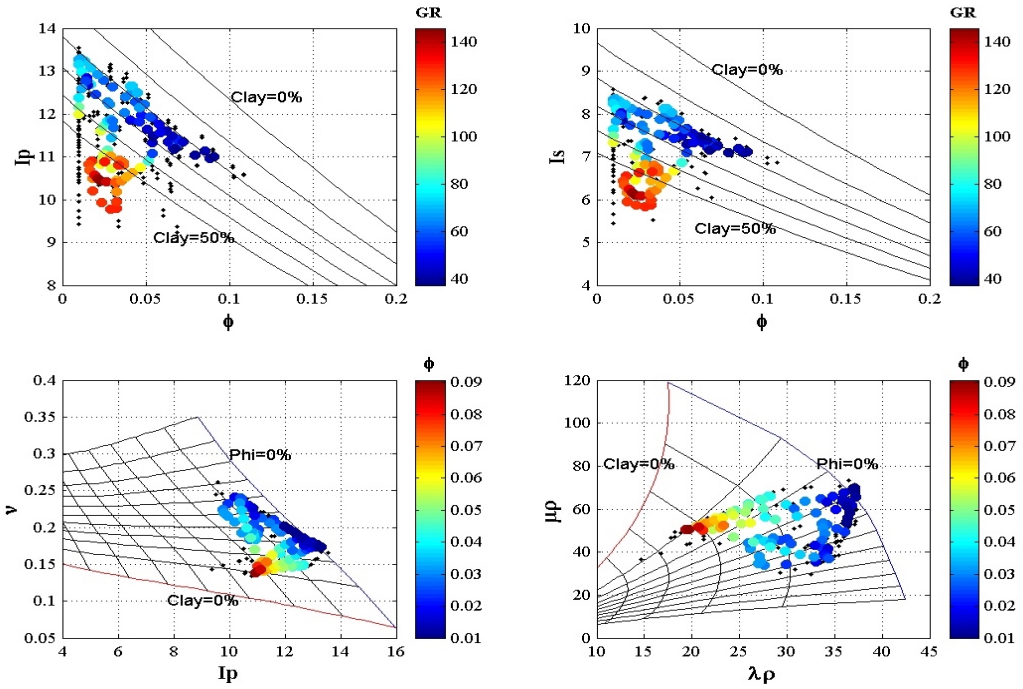

Figure 7.16: Plots of Ip versus ϕ; Is versus ϕ; ν versus Ip, μρ versus λρ from well W16. The lines are the theoretical curves for 10% clay increments and 5% porosity increments. The actual log values at in situ conditions are in black symbols, whereas the upscaled values are color coded by GR or ϕ. n = 6, the window size is 1.2 m.

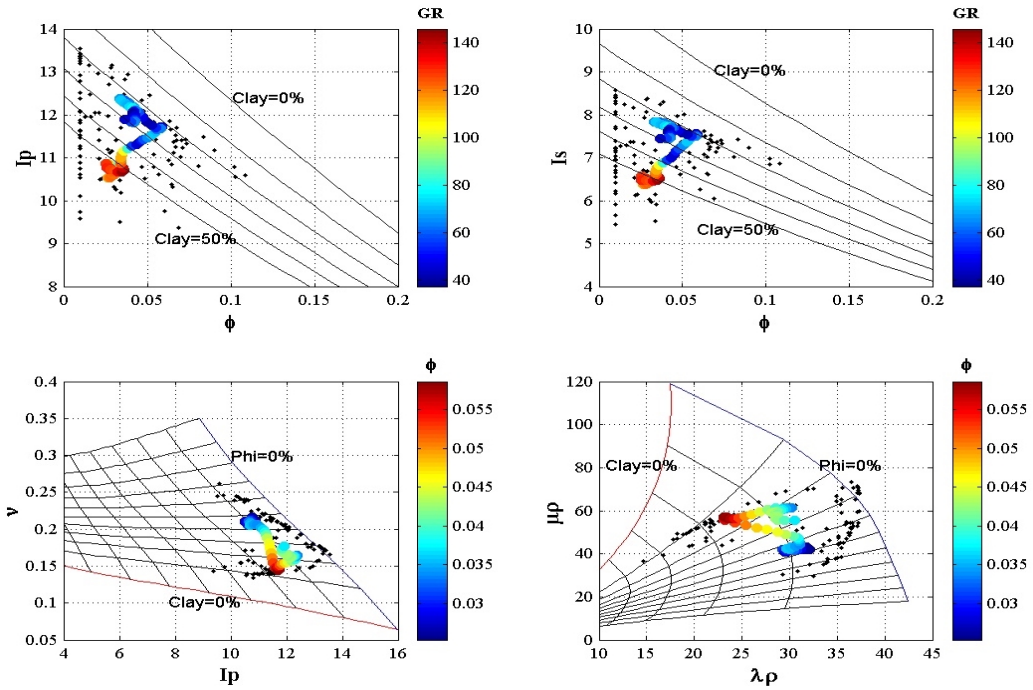

Figure 7.17: Plots of Ip versus ϕ; Is versus ϕ; ν versus Ip, μρ versus λρ from well W16. The lines are the theoretical curves for 10% clay increments and 5% porosity increments. The actual log values at in situ conditions are in black symbols, whereas the upscaled values are color coded by GR or ϕ. n = 20; the window size is 4 m.

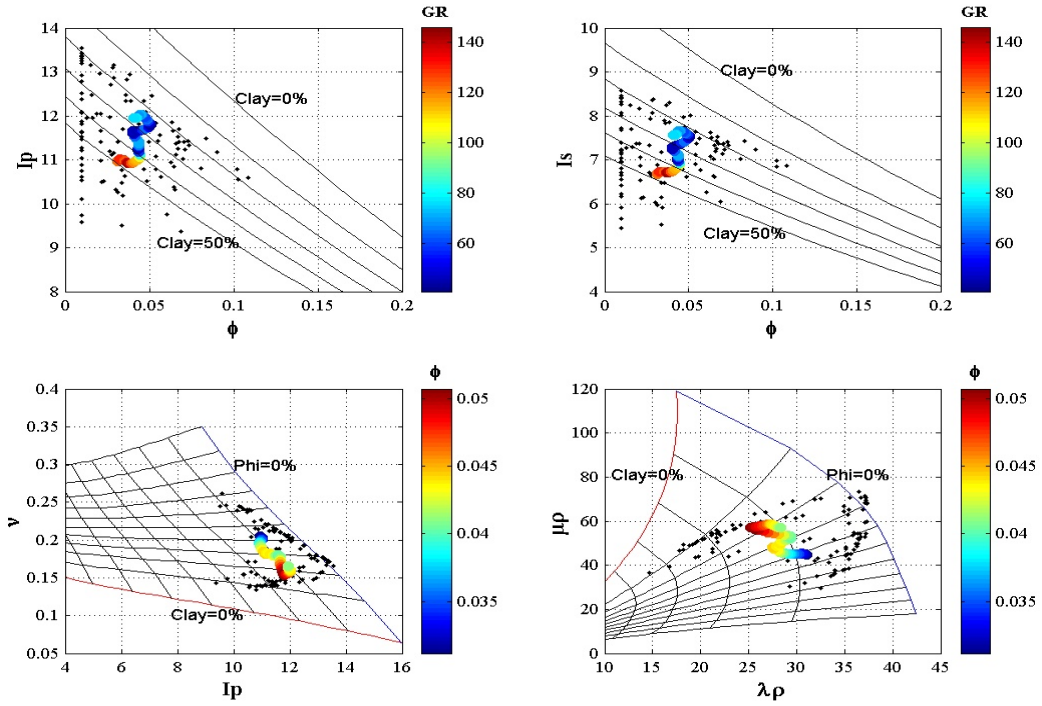

Figure 7.18: Plots of Ip versus ϕ; Is versus ϕ; ν versus Ip, μρ versus λρ from well W16. The lines are the theoretical curves for 10% clay increments and 5% porosity increments. The actual log values at in situ conditions are in black symbols, whereas the upscaled values are color coded by GR or ϕ. n = 50; the window size is 10 m.

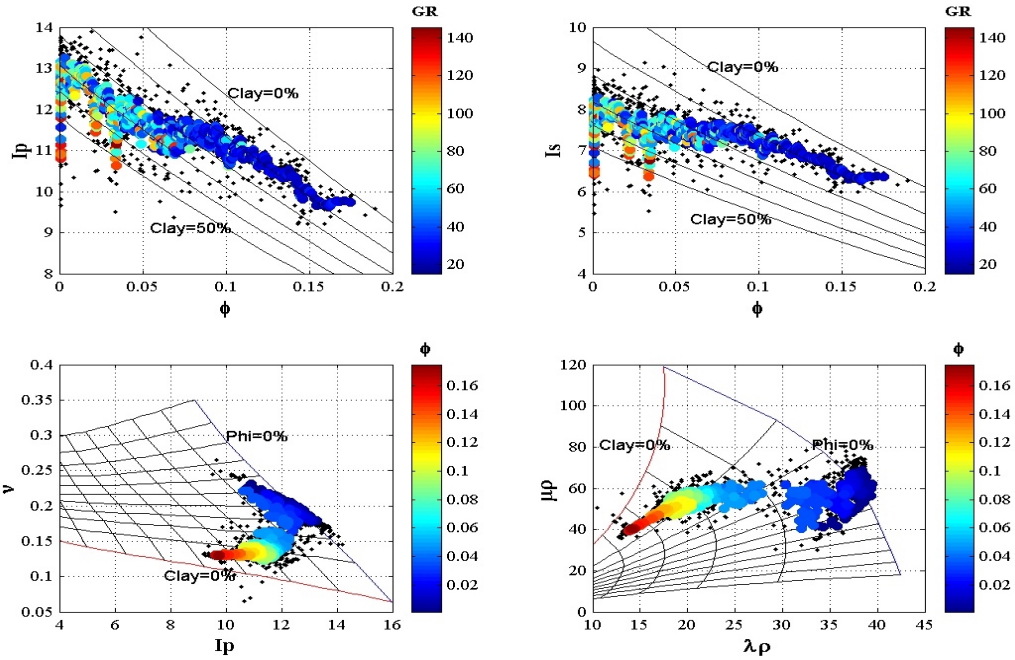

Figure 7.19: Plots of Ip versus ϕ; Is versus ϕ; ν versus Ip, μρ versus λρ from all 5 wells (wc,wk,w2,w7 and w16 combined). The lines are the theoretical curves for 10% clay increments and 5% porosity increments. The actual log values at in situ conditions are in black symbols, whereas the upscaled values are color coded by GR or ϕ. n = 6 the window size is 1.2 m.

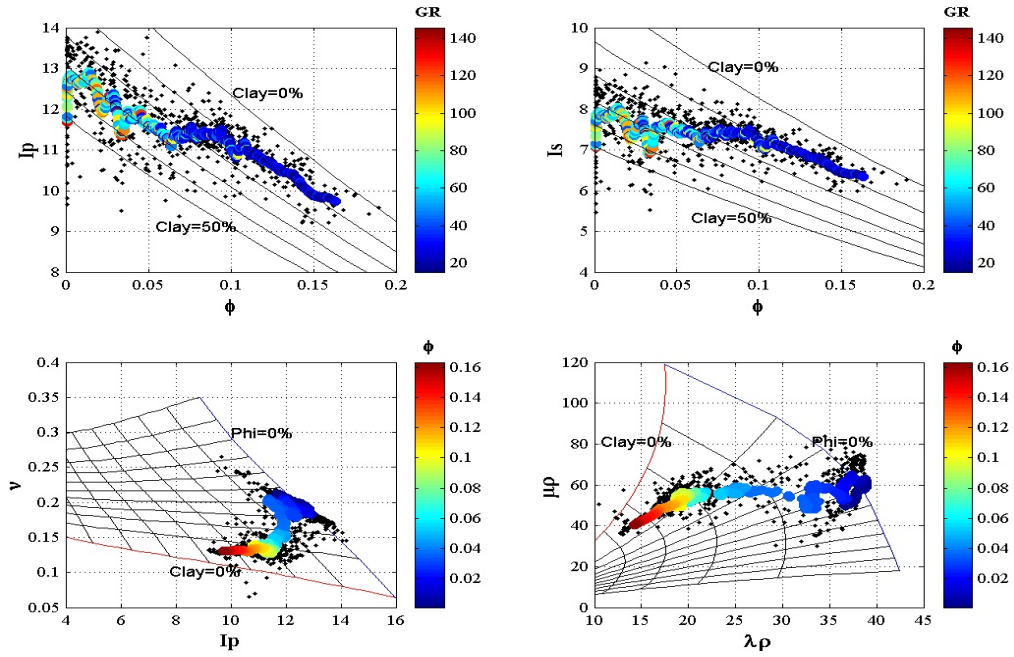

Figure 7.20: Plots of Ip versus ϕ; Is versus ϕ; ν versus Ip, μρ versus λρ from all 5 wells (wc,wk,w2,w7 and w16 combined). The lines are the theoretical curves for 10% clay increments and 5% porosity increments. The actual log values at in situ conditions are in black symbols, whereas the upscaled values are color coded by GR or ϕ. n = 20, the window size is 4 m.

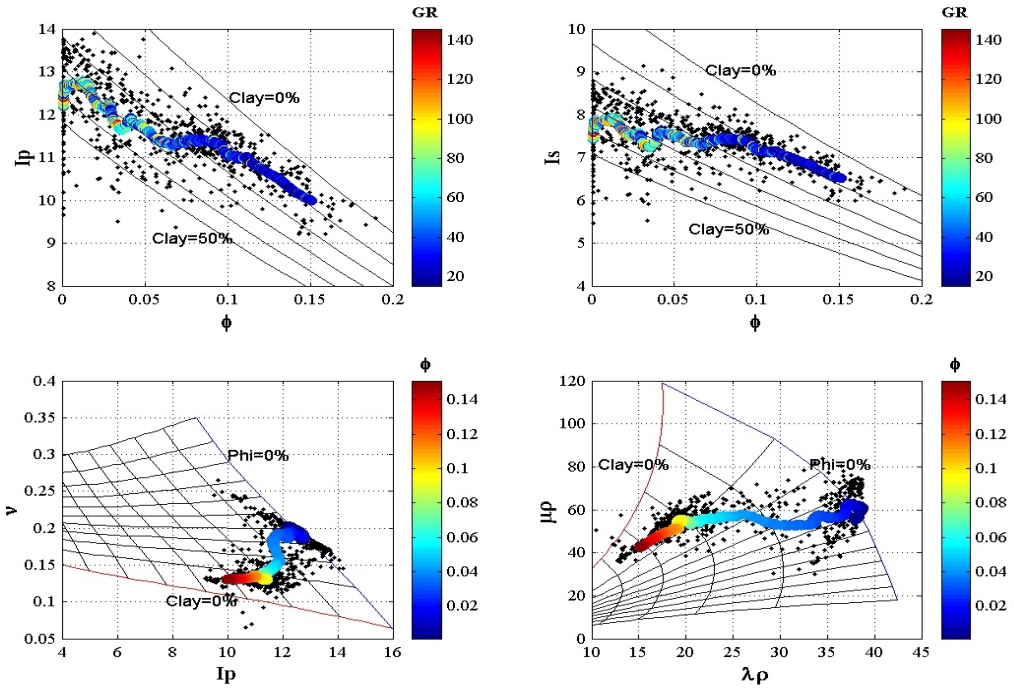

Figure 7.21: Plots of Ip versus ϕ; Is versus ϕ; ν versus Ip, μρ versus λρ from all 5 wells (wc,wk,w2,w7 and w16 combined). The lines are the theoretical curves for 10% clay increments and 5% porosity increments. The actual log values at in situ conditions are in black symbols, whereas the upscaled values are color coded by GR or ϕ. n = 50; the window size is 10 m.

7.6 EFFECT OF UPSCALING ON THE COMBINED RAYMER ET AL (1980) AND GREENBERG AND CASTAGNA (1992) EMPIRICAL MODELS

Figures 7.22 to 7.24 show the crossplots of elastic and acoustic properties from the 5 wells combined, superimposed on the porosity and clay theoretical lines from the combined Raymer et al. (1980) and Greenberg and Castagna (1992) models described in Chapter 6. These Figures demonstrate that the combined Raymer et al. (1980) and Greenberg and Castagna (1992) models will hold at the seismic scale. However, HMwMUHS describes the data with better accuracy and we will use it in seismic interpretation.

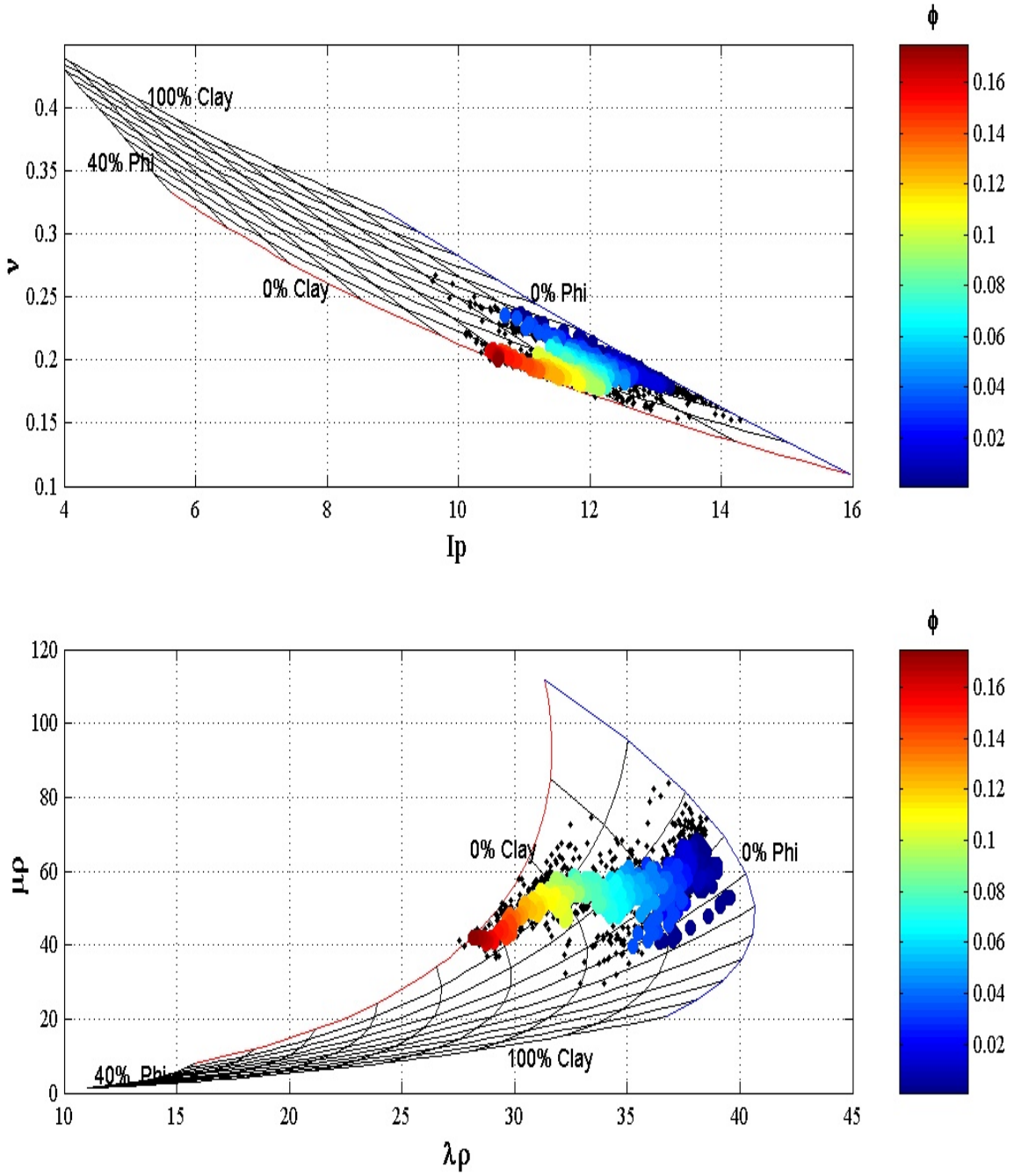

Figure 7.22: From top to bottom: plots of ν versus Ip, and μρ versus λρ. The lines are the theoretical curves for 10% clay increments and 5% porosity increments generated from the combined Raymer et al. (1980) and Greenberg and Castagna (1992) models. The black symbols are the actual log data from 5 wells (wc,wk,w2,w7 and w16 combined) at 100% water saturation, and the upscaled values are color coded by porosity. n = 6; the window size is 1.2 m.

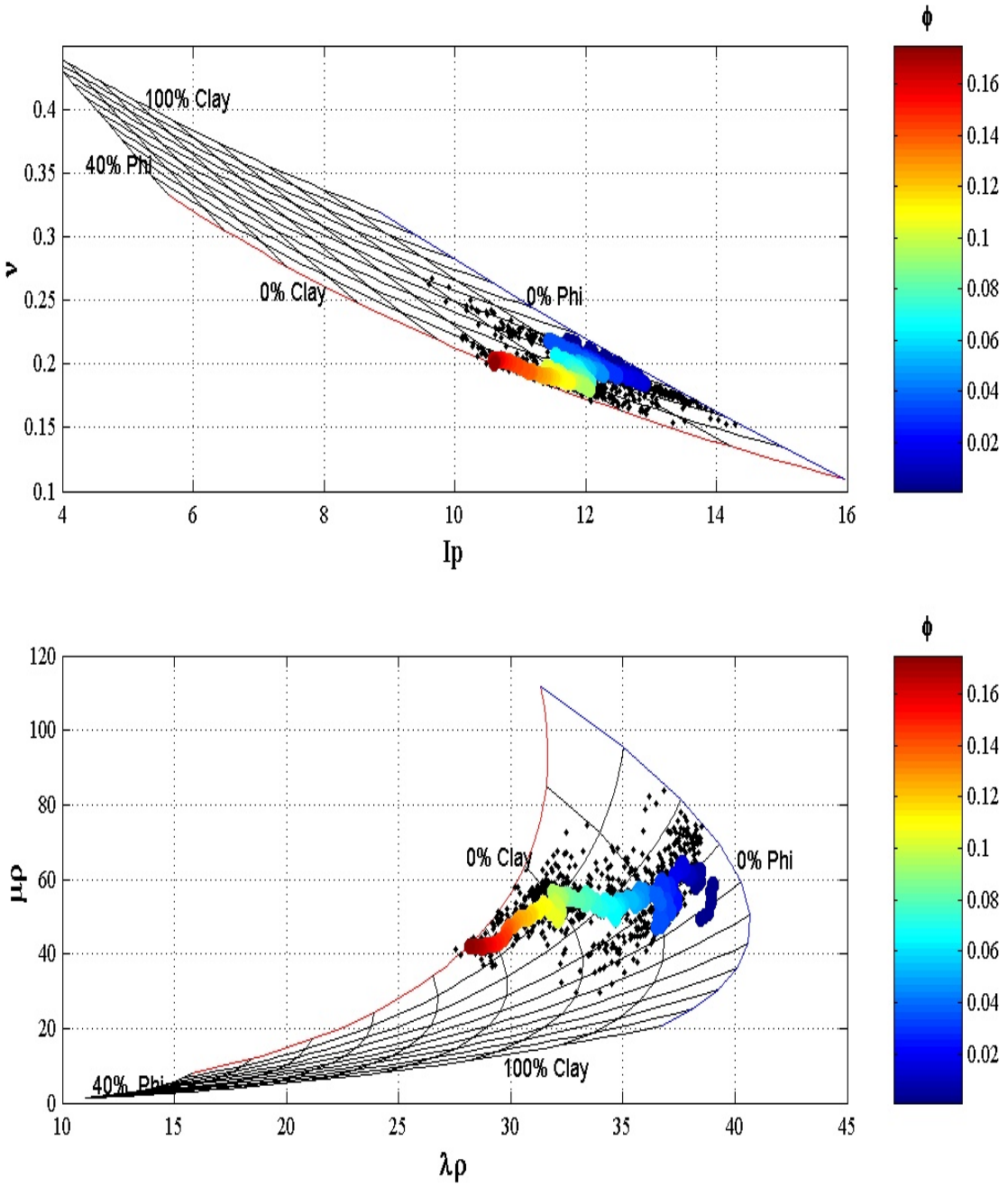

Figure 7.23: From top to bottom: plots of ν versus Ip, and μρ versus λρ. The lines are the theoretical curves for 10% clay increments and 5% porosity increments generated from the combined Raymer et al. (1980) and Greenberg and Castagna (1992) models. The black symbols are the actual log data from 5 wells (wc,wk,w2,w7 and w16 combined) at 100% water saturation, and the upscaled values are color coded by porosity. n = 20; the window size is 4 m.

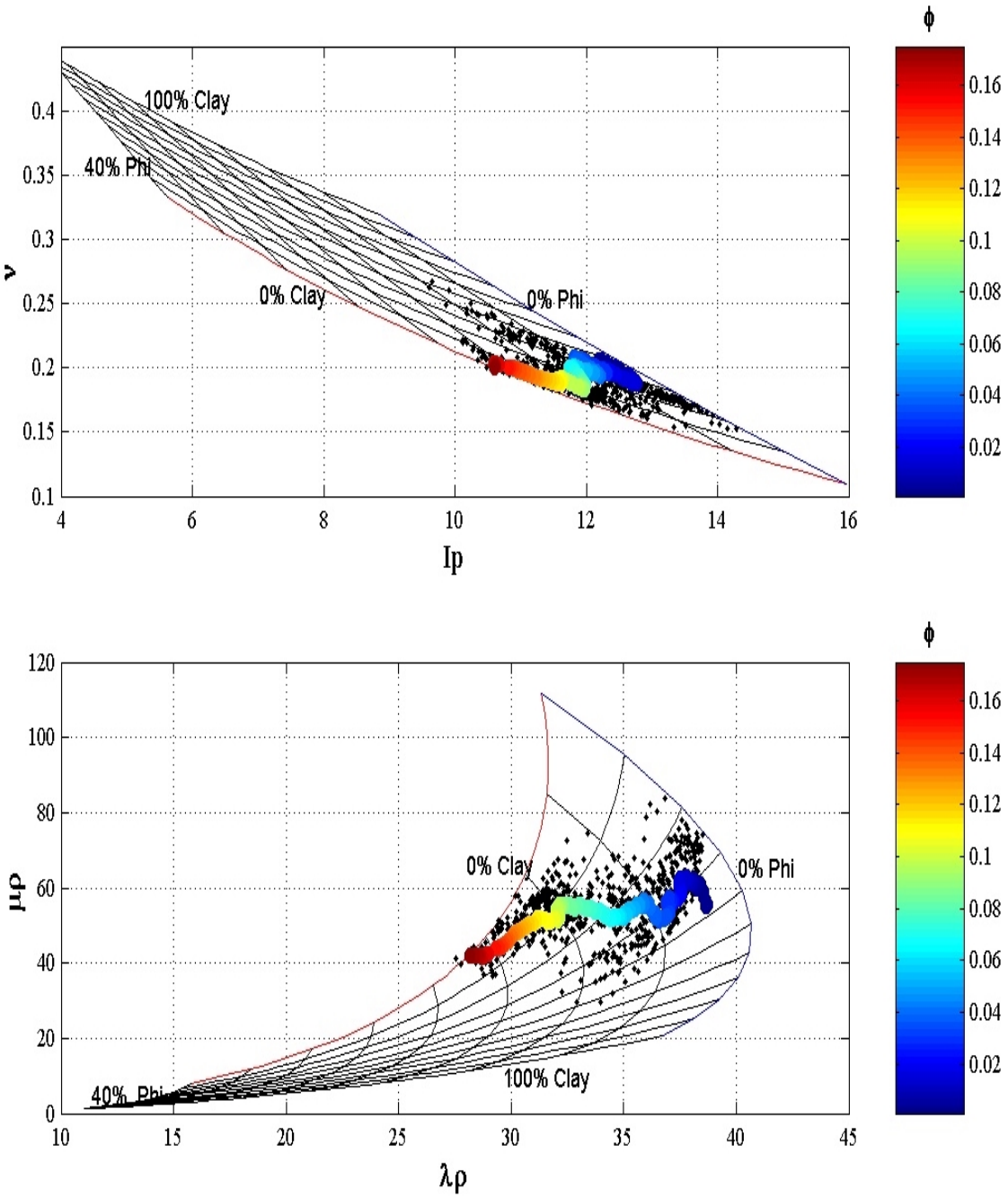

Figure 7.24: From top to bottom: plots of ν versus Ip, and μρ versus λρ. The lines are the theoretical curves for 10% clay increments and 5% porosity increments generated from the combined Raymer et al. (1980) and Greenberg and Castagna (1992) models. The black symbols are the actual log data from 5 wells (wc,wk,w2,w7 and w16 combined) at 100% water saturation, and the upscaled values are color coded by porosity. n = 50; the window size is 10 m.

7.7 CONCLUSION

- For small windows (e.g., 0.3 m), the upscaled values and the actual values are almost the same (within 80%). The upscaled parameters reflect most of the heterogeneity (fluctuations), and cover the entire range of the actual values. For the larger windows (e.g., 10 m), the upscaled parameters show significant reduction of fluctuations and trace only trace the main trend of the actual log parameters, skipping the fine details.
- We conclude that both the HMwMUHS and RCG models can be used to characterize BQ field at seismic scales. However, HMwMUHS is more accurate and will be applied to seismic data.

7.8 REFERENCES

Gold, N., Shapiro, S. A., Bojinski, S., Mueller, T. M., November-December 2000, An Approach to Upscaling for Seismic Waves in Statistically Isotropic Heterogeneous Elastic Media, Geophysics, vol. 65, no. 6, p. 1837-1850, 20 Figs.

Greenberg, M. L., and Castagna, J. P., 1992, Shear-wave Velocity Estimation in Porous Rocks: Theoretical Formulation, Preliminary Verification and Applications, Geophysics Prospecting, 40, 195-209.

Mavko G., Mukerji T., Dvorkin J., 1998, Rock physics Handbooks, Cambridge University Press.

Rio P., Mukerji, T., Mavko, G., and Marion D., March-April 1996, Velocity Dispersion and Upscaling in Laboratory-Simulated VSP, Geophysics, vol. 61, no. 2, p.584-593, 8 Figs, 1 Tables.

Raymer, L. L., Hunt, E. R., and Gardner, J. S., 1980, An Improved Sonic Transit Time-to-Porosity Transform, Trans. Soc. Prof. Well Log Analysts, 21st Annual Logging Symposium, Paper P.

Tomutsa, L., June 2000, Upscaling of Petrophysical properties using wavelet transforms and its comparison to other methods of upscaling; AAPG Bulletin, vol. 84, no. 6, p. 899.

CHAPTER 8

APPLICATION OF ROCK PHYSICS TO REAL SEISMIC

8.1 INTRODUCTION

Advanced seismic reservoir characterization involves the application of rock physics relations to real seismic data to map porosity, lithology, permeability, pore fluid and pore pressure. The bases of this advanced seismic reservoir characterization are transforms between rock elastic properties (e.g., P-wave impedance and Poisson's ratio) and rock bulk properties (e.g., porosity, lithology) and conditions (pore fluid and pressure). Such rock physics transforms are derived from log and core data, theoretically generalized, and then applied to seismic data.

The goal of this chapter is to apply the rock physics models that we developed from core and log data to real seismic data to map porosity and permeability.

8.2 DISPLAY OF THE DATA

The P-impedance (Ip) and Poisson's ratio (ν) inversion of seismic data from lines 77559 and 56302A come from PanCanadian and are available for the application of rock physics to real seismic. Figures 8.1 to 8.4 display the 2-D images of P-impedance and Poisson's ratio in the two-way travel time versus CDP numbers from line 77559 and 56302A in BQ field.

Figures 8.2 shows bright spots at about 1350 ms two way travel time. Similarly, Figure 8.4 shows bright spots at about 1340 ms two way travel time. The cross-plot of Poisson's ratio versus P-impedance, shown in Fig. 6.9 in Chapter 6, illustrates that the good quality rocks have low Poisson's ratio and medium P-impedance values. The seismic inversion shown in Fig. 8.1 to 8.4 confirms this rock physics principle, at about 1350 ms and 1340 ms two way travel time for line 56302A and 77559 respectively. We conclude that it is possible to delineate the reservoir sands from seismic inversion.

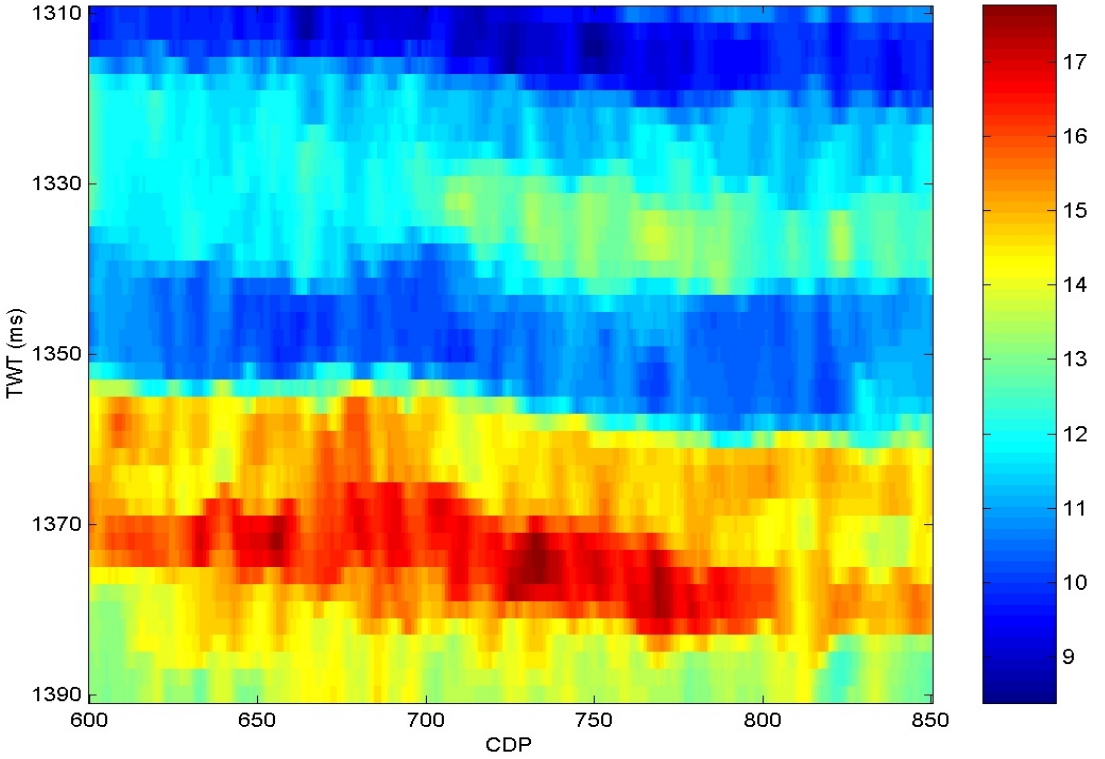

Figure 8.1: 56302A seismic line from BQ field showing the P-impedance inversion in two-way travel time versus CDP numbers.

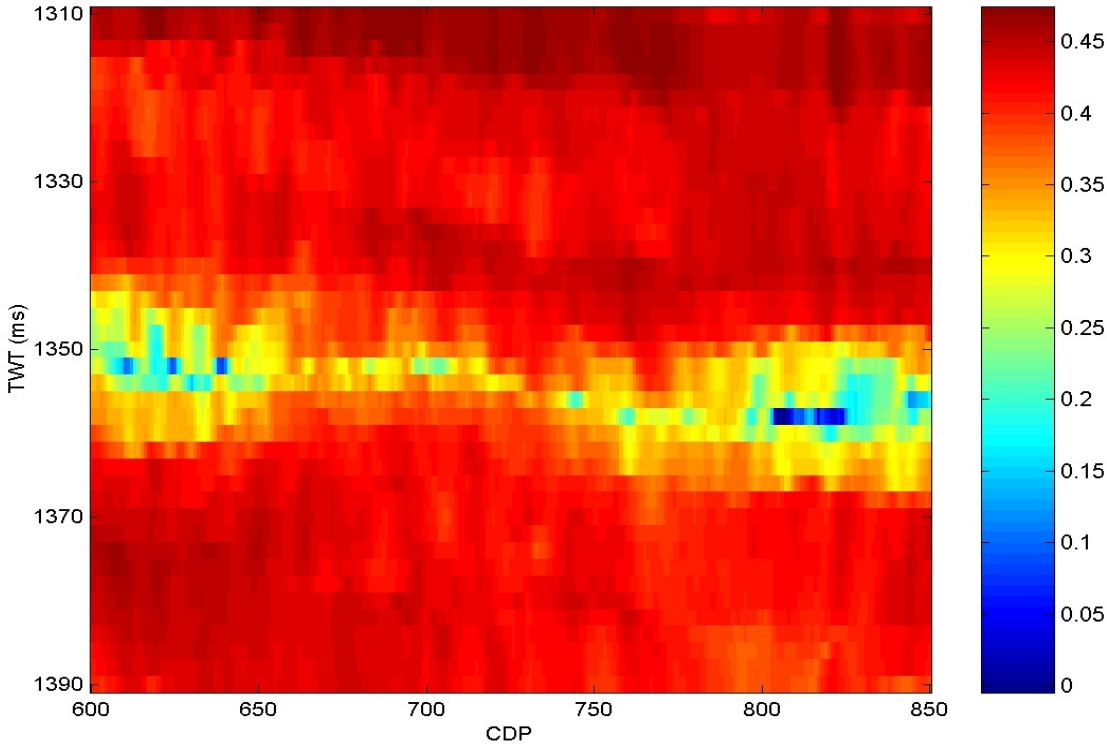

Figure 8.2: 56302A seismic line from BQ field showing the Poisson's ratio inversion in two-way travel time versus CDP numbers.

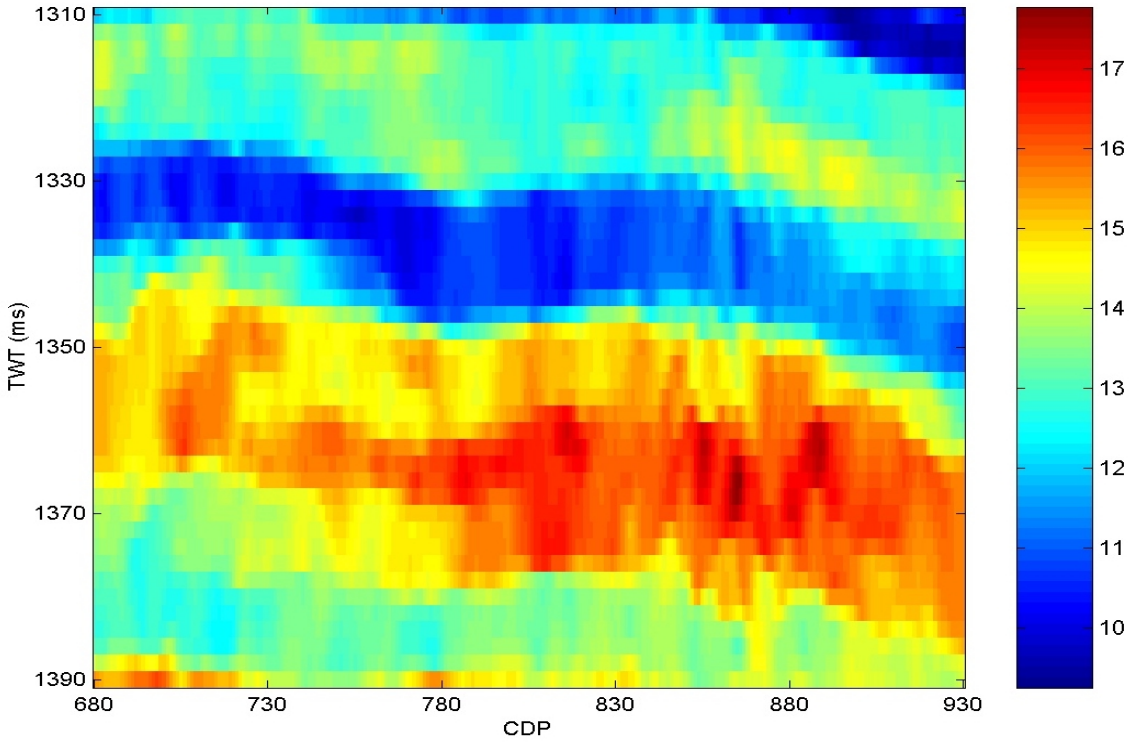

Figure 8.3: 77559 seismic line from BQ field showing the P-impedance inversion in two-way travel time versus CDP numbers.

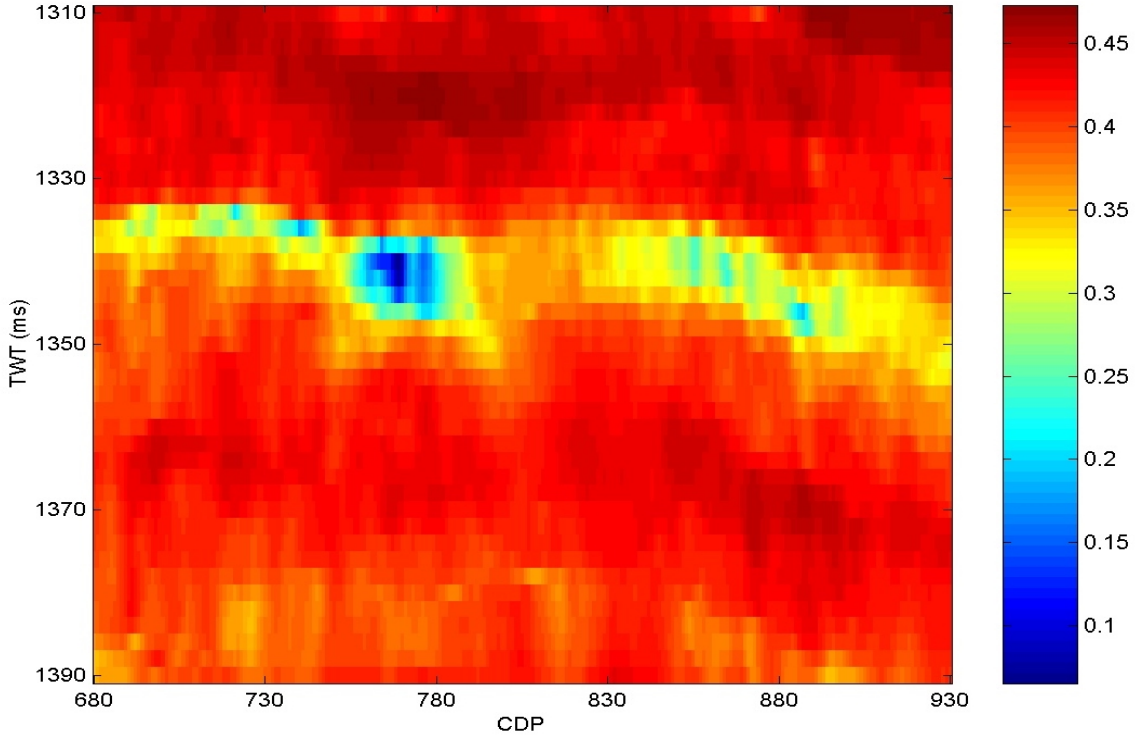

Figure 8.4: 77559 seismic line from BQ field showing the Poisson's ratio inversion in two-way travel time versus CDP numbers.

8.3 APPLICATION OF THE ROCK PHYSICS MODELS TO SEISMIC

We demonstrated in Chapter 6 that good quality rocks have low Poisson ratio values. Based on this rock physics principle, we use Poisson's ratio to delineate the BQ sands and focus on the domains where Poisson's ratio is less than 0.35. The upscaling results, shown in Fig. 7.21 in Chapter 7, show that the clean sands have P-impedance less than or equal to 11.3 km/s g/cc and can be modeled by the Ip-ϕ curve for 10% clay; whereas, the shaley sands have P-impedance greater than 11.3 km/s g/cc and can be modeled by the Ip-ϕ curve of 30% clay. We use these two Ip-ϕ transforms to derive porosity from the acoustic P-impedance inversion from seismic.

8.3.1 Porosity Maps

The plot of the Ip versus ϕ at seismic scale in Fig. 7.21 indicates that for Ip less than or equal to 11.3 km/s g/cc, the reservoir is low-clay-content and gas bearing, the data lie around the 10% clay line, thus we use the Ip-ϕ transform for 10% clay and 80% gas to predict porosity from Ip inversion from line 56302A and 77559. However, for Ip greater than 11.3 km/s g/cc, the reservoir is shaley sands and water saturated, and the data lie around the 30% clay line, thus we use the Ip-ϕ transform for 30% clay and 100% water saturated to predict porosity from Ip inversion from line 56302A and 77559. The predicted porosities for these two lines are shown in Fig. 8.5 and 8.10.

8.3.2 Sensitivity Analysis on Porosity Estimates

8.3.2.1 Possible ϕ over/under estimate due to $\pm$ 5% clay content variation

We perform sensitivity analysis on porosity prediction due to ± 5% clay content variation. We compute the possible porosity underestimate if the clay content is 5% less than assumed and the possible porosity overestimate if the clay content is 5% more than assumed. The results of these sensitivity analyses are presented in Fig. 8.6 and 8.7 for line 56302A, and Fig. 8.11 and 8.12 for line 77559. These figures show that the maximum possible porosity under prediction or over prediction is 1.5% in high porosity zones and 2.5% in low porosity zones

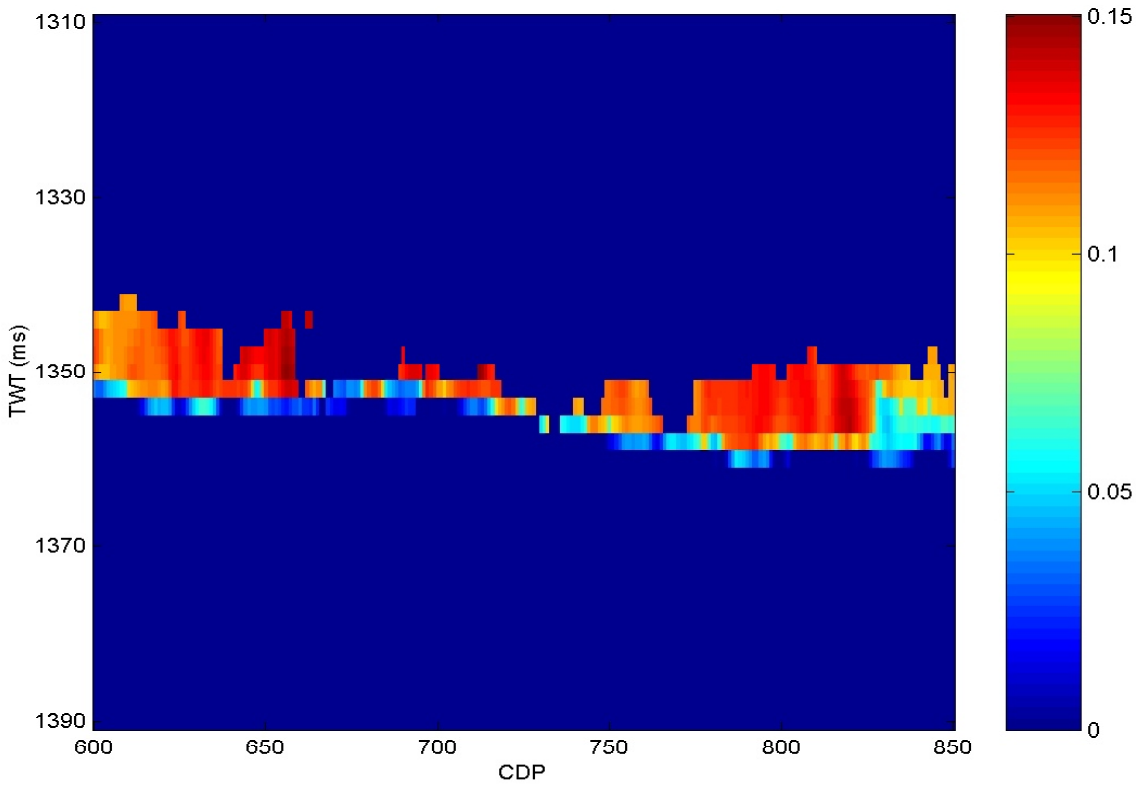

Figure 8.5: 56302A seismic line from BQ field showing the predicted porosity section in two-way travel time versus CDP numbers.

8.3.2.2 Possible ϕ over/under estimate due to $\pm$ 0.5 km/s g/cc Ip variation

We perform sensitivity analysis on porosity prediction due to $\pm$ 0.5 km/s g/cc possible error in P-impedance from the seismic inversion. The results of these sensitivity analyses are presented in Fig. 8.8 and 8.9 for line 56302A, and Fig.8.13 and 8.14 for line 77559. These figures show that the maximum possible porosity under prediction is 1.95% and maximum possible over prediction is 1.85%.

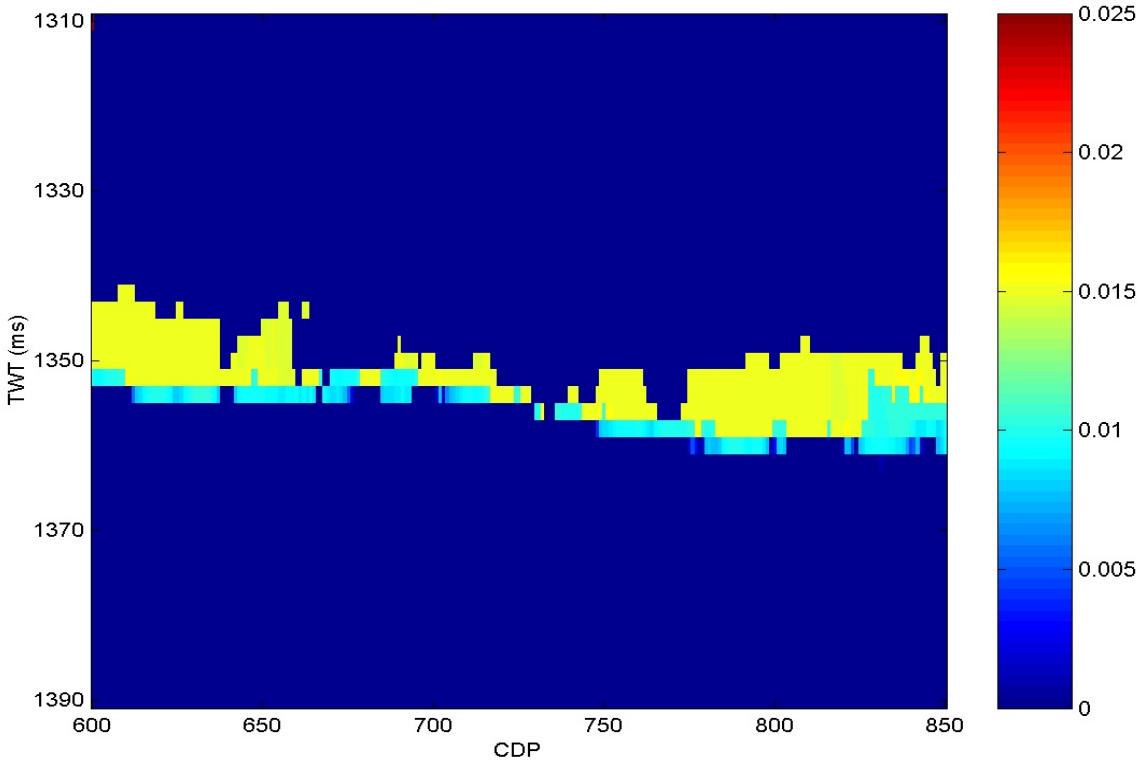

Figure 8.6: 56302A seismic line from BQ field showing possible porosity underestimate for the image in Fig. 8.5, due to +5% clay.

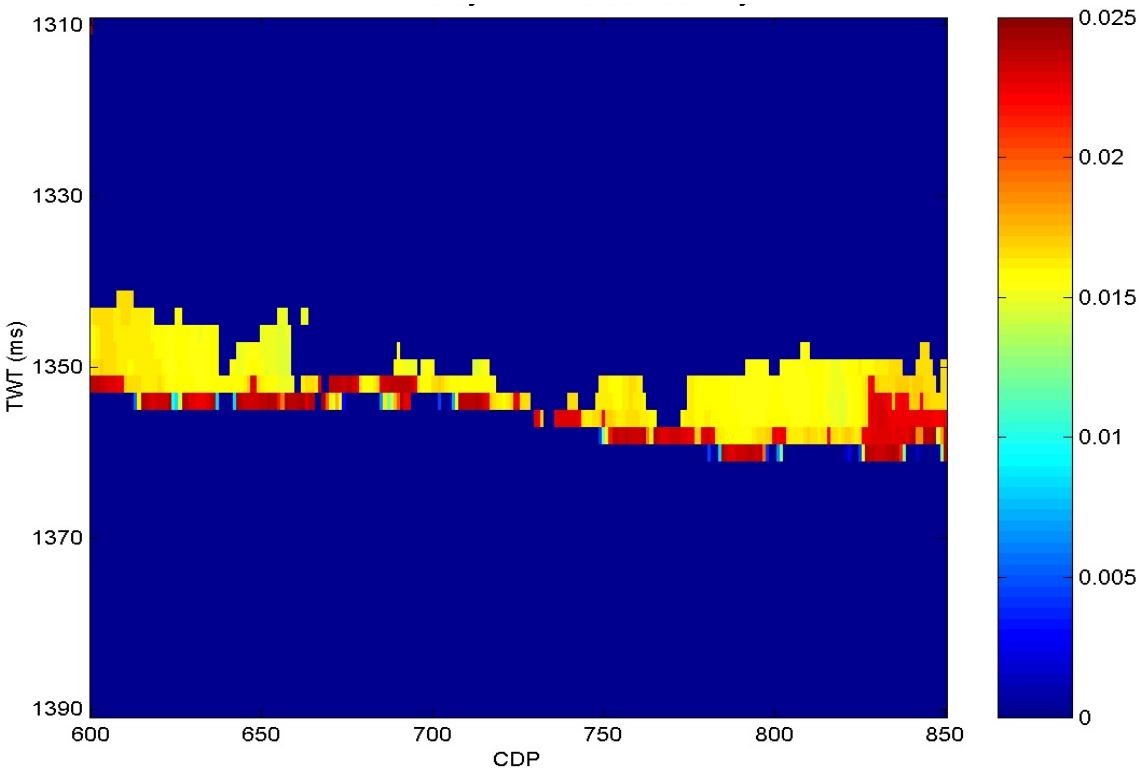

Figure 8.7: 56302A seismic line from BQ field showing possible porosity overestimate for the image in Fig. 8.5, due to –5% clay.

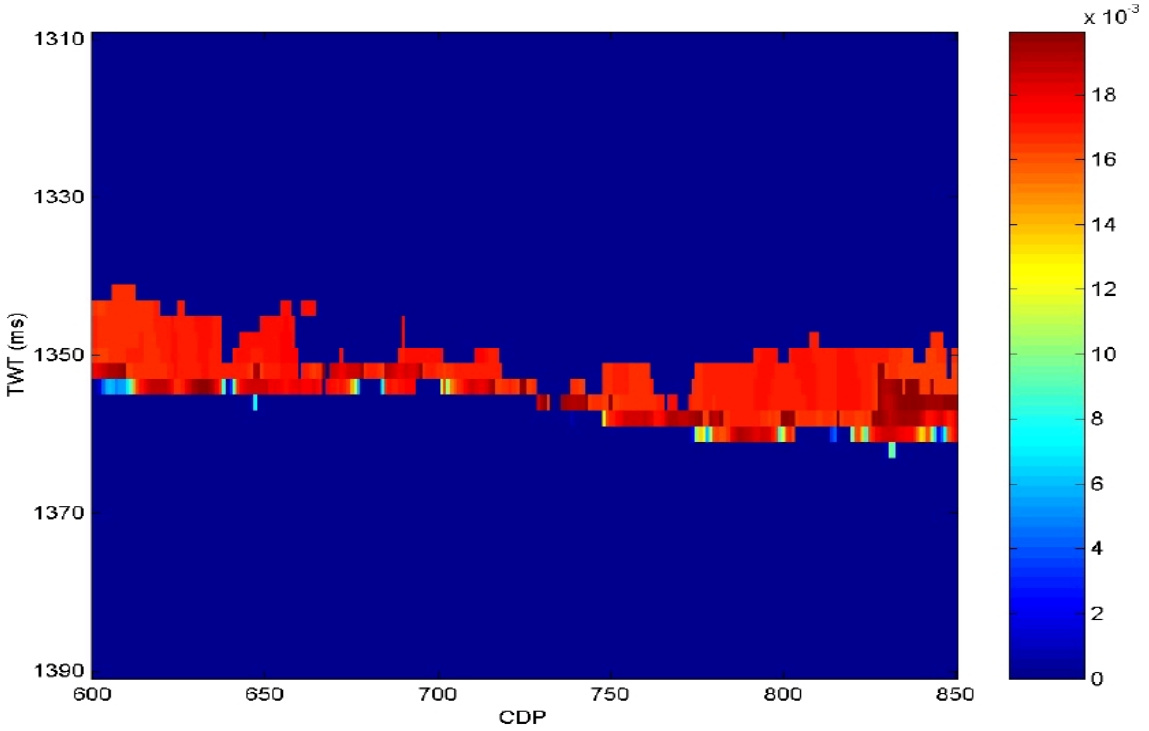

Figure 8.8: 56302A seismic line from BQ field showing possible porosity underestimate for the image in Fig. 8.5, due to +0.5 km/s g/cc error in P-impedance inversion.

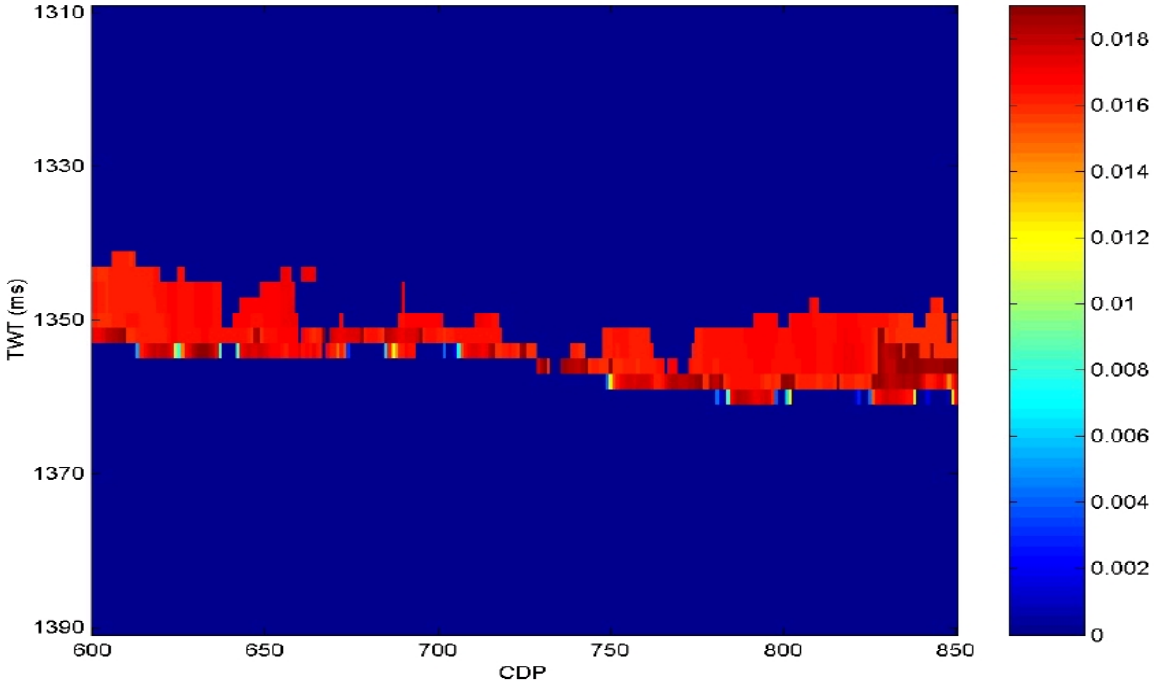

Figure 8.9: 56302A seismic line from BQ field showing possible porosity overestimate for the image in Fig. 8.5, due to -0.5 km/s g/cc error in P-impedance inversion.

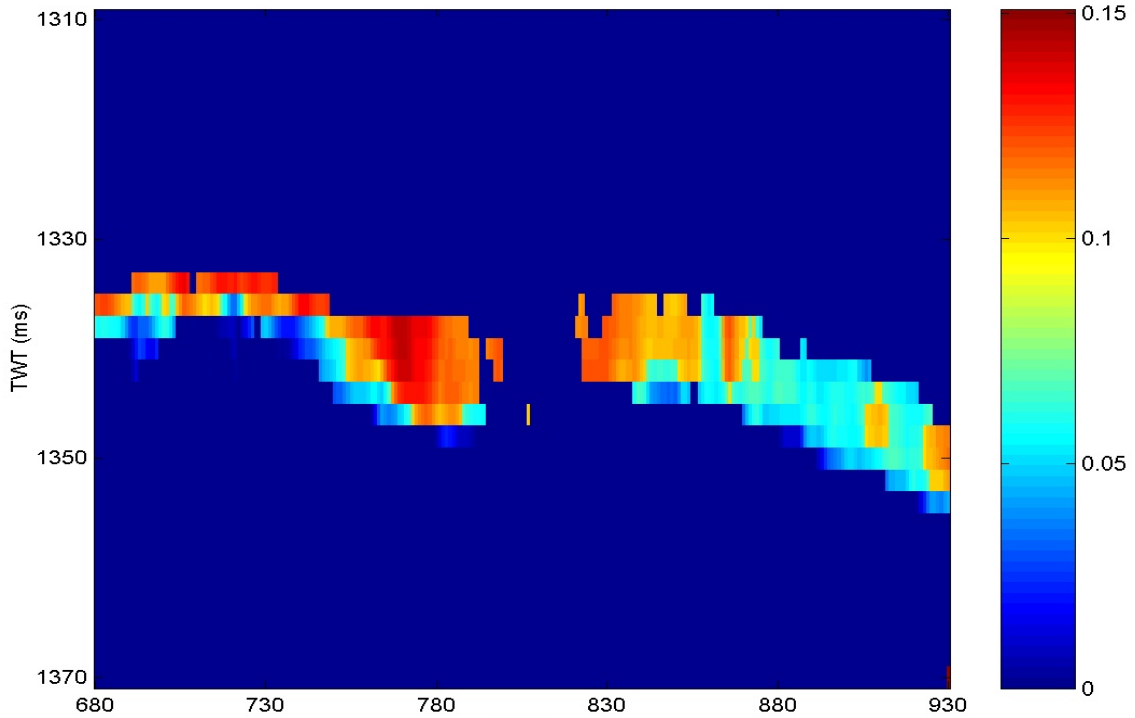

Figure 8.10: 77559 seismic line from BQ field showing the predicted porosity section in two-way travel time versus CDP numbers.

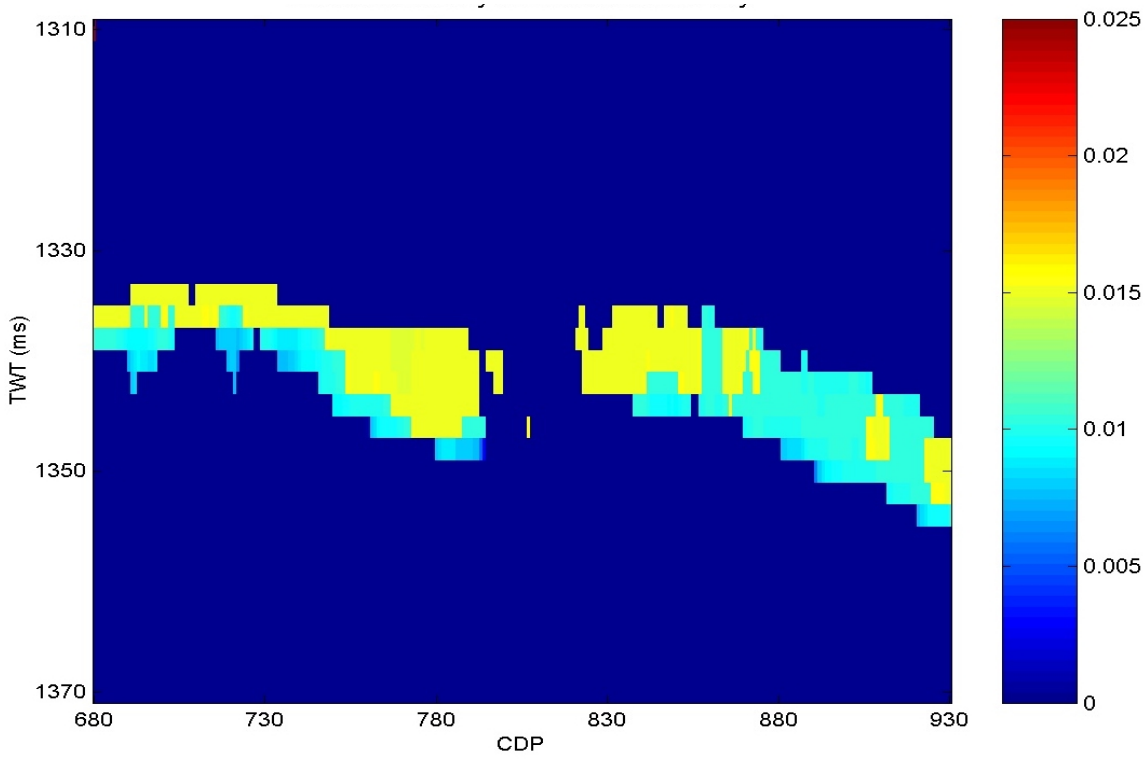

Figure 8.11: 77559 seismic line from BQ field showing possible porosity underestimate for the image in Fig. 8.10, due to +5% clay.

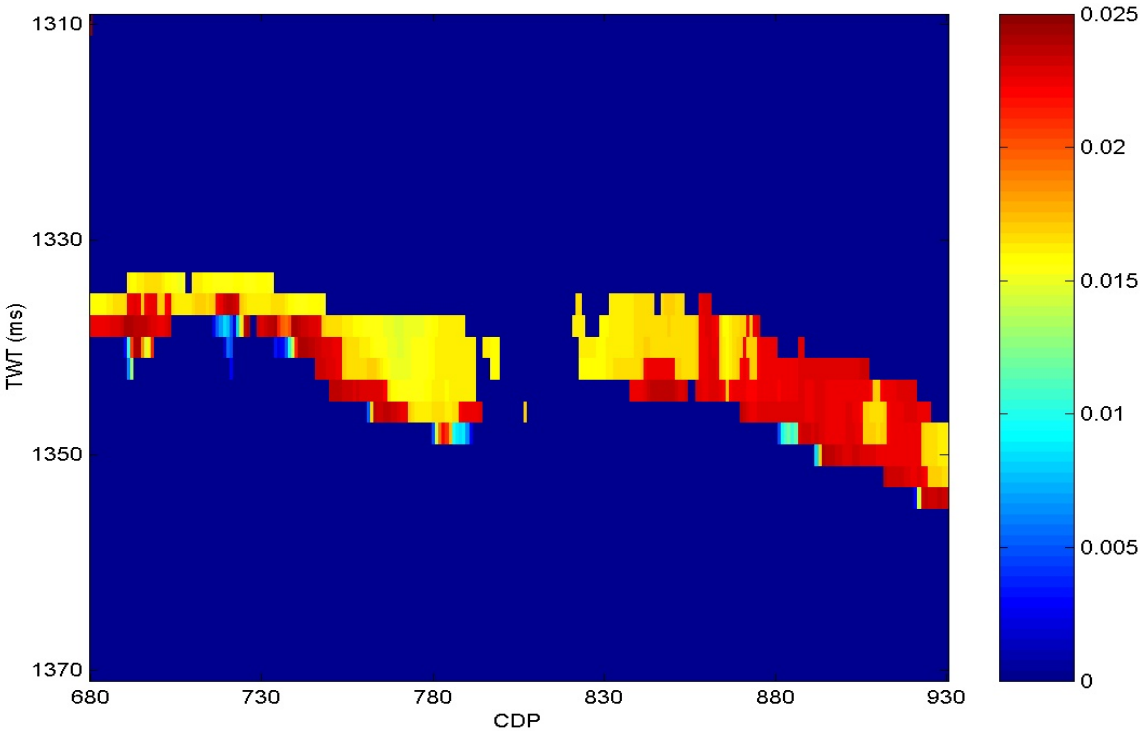

Figure 8.12: 77559 seismic line from BQ field showing possible porosity overestimate for the image in Fig. 8.10, due to -5% clay.

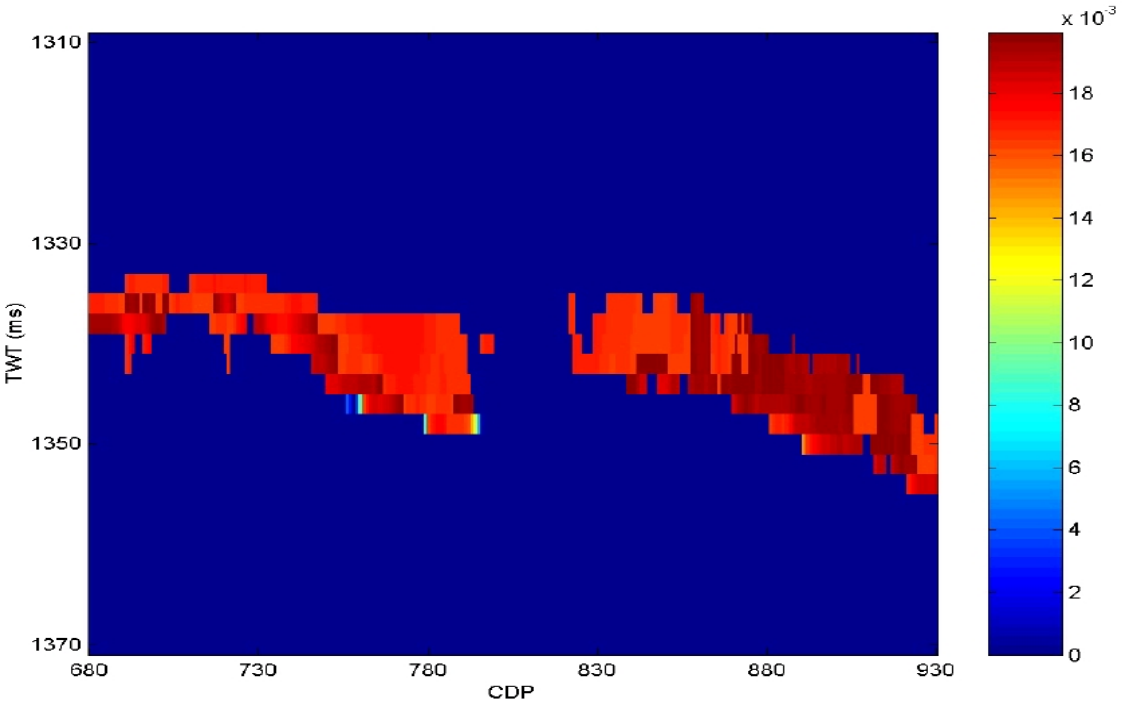

Figure 8.13: 77559 seismic line from BQ field showing possible porosity underestimate for the image in Fig. 8.10, due to +0.5 km/s g/cc error in P-impedance inversion.

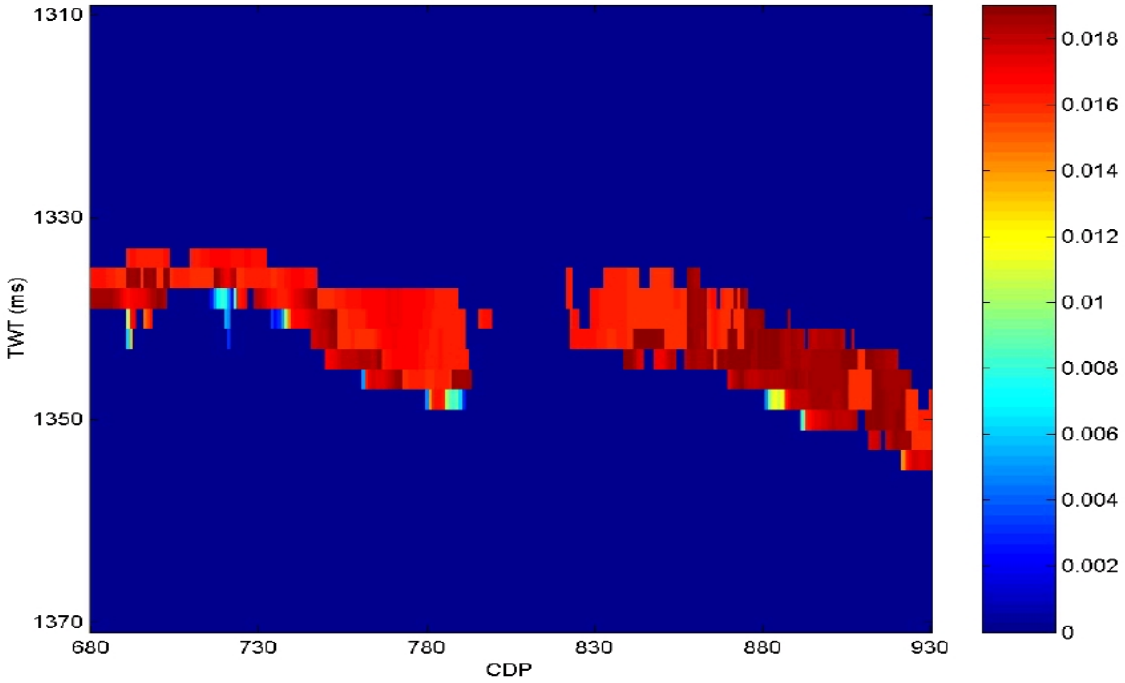

Figure 8.14: 77559 seismic line from BQ field showing possible porosity overestimate for the image in Fig. 8.10, due to -0.5 km/s g/cc error in P-impedance inversion.

8.3.3 Permeability section

We use the same approach as in the porosity prediction. The plot of the Ip versus ϕ at seismic scale in Fig. 7.21 indicates that for Ip less than or equal to 11.3 km/s g/cc, we assume that the reservoir is low-clay-content thus we use the permeability-porosity relation, given in Table 5.7, for Group I rocks to predict permeability from the predicted porosity for line 56302A and 77559. Whereas, for Ip greater than 11.3 km/s g/cc, we assume the reservoir to be shaley sands thus we use the permeability-porosity model for Group II rocks, given in Table 5.7, to predict permeability from porosity for line 56302A and 77559. The predicted permeability for these two lines are shown in Fig. 8.15 and 8.20 for line 56302A and 77559 respectively.

8.3.4 Sensitivity Analysis on Permeability Estimates

8.3.4.1 Possible Permeability over/under estimate due to ± 5% clay content variation

We perform sensitivity analysis on permeability prediction due to ± 5% clay content variation. We compute the possible permeability underestimate if the clay content is 5%

less than assumed and the possible permeability overestimate if the clay content is 5% more than assumed. These permeability variations are due to porosity underestimation or overestimation. The results of these sensitivity analyses are presented in Fig. 8.16 and 8.17 for line 56302A, and Fig. 8.21 and 8.22 for line 77559. These figures show that the maximum possible permeability under prediction or over prediction is 110 mD in high porosity zones and 20 mD in low porosity zones

8.3.4.2 Possible Permeability over/under estimate due to ± 0.5 km/s g/cc Ip variation

We perform sensitivity analysis on porosity prediction due to ± 0.5 km/s g/cc possible error in P-impedance from the seismic inversion. The results of these sensitivity analyses are presented in Fig. 8.18 and 8.19 for line 56302A, and Fig.8.23 and 8.24 for line 77559. These figures show that the maximum possible permeability under prediction is 105 mD in high permeability zones and 40 mD in low permeability zones, and maximum possible permeability over prediction is 135 mD in high permeability zones and 50 mD in low permeability zone.

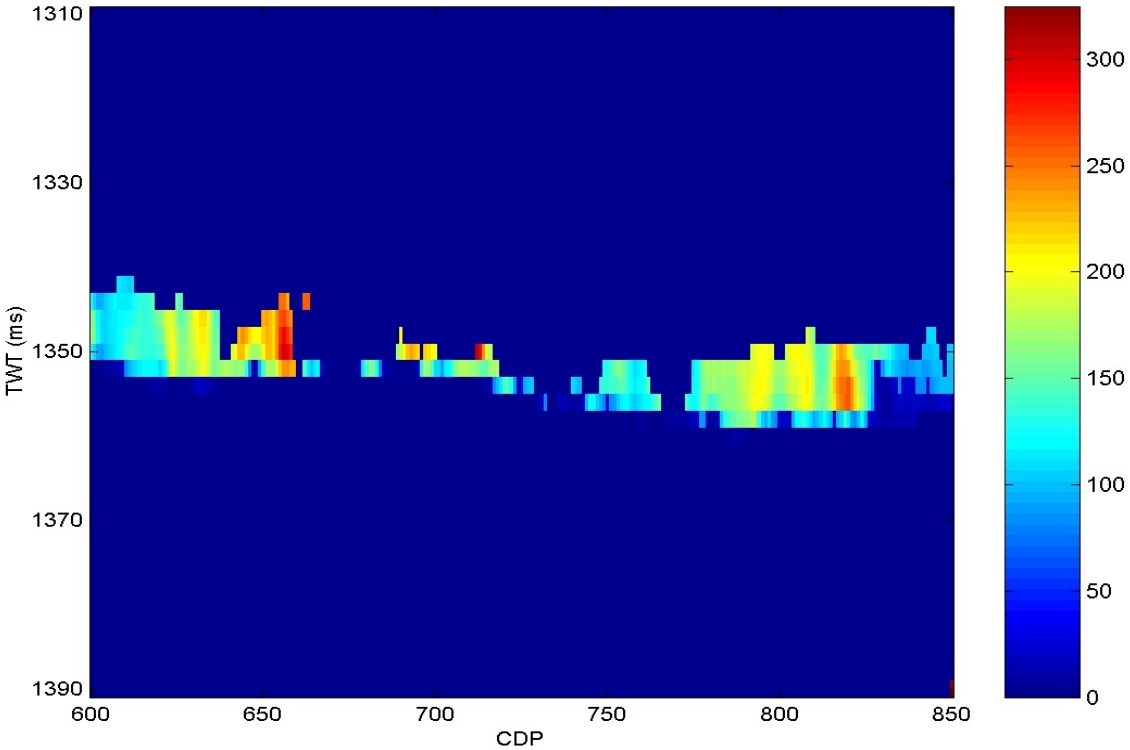

Figure 8.15: 56302A seismic line from BQ field showing the predicted permeability section in two way travel time versus CDP number.

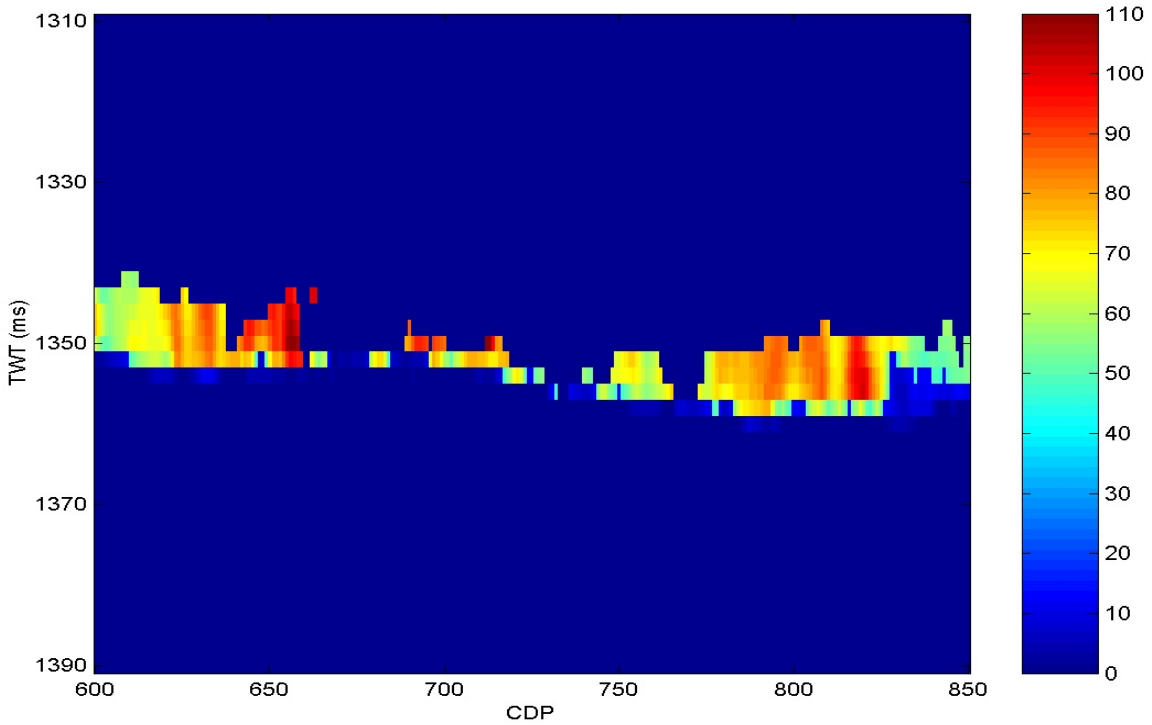

Figure 8.16: 56302A seismic line from BQ field showing the possible error in permeability if the clay content is 5% less than assumed.

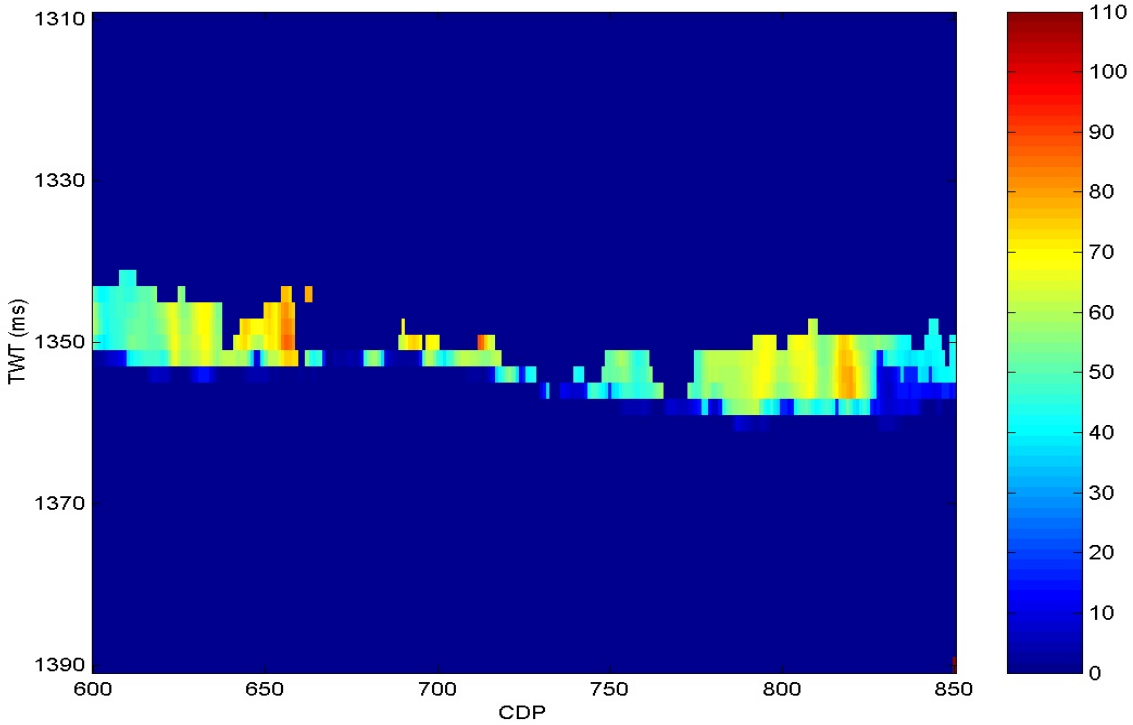

Figure 8.17: 56302A seismic line from BQ field showing the possible error in permeability if the clay content is 5% more than assumed.

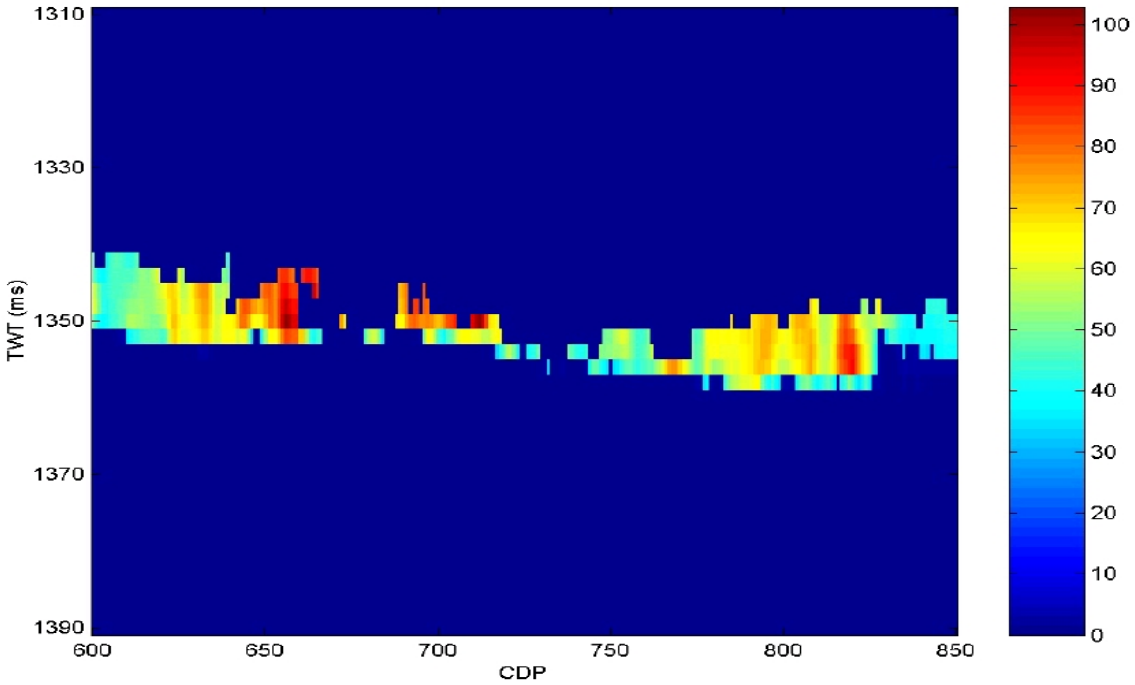

Figure 8.18: 56302A seismic line from BQ field showing permeability underestimate for the image in Fig. 8.15, due to +0.5 km/s g/cc possible error in P-impedance inversion.

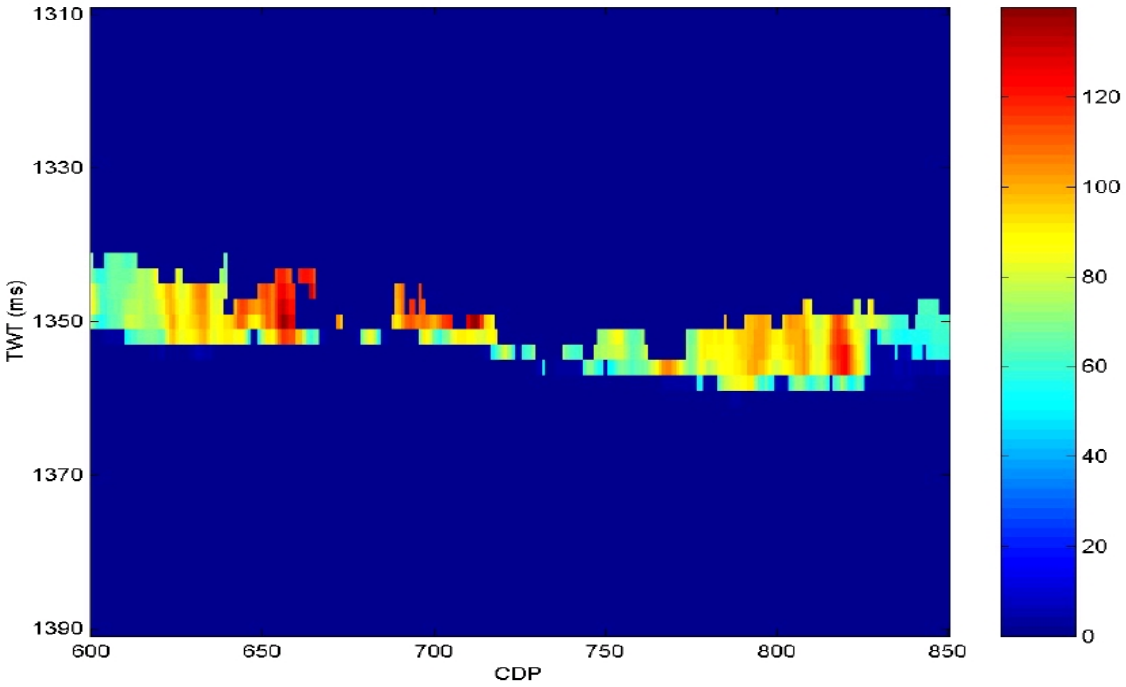

Figure 8.19: 56302A seismic line from BQ field showing permeability over prediction for the image in Fig. 8.15, due to -0.5 km/s g/cc possible error in P-impedance inversion.

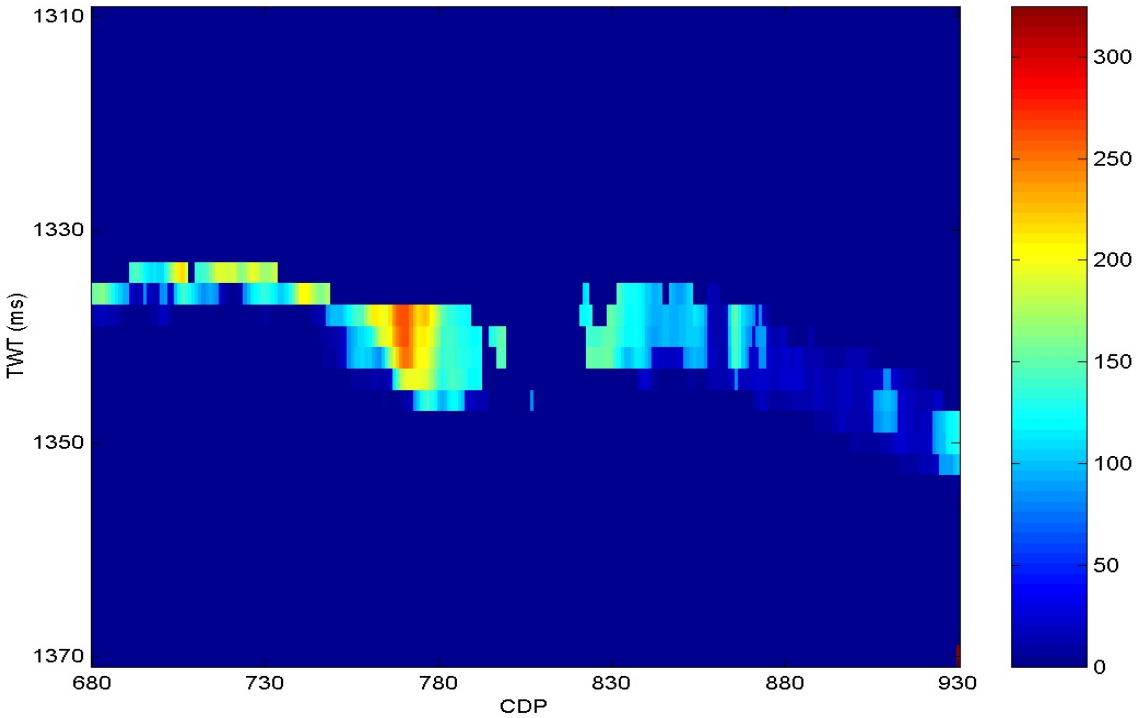

Figure 8.20: 77559 seismic line from BQ field showing the predicted permeability section in two way time versus CDP number.

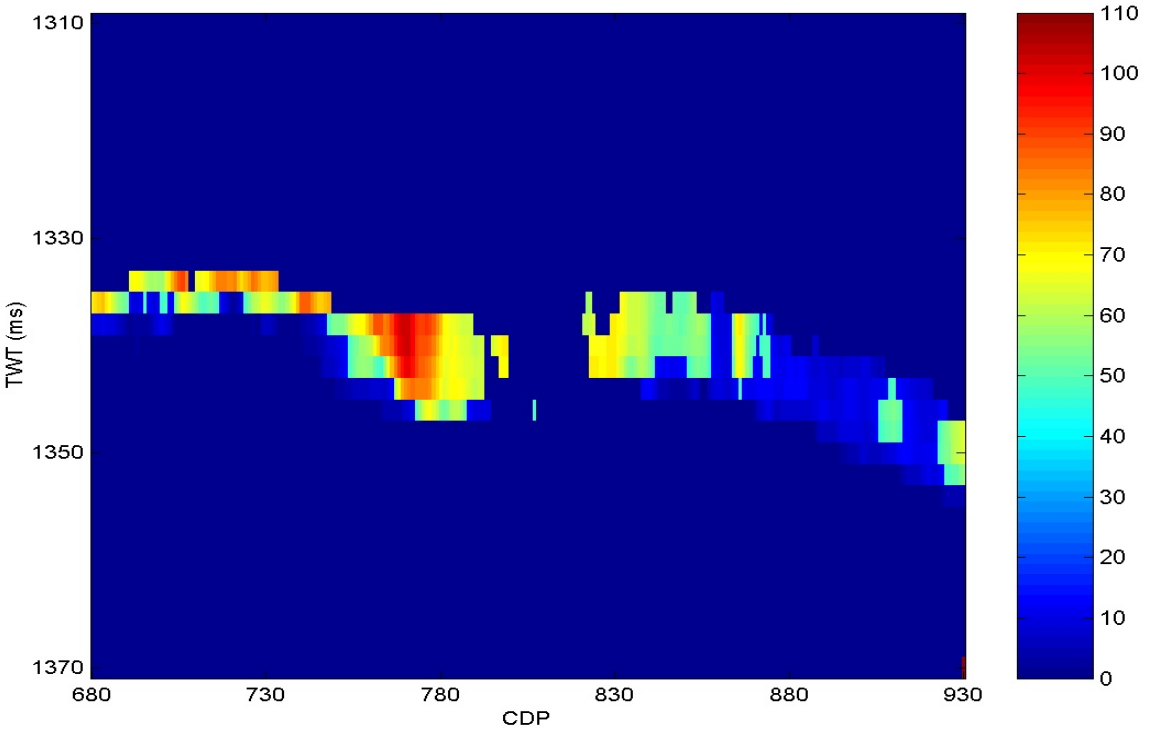

Figure 8.21: 77559 seismic line from BQ field showing the possible permeability under prediction if the clay content is 5% less than the assumed.

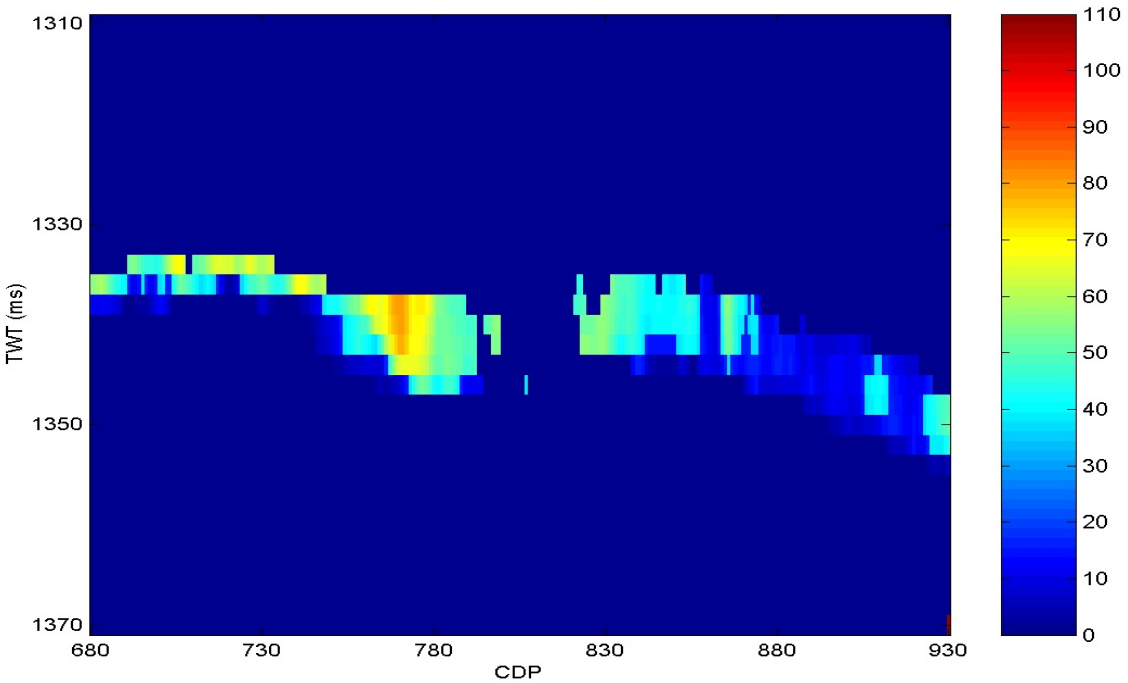

Figure 8.22: 77559 seismic line from BQ field showing the possible permeability over prediction if the clay content is 5% more than the assumed.

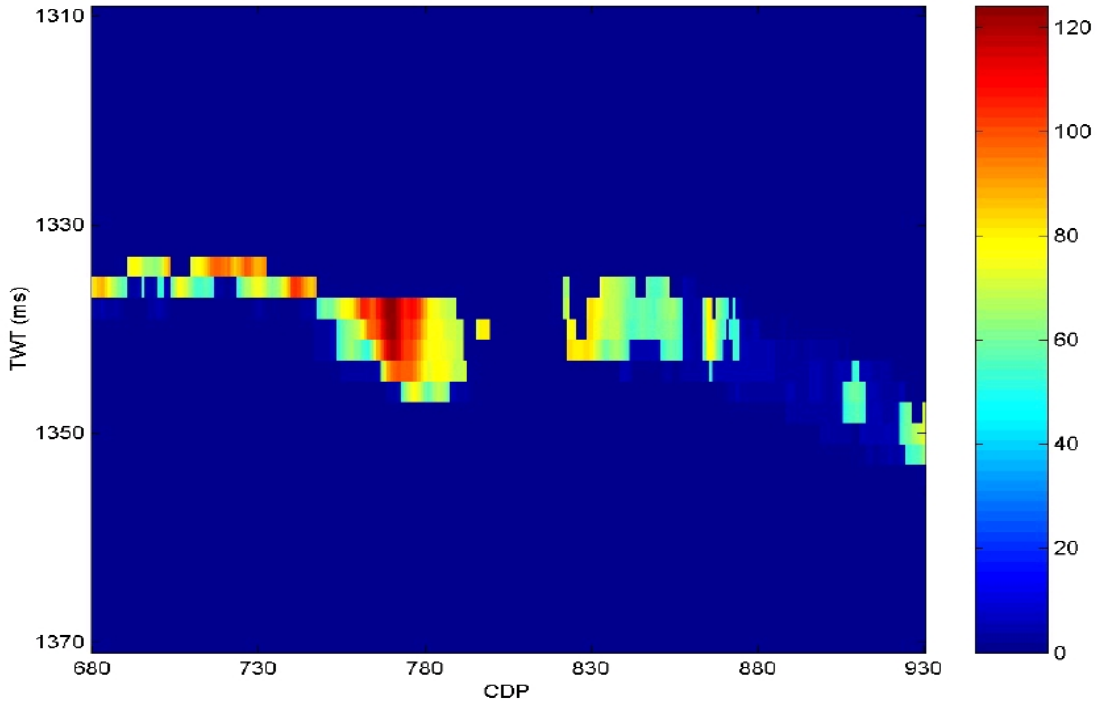

Figure 8.23: 77559 seismic line from BQ field showing possible permeability underestimate for the image in Fig. 8.20, due to +0.5 km/s g/cc error in P-impedance inversion.

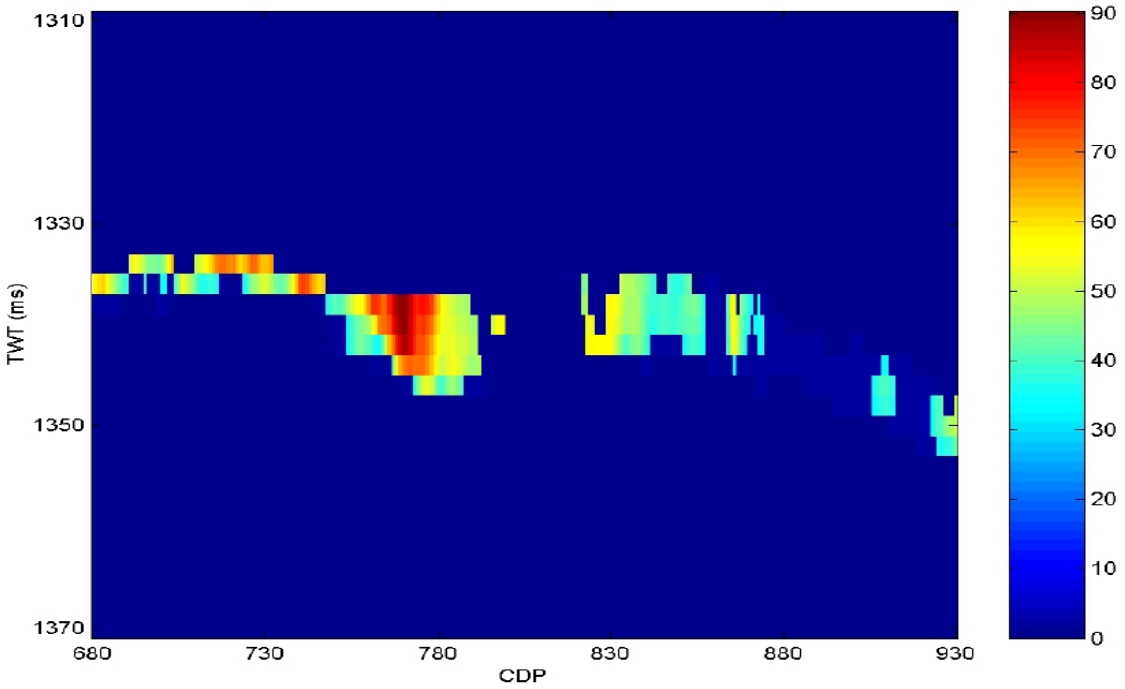

Figure 8.24: 77559 seismic line from BQ field showing possible permeability overestimate for the image in Fig. 8.20, due to -0.5 km/s g/cc error in P-impedance inversion.

8.4 CONCLUSION

- We successfully applied the rock physics theory to seismic data for the advanced reservoir characterization of low porosity sandstones in BQ field. We generated porosity and permeability sections for BQ reservoir.
- The porosity sections display maximum porosity of 15%, maximum porosity errors due to ±5% clay variations of 2.5%, and maximum porosity errors due to ±0.5 km/s g/cc P-impedance error of 1.95%.
- The permeability sections display maximum permeability of 325 mD, maximum permeability errors due to ±5% clay variations of 110 mD, and maximum permeability errors due to ±0.5 km/s g/cc P-impedance error of 135 mD.

8.5 REFERENCES

Mavko G., Mukerji T., Dvorkin J., 1998, Rock Physics Handbooks, Cambridge University Press.

CHAPTER 9

CONCLUSIONS

9.1 ROCK PHYSICS DIAGNOSTICS WORKFLOW

Followings are the major steps we completed for the rock physics diagnostics:

- We reviewed the geologic and diagenetic settings to identify the type of sand (consolidated low-porosity gas sand).
- We established general trends (velocity-porosity-clay) in the log data.
- We conducted lab measurements to quality control log data (porosity and Vs) and to determine pressure dependence of elastic properties.
- We established relations between porosity, lithology, and permeability.
- We corrected log data accordingly and conditioned log data for rock physics modeling.
- We created a rational rock physics model that links the P-wave and S-wave properties to (a) porosity; (b) clay content; (c) pore fluid; and (d) pressure
- The core and log data validated the model.
- We upscaled the model to ensure that it is applicable at the seismic scale.
- We generated sections of porosity and permeability from seismic inversion.

9.2 GENERAL CONCLUSION

We have developed a procedure for using rock physics for advanced seismic reservoir characterization of low porosity sandstones.

APPENDIX

ALL LABORATORY MEASUREMENTS

RESULTS

Sample P2

Type: **very fine**

Depth: **2121.29 - 2121.52 m**

Porosity: **1.1%**

Permeability: **0.01 mD**

Grain Density: **2.697 g/cc**

Bulk Density: **2.666 g/cc**

PanCanadian	**Depth**	Length (mm)	Diameter (mm)	Mass (g)	Phi (%)	Perm (md)	RhoG (g/cc)	RhoB (g/cc)
Sample: P2 Dry	**4072.90**	41.60	24.75	54.34	1.1	0.01	2.697	2.666

File-name P-waves	delta L (mm)	Pc (MPa)	Length (mm)	Vp (km/s)	Vs (km/s)	Vp/Vs	ν	Phi (%)	dPhi (%)	RhoB (g/cc)	Mu (GPa)	K (GPa)
UP												
P2DR1V00	0.00	0.00	41.60	5.109	3.131	1.63	0.20	1.26	0.06	2.72	26.62	35.38
P2DR1V01	0.04	0.60	41.56	5.123	3.138	1.63	0.20	1.17	7.39	2.72	26.76	35.64
P2DR1V02	0.12	1.05	41.48	5.155	3.140	1.64	0.21	0.98	22.55	2.72	26.85	36.56
P2DR1V03	0.17	1.55	41.43	5.206	3.143	1.66	0.21	0.85	32.46	2.73	26.93	37.98
P2DR1V04	0.23	2.60	41.37	5.269	3.161	1.67	0.22	0.73	41.91	2.73	27.28	39.42
P2DR1V05	0.32	5.00	41.28	5.327	3.172	1.68	0.23	0.50	60.55	2.74	27.53	40.94
P2DR1V06	0.41	9.70	41.19	5.380	3.196	1.68	0.23	0.30	76.38	2.74	28.01	42.02
P2DR1V07	0.43	14.70	41.17	5.423	3.206	1.77	0.27	0.26	79.61	2.74	25.72	46.38
P2DR1V08	0.45	20.25	41.15	5.488	3.238	1.69	0.23	0.19	84.73	2.74	28.78	44.30
P2DR1V09	0.47	24.85	41.13	5.494	3.278	1.68	0.22	0.16	87.26	2.75	29.51	43.54
P2DR1V10	0.48	30.00	41.12	5.492	3.290	1.67	0.22	0.13	89.32	2.75	29.73	43.20
P2DR1V11	0.48	34.90	41.12	5.547	3.294	1.68	0.23	0.12	90.71	2.75	29.81	44.78
P2DR1V12	0.49	40.00	41.11	5.626	3.300	1.70	0.24	0.10	91.86	2.75	29.92	47.07
P2DR1V13	0.50	45.00	41.10	5.618	3.301	1.70	0.24	0.09	92.82	2.75	29.94	46.80
P2DR1V14	0.50	50.25	41.10	5.629	3.311	1.70	0.24	0.08	93.63	2.75	30.13	46.91
P2DR1V15	0.50	55.00	41.10	5.632	3.314	1.70	0.24	0.07	94.05	2.75	30.18	46.93
P2DR1V16	0.51	59.50	41.09	5.691	3.317	1.72	0.24	0.07	94.63	2.75	30.24	48.70
DOWN												
P2DR1V17	0.50	56.10	41.10	5.636	3.326	1.69	0.23	0.07	94.05	2.75	30.40	46.76
P2DR1V18	0.50	52.40	41.10	5.632	3.322	1.70	0.23	0.08	93.91	2.75	30.33	46.73
P2DR1V19	0.50	47.50	41.10	5.632	3.355	1.68	0.22	0.08	93.66	2.75	30.93	45.93
P2DR1V20	0.50	42.20	41.10	5.629	3.315	1.70	0.23	0.09	93.16	2.75	30.20	46.81
P2DR1V21	0.49	38.00	41.11	5.629	3.314	1.70	0.23	0.09	92.61	2.75	30.18	46.49
P2DR1V22	0.49	33.00	41.11	5.618	3.312	1.70	0.23	0.10	91.79	2.75	29.99	46.63
P2DR1V23	0.49	28.00	41.11	5.615	3.304	1.70	0.24	0.11	90.91	2.75	29.95	44.74
P2DR1V24	0.48	23.00	41.12	5.552	3.302	1.68	0.23	0.13	89.90	2.75	29.93	44.43
P2DR1V25	0.47	18.00	41.13	5.541	3.301	1.68	0.22	0.15	88.48	2.75	29.67	44.60
P2DR1V26	0.46	12.50	41.14	5.536	3.287	1.68	0.23	0.18	85.39	2.75	29.48	43.25
P2DR1V27	0.43	7.50	41.17	5.484	3.277	1.67	0.22	0.25	80.55	2.74	28.50	41.50
P2DR1V28	0.33	2.00	41.27	5.383	3.223	1.67	0.22	0.48	61.91	2.74	28.32	38.36
P2DR1V29	0.16	0.60	41.44	5.274	3.217	1.64	0.20	0.89	29.58	2.73	27.98	37.39
P2DR1V30	0.05	0.10	41.55	5.235	3.204	1.63	0.20	1.15	8.89	2.72	0.00	0.00

Data Plots

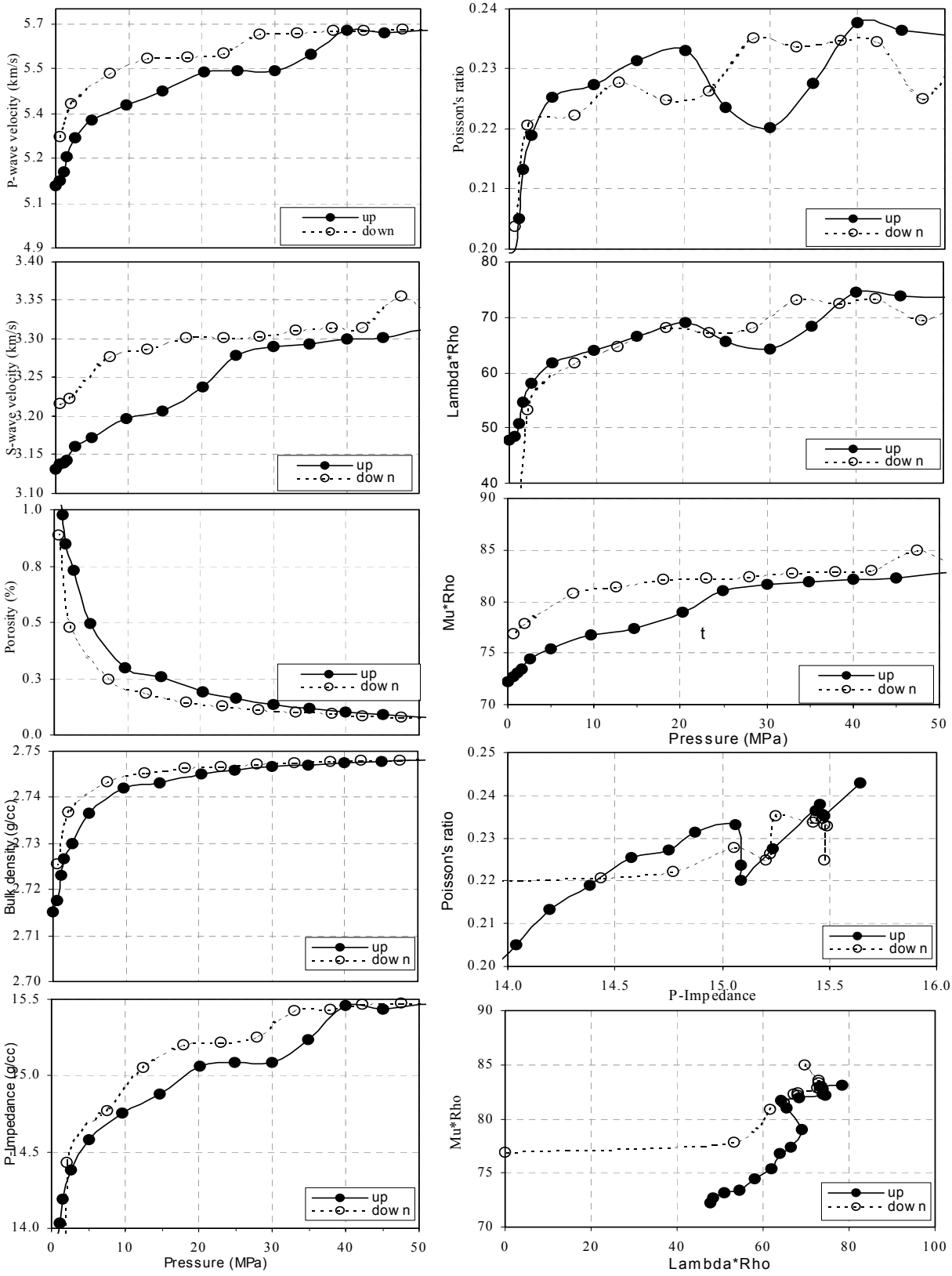
P-wave velocity (km/s)
S-wave velocity (km/s)
Porosity (%)
Bulk density (g/cc)
P-Impedance (g/cc)
Pressure (MPa)
Poisson's ratio
Lambda*Rho
Mu*Rho
Poisson's ratio
P-Impedance
Mu*Rho
Lambda*Rho
up
down
t

Sample P3

Type: **very fine**

Depth: **2121.52 - 2121.64 m**

Porosity: **2.0%**

Permeability: **0.02 mD**

Grain Density: **2.690 g/cc**

Bulk Density: **2.636 g/cc**

PanCanadian	**Depth**	Length (mm)	Diameter (mm)	Mass (g)	Phi (%)	Perm (md)	RhoG (g/cc)	RhoB (g/cc)
Sample: P3 Dry	**2121.52**	33.53	24.94	43.65	2.0	0.02	2.690	2.636

File-name P-waves	delta L (mm)	Pc (MPa)	Length (mm)	Vp (km/s)	Vs (km/s)	Vp/Vs	ν	Phi (%)	dPhi (%)	RhoB (g/cc)	Mu (GPa)	K (GPa)
UP												
Ref	0.00		33.53					0.92	0.00	2.67		
P3D1V00	0.27	30.5	33.26	5.448	3.283	1.66	0.21	0.12	86.65	2.69	28.96	41.13
P3D1V01	0.29	40.5	33.24	5.602	3.331	1.68	0.23	0.06	93.08	2.69	29.83	44.59
P3D1V02	0.31	50.0	33.21	5.606	3.365	1.67	0.22	0.00	100.00	2.69	30.46	43.93

Data Plots

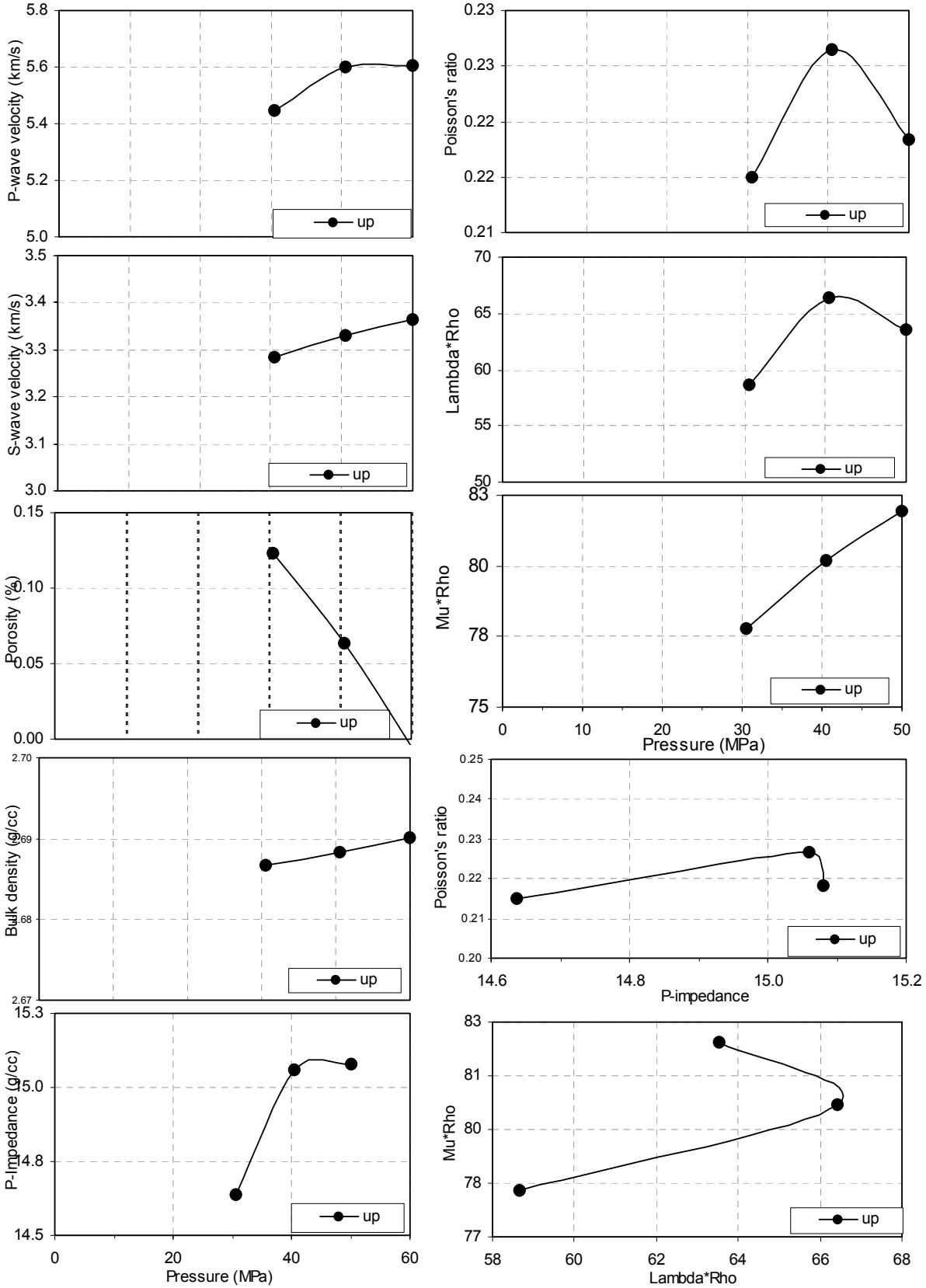
P-wave velocity (km/s)
5.8
5.6
5.4
5.2
5.0
up
Poisson's ratio
0.23
0.23
0.22
0.22
0.21
up
S-wave velocity (km/s)
3.5
3.4
3.3
3.2
3.1
3.0
up
Lambda*Rho
70
65
60
55
50
up
Porosity (%)
0.15
0.10
0.05
0.00
up
Mu*Rho
83
80
78
75
up
0
10
20
30
40
50
Pressure (MPa)
Bulk density (g/cc)
2.70
2.69
2.68
2.67
up
Poisson's ratio
0.25
0.24
0.23
0.22
0.21
0.20
up
14.6
14.8
15.0
15.2
P-impedance
P-Impedance (g/cc)
15.3
15.0
14.8
14.5
up
Mu*Rho
83
81
80
78
77
up
0
20
40
60
Pressure (MPa)
58
60
62
64
66
68
Lambda*Rho

Sample P13

Type: **fine to medium**

Depth: **2124.28 - 2124.46 m**

Porosity: **6.8%**

Permeability: **6.75 mD**

Grain Density: **2.640 g/cc**

Bulk Density: **2.461 g/cc**

PanCanadian	**Depth**	Length (mm)	Diameter (mm)	Mass (g)	Phi (%)	Perm (md)	RhoG (g/cc)	RhoB (g/cc)
Sample: P13 Dry	**2124.28**	27.41	24.98	33.31	6.8	6.75	2.640	2.461

File-name P-waves	delta L (mm)	Pc (MPa)	Length (mm)	Vp (km/s)	Vs (km/s)	Vp/Vs	ν	Phi (%)	dPhi (%)	RhoB (g/cc)	Mu (GPa)	K (GPa)
UP												
Ref	0.00		27.41					6.08	0.00	2.48		
P13D1V00	0.34	10.30	27.07	4.177	2.690	1.55	0.15	4.89	19.54	2.51	18.17	19.58
P13D1V01	0.39	20.10	27.02	4.641	2.886	1.61	0.18	4.73	22.15	2.52	20.95	26.24
P13D1V02	0.42	30.00	27.00	4.779	2.995	1.60	0.18	4.63	23.83	2.52	22.58	27.39
P13D1V03	0.44	40.20	26.97	4.896	3.093	1.58	0.17	4.55	25.23	2.52	24.11	28.26
P13D1V04	0.46	50.00	26.95	5.070	3.147	1.61	0.19	4.47	26.45	2.52	24.98	31.52
DOWN												
P13D1V05	0.46	44.50	26.95	4.952	3.125	1.58	0.17	4.47	26.43	2.52	24.63	29.01
P13D1V06	0.45	34.80	26.96	4.911	3.076	1.60	0.18	4.50	25.95	2.52	23.85	29.00
P13D1V07	0.44	25.10	26.98	4.791	3.006	1.59	0.18	4.56	24.96	2.52	22.77	27.48
P13D1V08	0.41	15.20	27.00	4.630	2.884	1.61	0.18	4.66	23.41	2.52	20.94	26.04

Data Plots

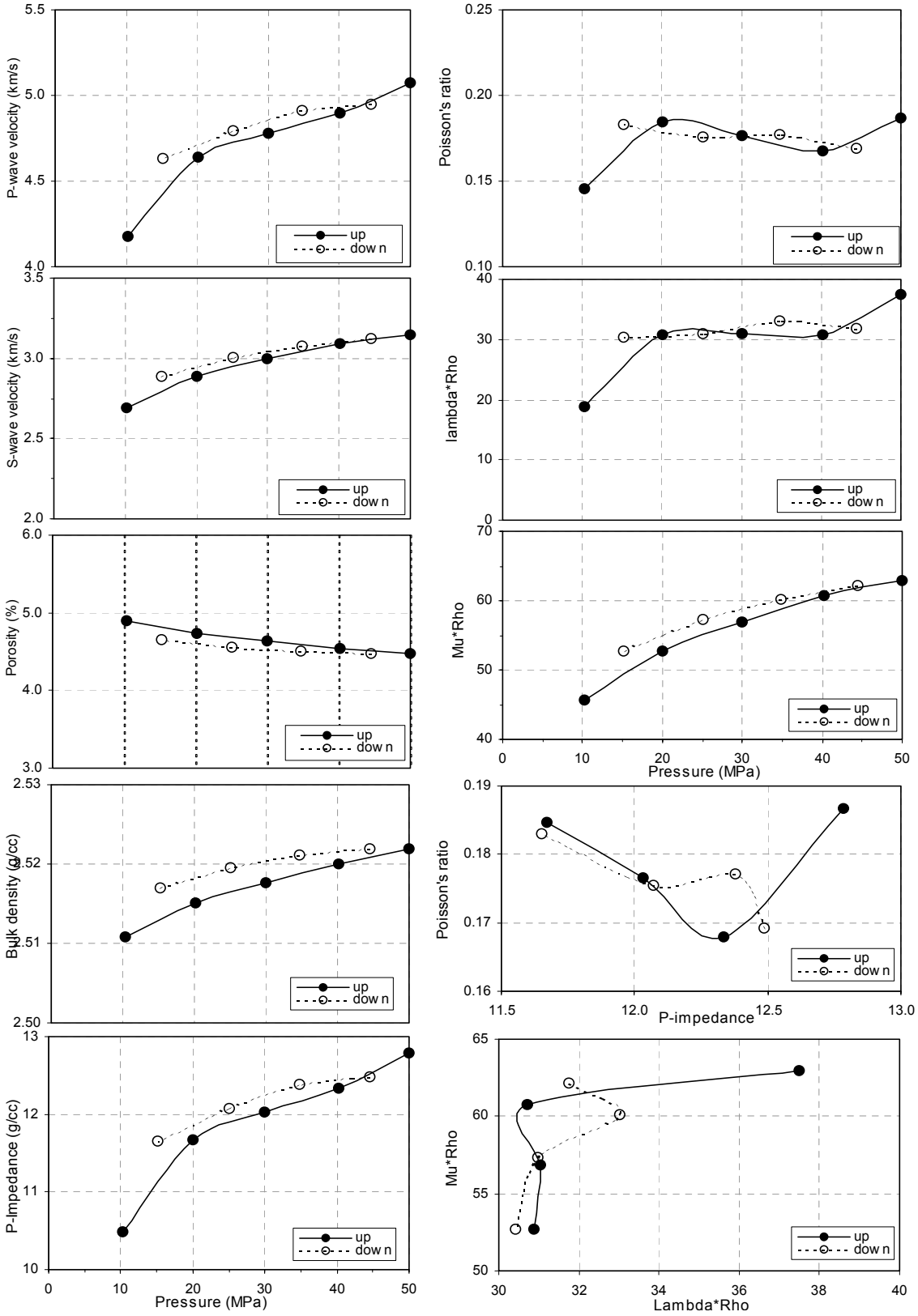
P-wave velocity (km/s)
Poisson's ratio
S-wave velocity (km/s)
lambda*Rho
Porosity (%)
Mu*Rho
Pressure (MPa)
Bulk density (g/cc)
Poisson's ratio
P-impedance
P-Impedance (g/cc)
Mu*Rho
Pressure (MPa)
Lambda*Rho
up
down

Sample P17

Type: **medium**

Depth: **2125.65 - 2125.81 m**

Porosity: **12.1%**

Permeability: **151.82 mD**

Grain Density: **2.660 g/cc**

Bulk Density: **2.338 g/cc**

PanCanadian	**Depth**	Length (mm)	Diameter (mm)	Mass (g)	Phi (%)	Perm (md)	RhoG (g/cc)	RhoB (g/cc)
Sample: P17 Dry	**2125.65**	18.93	24.90	20.94	12.1	151.82	2.660	2.338

File-name P-waves	delta L (mm)	Pc (MPa)	Length (mm)	Vp (km/s)	Vs (km/s)	Vp/Vs	ν	Phi (%)	dPhi (%)	RhoB (g/cc)	Mu (GPa)	K (GPa)
UP												
Ref	0.00		18.93					14.60	0.00	2.27		
P17D1V00	0.51	30.5	18.42	4.497	2.578	1.74	0.26	12.26	16.05	2.33	15.51	26.52
P17D1V01	0.53	50.0	18.40	4.697	2.763	1.70	0.24	12.12	16.99	2.34	17.85	27.78

Data Plots

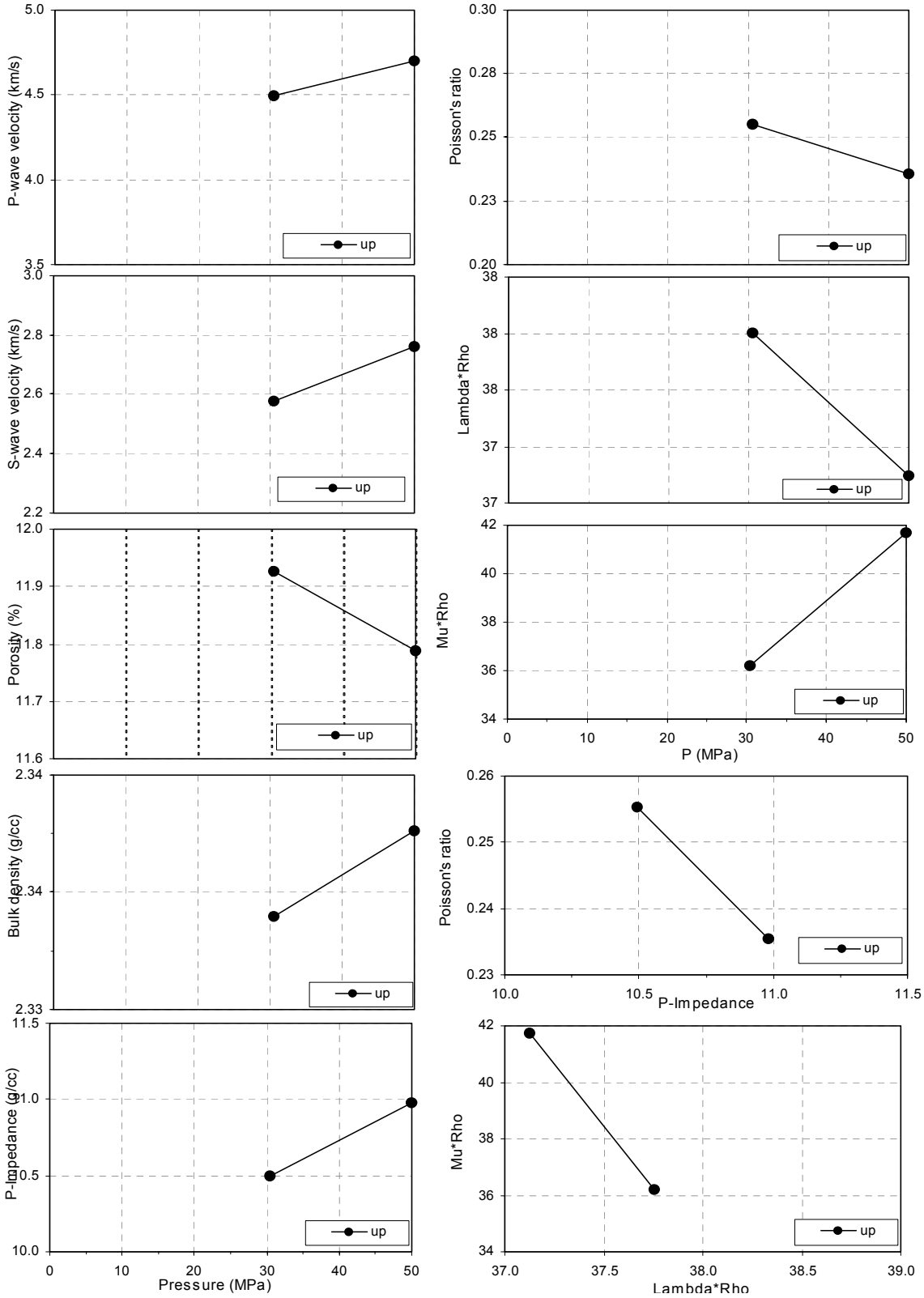
P-wave velocity (km/s)
Poisson's ratio
S-wave velocity (km/s)
Lambda*Rho
Porosity (%)
Mu*Rho
P (MPa)
Bulk density (g/cc)
Poisson's ratio
P-Impedance
P-Impedance (g/cc)
Mu*Rho
Pressure (MPa)
Lambda*Rho
up

Sample P20

Type: **medium**

Depth: **2126.46 - 2126.65 m**

Porosity: **12.0%**

Permeability: **119.52 mD**

Grain Density: **2.640 g/cc**

Bulk Density: **2.323 g/cc**

PanCanadian	**Depth**	Length (mm)	Diameter (mm)	Mass (g)	Phi (%)	Perm (md)	RhoG (g/cc)	RhoB (g/cc)
Sample: P20 Dry	**2126.46**	33.88	24.84	37.43	12.0	119.52	2.640	2.323

File-name P-waves	delta L (mm)	Pc (MPa)	Length (mm)	Vp (km/s)	Vs (km/s)	Vp/Vs	ν	Phi (%)	dPhi (%)	RhoB (g/cc)	Mu (GPa)	K (GPa)
UP												
P20D1V00	0.00	0.20	33.88	2.147	1.417	1.52	0.11	13.64	0.00	2.28	4.58	4.41
P20D1V01	0.03	0.50	33.85	2.168	1.455	1.49	0.09	13.57	0.53	2.28	4.83	4.28
P20D1V02	0.09	1.00	33.78	2.198	1.516	1.45	0.05	13.40	1.77	2.29	5.25	4.04
P20D1V03	0.22	2.50	33.66	3.051	1.541	1.98	0.33	13.09	4.04	2.29	5.45	14.09
P20D1V04	0.70	5.00	33.18	3.364	1.703	1.98	0.33	11.82	13.36	2.33	6.75	17.34
P20D1V05	0.84	9.90	33.03	3.774	1.909	1.98	0.33	11.43	16.20	2.34	8.52	21.94
P20D1V06	0.91	19.30	32.97	4.303	2.424	1.78	0.27	11.25	17.51	2.34	13.77	25.03
P20D1V07	0.94	29.70	32.94	4.396	2.666	1.65	0.21	11.17	18.09	2.35	16.67	23.09
P20D1V08	0.96	39.90	32.92	4.580	2.791	1.64	0.20	11.13	18.41	2.35	18.28	24.85
P20D1V09	0.97	49.90	32.91	4.687	2.891	1.62	0.19	11.10	18.61	2.35	19.62	25.40
P20D1V10	0.98	59.70	32.90	4.706	2.973	1.58	0.17	11.08	18.76	2.35	20.75	24.32
DOWN												
P20D1V11	0.97	55.00	32.90	4.827	2.954	1.63	0.20	11.08	18.76	2.35	20.48	27.38
P20D1V12	0.97	45.50	32.90	4.686	2.887	1.62	0.19	11.09	18.73	2.35	19.56	25.46
P20D1V13	0.97	35.80	32.91	4.579	2.790	1.64	0.20	11.09	18.68	2.35	18.27	24.85
P20D1V14	0.96	25.95	32.92	4.427	2.659	1.66	0.22	11.13	18.40	2.35	16.59	23.86
P20D1V15	0.93	15.70	32.95	4.198	2.409	1.74	0.25	11.20	17.92	2.34	13.61	23.18
P20D1V16	0.88	7.80	32.99	3.774	1.888	2.00	0.33	11.33	16.97	2.34	8.34	22.22
P20D1V17	0.37	1.00	33.51	2.700	1.414	1.91	0.31	12.69	6.99	2.31	4.61	10.66
P20D1V18	0.20	0.50	33.68	2.460	1.362	1.81	0.28	13.14	3.67	2.29	4.25	8.21

Data Plots

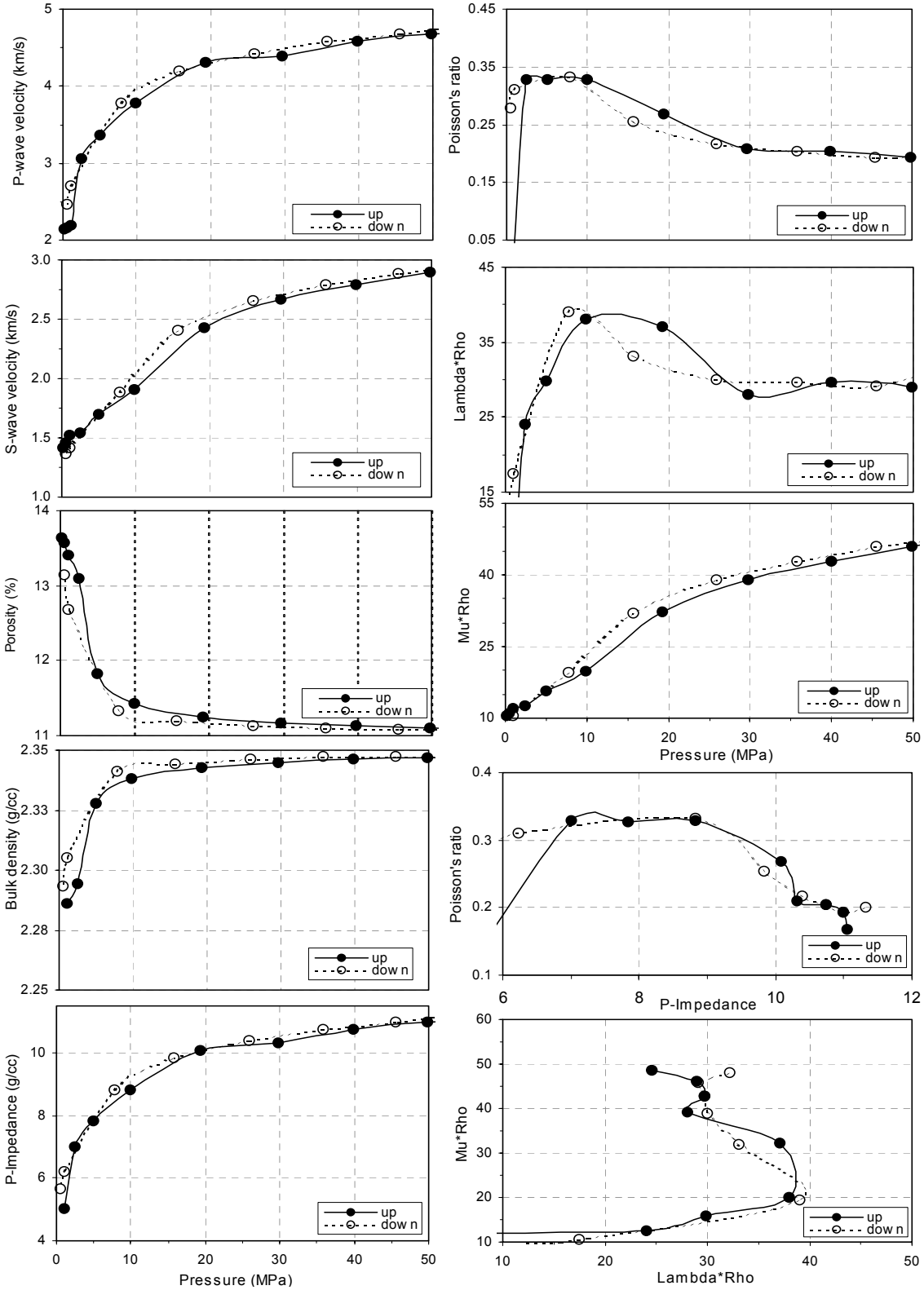
P-wave velocity (km/s)
Poisson's ratio
S-wave velocity (km/s)
Lambda*Rho
Porosity (%)
Mu*Rho
Pressure (MPa)
Bulk density (g/cc)
Poisson's ratio
P-Impedance
P-Impedance (g/cc)
Mu*Rho
Pressure (MPa)
Lambda*Rho
up
down

Sample P30

Type: **medium**

Depth: **2128.95 - 2129.14 m**

Porosity: **9.2%**

Permeability: **11.75 mD**

Grain Density: **2.630 g/cc**

Bulk Density: **2.388 g/cc**

PanCanadian	**Depth (m)**	Length (mm)	Diameter (mm)	Mass (g)	Phi (%)	Perm (mD)	RhoG (g/cc)	RhoB (g/cc)
Sample: P30 Dry	**2128.95**	33.93	24.96	39.58	9.2	11.75	2.630	2.388

File-name P-waves	delta L (mm)	Pc (MPa)	Length (mm)	Vp (km/s)	Vs (km/s)	Vp/Vs	ν	Phi (%)	dPhi (%)	RhoB (g/cc)	Mu (GPa)	K (GPa)
UP												
P30D1V00	0.23	9.6	33.70	4.047	2.508	1.61	0.19	8.72	-61.46	2.40	15.10	19.18
P30D1V01	0.29	20.2	33.64	4.342	2.698	1.61	0.19	8.57	-87.17	2.40	17.50	22.00
P30D1V02	0.32	30.0	33.61	4.622	2.900	1.59	0.18	8.48	-116.44	2.41	20.24	24.43
P30D1V03	0.34	40.2	33.59	4.769	2.974	2.42	0.40	8.42	-0.35	2.41	9.38	42.26
P30D1V04	0.36	50.1	33.57	4.801	3.050	1.57	0.16	8.38	-139.68	2.41	22.42	25.65
DOWN												
P30D1V05	0.36	44.6	33.57	4.781	3.031	1.58	0.16	8.39	-136.69	2.41	22.14	25.56
P30D1V06	0.34	34.9	33.59	4.699	2.974	1.58	0.17	8.42	-127.78	2.41	21.30	24.78
P30D1V07	0.33	25.3	33.60	4.608	2.869	1.61	0.18	8.47	-111.88	2.41	19.82	24.70
P30D1V08	0.30	15.0	33.63	4.389	2.700	1.63	0.20	8.54	-87.50	2.41	17.54	22.96
P30D1V09	0.26	7.7	33.67	3.953	2.428	1.63	0.20	8.64	-51.46	2.40	14.16	18.66

Data Plots

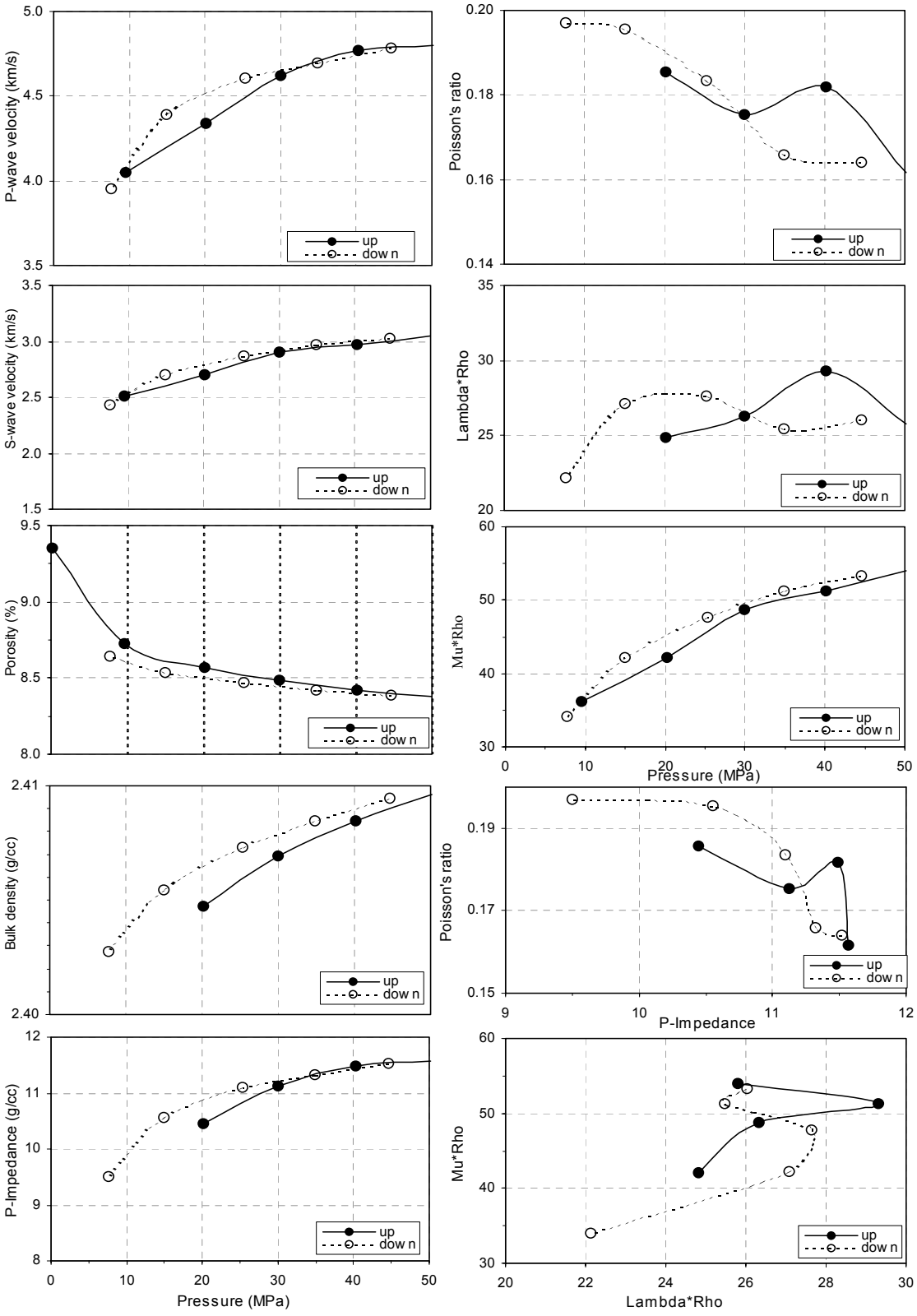
P-wave velocity (km/s)
Poisson's ratio
S-wave velocity (km/s)
Lambda*Rho
Porosity (%)
Mu*Rho
Pressure (MPa)
Bulk density (g/cc)
Poisson's ratio
P-Impedance
P-Impedance (g/cc)
Mu*Rho
Pressure (MPa)
Lambda*Rho
up
down

Sample P35

Type: **medium to coarse**

Depth: **2130.27 - 2130.45 m**

Porosity: **9.6%**

Permeability: **23.95 mD**

Grain Density: **2.650 g/cc**

Bulk Density: **2.396 g/cc**

PanCanadian	Depth (m)	Length (mm)	Diameter (mm)	Mass (g)	Phi (%)	Perm (mD)	RhoG (g/cc)	RhoB (g/cc)
Sample: P35 Dry	2130.27	34.34	24.98	40.14	9.6	23.95	2.650	2.396

File-name P-waves	delta L (mm)	Pc (MPa)	Length (mm)	Vp (km/s)	Vs (km/s)	Vp/Vs	ν	Phi (%)	dPhi (%)	RhoB (g/cc)	Mu (GPa)	K (GPa)
UP												
P35D1V03	0.08	2.5	34.26	2.653	1.505	1.76	0.26	9.81	2.07	2.39	5.41	9.60
P35D1V04	0.10	5.0	34.24	3.027	1.778	1.70	0.24	9.75	2.70	2.39	7.56	11.83
P35D1V05	0.13	10.0	34.21	3.383	2.014	1.68	0.23	9.67	3.50	2.39	9.71	14.45
P35D1V06	0.17	20.2	34.17	3.896	2.360	1.65	0.21	9.58	4.36	2.40	13.35	18.58
P35D1V07	0.19	30.0	34.15	4.253	2.570	1.65	0.21	9.53	4.88	2.40	15.83	22.25
P35D1V08	0.20	40.0	34.14	4.456	2.739	1.63	0.20	9.49	5.29	2.40	17.99	23.63
P35D1V09	0.21	50.3	34.13	4.664	2.894	1.61	0.19	9.45	5.63	2.40	20.10	25.40
P35D1V10	0.22	59.5	34.12	4.760	2.977	1.60	0.18	9.43	5.91	2.40	21.27	26.02
DOWN												
P35D1V11	0.10	55.0	34.24	4.774	2.975	1.60	0.18	9.76	2.60	2.39	21.17	26.28
P35D1V12	0.10	45.5	34.24	4.677	2.899	1.61	0.19	9.76	2.54	2.39	20.10	25.51
P35D1V13	0.09	35.1	34.25	4.482	2.748	1.63	0.20	9.78	2.33	2.39	18.05	23.95
P35D1V14	0.08	25.5	34.26	4.369	2.583	1.69	0.23	9.81	2.13	2.39	15.95	24.36
P35D1V15	0.07	15.4	34.27	4.016	2.339	1.72	0.24	9.83	1.89	2.39	13.07	21.11
P35D1V16	0.06	7.7	34.28	3.476	1.998	1.74	0.25	9.86	1.62	2.39	9.54	16.15

Data Plots

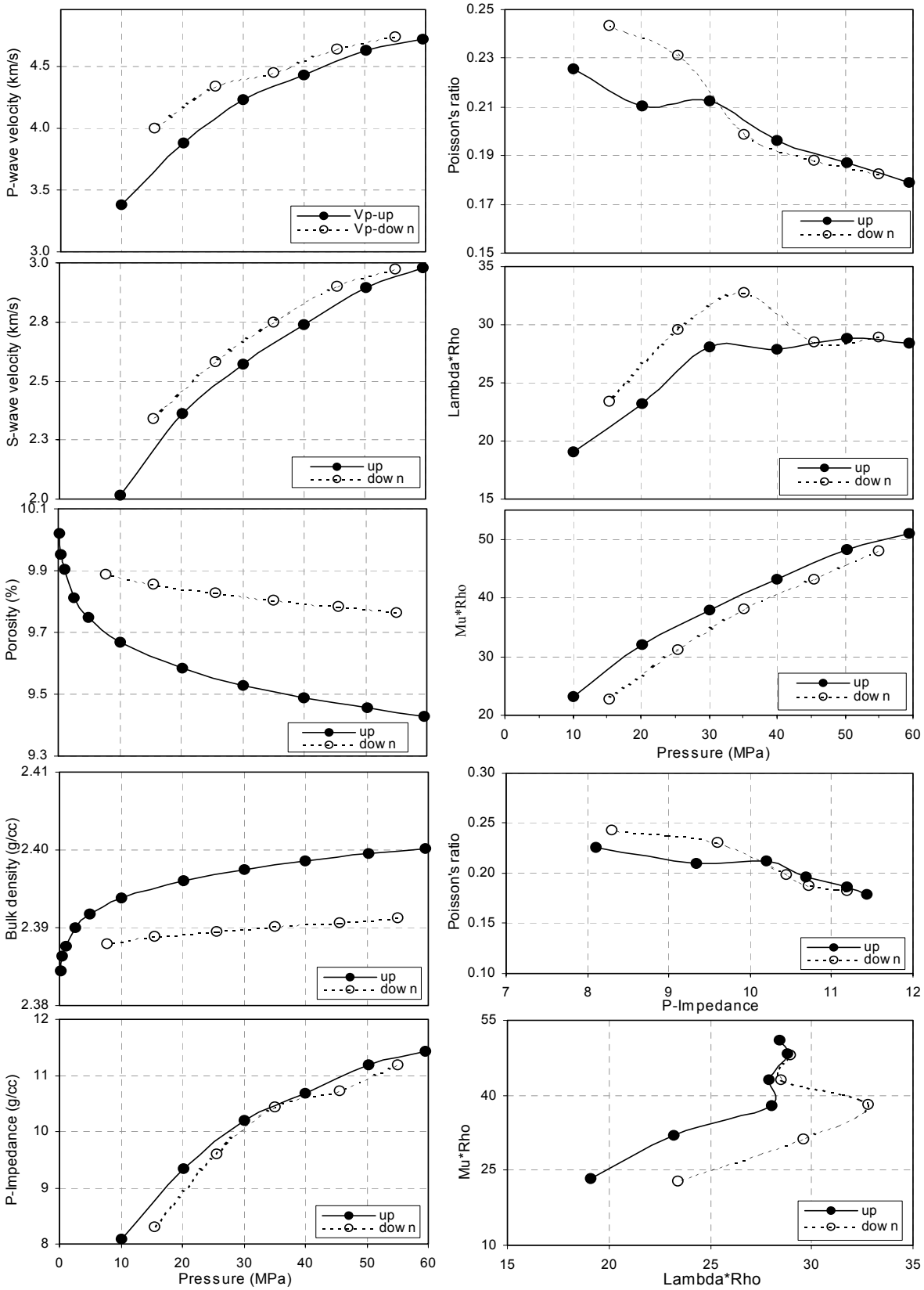
P-wave velocity (km/s)
Vp-up
Vp-down
Poisson's ratio
up
down
S-wave velocity (km/s)
Lambda*Rho
Porosity (%)
Mu*Rho
Pressure (MPa)
Bulk density (g/cc)
P-Impedance
P-Impedance (g/cc)
Mu*Rho
Lambda*Rho

Sample P41

Type: **medium to coarse**

Depth: **2132.08 - 2132.28 m**

Porosity: **11.7%**

Permeability: **45.73 mD**

Grain Density: **2.660 g/cc**

Bulk Density: **2.349 g/cc**

PanCanadian	**Depth**	Length (mm)	Diameter (mm)	Mass (g)	Phi (%)	Perm (md)	RhoG (g/cc)	RhoB (g/cc)
Sample: P41 Dry	**2132.08**	34.24	24.98	39.53	11.7	45.73	2.660	2.349

File-name P-waves	delta L (mm)	Pc (MPa)	Length (mm)	Vp (km/s)	Vs (km/s)	Vp/Vs	ν	Phi (%)	dPhi (%)	RhoB (g/cc)	Mu (GPa)	K (GPa)
UP												
P41D1V00	0.00		34.24					11.11	0.00	2.36	0.00	0.00
P41D1V01	0.15	10.0	34.09	2.961	2.096	1.41	0.00	10.71	3.53	2.37	10.39	6.89
P41D1V02	0.19	20.0	34.05	3.89	2.392	1.63	0.20	10.60	4.55	2.37	13.56	17.78
P41D1V03	0.22	30.4	34.02	4.431	2.650	1.67	0.22	10.53	5.17	2.37	16.65	24.35
P41D1V04	0.24	40.2	34.00	4.435	2.756	1.61	0.19	10.48	5.64	2.37	18.02	22.64
P41D1V05	0.26	50.2	33.98	4.545	2.843	1.60	0.18	10.43	6.05	2.37	19.18	23.45
DOWN												
P41D1V06	0.25	44.7	33.99	4.548	2.819	1.61	0.25	10.44	5.99	2.37	16.33	27.32
P41D1V07	0.24	35.3	34.00	4.428	2.753	1.61	0.27	10.47	5.72	2.37	14.71	26.91
P41D1V08	0.22	25.4	34.02	4.092	2.623	1.56	0.32	10.52	5.29	2.37	10.40	25.84
P41D1V09	0.20	15.4	34.04	3.890	2.490	1.56	0.50	10.59	4.67	2.37	0.00	35.85
P41D1V10	0.16	7.6	34.08	3.455	2.094	1.65	0.50	10.68	3.87	2.37	0.00	28.26

Data Plots

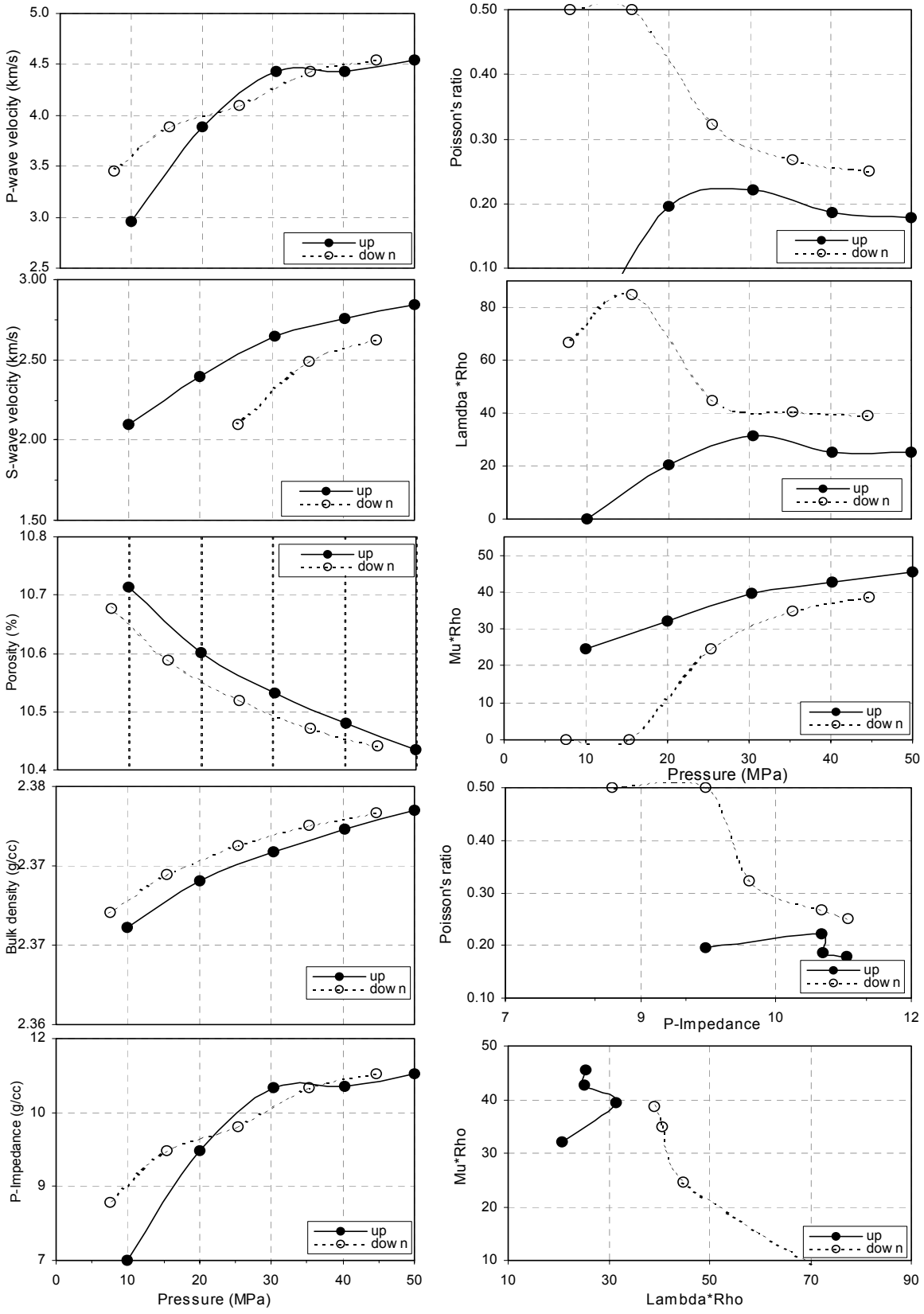
P-wave velocity (km/s)
Poisson's ratio
S-wave velocity (km/s)
Lamdba *Rho
Porosity (%)
Mu*Rho
Pressure (MPa)
Bulk density (g/cc)
Poisson's ratio
P-Impedance
P-Impedance (g/cc)
Mu*Rho
Pressure (MPa)
Lambda*Rho
up
down

Sample P53

Type: **coarse**

Depth: **2135.44 - 2135.57 m**

Porosity: **13.9%**

Permeability: **16.68 mD**

Grain Density: **2.650 g/cc**

Bulk Density: **2.316 g/cc**

PanCanadian	**Depth**	Length (mm)	Diameter (mm)	Mass (g)	Phi (%)	Perm (md)	RhoG (g/cc)	RhoB (g/cc)
Sample: P53 Dry	**2124.28**	34.36	24.94	39.29	11.7	16.68	2.650	2.340

File-name P-waves	delta L (mm)	Pc (MPa)	Length (mm)	Vp (km/s)	Vs (km/s)	Vp/Vs	ν	Phi (%)	dPhi (%)	RhoB (g/cc)	Mu (GPa)	K (GPa)
UP												
Ref	0.00		34.36					11.66	0.00	2.34		
P82D1V00	0.35	19.8	34.01	3.926	2.595	1.51	0.11	10.75	7.83	2.37	15.93	15.22
P82D1V01	0.37	30.0	34.00	4.628	2.747	1.68	0.23	10.71	8.17	2.37	17.86	26.87
P82D1V02	0.38	40.0	33.98	4.553	2.850	1.60	0.18	10.67	8.45	2.37	19.23	23.43
P82D1V03	0.39	49.6	33.97	4.547	2.938	1.55	0.14	10.65	8.70	2.37	20.44	21.70
DOWN												
P82D1V04	0.39	44.6	33.97	4.562	2.920	1.56	0.15	10.65	8.68	2.37	20.19	22.36
P82D1V05	0.38	35.0	33.98	4.553	2.846	1.60	0.18	10.67	8.51	2.37	19.17	23.51
P82D1V06	0.37	24.8	33.99	4.548	2.725	1.67	0.22	10.70	8.27	2.37	17.57	25.52
P82D1V07	0.35	15.2	34.01	4.006	2.546	1.57	0.16	10.74	7.91	2.37	15.33	17.52

Data Plots

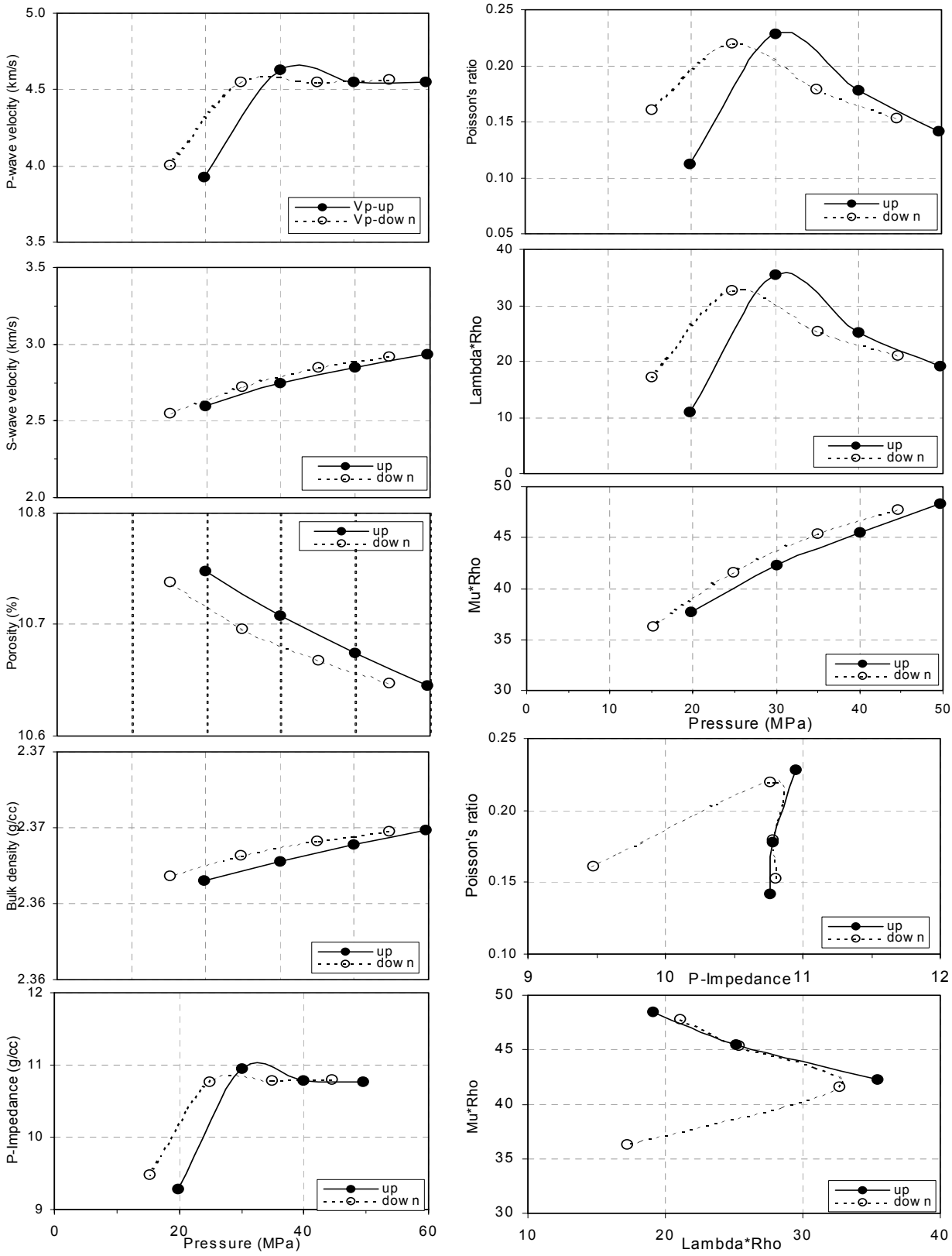
P-wave velocity (km/s)
Vp-up
Vp-down
S-wave velocity (km/s)
Porosity (%)
Bulk density (g/cc)
P-Impedance (g/cc)
Pressure (MPa)
Poisson's ratio
Lambda*Rho
Mu*Rho
P-Impedance
Lambda*Rho
up
down

Sample P54

Type: **coarse**

Depth: **2135.57 - 2135.78 m**

Porosity: **13.3%**

Permeability: **246.25 mD**

Grain Density: **2.650 g/cc**

Bulk Density: **2.298 g/cc**

PanCanadian	**Depth**	Length (mm)	Diameter (mm)	Mass (g)	Phi (%)	Perm (md)	RhoG (g/cc)	RhoB (g/cc)
Sample: P54 Dry	**2135.57**	34.76	24.79	36.80	13.3	246.25	2.650	2.298

File-name P-waves	delta L (mm)	Pc (MPa)	Length (mm)	Vp (km/s)	Vs (km/s)	Vp/Vs	ν	Phi (%)	dPhi (%)	RhoB (g/cc)	Mu (GPa)	K (GPa)
UP												
P54D1V00	0.00	1.0	34.76	2.623	1.643	1.60		17.25	0.00	2.19		
P54D1V01	0.68	5.0	34.08	3.305	2.169	1.52	0.12	15.60	9.56	2.24	10.52	10.40
P54D1V02	0.93	10.0	33.83	3.505	2.346	1.49	0.09	14.98	13.17	2.25	12.40	11.15
P54D1V03	1.12	19.6	33.64	3.943	2.462	1.60	0.18	14.49	16.00	2.27	13.74	16.92
P54D1V04	1.20	30.0	33.56	4.266	2.598	1.64	0.21	14.30	17.13	2.27	15.33	20.89
P54D1V05	1.25	40.0	33.52	4.260	2.666	1.60	0.18	14.17	17.83	2.27	16.17	19.72
P54D1V06	1.28	50.0	33.48	4.378	2.730	1.60	0.18	14.09	18.35	2.28	16.97	21.01
DOWN												
P54D1V07	1.27	44.8	33.49	4.362	2.713	1.61	0.18	14.10	18.26	2.28	16.75	20.97
P54D1V08	1.25	35.3	33.51	4.262	2.679	1.59	0.17	14.15	17.95	2.27	16.33	19.55
P54D1V09	1.23	25.0	33.54	4.134	2.601	1.59	0.17	14.23	17.53	2.27	15.38	18.34
P54D1V10	1.17	15.5	33.60	3.945	2.566	1.54	0.13	14.38	16.66	2.27	14.94	15.39
P54D1V11	1.00	7.5	33.77	3.427	2.184	1.57	0.16	14.81	14.17	2.26	10.77	12.16
P54D1V12	0.28	1.1	34.48	2.73	1.548	1.76	0.26	16.58	3.91	2.21	5.30	9.41

Data Plots

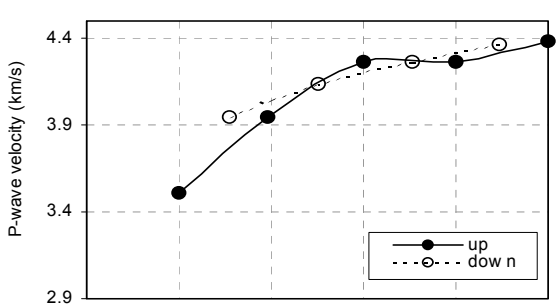
P-wave velocity (km/s)
4.4
3.9
3.4
2.9
up
down

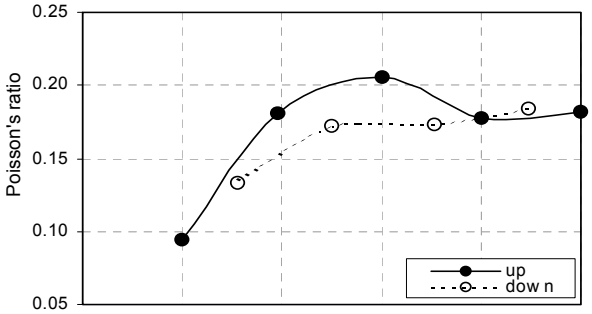
Poisson's ratio
0.25
0.20
0.15
0.10
0.05
up
down

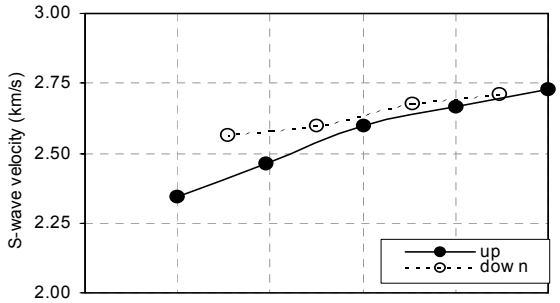
S-wave velocity (km/s)
3.00
2.75
2.50
2.25
2.00
up
down

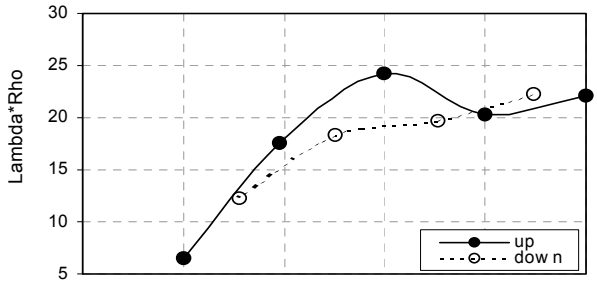
Lambda*Rho
30
25
20
15
10
5
up
down

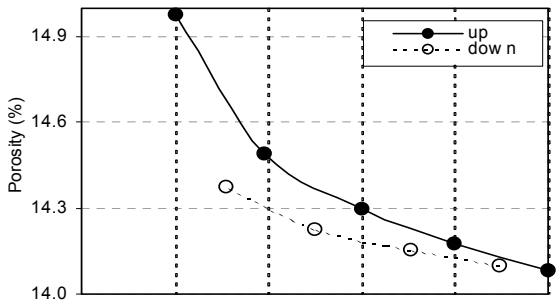
Porosity (%)
14.9
14.6
14.3
14.0
up
down

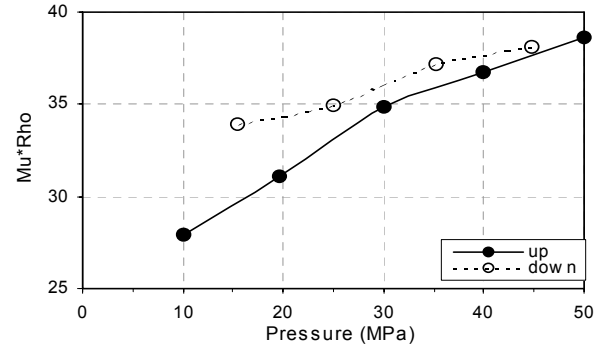
Mu*Rho
40
35
30
25
0
10
20
30
40
50
Pressure (MPa)
up
down

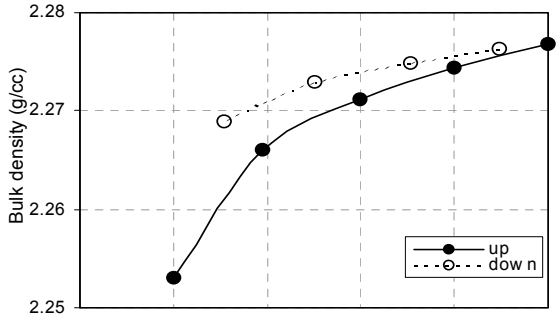
Bulk density (g/cc)
2.28
2.27
2.26
2.25
up
down

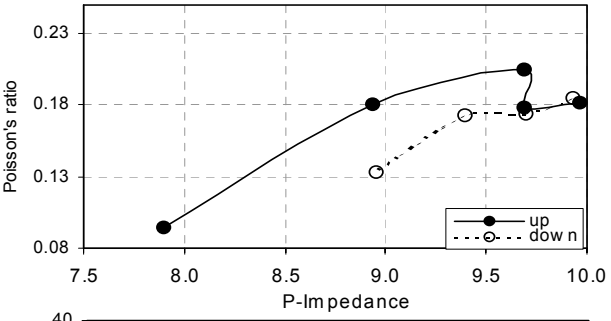
Poisson's ratio
0.23
0.18
0.13
0.08
7.5
8.0
8.5
9.0
9.5
10.0
P-Impedance
up
down

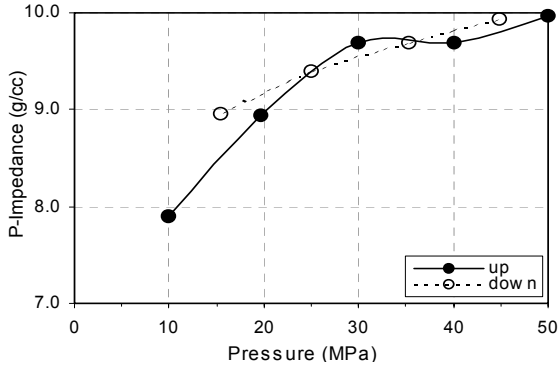
P-Impedance (g/cc)
10.0
9.0
8.0
7.0
0
10
20
30
40
50
Pressure (MPa)
up
down

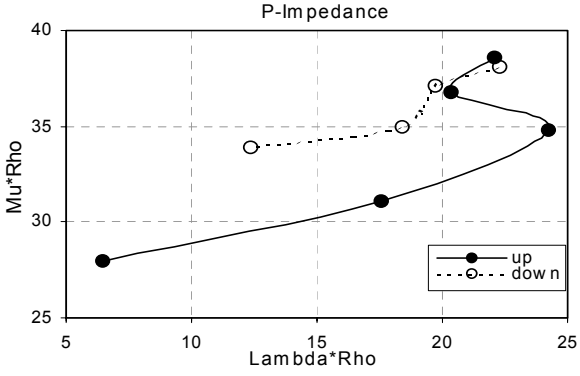
Mu*Rho
40
35
30
25
5
10
15
20
25
Lambda*Rho
up
down

Sample P63

Type: **fine**

Depth: **2138.12 - 2138.25 m**

Porosity: **13.5%**

Permeability: **22.13 mD**

Grain Density: **2.650 g/cc**

Bulk Density: **2.292 g/cc**

PanCanadian	**Depth**	Length (mm)	Diameter (mm)	Mass (g)	Phi (%)	Perm (md)	RhoG (g/cc)	RhoB (g/cc)
Sample: P63 Dry	**2138.12**	33.74	24.78	36.71	13.5	22.13	2.650	2.292

File-name P-waves	delta L (mm)	Pc (MPa)	Length (mm)	Vp (km/s)	Vs (km/s)	Vp/Vs	ν	Phi (%)	dPhi (%)	RhoB (g/cc)	Mu (GPa)	K (GPa)
UP												
P63D1V01	0.17	5.0	33.57	2.82	1.872	1.51	0.11	14.40	2.96	2.27	7.95	7.44
P63D1V02	0.27	10.0	33.47	3.109	2.012	1.55	0.14	14.16	4.60	2.27	9.21	9.71
P63D1V03	0.28	20.0	33.46	3.620	2.326	1.56	0.15	14.12	4.82	2.28	12.31	13.41
P63D1V04	0.32	30.0	33.43	3.931	2.561	1.53	0.13	14.03	5.44	2.28	14.94	15.28
P63D1V05	0.34	40.1	33.40	4.262	2.720	1.57	0.16	13.97	5.88	2.28	16.87	18.92
P63D1V06	0.36	50.0	33.38	4.470	2.849	1.57	0.17	13.91	6.24	2.28	18.03	21.55
DOWN												
P63D1V07	0.36	43.8	33.39	4.365	2.811	1.55	0.31	13.93	6.13	2.28	12.08	27.36
P63D1V08	0.34	35.0	33.40	4.263	2.709	1.57	0.35	13.97	5.88	2.28	9.52	28.75
P63D1V09	0.32	25.0	33.42	3.926	2.548	1.54	0.50	14.03	5.47	2.28	0.00	35.12
P63D1V10	0.28	15.0	33.46	3.472	2.301	1.51	0.50	14.12	4.84	2.28	0.00	27.43
P63D1V11	0.24	7.5	33.51	3.102	2.043	1.52	0.50	14.24	4.04	2.27	0.00	21.87

Data Plots

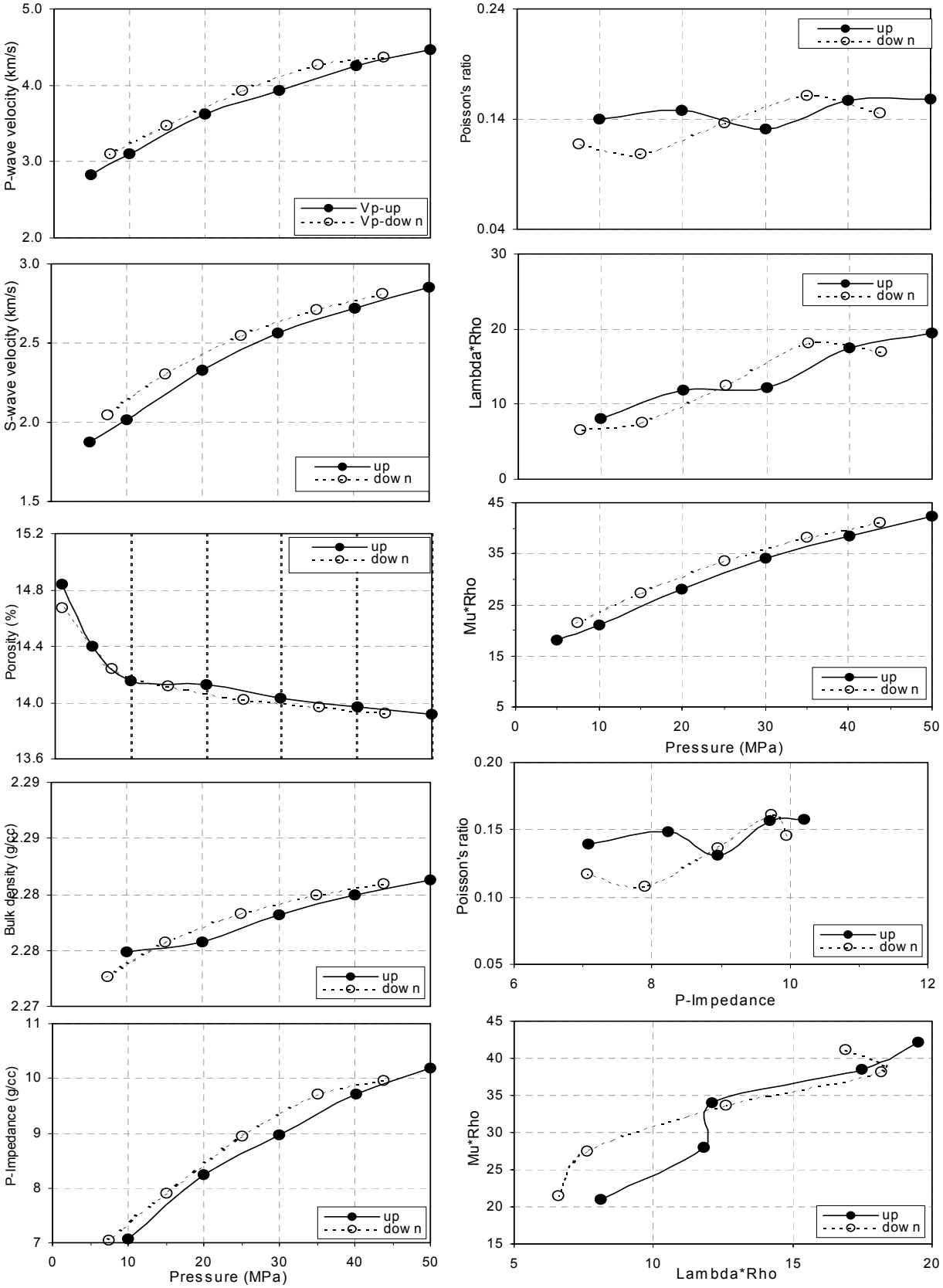
P-wave velocity (km/s)
Vp-up
Vp-down
Poisson's ratio
up
down
S-wave velocity (km/s)
Lambda*Rho
Porosity (%)
Mu*Rho
Pressure (MPa)
Bulk density (g/cc)
Poisson's ratio
P-Impedance
P-Impedance (g/cc)
Mu*Rho
Lambda*Rho

Sample P67

Type: **very fine**

Depth: **2139.00 - 2139.14 m**

Porosity: **9.3%**

Permeability: **0.12 mD**

Grain Density: **2.650 g/cc**

Bulk Density: **2.388 g/cc**

PanCanadian	**Depth**	Length (mm)	Diameter (mm)	Mass (g)	Phi (%)	Perm (md)	RhoG (g/cc)	RhoB (g/cc)
Sample: P67 Dry	**2139.00**	34.53	24.96	39.86	9.3	0.12	2.650	2.404

File-name P-waves	delta L (mm)	Pc (MPa)	Length (mm)	Vp (km/s)	Vs (km/s)	Vp/Vs	ν	Phi (%)	dPhi (%)	RhoB (g/cc)	Mu (GPa)	K (GPa)
UP												
P67D1V00	0.00	1.0	34.53	3.334	2.190	1.52	0.12	10.95	0.00	2.36	11.32	11.14
P67D1V01	0.11	2.5	34.41	3.417	2.243	1.52	0.12	10.66	2.67	2.37	11.91	11.76
P67D1V02	0.20	5.0	34.33	3.556	2.304	1.54	0.14	10.43	4.75	2.37	12.60	13.21
P67D1V03	0.30	10.2	34.23	3.902	2.462	1.58	0.17	10.17	7.10	2.38	14.43	17.01
P67D1V04	0.38	19.9	34.15	4.236	2.644	1.60	0.18	9.96	9.03	2.39	16.68	20.57
P67D1V05	0.43	30.0	34.10	4.545	2.819	1.61	0.19	9.83	10.20	2.39	18.99	24.04
P67D1V06	0.46	40.3	34.07	4.707	2.934	1.60	0.18	9.75	10.98	2.39	20.59	25.54
P67D1V07	0.48	50.4	34.04	4.834	3.011	1.61	0.18	9.68	11.55	2.39	21.70	27.00
DOWN												
P67D1V08	0.48	44.8	34.05	4.831	2.998	1.61	0.19	9.69	11.51	2.39	21.51	27.17
P67D1V09	0.47	35.2	34.06	4.723	2.943	1.60	0.18	9.73	11.11	2.39	20.72	25.73
P67D1V10	0.44	25.2	34.09	4.559	2.841	1.60	0.18	9.80	10.51	2.39	19.29	23.96
P67D1V11	0.40	15.3	34.13	4.338	2.693	1.61	0.19	9.90	9.55	2.39	17.31	21.84
P67D1V12	0.33	7.4	34.20	4.010	2.500	1.60	0.18	10.09	7.88	2.38	14.89	18.46
P67D1V13	0.21	2.4	34.32	3.483	2.283	1.53	0.12	10.41	4.94	2.37	12.37	12.30
P67D1V14	0.11	1.0	34.42	3.414	2.199	1.55	0.15	10.67	2.59	2.37	11.45	0.42

Data Plots

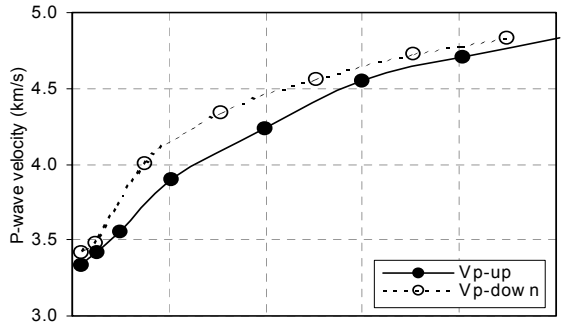
P-wave velocity (km/s)
Vp-up
Vp-down

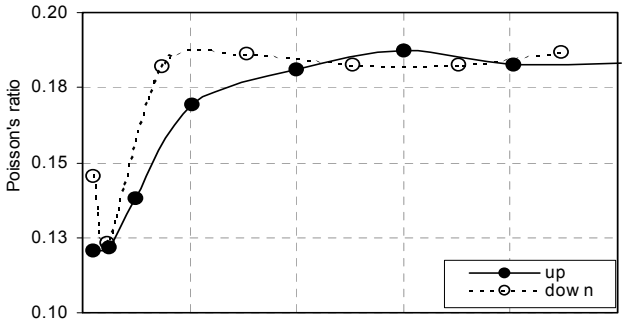
Poisson's ratio
up
down

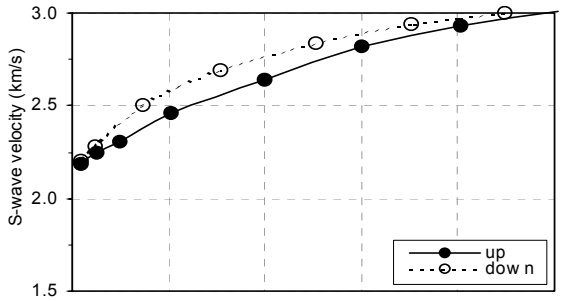
S-wave velocity (km/s)
up
down

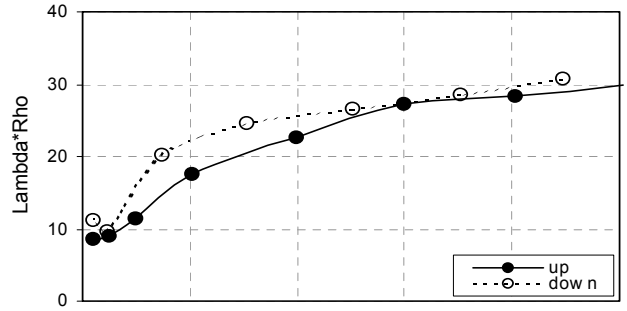
Lambda*Rho
up
down

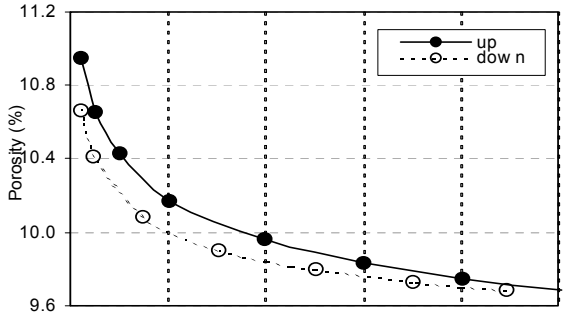
Porosity (%)
up
down

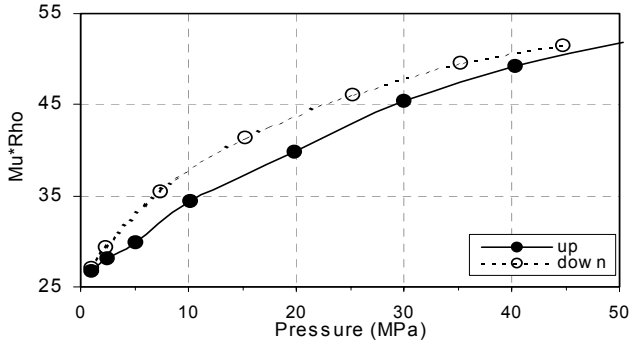
Mu*Rho
up
down
Pressure (MPa)

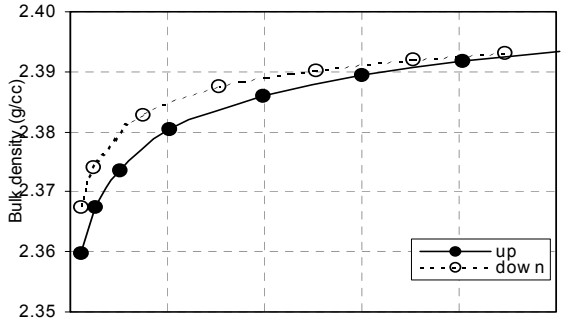
Bulk density (g/cc)
up
down

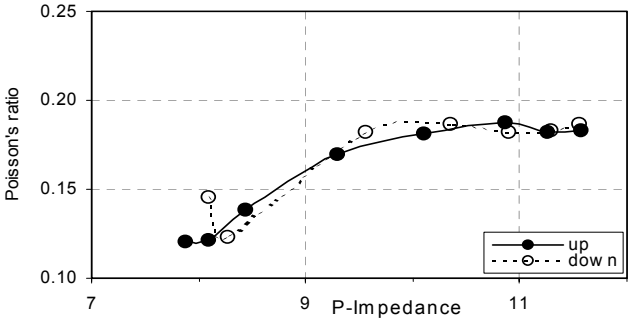
Poisson's ratio
up
down
P-Impedance

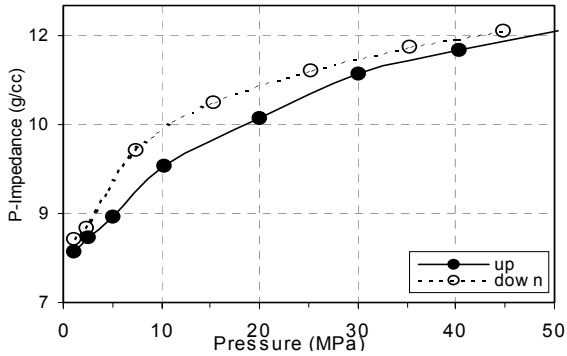
P-Impedance (g/cc)
up
down
Pressure (MPa)

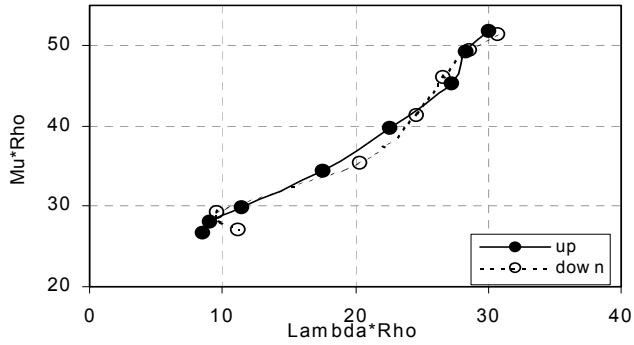
Mu*Rho
up
down
Lambda*Rho

Sample P71

Type: **very fine**

Depth: **2140.14 - 2140.56 m**

Porosity: **11.5%**

Permeability: **0.50 mD**

Grain Density: **2.650 g/cc**

Bulk Density: **2.345 g/cc**

PanCanadian	**Depth**	Length (mm)	Diameter (mm)	Mass (g)	Phi (%)	Perm (md)	RhoG (g/cc)	RhoB (g/cc)
Sample: P71 Dry	**2140.14**	33.94	24.94	39.14	11.5	0.50	2.650	2.345

File-name P-waves	delta L (mm)	Pc (MPa)	Length (mm)	Vp (km/s)	Vs (km/s)	Vp/Vs	ν	Phi (%)	dPhi (%)	RhoB (g/cc)	Mu (GPa)	K (GPa)
UP												
Ref	0.00		33.94					10.88	0.00	2.36		
P71D1V00	0.17	30.0	33.77	4.43	2.860	1.55	0.14	10.44	4.05	2.37	19.41	20.69
P71D1V01	0.19	40.0	33.75	4.616	2.959	1.56	0.15	10.38	4.59	2.37	20.79	22.88
P71D1V02	0.21	50.0	33.73	4.725	3.023	1.56	0.15	10.33	5.05	2.38	21.72	24.10

Data Plots

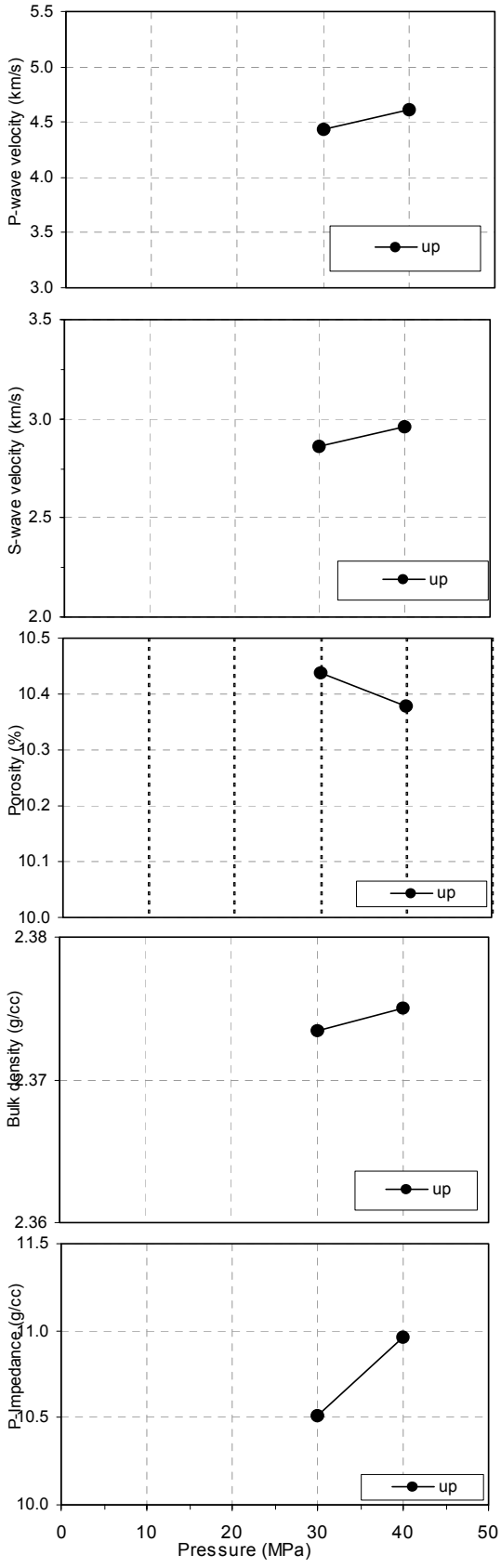
P-wave velocity (km/s)
5.5
5.0
4.5
4.0
3.5
3.0
up
S-wave velocity (km/s)
3.5
3.0
2.5
2.0
up
Porosity (%)
10.5
10.4
10.3
10.2
10.1
10.0
up
Bulk density (g/cc)
2.38
2.37
2.36
up
P-Impedance (g/cc)
11.5
11.0
10.5
10.0
up
0
10
20
30
40
50
Pressure (MPa)

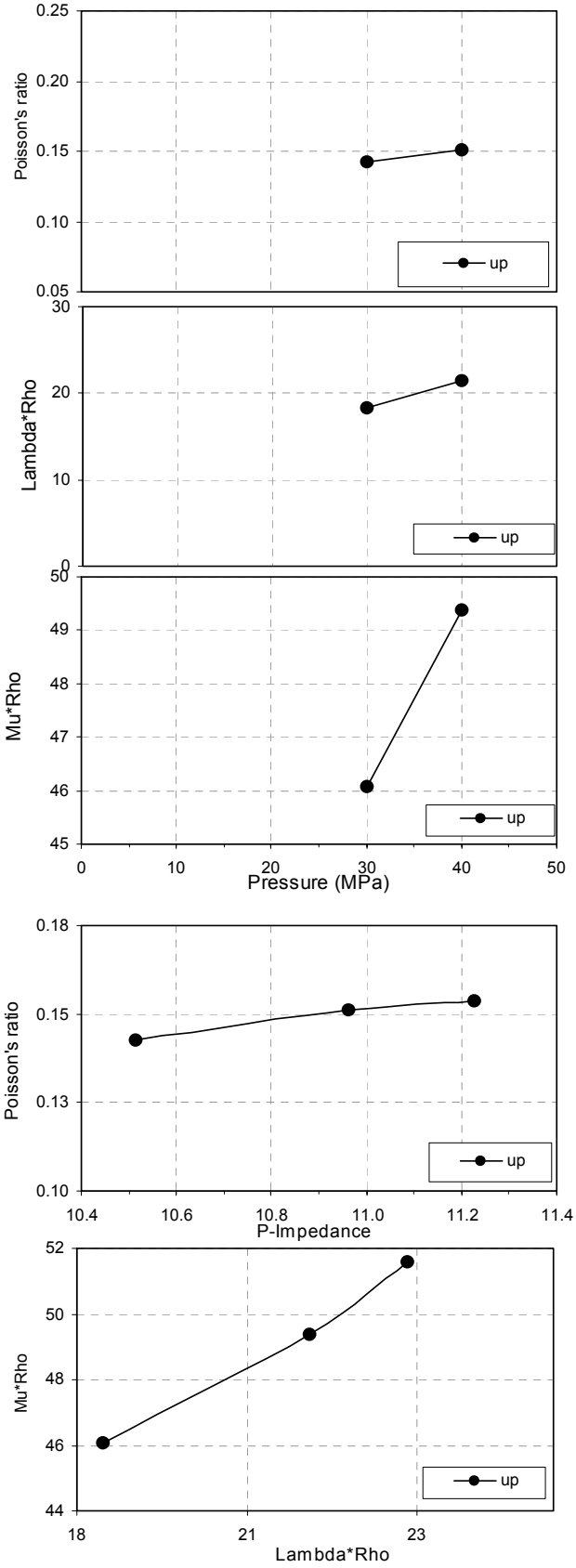
Poisson's ratio
0.25
0.20
0.15
0.10
0.05
up
Lambda*Rho
30
20
10
0
up
Mu*Rho
50
49
48
47
46
45
up
0
10
20
30
40
50
Pressure (MPa)
Poisson's ratio
0.18
0.15
0.13
0.10
up
10.4
10.6
10.8
11.0
11.2
11.4
P-Impedance
Mu*Rho
52
50
48
46
44
up
18
21
23
Lambda*Rho

Sample P74

Type: **medium**

Depth: **2141.10 - 2141.79 m**

Porosity: **13.7%**

Permeability: **10.60 mD**

Grain Density: **2.650 g/cc**

Bulk Density: **2.287 g/cc**

PanCanadian	**Depth**	Length (mm)	Diameter (mm)	Mass (g)	Phi (%)	Perm (md)	RhoG (g/cc)	RhoB (g/cc)
Sample: P74 Dry	**2141.10**	33.81	24.89	36.93	13.7	15.15	2.650	2.287

File-name P-waves	delta L (mm)	Pc (MPa)	Length (mm)	Vp (km/s)	Vs (km/s)	Vp/Vs	ν	Phi (%)	dPhi (%)	RhoB (g/cc)	Mu (GPa)
UP											
P74D1V00	0.00	1.0	33.81	2.458	1.615	1.52	0.12	15.25	0.00	2.25	5.86
P74D1V01	0.06	5.0	33.75	3.059	1.865	1.64	0.20	15.10	0.94	2.25	7.83
P74D1V02	0.09	10.1	33.71	3.420	2.212	1.55	0.14	15.01	1.53	2.25	11.02
P74D1V03	0.14	19.9	33.67	3.948	2.437	1.62	0.19	14.90	2.31	2.26	13.39
1V04 doesn't exist											
P74D1V05	0.17	30.2	33.64	4.394	2.578	1.70	0.24	14.83	2.74	2.26	15.00
P74D1V06	0.18	40.1	33.62	4.403	2.703	1.63	0.20	14.79	3.03	2.26	16.50
P74D1V07	0.20	50.0	33.61	4.606	2.801	1.64	0.21	14.74	3.30	2.26	17.73
DOWN											
P74D1V08	0.19	44.8	33.61	4.507	2.776	1.62	0.19	14.76	3.19	2.26	17.41
P74D1V08	0.18	35.4	33.63	4.386	2.690	1.63	0.20	14.80	2.95	2.26	16.34
P74D1V09	0.16	25.2	33.65	4.288	2.560	1.68	0.22	14.84	2.65	2.26	14.79
P74D1V10	0.13	15.4	33.67	3.850	2.456	1.57	0.16	14.91	2.22	2.25	13.60
P74D1V11	0.10	7.8	33.70	3.417	2.233	1.53	0.13	14.98	1.73	2.25	11.23
P74D1V12	0.03	1.2	33.78	2.632	1.663	1.58	0.17	15.17	0.52	2.25	6.22

Data Plots

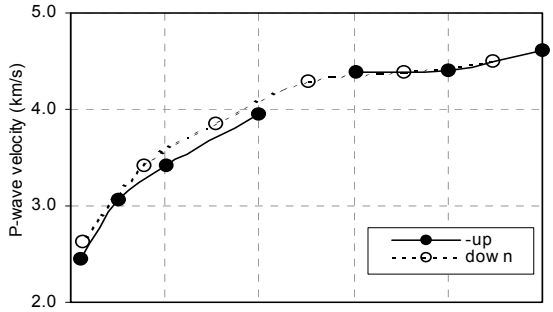
P-wave velocity (km/s)
5.0
4.0
3.0
2.0
up
down

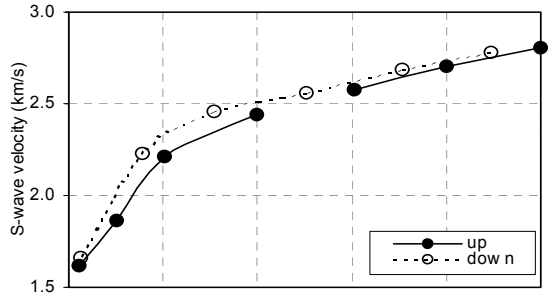
S-wave velocity (km/s)
3.0
2.5
2.0
1.5
up
down

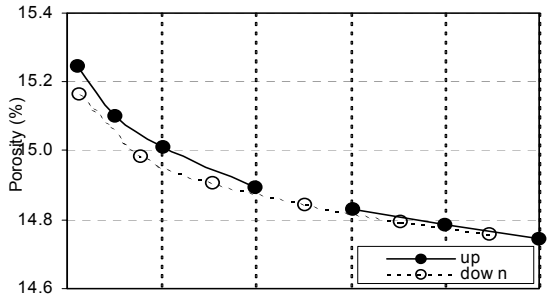
Porosity (%)
15.4
15.2
15.0
14.8
14.6
up
down

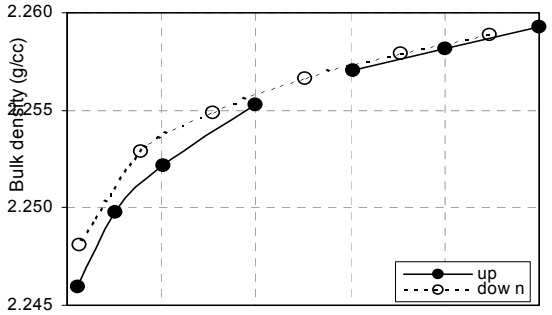
Bulk density (g/cc)
2.260
2.255
2.250
2.245
up
down

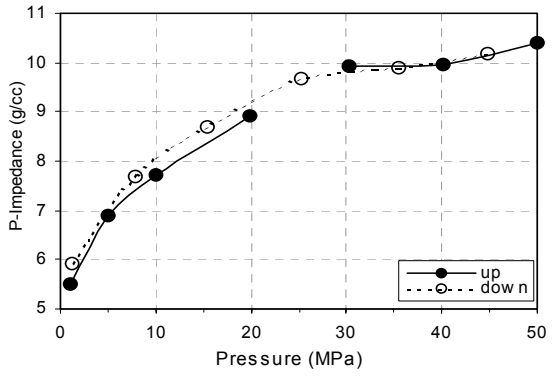
P-Impedance (g/cc)
11
10
9
8
7
6
5
0
10
20
30
40
50
Pressure (MPa)
up
down

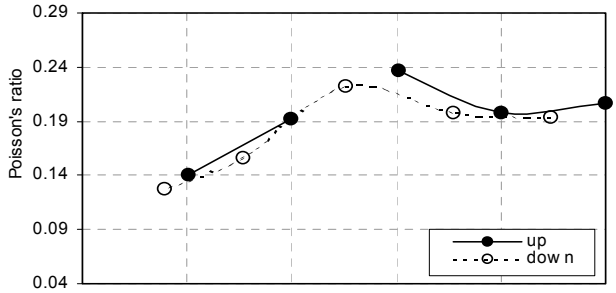
Poisson's ratio
0.29
0.24
0.19
0.14
0.09
0.04
up
down

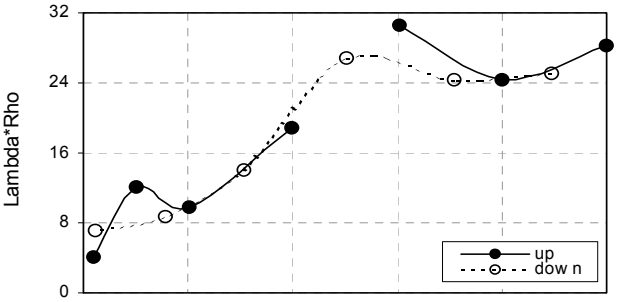
Lambda*Rho
32
24
16
8
0
up
down

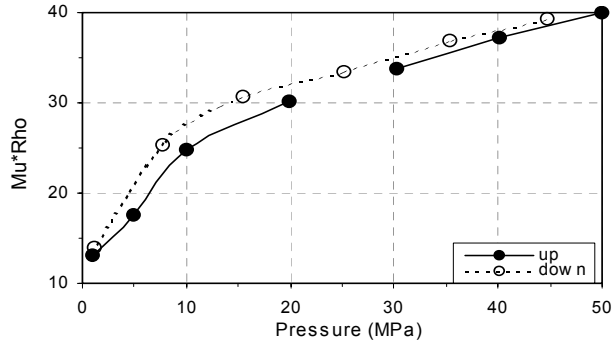
Mu*Rho
40
30
20
10
0
10
20
30
40
50
Pressure (MPa)
up
down

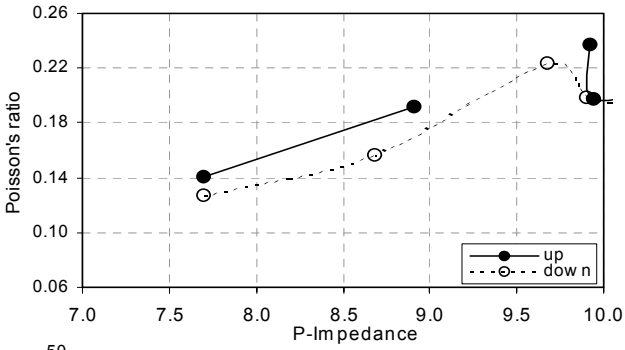
Poisson's ratio
0.26
0.22
0.18
0.14
0.10
0.06
7.0
7.5
8.0
8.5
9.0
9.5
10.0
P-Impedance
up
down

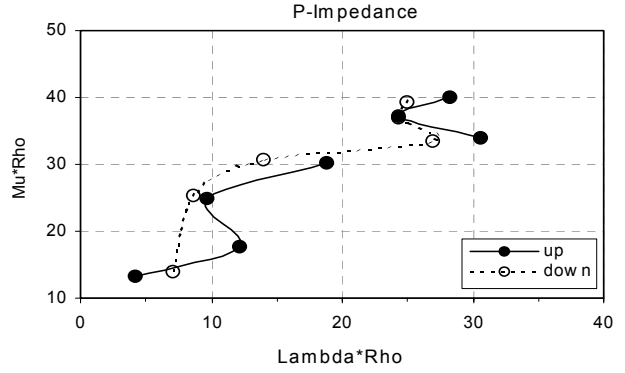
Mu*Rho
50
40
30
20
10
0
10
20
30
40
Lambda*Rho
up
down

Sample P79

Type: **medium**

Depth: **2143.27 - 2143.35 m**

Porosity: **13.3%**

Permeability: **67.84 mD**

Grain Density: **2.650 g/cc**

Bulk Density: **2.298 g/cc**

PanCanadian	**Depth**	Length (mm)	Diameter (mm)	Mass (g)	Phi (%)	Perm (md)	RhoG (g/cc)	RhoB (g/cc)
Sample: P79 Dry	**2143.27**	33.51	24.81	36.31	13.3	67.84	2.650	2.298

File-name P-waves	delta L (mm)	Pc (MPa)	Length (mm)	Vp (km/s)	Vs (km/s)	Vp/Vs	ν	Phi (%)	dPhi (%)	RhoB (g/cc)	Mu (GPa)	K (GPa)
UP												
P79D1V05	0.51	10.0	33.01	3.343	1.729	1.93	0.32	14.13	8.39	2.28	6.80	16.36
P79D1V06	0.60	19.9	32.92	3.755	2.015	1.86	0.30	13.90	9.93	2.28	9.26	19.82
P79D1S07	0.64	30.3	32.87	4.284	2.488	1.72	0.25	13.77	10.72	2.29	14.14	23.08
P79D1V08	0.67	40.1	32.84	4.286	2.575	1.66	0.22	13.69	11.26	2.29	15.17	21.79
P79D1V09	0.70	50.2	32.82	4.433	2.686	1.65	0.21	13.63	11.63	2.29	16.51	22.96
P79D1V10	0.71	59.7	32.80	4.651	2.776	1.68	0.22	13.58	11.95	2.29	17.65	26.01
DOWN												
P79D1V11	0.71	54.7	32.80	4.596	2.752	1.67	0.22	13.59	11.92	2.29	17.34	25.25
P79D1V12	0.70	45.1	32.81	4.487	2.673	1.68	0.22	13.62	11.73	2.29	16.36	24.28
P79D1V13	0.68	35.5	32.83	4.293	2.575	1.67	0.22	13.66	11.43	2.29	15.17	21.94
P79D1V14	0.65	25.0	32.86	4.048	2.437	1.66	0.22	13.74	10.92	2.29	13.58	19.36
P79D1V15	0.61	15.1	32.90	3.682	2.083	1.77	0.26	13.86	10.15	2.28	9.90	17.74
P79D1V16	0.54	7.4	32.97	3.267	1.976	1.65	0.21	14.03	9.04	2.28	8.90	12.45

Data Plots

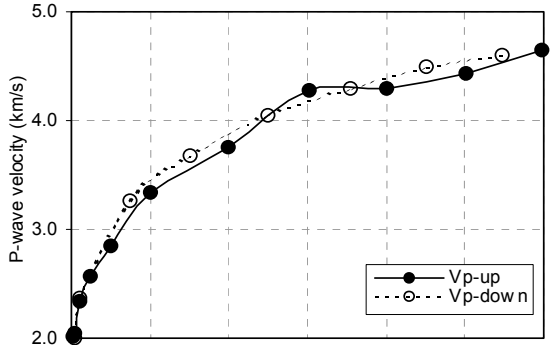
P-wave velocity (km/s)
5.0
4.0
3.0
2.0
Vp-up
Vp-down

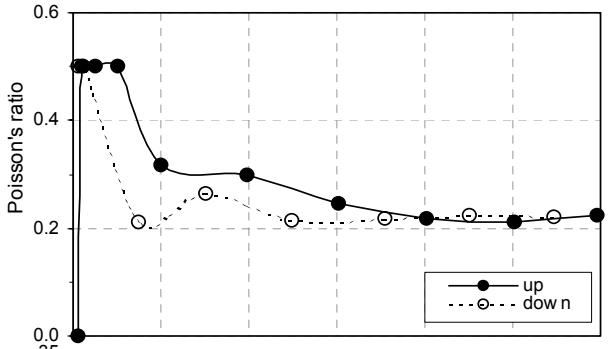
Poisson's ratio
0.6
0.4
0.2
0.0
up
down

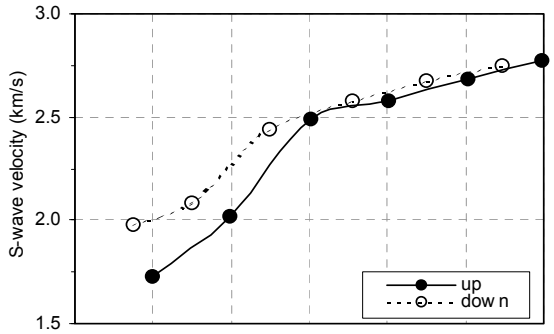
S-wave velocity (km/s)
3.0
2.5
2.0
1.5
up
down

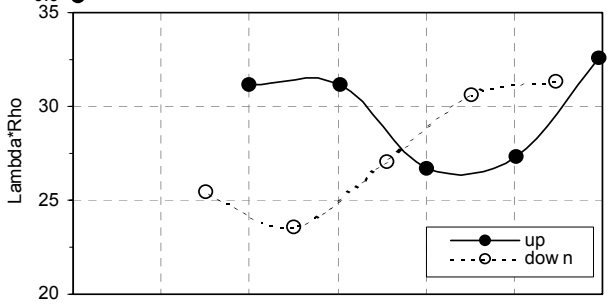
Lambda*Rho
35
30
25
20
up
down

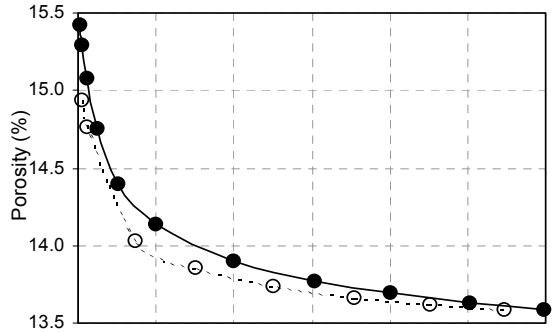
Porosity (%)
15.5
15.0
14.5
14.0
13.5

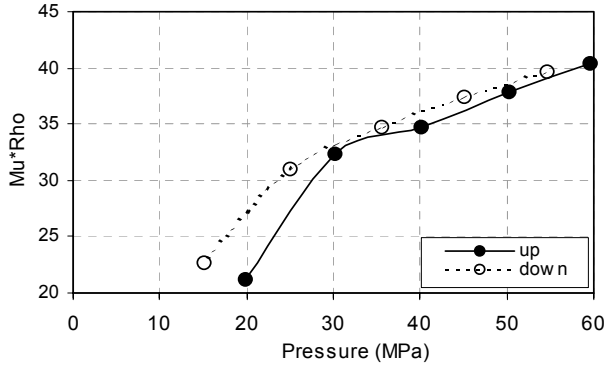
Mu*Rho
45
40
35
30
25
20
0
10
20
30
40
50
60
Pressure (MPa)
up
down

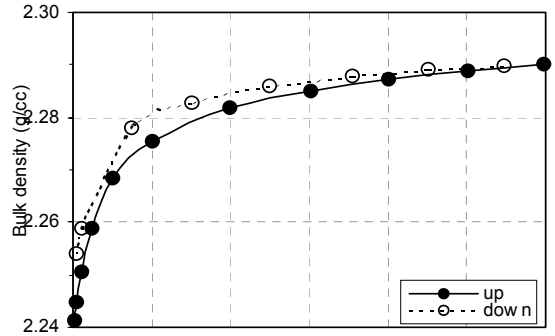
Bulk density (g/cc)
2.30
2.28
2.26
2.24
up
down

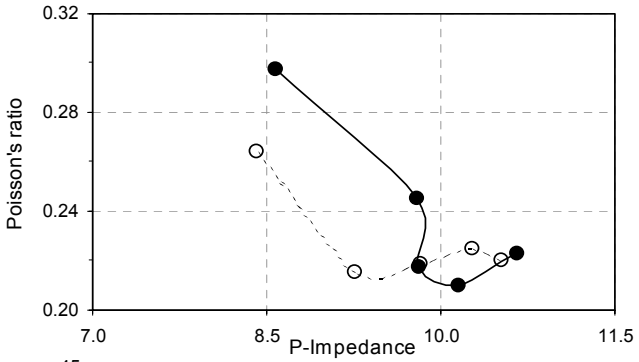
Poisson's ratio
0.32
0.28
0.24
0.20
7.0
8.5
10.0
11.5
P-Impedance

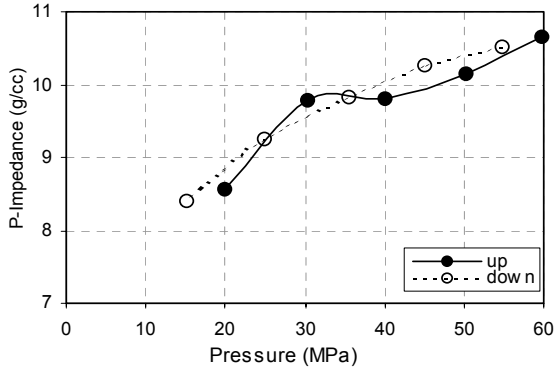
P-Impedance (g/cc)
11
10
9
8
7
0
10
20
30
40
50
60
Pressure (MPa)
up
down

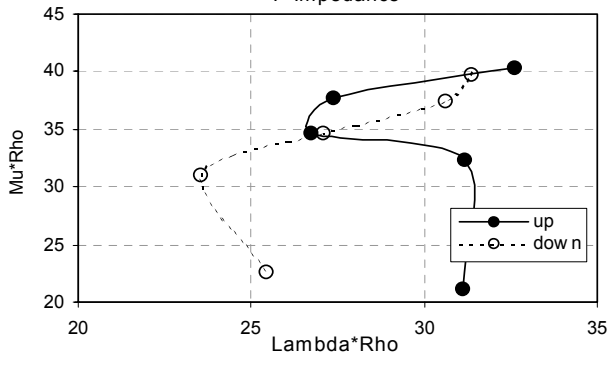
Mu*Rho
45
40
35
30
25
20
20
25
30
35
Lambda*Rho
up
down

Sample P82

Type: **very fine**

Depth: **2146.02 - 2146.29 m**

Porosity: **10.9%**

Permeability: **0.16 mD**

Grain Density: **2.660 g/cc**

Bulk Density: **2.370 g/cc**

PanCanadian	**Depth**	Length (mm)	Diameter (mm)	Mass (g)	Phi (%)	Perm (md)	RhoG (g/cc)	RhoB (g/cc)
Sample: P82 Dry	**2146.02**	34.25	24.90	39.73	10.9	0.16	2.660	2.37

File-name P-waves	delta L (mm)	Pc (MPa)	Length (mm)	Vp (km/s)	Vs (km/s)	Vp/Vs	ν	Phi (%)	dPhi (%)	RhoB (g/cc)	Mu (GPa)	K (GPa)
UP												
P82D1V02	0.19	10.0	34.06	3.534	2.392	1.48	0.08	9.94	4.86	2.40	13.71	11.64
P82D1V03	0.27	19.9	33.98	4.088	2.520	1.62	0.19	9.74	6.79	2.40	15.25	19.80
P82D1V04	0.30	30.0	33.95	4.552	2.692	1.69	0.23	9.64	7.69	2.40	17.42	26.58
P82D1V05	0.34	40.1	33.91	4.544	2.788	1.63	0.20	9.54	8.65	2.41	18.70	24.75
P82D1V06	0.35	50.0	33.90	4.661	2.869	1.62	0.20	9.51	8.96	2.41	19.81	25.88
DOWN												
P82D1V07	0.35	44.5	33.90	4.668	2.849	1.64	0.20	9.52	8.87	2.41	19.54	26.40
P82D1V08	0.39	35.1	33.86	4.657	2.803	1.66	0.22	9.42	9.79	2.41	18.93	27.01
P82D1V09	0.36	25.3	33.89	4.535	2.722	1.67	0.22	9.49	9.18	2.41	17.84	25.73
P82D1V10	0.33	15.3	33.92	4.184	2.594	1.61	0.19	9.57	8.42	2.41	16.19	20.53

Data Plots

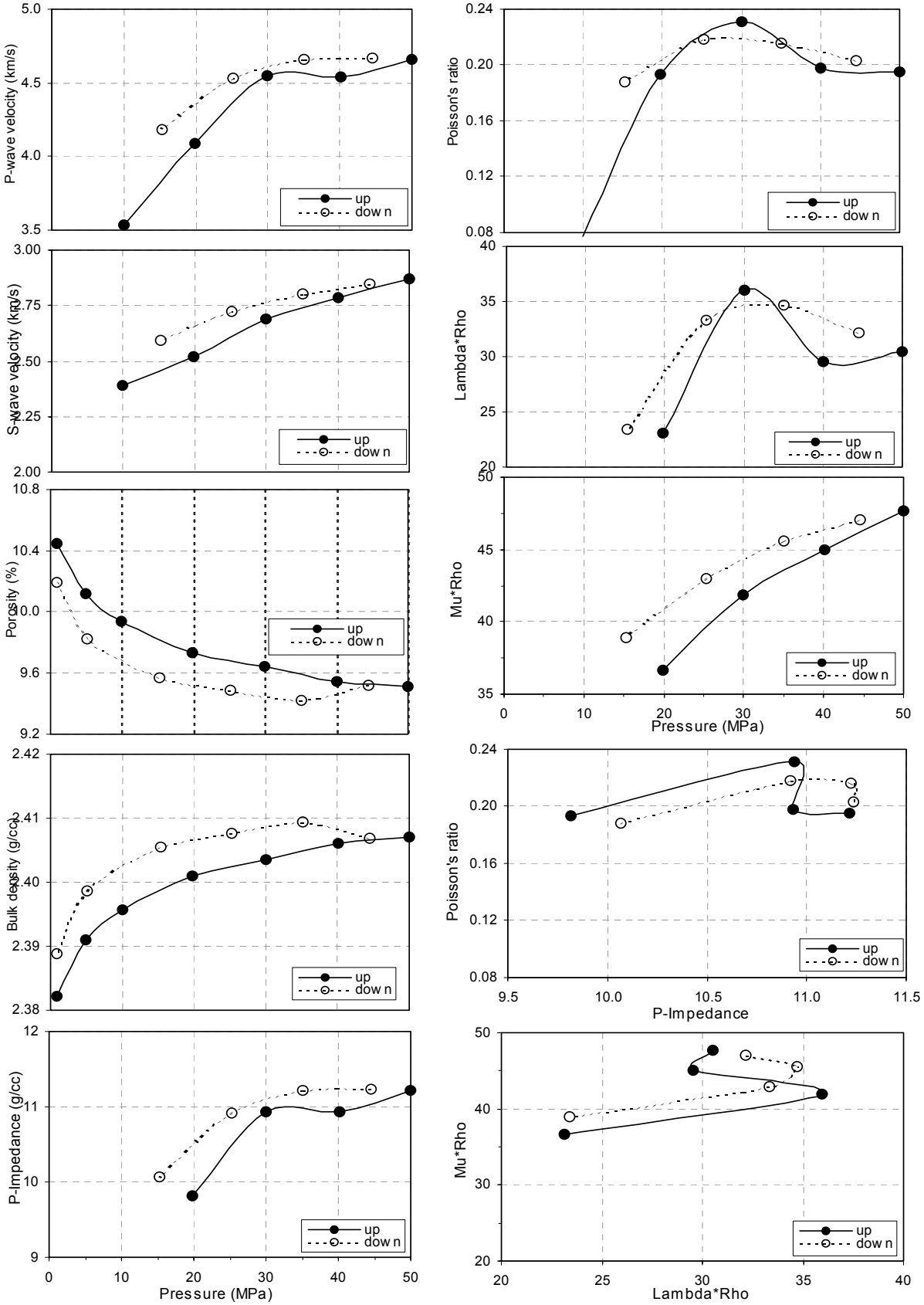
P-wave velocity (km/s)
S-wave velocity (km/s)
Porosity (%)
Bulk density (g/cc)
P-Impedance (g/cc)
Pressure (MPa)
Poisson's ratio
Lambda*Rho
Mu*Rho
P-Impedance
up
down

Sample P83

Type: **very fine**

Depth: **2146.29 - 2146.61 m**

Porosity: **10.9%**

Permeability: **0.26 mD**

Grain Density: **2.650 g/cc**

Bulk Density: **2.361 g/cc**

PanCanadian	**Depth**	Length (mm)	Diameter (mm)	Mass (g)	Phi (%)	Perm (md)	RhoG (g/cc)	RhoB (g/cc)
Sample: P83 Dry	**2146.29**	33.83	24.90	39.18	10.9	0.26	2.650	2.361

File-name P-waves	delta L (mm)	Pc (MPa)	Length (mm)	Vp (km/s)	Vs (km/s)	Vp/Vs	ν	Phi (%)	dPhi (%)	RhoB (g/cc)	Mu (GPa)	K (GPa)
UP												
Ref	0.00		33.83					10.26	0.00	2.38		
P83D1V00	0.22	30.8	33.61	4.299	2.700	1.59	0.17	9.66	5.85	2.39	17.45	20.97
P83D1V01	0.26	50.2	33.57	4.579	2.873	1.59	0.18	9.56	6.82	2.40	19.78	23.87

Data Plots

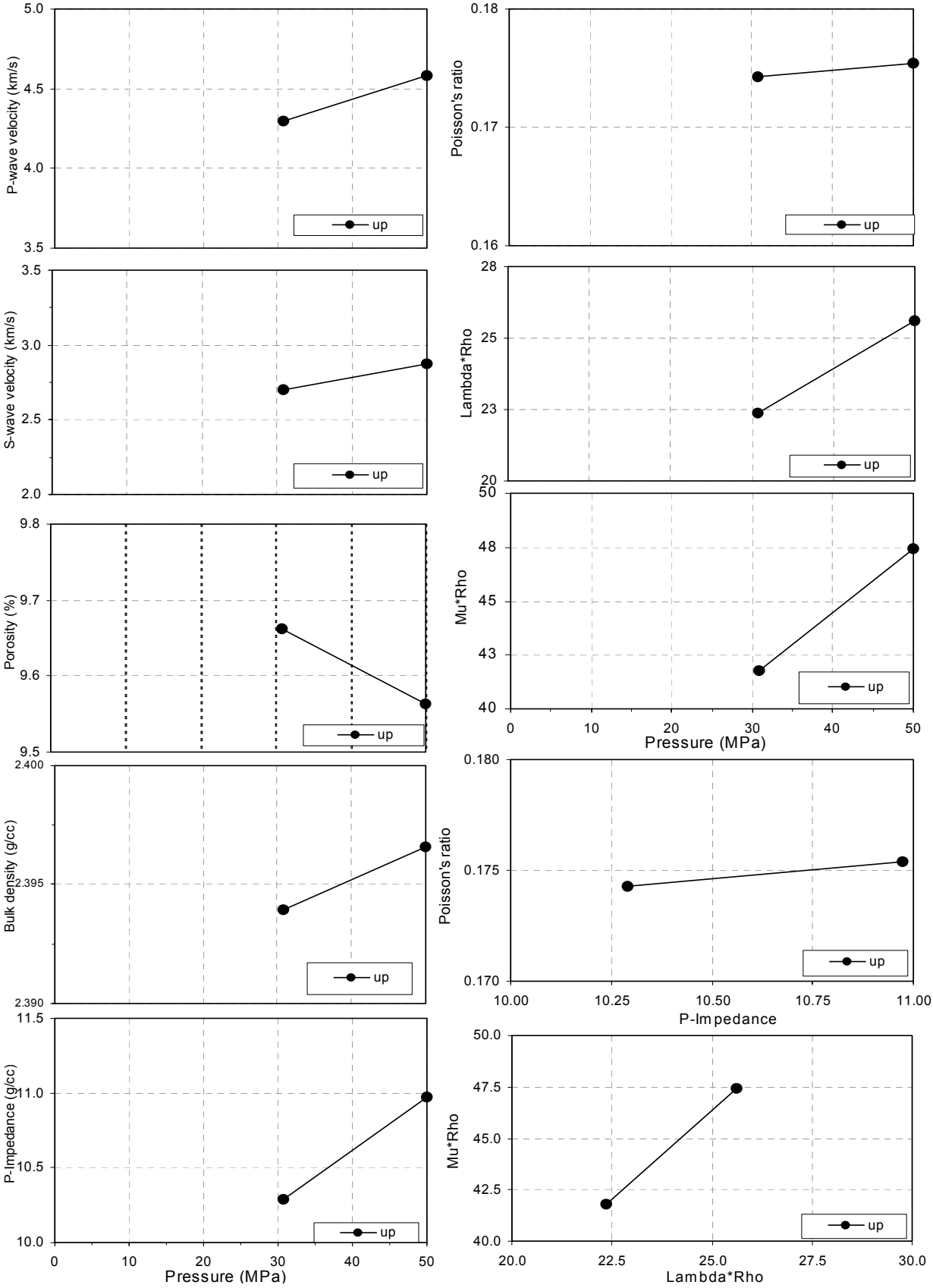
P-wave velocity (km/s)
5.0
4.5
4.0
3.5
up
Poisson's ratio
0.18
0.17
0.16
up
S-wave velocity (km/s)
3.5
3.0
2.5
2.0
up
Lambda*Rho
28
25
23
20
up
Porosity (%)
9.8
9.7
9.6
9.5
up
Mu*Rho
50
48
45
43
40
up
0
10
20
30
40
50
Pressure (MPa)
Bulk density (g/cc)
2.400
2.395
2.390
up
Poisson's ratio
0.180
0.175
0.170
up
10.00
10.25
10.50
10.75
11.00
P-Impedance
P-Impedance (g/cc)
11.5
11.0
10.5
10.0
up
Mu*Rho
50.0
47.5
45.0
42.5
40.0
up
0
10
20
30
40
50
Pressure (MPa)
20.0
22.5
25.0
27.5
30.0
Lambda*Rho